
Electronic Thesis and Dissertation Repository

12-15-2010 12:00 AM

Wake Dynamics and Passive Flow Control of a Blunt Trailing Edge Profiled Body

Lakshmana Sampat Doddipatla
The University of Western Ontario

Supervisor
Dr.Horia Hangan
The University of Western Ontario

Graduate Program in Civil and Environmental Engineering
A thesis submitted in partial fulfillment of the requirements for the degree in Doctor of Philosophy
© Lakshmana Sampat Doddipatla 2010

Follow this and additional works at: <https://ir.lib.uwo.ca/etd>



Part of the [Civil and Environmental Engineering Commons](#)

Recommended Citation

Doddipatla, Lakshmana Sampat, "Wake Dynamics and Passive Flow Control of a Blunt Trailing Edge Profiled Body" (2010). *Electronic Thesis and Dissertation Repository*. 71.
<https://ir.lib.uwo.ca/etd/71>

This Dissertation/Thesis is brought to you for free and open access by Scholarship@Western. It has been accepted for inclusion in Electronic Thesis and Dissertation Repository by an authorized administrator of Scholarship@Western. For more information, please contact wlsadmin@uwo.ca.

**WAKE DYNAMICS AND PASSIVE FLOW CONTROL OF A BLUNT TRAILING
EDGE PROFILED BODY**

(Thesis Format: Monograph)

by:

Lakshmana Sampat Doddipatla

Department of Civil and Environmental Engineering
Faculty of Engineering Science

A thesis submitted in partial fulfillment
of the requirements for the degree of
Doctor of Philosophy

The School of Graduate and Postdoctoral Studies
The University of Western Ontario
London, Ontario, Canada

© Lakshmana Sampat Doddipatla, 2010

**THE UNIVERSITY OF WESTERN ONTARIO
THE SCHOOL OF GRADUATE AND POSTDOCTORAL STUDIES**

CERTIFICATE OF EXAMINATION

Supervisor

Dr. Horia Hangan

Examiners

Dr. Craig Miller

Dr. Diana Inculet

Dr. Kamran Siddiqui

Dr. Serhiy Yarusevych

The thesis by
Lakshmana Sampat Doddipatla

Entitled

**WAKE DYNAMICS AND PASSIVE FLOW CONTROL OF A BLUNT TRAILING
EDGE PROFILED BODY**

is accepted in partial fulfillment of the
requirements for the degree of
Doctor of Philosophy

Date _____

Chair of the Thesis Examination Board

ABSTRACT

Wake flows behind two-dimensional bodies are dominated mainly by two types of coherent structures, namely, the Karman Benard vortices and the streamwise vortices, also referred to as rolls and ribs respectively. The three-dimensional wake instabilities lead to distinct instability modes (mode-A, mode-B and mode-C or mode S) depending on the flow Reynolds number and geometric shape. The present investigation explores the mechanism by which the flow transitions take place to three-dimensionality in the near wake of a profiled leading edge and blunt trailing edge body. Experiments consisting of a combination of Planar Laser Induced Fluorescence visualizations and Particle Image Velocimetry measurements are conducted for Reynolds numbers ranging from 250 to 46000. The results indicate that three instability modes, denoted by mode-A, mode-B and mode-C, appear in the wake transition to three-dimensionality, but their order of appearance does not occur through the traditional route as observed in circular cylinder flows. It is found that mode-C instability with a spanwise spacing varying between 1.2 to 2.8D (D being the trailing edge thickness) dominates the near wake development. This result is explored further with the aim to devise a simple passive control method to mitigate vortex shedding for blunt trailing edge bodies.

The effect of a trailing edge spanwise sinusoidal perturbation (SSP) is investigated for a range of Reynolds numbers (Re_D) spanning the transition range from $Re_D = 550$ up to 46000. PIV measurements at different vertical and horizontal locations are performed to study changes in the streamwise and spanwise vortices. The base drag and strength of vortex shedding decrease with wavy trailing edge compared to the straight trailing edge. Proper Orthogonal Decomposition (POD) of the obtained PIV data indicates that the spanwise sinusoidal perturbation redistributes the relative energy, enhancing the streamwise vortices and, as a result, suppressing the Karman Benard rolls.

KEYWORDS: Blunt Trailing-Edge-Profiled Body, Vortex Shedding, Wake Instabilities, Passive Flow Control, Drag Reduction, Particle Image Velocimetry (PIV), Planar Laser Induced Fluorescence (PLIF), Proper Orthogonal Decomposition (POD)

CO-AUTHORSHIP

The dissertation uses monograph format specified by the school of graduate and postdoctoral studies, The University of Western Ontario, London, Ontario, Canada. Chapters 3 and 4 will be submitted for publication to *Journal of Fluid Mechanics* and *Experiments in Fluids*, respectively. These papers are authored by Lakshmana Sampat Doddipatla along with his supervisor, Horia Hangan, and co-authors Arash Naghib-Lahouti, Vibhav Durgesh and Jonathan Naughton. Lakshmana Sampat Doddipatla is the principal author, who conducted all the experiments and the data analysis, except for PLIF and PIV water tunnel measurements for which the experimental data are shared with Arash Naghib-Lahouti. The analysis however is carried independently. Vibhav Durgesh helped with the experimental setup at the University of Wyoming Aeronautics Laboratory under the supervision of Prof. Jonathan Naughton.

Chapter 3

Doddipatla, L.S., Lahouthi, A.N. & Hangan, H. Near wake topology of a profiled blunt trailing edge body. To be submitted to *J. Fluid Mech.*

Chapter 4

Doddipatla, L.S., Hangan, H., Durgesh, V. & Naughton, J.W. Wake dynamics resulting from trailing edge spanwise sinusoidal perturbation. To be submitted to *Exp. Fluids*

Dedicated to my parents

ACKNOWLEDGEMENT

It is with immense pleasure that I begin to write this section and I would like to thank all those who have helped me to get to this stage. I sincerely thank my supervisor Dr. Horia Hangan for his patience, guidance and direction throughout this work. I would also like to thank Dr. Vibhav Durgesh and Dr. Jonathan Naughton at the University of Wyoming for assisting me with wind tunnel experiments and providing helpful discussions on the implementation of Proper Orthogonal Decomposition. I would also like to thank Arash Naghib-Lahouti for assisting me with water tunnel measurements. Thanks are due to Dr. Kamran Siddiqui for providing the PIV system for the water tunnel experiments at The University of Western Ontario. Finally, I am grateful to Mr. Chris Vandelaar for his assistance in the machine shop.

I want to express thanks to all of my colleagues at The Boundary Layer Wind Tunnel Laboratory for their kindness and support. I am grateful to my friends Diwakar Natrajan, Padmavathi Sagi and Bilal Bakht for making my stay in Canada a cherishable experience.

I express my deep gratitude to my parents, Dr. Vivekananda Prasad Doddipatla and Giri Kumari Doddipatla, and my brother, Dr. Rama Sanand Doddipatla, for their unwavering faith and continuous support during the long period of my education. I would like to especially thank my wife, Kranthi, for her unlimited support, encouragement and patience.

TABLE OF CONTENTS

Certificate of Examination	ii
Abstract	iii
Co-Authorship	v
Acknowledgement	vii
Table of Contents	viii
List of Figures	xi
List of Tables	xix
List of Symbols	xx
1 Introduction.....	1
1.1 Previous Studies on Three-Dimensional Near Wakes	4
1.2 Previous Studies on Flow Control Using Spanwise Sinusoidal Perturbation (SSP).....	8
1.3 Motivation and Objectives	12
2 Experimental Setup and Analysis Approach.....	15
2.1 Experimental Facility.....	15
2.1.1 Water Tunnel Facility	15
2.1.2 Wind Tunnel Facility.....	19
2.2 Models	21
2.2.1 Water Tunnel Model	21
2.2.2 Wind Tunnel Model.....	23
2.3 Instrumentation.....	25
2.3.1 Planar Laser Induced Fluorescence (PLIF).....	26
2.3.2 Particle Image Velocimetry (PIV)	26
2.3.3 Pressure Transducers	30
2.3.4 Data Acquisition	33
2.4 Analysis Approach.....	35
2.4.1 Proper Orthogonal Decomposition (POD)	35

2.4.1.1	Mathematical Description	36
2.4.1.2	POD Convergence	38
2.4.2	Phase Averaging	42
3	Near Wake Coherent Structures of a Blunt Trailing-edge-profiled Body	47
3.1	Integral Parameters	48
3.2	Water Tunnel Measurements.....	51
3.2.1	XY Plane Results	51
3.2.2	XZ Plane Results	63
3.2.2.1	Different Near Wake Transition Modes	63
3.2.2.2	Schematics of mode-A and mode-B	71
3.2.2.3	Origin of Asymmetric Mode C Instability	72
3.2.2.4	Instantaneous Velocity and Vorticity Field.....	75
3.2.2.5	POD Analysis Results	77
3.2.2.6	Effect of Higher Reynolds Numbers	86
3.3	Wind Tunnel Measurements	93
3.3.1	XY Plane Result.....	93
3.3.2	XZ Plane Results	96
3.4	Summary.....	103
4	Wake Dynamics Resulting From Trailing Edge Spanwise Sinusoidal Perturbation (SSP)	104
4.1	Wavelength selection for SSP	104
4.2	Mean Flow Analysis	107
4.2.1	Mean Drag and Base Pressure Coefficient.....	107
4.2.2	Mean Velocity	111
4.2.3	Formation Length.....	114

4.3	Turbulent Flow Analysis.....	118
4.3.1	Power Spectral Density	118
4.3.2	POD Modes and Coefficients	120
4.3.3	Wake Topology.....	125
4.4	Summary.....	130
5	Conclusions and Recommendations	131
5.1	Near Wake Structure of a Blunt Trailing-Edge-Profiled Body	132
5.2	Near Wake Dynamics Resulting From Trailing Edge Spanwise Sinusoidal Perturbation (SSP).....	133
5.3	Recommendations for Future Work.....	134
5.3.1	Near Wake Instabilities	134
5.3.2	SSP Control	135
5.3.3	Future Direction	136
	Appendix.....	137
A.1	PIV Measurement Error Analysis	137
A.2	POD Formulation	142
A.3	Sample POD Code	144
A.4	Hilbert Transform	152
	References	153
	Curriculum Vitae	160

LIST OF FIGURES

Figure 1-1 Leonardo da Vinci: seated man and water studies (http://www.royalcollection.org.uk).....	2
Figure 1-2 Schematic of dominant near wake instabilities	3
Figure 1-3 Description of Mode-A, Mode-B and Mode-C structures in XY and XZ planes (arrows indicate the vorticity direction)	5
Figure 2-1 Water tunnel experimental setup	16
Figure 2-2 Mean streamwise velocity at the centre line of the water tunnel at different downstream locations (Sarathi 2009)	17
Figure 2-3 Variation of (a) mean streamwise velocity and (b) turbulence intensity at different spanwise locations at $X/h = 0.33$ (Sarathi 2009).....	18
Figure 2-4 Wind tunnel experimental setup.....	19
Figure 2-5 Variation of (a) mean streamwise velocity and (b) turbulence intensity profile in the boundary layer at $X/D = 0.4$ before separation	20
Figure 2-6 A schematic showing the flat plate model used in the water tunnel, along with the field of view for imaging planes and the coordinate axis.....	22
Figure 2-7 A schematic showing the flat plate model used in the wind tunnel, and the major dimensions along with the field of view for PIV images and the coordinate axis	24
Figure 2-8 Location of the pressure transducers.....	24
Figure 2-9 Details of the different trailing edges used in the wind tunnel measurements	25
Figure 2-10 Typical PIV system with (a) Integrated Cooling and Electronics (ICE) unit, (b) laser head with sheet optics attached and (c) dual frame CCD camera and the particle seeder.....	28

Figure 2-11 The calibration sheet used for the PIV measurements in (a) water tunnel and (b) wind tunnel	29
Figure 2-12 The velocity flow field data obtained after processing the PIV images	30
Figure 2-13 Flush mounted high speed transducers used in this investigation	31
Figure 2-14 Typical high speed pressure data acquisition setup.....	32
Figure 2-15 Calibration for (a) DP-15 transducer and (b) High speed pressure transducer	34
Figure 2-16 Acquisition timing for PIV and pressure records in wind tunnel measurements.....	35
Figure 2-17 Cumulative convergence of energy using snapshot POD in vertical plane for straight trailing edge at $Re_D = 24000$	38
Figure 2-18 Convergence of energy captured by (a) mode 1 and (b) mode 2 in XY plane, (c) mode 1 and (d) mode 2 in XZ plane ($Y/D = -0.5$), and (e) mode 1 and (f) mode 2 in XZ plane ($Y/D = -0.5$) at $Re_D = 24000$. Energy is calculated using 10, 50, 100, 200, 300, 400, 500, 600, 700, 800, 900 and 1000 PIV images.	40
Figure 2-19. Comparison of streamwise turbulence intensity along the centre line calculated using standard deviation of the PIV data and reconstructed using different number of POD modes at (a) $Re_D = 550$, (b) $Re_D = 1050$, (c) $Re_D = 1550$, (d) $Re_D = 2300$, (e) $Re_D = 24000$ and (f) $Re_D = 46000$	41
Figure 2-20. % error in predicting centre line streamwise turbulence intensity by combining different number of POD modes for $Re_D = 550, 1050, 1500, 2300, 24000$ and 46000	42
Figure 2-21 Correlation of phase angles determined from the POD coefficients and pressure signal in XY plane	44
Figure 2-22 Correlation of phase angles determined from the POD coefficients and pressure signal in XZ plane	45

Figure 2-23 Phase averaged streakline plots obtained by calculating the phase from the (a) pressure signal, (b) POD coefficients and (c) conditional averaging approach.....	46
Figure 3-1. Comparison of Strouhal number as a function of Reynolds number with Petrusma and Gai (1996).....	48
Figure 3-2. Comparison of Roshko number as a function of Reynolds number with Bull et al. (1995).....	50
Figure 3-3. Comparison of Roshko number as a function of Reynolds number with Ryan et al. (2005)	51
Figure 3-4. Instantaneous (a) streamwise velocity, (b) transverse velocity and (c) ω_z vorticity for Reynolds numbers of (I) $Re_D = 550$, (II) $Re_D = 1050$, (III) $Re_D = 1550$ and (IV) $Re_D = 2300$	53
Figure 3-5. (a) Streamwise and (b) transverse velocity components for the first nine POD modes in XY plane at $Re_D = 550$	54
Figure 3-6. Relative energy captured by first ten POD modes in XY plan at $Re_D = 550$	56
Figure 3-7. Phase averaged time varying coefficient in XY plane at $Re_D = 550$	56
Figure 3-8. Phase portraits of time varying coefficient in XY plane at $Re_D = 550$. The solid line indicates the phase averaged relation between these POD modes.	57
Figure 3-9. (a) PLIF Visualization (b) streakline plot along with vorticity contours of the first two POD modes in XY plane at $Re_D = 550$	59
Figure 3-10. Streamwise and transverse velocity components for the first five POD modes in XY plane at (a) $Re_D = 1050$, (b) $Re_D = 1550$ and $Re_D = 2300$	60
Figure 3-11. (a) Relative energy captured by first ten POD modes in XY plan at $Re_D =$ 1050, 1550 and 2300. Phase averaged time varying coefficient in XY plane at (b) $Re_D = 1050$, (c) $Re_D = 1550$ and (a) $Re_D = 2300$	61
Figure 3-12. PLIF visualization and the streakline plots along with vorticity contours by combining first two POD modes of in XY plane for (a) $Re_D = 1050$, (b) $Re_D =$ 1550 and (c) $Re_D = 2300$	62

Figure 3-13. Streamwise spacing of spanwise vortices as a function of Reynolds number	63
Figure 3-14. PLIF visualization at $Re_D = 250$ in XZ plane ($Y/D = -0.5$) (a) parallel vortex shedding (b) vortex dislocation, (c) visualization of the vortex dislocation (Williamson 1992), and (d) schematic representation of vortex dislocation (Williamson 1992).	64
Figure 3-15. PLIF visualization at $Re_D = 300$ in XZ plane ($Y/D = -0.5$) (a) parallel vortex shedding (b) vortex dislocation and (c) three-dimensional features.....	65
Figure 3-16. PLIF visualization at $Re_D = 350$ in XZ plane ($Y/D = -0.5$) (a) parallel vortex shedding (b) vortex dislocation and (c) mushroom structures.....	66
Figure 3-17. PLIF Visualization in XZ plane ($Y/D = -0.5$) at $Re_D = 400$	67
Figure 3-18. PLIF Visualization in YZ plane ($X/D = 3$) at $Re_D = 400$	68
Figure 3-19. PLIF Visualization in XZ plane ($Y/D = -0.5$) at $Re_D = 550$	69
Figure 3-20. PLIF Visualization in YZ plane ($X/D = 3$) showing the dislocations caused due to streamwise vortices in spanwise vortices at $Re_D = 550$	70
Figure 3-21. Schematics of the primary and secondary vortices of (a) mode-A (b) mode-B topologies. Vorticity sign is marked by arrows.	71
Figure 3-22. PLIF Visualization in XZ plane ($Y/D = -0.5$) at $Re_D = 550$ for (a) straight trailing edge and (b) sinusoidal trailing edge	73
Figure 3-23. Mean streamwise velocity contours in XZ plane ($Y/D = -0.5$) at $Re_D = 550$ for (a) straight trailing edge and (b) sinusoidal trailing edge	74
Figure 3-24. Comparison of mean centre line velocity for straight trailing edge and sinusoidal trailing edge.....	74
Figure 3-25. Instantaneous (a) streamwise velocity, (b) spanwise velocity and (c) ω_y vorticity for Reynolds numbers of (I) $Re_D = 550$, (II) $Re_D = 1050$, (III) $Re_D = 1550$ and (IV) $Re_D = 2300$	76
Figure 3-26. Relative energy captured by first fifteen POD modes in XZ plane at (a) $Y/D = -0.5$ and (b) $Y/D = 0$ for $Re_D = 400$ and 550	77

Figure 3-27. ω_y vorticity contours in XZ plane ($Y/D = -0.5$) at $Re_D = 400$ by combining POD modes (a) 1 to 4, (b) 5 to 8, and (c) 9 and 10.....	79
Figure 3-28. Schematic of the primary and secondary structures	80
Figure 3-29. Streamwise velocity contour in XZ plane ($Y/D = -0.5$) at $Re_D = 400$ by combining POD modes 1 to 32.....	80
Figure 3-30. Schematic of mode-A in (a) XY plane and (b) XZ plane	80
Figure 3-31. ω_y vorticity contours in XZ plane ($Y/D = -0.5$) at $Re_D = 550$ by combining POD modes (a) 1 to 4, (b) 5 and 6, (c) 7 and 8, and (d) 9 to 12.....	82
Figure 3-32 Relative energy captured by first 15 POD modes in XZ planes ($Y/D = -0.5$ and $Y/D = 0$) at $Re_D = 550$	83
Figure 3-33 ω_y vorticity contours in XZ plane ($Y/D = 0$) at $Re_D = 550$ by combining POD modes 1 to 10.....	83
Figure 3-34. ω_y vorticity contour in XZ plane ($Y/D = -0.5$) at $Re_D = 550$ by combining POD modes (a) 1 and 2, (b) 3 and 4, (c) 5 and 6, (d) 7 and 9, (e) 9 to 12. (f) Streamwise velocity contour by combining POD modes 1 to 32.....	85
Figure 3-35. (a) ω_y vorticity contour in XZ plane ($Y/D = 0$) at $Re_D = 550$ by combining POD modes 1 to 10 and (b) streamwise velocity contour by combining POD modes 1 to 32.....	86
Figure 3-36. PLIF visualization in XZ plane ($Y/D = -0.5$) at $Re_D = 1050$	87
Figure 3-37. PLIF visualization in XZ plane ($Y/D = -0.5$) at $Re_D = 1550$	88
Figure 3-38. PLIF visualization in XZ plane ($Y/D = -0.5$) at $Re_D = 2300$	88
Figure 3-39 Relative energy captured by first 15 POD modes in XZ planes ($Y/D = -0.5$) at $Re_D = 1050, 1550$ and 2300	89
Figure 3-40. (a) ω_y vorticity contour in XZ plane ($Y/D = -0.5$) at $Re_D = 1050$ by combining POD modes (a) 1 and 2, (b) 3 and 4, (c) 5 and 6, (d) 7 and 8. (e) Streamwise velocity contour by combining POD modes 1 to 32.....	90

Figure 3-41. (a) ω_y vorticity contour in XZ plane ($Y/D = -0.5$) at $Re_D = 1550$ by combining POD modes (a) 1 and 2, (b) 3 and 4, (c) 5 and 6, (d) 7 and 8. (e) Streamwise velocity contour by combining POD modes 1 to 32.....	91
Figure 3-42. (a) ω_y vorticity contour in XZ plane ($Y/D = -0.5$) at $Re_D = 2300$ by combining POD modes (a) 1 and 2, (b) 3 and 4, (c) 5 and 6, (d) 7 and 8. (f) Streamwise velocity contour by combining POD modes 1 to 32.....	92
Figure 3-43. Streamwise and transverse velocity components for the first five POD modes in XY plane for the base case at $Re_D = 24000$	94
Figure 3-44. Streamwise and transverse velocity components for the first five POD modes in XY plane for the base case at $Re_D = 46000$	94
Figure 3-45. (a) Relative energy captured by first ten POD modes in XY plane at $Re_D = 24000$ and 46000 . Phase averaged time varying coefficient in XY plane at (b) $Re_D = 24000$ and (c) $Re_D = 46000$	95
Figure 3-46. Streakline plots along with vorticity contours by combining first two POD modes of in XY plane for (a) $Re_D = 24000$ and (b) $Re_D = 46000$	96
Figure 3-47. Relative energy captured by first 15 POD modes in XZ at (a) $Y/D = -0.5$ and (b) $Y/D = 0$ plane for $Re_D = 24000$ and $Re_D = 46000$	97
Figure 3-48. Streamwise and transverse velocity components for the first ten POD modes in XZ plane for the base case at $Re_D = 24000$	98
Figure 3-49. Streamwise and transverse velocity components for the first ten POD modes in XZ plane for the base case at $Re_D = 46000$	99
Figure 3-50 Streamwise velocity contours in XZ plane ($Y/D = -0.5$) at $Re_D = 24000$ by combining POD modes 1 to 32 at different instances in flow	100
Figure 3-51 Streamwise velocity contours in XZ plane ($Y/D = -0.5$) at $Re_D = 46000$ by combining POD modes 1 to 32 at different instances in flow	101
Figure 4-1. Wavy square cylinder flow regime (Darekar and Sherwin 2001).....	105
Figure 4-2. Comparison of base pressure coefficient for (a) straight and SSP($\lambda_z/D = 2.4$ and 5.6) trailing edges, and (b) straight and SSP ($\lambda_z/D = 2.4$) trailing edges .	108

Figure 4-3. Comparison of the mean streamwise velocity profiles at various downstream locations for $Re_D = 550$	110
Figure 4-4. Comparison of base drag coefficient for straight and SSP ($\lambda_z/D = 2.4$) trailing edges at $Re_D = 550, 1550$ and 2300	111
Figure 4-5. Streamwise mean velocity contour at $Y/D = -0.5$ for SSP ($\lambda_z/D = 2.4$) trailing edge at $Re_D = 24000$	112
Figure 4-6. Comparison of mean streamwise centre line velocity for straight and SSP ($\lambda_z/D = 2.4$) trailing edges at (a) $Re_D = 550$, (b) $Re_D = 1550$, (c) $Re_D = 2300$, (d) $Re_D = 24000$ and (e) $Re_D = 46000$	113
Figure 4-7. Comparing streamwise turbulence intensity profiles at mid-plane for base case and SSP ($\lambda_z/D = 2.4$) control case at (a) $Re_D = 550$, (b) $Re_D = 1550$, (c) $Re_D = 2300$, (d) $Re_D = 24000$ and (e) $Re_D = 46000$. (f) Comparing formation lengths for base case and SSP ($\lambda_z/D = 2.4$) control case at different Reynolds numbers	115
Figure 4-8. Schematic of the PIV measurement window in the horizontal (XZ) plane ..	116
Figure 4-9. Streakline plots at different phases of vortex shedding in XY for base case and SSP ($\lambda_z/D = 2.4$) control case at $Re_D = 24000$	117
Figure 4-10. Comparison of peak vorticity variation for straight and SSP ($\lambda_z/D = 2.4$) trailing edges at different Reynolds numbers.....	118
Figure 4-11. Comparison of power spectral density for straight and SSP ($\lambda_z/D = 2.4$) trailing edges for (a) base case (b) MAX (c) MED (d) MIN at (I) $Re_D = 550$, (II) $Re_D = 1550$, (III) $Re_D = 2300$, (IV) $Re_D = 24000$ and (V) $Re_D = 46000$	119
Figure 4-12. Streamwise and transverse velocity components for the first five POD modes in XY plane for SSP ($\lambda_z/D = 2.4$) control case at (a) MAX and (b) MIN locations for $Re_D = 24000$	122
Figure 4-13. Phase averaged time varying coefficient in XY plane for (a) SSP 2.4: MAX and (b) SSP 2.4: MIN locations at $Re_D = 24000$	122

Figure 4-14. Streamwise and transverse velocity components for the first nine POD modes in XY plane for SSP ($\lambda_z/D = 2.4$) control case at MAX location for $Re_D = 550$	123
Figure 4-15. Streamwise and transverse velocity components for the first nine POD modes in XY plane for SSP ($\lambda_z/D = 2.4$) control case at MIN location for $Re_D = 550$	124
Figure 4-16. Phase averaged spanwise velocity component in XZ plane ($Y/D = 0$) for (a) Base case: Reconstructed using first 10 modes and (b) SSP ($\lambda_z/D = 2.4$) : Reconstructed using first two modes	126
Figure 4-17. Comparison of relative energy for straight and SSP ($\lambda_z/D = 2.4$) trailing edges captured by first ten POD modes in XY plane at (a) $Re_D = 550$, (b) $Re_D = 1550$, (c) $Re_D = 2300$, (d) $Re_D = 24000$ and (e) $Re_D = 46000$	128
Figure 4-18. Comparison of relative energy for straight and SSP ($\lambda_z/D = 2.4$) trailing edges captured by first ten POD modes in XZ mid-plane ($Y/D = 0$) at (a) $Re_D = 550$, (b) $Re_D = 1550$, (c) $Re_D = 2300$, (d) $Re_D = 24000$ and (e) $Re_D = 46000$	129

LIST OF TABLES

Table 1.1 Summary of the application of wavy leading and/or trailing edges used for wake control.....	10
Table 1.2 Summary of the near wake studies on different wake generators	11
Table 1.3 Summary of the near wake instabilities for blunt trailing-edge-profiled body (Ryan et al. 2005).....	13
Table 2.1 Comparison of different dimensions of the tunnels and the models used in the study	25
Table 3.1 Summary of the streamwise and spanwise wavelengths observed from PLIF and PIV measurements	102
Table 4.1 Measurements performed for this study.....	107
Table 4.2 Comparison of base pressure coefficients with different experimental studies	107
Table 4.3 Comparison of Strouhal number for straight and SSP ($\lambda_z/D = 2.4$) trailing edges at $Re_D = 550, 1550, 2300, 24000$ and 46000	120
Table A-1 PIV measurement error for low Reynolds numbers ($550 < Re_D < 2300$) in both vertical (XY) and horizontal (XZ) planes.....	139
Table A-2 PIV measurement error for high Reynolds numbers ($24000 < Re_D < 46000$) in both vertical (XY) and horizontal (XZ) planes.....	140

LIST OF SYMBOLS

a	time varying coefficient, amplitude
b	frequency
c	phase
dt	time difference
d_1	scaling factor ($D + 2\delta_1$)
d_2	scaling factor ($D + 2\delta_2$)
f	variable
f_s	Shedding frequency
h	height of the water tunnel
i, j, k	index
m	index
n	n^{th} mode, number of velocity vectors, index
n_c	number of velocity vectors
p	pressure
p_o	free stream pressure
t	time
u, v, w	streamwise, transverse, spanwise velocities
u'	random fluctuating component
u_{rms}	root mean square velocity
x_r	time signal
x_h	Hilbert transform
x_a	analytic signal
A	reference area ($L_z \times D$)
$C(t, t')$	temporal two-point correlation tensor

C_{pb}	base pressure coefficient
D	thickness of the wake generator
I_u	streamwise turbulence intensity
L_f	wake formation length
L_x	fore-body length
L_z	spanwise length
M	error
N	number of snapshots
R_{ij}	cross-correlation coefficient
Re_c	critical Reynolds number
Re_D	Reynolds number based on thickness of the wake generator
Ro	Roshko number
St	Strouhal number
T	vortex shedding period
\bar{U}	mean velocity
\tilde{U}	quasi periodic component
U_o	free stream velocity
W	wave steepness
X, Y, Z	Cartesian coordinates
α	inclination
δ	Kronecker delta, Boundary layer thickness
δ_1	displacement thickness
δ_2	momentum thickness
ρ	density
ϕ	mode or eigenvector, phase
$\phi_{\alpha_1-\alpha_2}$	phase angle determined from POD modes
$\phi_{pressure}$	phase angle determined from pressure signal

λ	eigenvalue
λ_x	streamwise spacing of the spanwise vortices
λ_z	spanwise spacing of streamwise vortices
μ	micro
ω	vorticity
Ω	domain

Abbreviations

<i>AR</i>	aspect ratio
<i>CCD</i>	charge-coupled device
<i>ICE</i>	integrated cooling unit
<i>LSE</i>	liner stochastic estimation
<i>Nd: YAG</i>	Neodymium-doped Yttrium Aluminium Garnet
<i>PCI</i>	peripheral component interconnect
<i>PID</i>	proportional integral differential
<i>PIV</i>	particle image velocimetry
<i>PLIF</i>	planar laser induced fluorescence
<i>PLL</i>	phase locked loop
<i>POD</i>	proper orthogonal decomposition
<i>PSD</i>	power spectral density
<i>PTU</i>	programmable timing unit
<i>SSP</i>	spanwise sinusoidal perturbation
<i>VFD</i>	variable frequency driven
<i>VFL</i>	vortex formation length

1 INTRODUCTION

The statistical view of turbulence as a stochastic phenomenon having only mean and turbulent components has changed during recent decades. The importance of large-scale organized (coherent) motions in turbulent flows has been recognized. Experimentally, the turbulent component has been divided into random and coherent parts (Cantwell and Coles 1983). Robinson (1991) defines coherent structure as a “coherent motion of a defined three-dimensional region of flow over which at least one fundamental flow variable (velocity component, density, temperature, etc.) exhibits significant correlation with itself or with other variables over a range of space and/or time that is significantly larger than the smallest local scale of the flow”. Knowledge of coherent structures in many different turbulent flows is important for developing an understanding of turbulent fluid flow dynamics. The realization that organized or coherent motion plays an important role in all turbulent flows leads naturally to the concept of turbulence control by manipulating these recurring events to achieve various enhancements such as drag reduction and lift enhancement (Gad-el-Hak et al. 1998).

One of the most widespread tools to tackle any fluid mechanics problem, especially turbulence, is flow visualization, a method pioneered by Leonardo da Vinci close to 500 years ago. Figure 1-1 shows one of his renderings, which depicts the wakes formed behind obstacles. The rendering depicts that the structure of the wakes is dominated by a pair of counter rotating vortices (coherent structures) along with the random or chaotic structure of the wake. Flow visualizations are simple, providing an indication of both global and local behaviour. However, the results of visualization have to be interpreted with caution because the dye diffuses and may sometimes conceal the details of the coherent structure (Gad-el-Hak 1988). Even though flow visualization provides a good idea of the qualitative behaviour of the flow, further quantitative information is always needed.



Figure 1-1 Leonardo da Vinci: seated man and water studies (<http://www.royalcollection.org.uk>)

With the advancements in computational power in recent decades, mathematical techniques such as Wavelet Transform, Proper Orthogonal Decomposition (POD), and Linear Stochastic Estimation (LSE) in conjunction with POD have gained importance in providing quantitative information of coherent structures in turbulent flows (Bonnet et al. 1996). In the current study, Planar Laser Induced Fluorescence (PLIF) visualizations and application of POD on the Particle Image Velocimetry (PIV) measurements are used to qualitatively and quantitatively identify the dominant coherent structures in the near wake of the blunt trailing-edge-profiled body. Further, this information of the dominant coherent structures is used to design a passive flow control.

Wake flows behind nominally two-dimensional bodies are dominated mainly by two types of coherent structures, namely the Karman Benard spanwise vortices and the streamwise vortices (Figure 1-2), also referred to as rolls and ribs respectively. It has been established that ribs wrap around rolls, and are interconnected (Hussain and

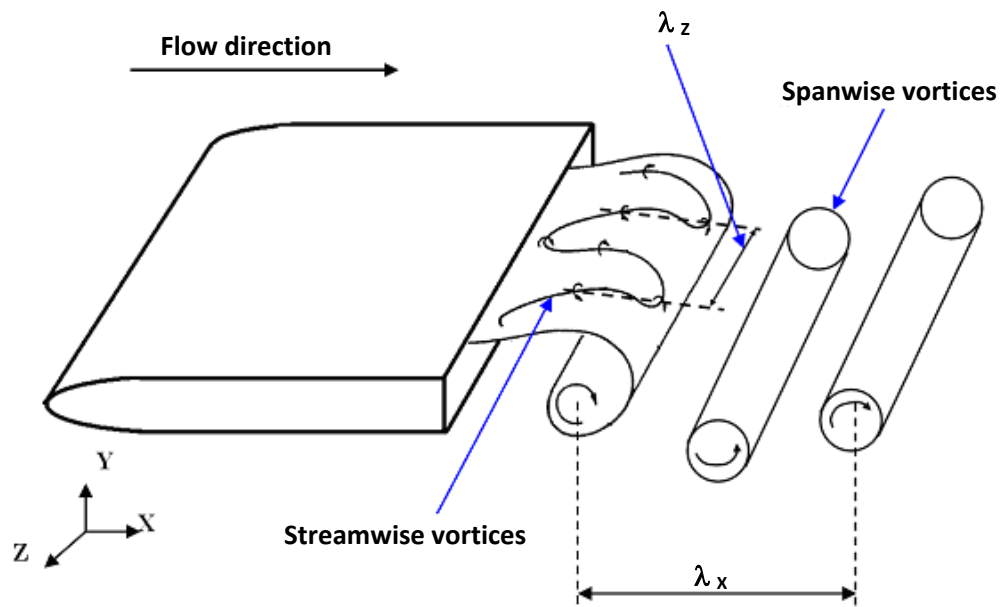


Figure 1-2 Schematic of dominant near wake instabilities

Hayakawa 1987). Development of two- and three-dimensional instabilities in the near wake of a two-dimensional body is sensitive to external actuation, which can be used in the design of control strategies to mitigate vortex shedding and minimize lift fluctuations and drag (Tombazis and Bearman 1997; Darekar and Sherwin 2001; Julien et al. 2003; Dobre et al. 2006; Lam and Lin 2009). Identifying the most unstable secondary wake instability and triggering it would be the most efficient way to develop a wake control mechanism. The present work is a step towards the longer term goal of developing a robust wake control methodology based on the manipulation of streamwise vortices as a function of Reynolds (Re) and Strouhal (St) numbers for blunt trailing-edge-profiled bodies. In essence, the normalization proposed by Dobre et al. (2006) for different wake generators is extended as

$$\frac{\lambda_z}{\lambda_x} \propto \frac{\lambda_z}{D} \cdot St$$

1.1)

where λ_x and λ_z are the streamwise spacing between the consecutive rolls and the spanwise spacing between the consecutive ribs, respectively (Figure 1-2), and D is the thickness of the wake generator.

The following sections review the literature on three-dimensional near wakes and passive flow control using Spanwise Sinusoidal Perturbation (SSP), and identify background work motivating the present study and specific objectives of the experimental work.

1.1 Previous Studies on Three-Dimensional Near Wakes

It is only in the last two decades that research has been conducted on the three-dimensional near wake flow topology for various wake generators, such as circular cylinders (Karniadakis and Triantafyllou 1992; Bays-Muchmore and Ahmed 1993; Mansy et al. 1994; Zhang et al. 1995; Brede et al. 1996; Williamson 1996; Barkley and Henderson 1996), square cylinders (Robichaux et al. 1999; Luo et al. 2003; Dobre and Hangan 2004; Luo et al. 2007; Sheard et al. 2009), thin flat plates (Meiburg and Lashares 1988; Julien et al. 2003), blunt trailing-edge-profiled body (Ryan et al. 2005), bluff rings (Sheard et al. 2005), and blunt trailing edge airfoil (El-Gammal and Hangan 2008).

The near wake of a two-dimensional body is critical because of dominant primary instability, which leads to the vortex street formation (Unal and Rockwell 1988). For circular cylinders, this bifurcation occurs at the critical Reynolds number of $Re_c \approx 45$. Further transition in the near wake is responsible for the formation of three-dimensional secondary instabilities, leading to the turbulent state, experimentally investigated by Williamson (1996) and numerically by Barkely and Henderson (1996). According to these studies, the transition from two- to three-dimensional instabilities occurs for a wide range of Reynolds numbers from $Re_c \approx 140$ to ≈ 190 . The possible reason for this variability is that the background disturbances are influencing the critical Reynolds number (Re_c) (Unal and Rockwell 1988). Other factors such as aspect ratio (height to streamwise length), end conditions, and shedding modes such as parallel or oblique can

influence Re_c (Prasad and Williamson 1997). Williamson (1996) demonstrated that for circular cylinder flows, two distinct three-dimensional streamwise instability modes occur, specifically mode-A and mode-B, depending on the flow Reynolds numbers. Mode-A occurs at $Re_D > 180$, Re_D being the Reynolds number based on the thickness of the wake generator, and is gradually replaced by mode-B at $Re_D > 230$. The spanwise spacing between streamwise vortices of Mode-A is scattered between $4D$ and $5D$ (Williamson 1996), but for Mode-B it is consistently found to be around $1D$ (Williamson 1996) for various Reynolds numbers. The spatio-temporal symmetries of mode-A and mode-B are shown in Figure 1-3. For mode-A, the region of positive and negative streamwise vorticity alternates in the spanwise direction and with time. The sign of

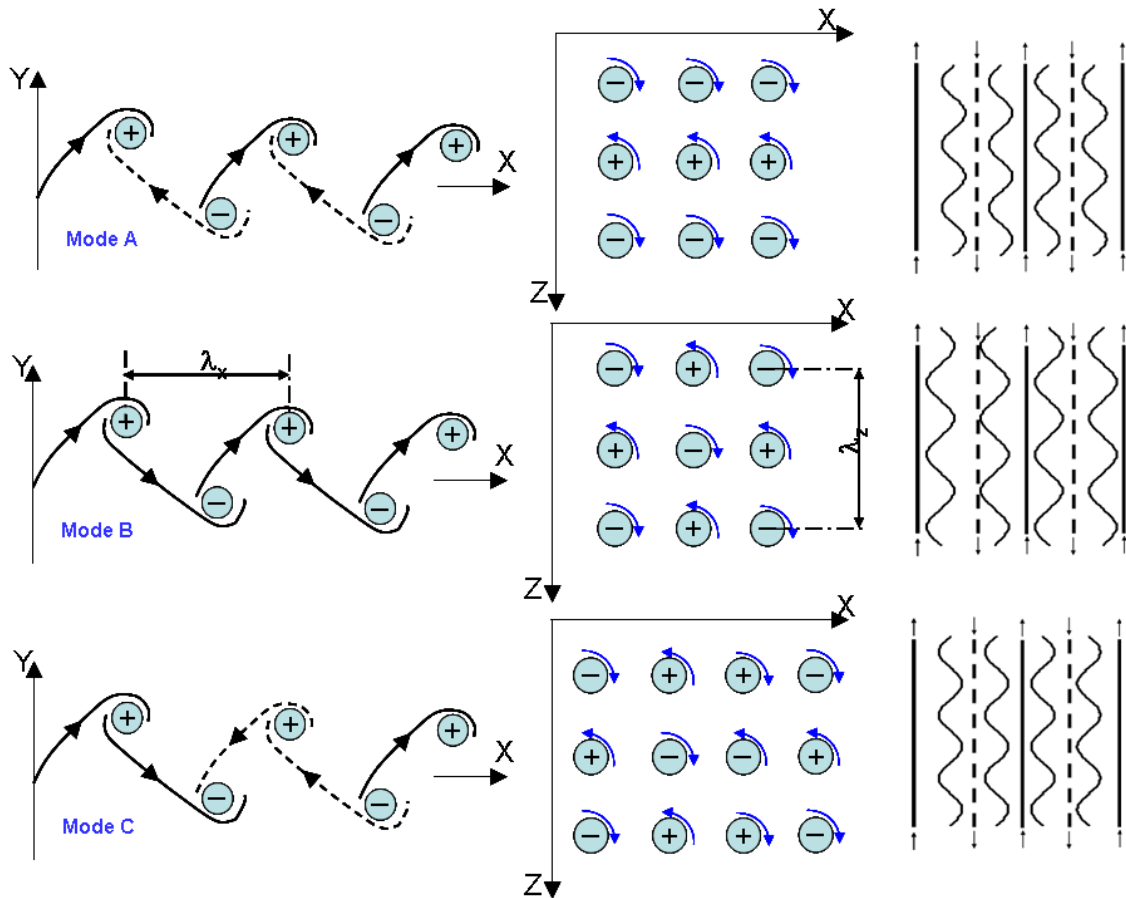


Figure 1-3 Description of Mode-A, Mode-B and Mode-C structures in XY and XZ planes (arrows indicate the vorticity direction)

streamwise vorticity, and thereby direction of the secondary vortices, alternates twice every Karman cycle. For mode-B, the streamwise vorticity pattern shows spanwise periodicity. Yet in contrast to mode-A, the sense of rotation does not change with time for a given spanwise location. Furthermore, the secondary vortices of mode-B seem to be persistent in time and remain connected over many Karman cycles. The entire patterns of secondary vortices oscillate up and down sinusoidally during each cycle of Karman vortex formation. Zhang et al. (1995) showed that a third mode, mode-C, appears when the flow is forced externally using an interference wire very close to the cylinder. Mode-C appears with a spanwise wavelength of $2.0D$. For this mode, the vorticity direction of streamwise vortices connecting the spanwise vortices alternates every Karman vortex cycle at a particular spanwise location with time (Figure 1-3). However, the full Floquet stability analysis of an unforced cylinder wake by Barkley and Henderson (1996) captures only mode-A and mode-B instabilities. Hence, it can be inferred that other three-dimensional instabilities can be triggered with suitable forcing.

For a square cylinder, Robichaux et al. (1999) conducted low Re_D numerical simulation based on Floquet analysis. They found the same natural modes with larger spanwise spacing of $5.22D$ for Mode-A and $1.2D$ for Mode-B. Luo et al. (2003, 2007) made a similar type of observation from the PLIF and PIV measurements. Robichaux et al. (1999) also predicted a third instability mode, mode-S, with a spanwise spacing of $2.8D$. This mode has similar features to mode-C observed by Zhang et al. (1995). As opposed to mode-C, however, mode-S naturally evolves in the flow without any external forcing. While Robichaux et al. (1999) inferred that mode S is subharmonic, with periodic double of the base flow, Blackburn and Lopez (2003) demonstrated that it is not true subharmonic but repeats every second cycle. Dobre and Hangan (2004) proposed a structure similar to Mode-A with a spanwise spacing of $2.4D$ at high Reynolds numbers ($Re_D = 22000$) in the intermediate wake of the square cylinder.

Mieburg and Lashares (1988) and Julien et al. (2003) experimentally studied the dynamics of three-dimensional secondary instabilities developing in the wake of a thin flat plate; they proposed that Mode-B structure dominates the near wake development

with a spanwise wavelength $\lambda_z/\lambda_x = 1$, whereas in the far wake both modes (mode-A and mode-B) coexist and grow equally.

It appears that the wake of two-dimensional bluff bodies undergoes transition to three-dimensional flow and eventually turbulence, through the same sequence of transition as observed for circular cylinder (Williamson 1996), and that mode-B dominates the flow after a certain transition Reynolds number. Previous studies on square cylinder (Robichaux et al. 1996; Luo et al. 2003; Luo et al. 2007) and thin flat plate (Mieburg and Lashares 1988; Julien et al. 2003) support this assumption, but with a slight variation in the spanwise spacing of these instabilities. However, for blunt trailing-edge-profiled bodies, Ryan et al. (2005) showed that when aspect ratio (AR) < 7.5 , the flow transition to three-dimensionality is through mode-A and mode-B respectively, and that mode-A instability dominates the near wake development. For intermediate and long bodies (AR > 7.5), the flow transition to three-dimensionality is through mode-B first and then through mode-A at higher Reynolds number, while mode-B instability plays a dominant role in the near wake dynamics. They reported a spanwise spacing (λ_z/D) of 3.5 for Mode-A and of 2.2 for Mode-B. They also observed a third instability mode, mode S, with a similar spatio-temporal structure to mode-C, but with a spanwise spacing of the order of one diameter (spacing similar to mode-B instability in circular cylinder flows). Adding further support to this argument, Sheard et al. (2005) confirmed that the near wake flow of a bluff ring is dominated by sub-harmonic three-dimensional instability mode-C. Sheard et al. (2009) also demonstrated that the transition to three-dimensional flow in the near wake of a square cylinder with variation in incidence angles, mode-A instability or mode-C instability dominated the flow structure. When studying the flow around two cylinders in a staggered arrangement, Carmo et al. (2008) showed that mode-C is also present along with mode-A and mode-B, depending on the relative position of the cylinders.

In summary, the transition to three-dimensional flow and the corresponding instabilities, which are mode-A, mode-B, mode-C or mode S, may vary in terms of the order of appearance and the dominance of these instability modes. The existence of a

preferred spanwise wavelength associated with streamwise vortices is not clear. While some researchers indicate that spanwise wavelength is broadband (Mieburg and Lashares 1988; Julien et al. 2003; Ryan et al. 2005), being imposed by the upstream conditions, others have shown evidence of a preferred natural spanwise wavelength (Zhang et al. 1995; Williamson 1996; Robichaux et al. 1999). The preferred spanwise wavelength is rather scattered, and is explained by the presence of ribs or by the spanwise roll distortions or both. However, it appears that the preferred spanwise wavelength is a function of flow configuration, meaning geometry (Ryan et al. 2005; Sheard et al. 2005; Sheard et al. 2009; Carmo et al. 2008), and aspect ratio (Ryan et al. 2005) of the wake generator, inflow conditions such as the Reynolds number, and turbulence characteristics (Williamson 1996; Wu et al. 1996).

1.2 Previous Studies on Flow Control Using Spanwise Sinusoidal Perturbation (SSP)

The control of vortex shedding in the wake of the bluff bodies by both active and passive means has been extensively investigated. Gad-el-Hak et al. (1998) provided a first comprehensive review. Passive control is reliable because of simplicity and cost effectiveness, and hence, is often preferred over active control methods. Successful passive control of vortex shedding in bluff bodies has been obtained with splitter plates (Bearman 1965), base bleed (Bearman 1967), three-dimensional disturbances (Tanner 1972), surface protrusions (Zdravkovich 1981), segmented trailing edges (Petrusma and Gai 1996), wavy trailing edges (Tombazis and Bearman; 1997, El-Gammal 2007), wavy leading edges (Bearman and Owen 1998; Darekar and Sherwin 2001; Dobre et al. 2006), and vortex generators (Park et al. 2006; El-Gammal 2007).

The control of vortex shedding by application of Spanwise Sinusoidal Perturbation (SSP) has recently gained interest because of its simplicity in design and its applicability to different wake generators (see Table 1.1). SSP control has been successfully applied to circular cylinders (Lam et al. 2004; Kim and Choi 2005; Lee and Nguyen 2007; Lam and

Lin2009), square cylinders (Bearman and Owen 1998; Darekar and Sherwin 2001; Dobre et al. 2006), elliptic leading and blunt trailing edge body (Tombazis and Bearman 1997), and divergent trailing edge airfoil (El-Gammal 2007). Table 1.1 summarizes most of these investigations. The literature indicates that there is no preferred spanwise wavelength that is common across various geometries. Several researchers (Darekar and Sherwin 2001; Kim and Choi 2005; Dobre et al. 2006) have indicated that maximum reduction in the dynamic loads and suppression of vortex shedding were obtained when the perturbation length was close to the spanwise spacing of the secondary wake instabilities. Three-dimensional wake instabilities lead to distinct instability modes (mode-A, mode-B and mode-C/mode-S) depending on the flow Reynolds number, Strouhal number and shape of the wake generator (Zhang 1995; Williamson 1996; Robichaux et al. 1999). Drawing on previous studies, Table 1.2 summarizes the spanwise spacing of the secondary wake instabilities for various wake generators. The spanwise spacing of the secondary wake instabilities varies with geometric shape, aspect ratio and Reynolds number. Based on the information from Table 1.1 and Table 1.2, it appears that, for a circular cylinder, the maximum base drag reduction using SSP control (Kim and Choi 2005; Lee and Nguyen 2007; Lam and Lin 2009) is obtained at wavelengths of 2.0 to 2.5D and of 5D to 6D. These wavelengths are very close to the wavelengths of the instabilities of the near wake observed for a circular cylinder. While mode-C with a spanwise wavelength of 2.0D does not occur naturally, Zhang et al. (1995) showed that this mode appears in the presence of an interference wire placed close to and parallel to the cylinder axis. The 5.0D wavelength corresponds to the naturally occurring mode-A instability. For a square cylinder, the maximum base drag reduction (Bearman and Owen 1998; Darekar and Sherwin 2001; Dobre et al. 2006) is obtained at wavelengths of 5.6D and 2.4D, which are close to naturally occurring instability wavelengths of mode-A (5.2D) and mode-C (2.8D). El-Gammal (2007) showed that vortex shedding can be suppressed, and achieved maximum base drag reduction for a diverging trailing edge airfoil by perturbing the near wake with the spanwise wavelength of the secondary wake instability. For the same elliptic leading edge and blunt trailing edge body used in the

Reference	Geometry	Method	Re _D	Tested wavelengths	Comments
Tombazis and Bearman 1997	Flat plate with elliptic leading and wavy trailing edge	Experimental	20000 to 60000	$3.5 < \lambda_z/D < 5.6$	Obtained maximum base drag reduction at $\lambda_z/D = 3.5$
Bearman and Owen 1998	Square cylinder with wavy leading edge	Experimental	40000	$3.5 < \lambda_z/D < 5.6$	Obtained maximum base drag reduction at $\lambda_z/D = 5.6$
Darekar and Sherwin 2001	Square cylinder with wavy leading and trailing edge	Numerical	100	$0 < \lambda_z/D < 10$	<ul style="list-style-type: none"> • Obtained maximum base drag reduction at $\lambda_z/D = 5.6$ and $W/\lambda_z = 0.03$ • Fluctuating lift was zero for <ul style="list-style-type: none"> ▪ $\lambda_z/D = 2.8$ and $W/\lambda_z = 0.2$ ▪ $\lambda_z/D = 4.0$ and $W/\lambda_z = 0.06$
Julien et al. 2003	Thin flat plate	Experimental	200	$0.5 < \lambda_z/\lambda_x < 1.1$	When instability perturbed with $\lambda_z/\lambda_x = 0.76$, it grew much faster than any other wavelength
Kim and Choi 2005	Circular cylinder	Numerical	40 to 3900	$2 < \lambda_z/D < 10$	Maximum base drag reduction obtained with $\lambda_z/D = 4.0$ to 5.0
Dobre et al. 2006	Square cylinder with wavy leading edge	Experimental	23500	$\lambda_z/D = 2.4$	Vortex shedding was completely mitigated and observed reduction in base drag
Lee and Nguyen 2007	Wavy circular cylinder	Experimental	5000 to 20000	$\lambda_z/D = 1$ and 2	Obtained maximum base drag reduction at $\lambda_z/D = 2.0$
Lam and Lin 2009	Wavy circular cylinder	Numerical	100	$1 < \lambda_z/D < 10$	Obtained maximum base drag reduction at $\lambda_z/D = 2.5$ and 6.0
El-Gammal 2007	Diverging trailing edge airfoil with wavy trailing edge	Experimental	13000	$\lambda_z/D = 2.4$	Vortex shedding was suppressed and observed reduction in base drag
Current study	Flat plate with elliptic leading and wavy trailing edge	Experimental	24000 to 46000	$\lambda_z/D = 2.4$ and 5.6	Obtained maximum base drag reduction at $\lambda_z/D = 2.4$

Table 1.1 Summary of the application of wavy leading and/or trailing edges used for wake control

Reference	Geometry	Method	Re _D	Wavelengths of Secondary Wake Instabilities
Mansy et al. 1994	Circular cylinder	Experimental	170 to 2200	Observed a structure with spanwise spacing of one diameter.
Zhang et al. 1994	Circular cylinder	Experimental	160 – 230	Mode A – 4D, Mode B – 1D and Mode C – 2D
Williamson 1996	Circular cylinder	Experimental	50 – 300	Mode A – 3 to 4D, Mode B – 1D
Brede et al. 1996	Circular cylinder	Experimental	160 – 500	Mode A – 4 to 5D and Mode B – 1D
Barkley and Henderson 1996	Circular cylinder	Numerical	140 – 300	Mode A -3.96D and Mode B - 0.822D
Chyu and Rockwell 1996	Circular cylinder	Experimental	10000	Mode A - 4D and Mode B - 1D
Robichaux et al. 1999	Square cylinder	Numerical	70 to 300	Mode A – 5.2D, Mode B – 1.2D and Mode S – 2.8D
Luo et al. 2003	Square cylinder	Experimental	100 – 500	Mode A – 5.2D and Mode B – 1.2D
Julien et al. 2003	Thin flat plate	Experimental	200	Instability wavelength - $\lambda_z/\lambda_x = 1.0$.
Dobre and Hangan 2004	Square cylinder	Experimental	23500	Mode A – 2.4 D
Ryan et al. 2005	Flat plate with elliptic leading and blunt trailing edge	Numerical	450 to 700	Based on Floquet analysis, most unstable wavelength for <ul style="list-style-type: none"> ▪Aspect ratio = 2.5 : Mode A = 3.5 ▪Aspect ratio = 7.5 : Mode A = 3.9 ▪Aspect ratio = 12.5 : Mode B = 2.2 ▪Aspect ratio = 17.5 : Mode B = 2.2
Luo et al. 2007	Square cylinder with different inclinations	Experimental	50 – 300	Mode A – 5.0-5.2D and Mode B – 1.0-1.4 D
Tong et al. 2008	Square cylinder with different inclinations	Experimental	150 – 300	Mode A – 4.0-5.0D and Mode B – 1.0-2.0 D
El-Gammal and Hangan 2008	Blunt trailing edge airfoil	Experimental	13000	Mode B – 2.4 D
Sheard et al. 2009	Square cylinder with different inclinations	Numerical	150-300	Based on Floquet analysis, most unstable wavelength for <ul style="list-style-type: none"> ▪$0^\circ < \alpha < 12^\circ$: Mode A = 5.2D ▪$12^\circ < \alpha < 26^\circ$: Mode C =2.1D ▪$26^\circ < \alpha < 45^\circ$: Mode A =5.7D
Current study	Flat plate with elliptic leading and blunt trailing edge	Experimental	250 - 2300	Mode A – 3.0-4.0D, Mode B – 1.0-1.5D, Mode C – 2.0-2.8D and Mode C' – 1.0D

Table 1.2 Summary of the near wake studies on different wake generators

current study, Ryan et al. (2005) showed that the spanwise wavelengths characterizing the instabilities change with aspect ratio. Tombazis and Bearman (1997) investigated an elliptic leading edge and blunt trailing edge body with an aspect ratio of 6.3, and obtained maximum base reduction with a perturbation wavelength of $3.5D$. This wavelength closely matches the wavelength of the dominant instability of $3.9D$ for this aspect ratio (Ryan et al. 2005). In the current study, an elliptic leading edge and blunt trailing edge body is studied with an aspect ratio of 12.5 and obtained maximum base drag reduction with a perturbation wavelength of $2.4 D$, which closely matches the wavelength of the dominant instability of $2.2D$ for this aspect ratio (Ryan et al. 2005). In summary, there is a clear correlation between the waviness of the spanwise sinusoidal perturbation (SSP) and the spanwise wavelength of the near wake instabilities. This information is used in the current study to design the passive flow control.

1.3 Motivation and Objectives

Two important reasons for choosing flat plate geometry with profiled leading and blunt trailing edge are: (i) it provides the desired upstream boundary layer velocity profile at the trailing edge without the uncontrollable effects of forced separation-reattachment associated with sharp corners of a square leading edge; and (ii) this geometry is of particular interest for aeronautical transonic divergent trailing edge airfoils (DTE), as well as for truncated wind turbine blade airfoils. The main outcome relates to the development of flow control strategies based on the natural flow instabilities.

The geometry used in the current study has been numerically investigated by Ryan et al. (2005) in a Reynolds number range of 250 to 700 for aspect ratios of 2.5, 7.5, 12.5 and 17.5. Numerical modeling was performed in two stages. First a time-dependent two-dimensional flow field around the blunt trailing edge profiled body is predicted by solving the time-dependent Navier-Stokes equations in two dimensions. Above a certain critical Reynolds number, the two-dimensional instabilities saturate to form the

familiar periodic flow field of Karman vortex street with a period T . The stability of this periodic two-dimensional base flow field to three-dimensional disturbances is then determined using Floquet stability analysis. Table 1.3 summarizes the observations from this work; it shows that the order of appearance of the near wake three-dimensional secondary-wake instabilities depends on the aspect ratio. The researchers reported that mode-A wake instability dominates the near wake development when $AR < 7.5$, with a spanwise wavelength of $3.5D$ to $3.9D$ and by mode-B for $AR > 7.5$ with a spanwise

Aspect Ratio (AR)	1 st Instability mode	2nd Instability mode	3rd Instability mode
2.5	Mode A – $3.5D$ ($Re_D = 400$)	--	--
7.5	Mode A – $3.9D$ ($Re_D \approx 470$)	Mode B – $2.2D$ ($400 < Re_D < 500$)	Mode C – $0.9-1.0D$ ($Re_D > 500$)
12.5	Mode B – $2.2D$ ($Re_D \approx 410$)	Mode A – $3.5D$ ($Re_D \approx 600$)	Mode C ($Re_D > 600$)
17.5	Mode B – $2.2D$ ($Re_D \approx 430$)	Mode C – $0.7D$ ($Re_D \approx 690$)	Mode A – $3.5D$ ($Re_D > 700$)

Table 1.3 Summary of the near wake instabilities for blunt trailing-edge-profiled body (Ryan et al. 2005)

wavelength of $2.2D$. Their study, however, is limited by the capability of the linear stability analysis to predict the transition regimes for higher Reynolds number. There has been no experimental verification of these numerical findings reported in the literature, and therefore this constitutes one of the objectives of the current investigation. The scope of the current investigation is as follows:

- Perform well-controlled experiments using Planar Laser Induced Fluorescence (PLIF) and Particle Image Velocimetry (PIV) to verify the findings of the numerical work by Ryan et al. (2005) for the same geometry with an aspect ratio of 12.5.
- Extract the dominant coherent structures by performing Proper Orthogonal Decomposition (POD) on the obtained PIV data, and relate the POD modes and associated eigenvalues to the dominant coherent structures in near wake.
- Identify the spatio-temporal topologies of the near wake instabilities and their corresponding unstable wavelengths.

- Extend the study to higher Reynolds numbers, check whether modes-A, -B and -C coexist, and identify which instability mode dominates the near wake development.
- Use these three-dimensional near wake dynamics to formulate a wake control methodology.
- Demonstrate the effectiveness of this control methodology by testing a simple passive control using Spanwise Sinusoidal Perturbation (SSP) with a design based on the natural spanwise spacing of the streamwise vortices.

2 EXPERIMENTAL SETUP AND ANALYSIS APPROACH

The wake dynamics of a blunt trailing-edge-profiled body, with and without the SSP passive control, is investigated in the current study using surface base pressure, Particle Image Velocimetry (PIV), and Planar Laser Induced Fluorescence (PLIF) techniques. In order to explore the influence of the inlet conditions and Reynolds number, and check the robustness of the proposed control methodology, experiments were conducted in two different facilities: Low Reynolds number PLIF and PIV measurements were conducted in the water tunnel of The Boundary Layer Wind Tunnel Laboratory at The University of Western Ontario, and high Reynolds simultaneous surface base pressure and PIV measurements were conducted in the wind tunnel at the University of Wyoming Aeronautics Laboratory. This chapter describes these two facilities, the PLIF, PIV, and pressure systems employed, as well as the data acquisition and primary processing.

2.1 Experimental Facility

2.1.1 Water Tunnel Facility

All the experiments for low Reynolds numbers (250 to 2300) were conducted in the 0.61 m x 0.305 m x 3 m water tunnel facility at The Boundary Layer Wind Tunnel Laboratory at the University of Western Ontario. Figure 2-1 shows the water tunnel experimental setup. This is an open return water tunnel producing a maximum free-stream velocity of 0.2 m/s. The water introduced into the water tunnel, passes through a settling chamber consisting of honeycomb and screens to break down large-scale non-uniformities. Access inside the water tunnel is provided from the side walls of the test section through two openings as shown in Figure 2-1. The model is supported using two aluminum rails attached to the side walls of the test section. There is also an access from the top of the test section through which the dye tubing system is routed. The

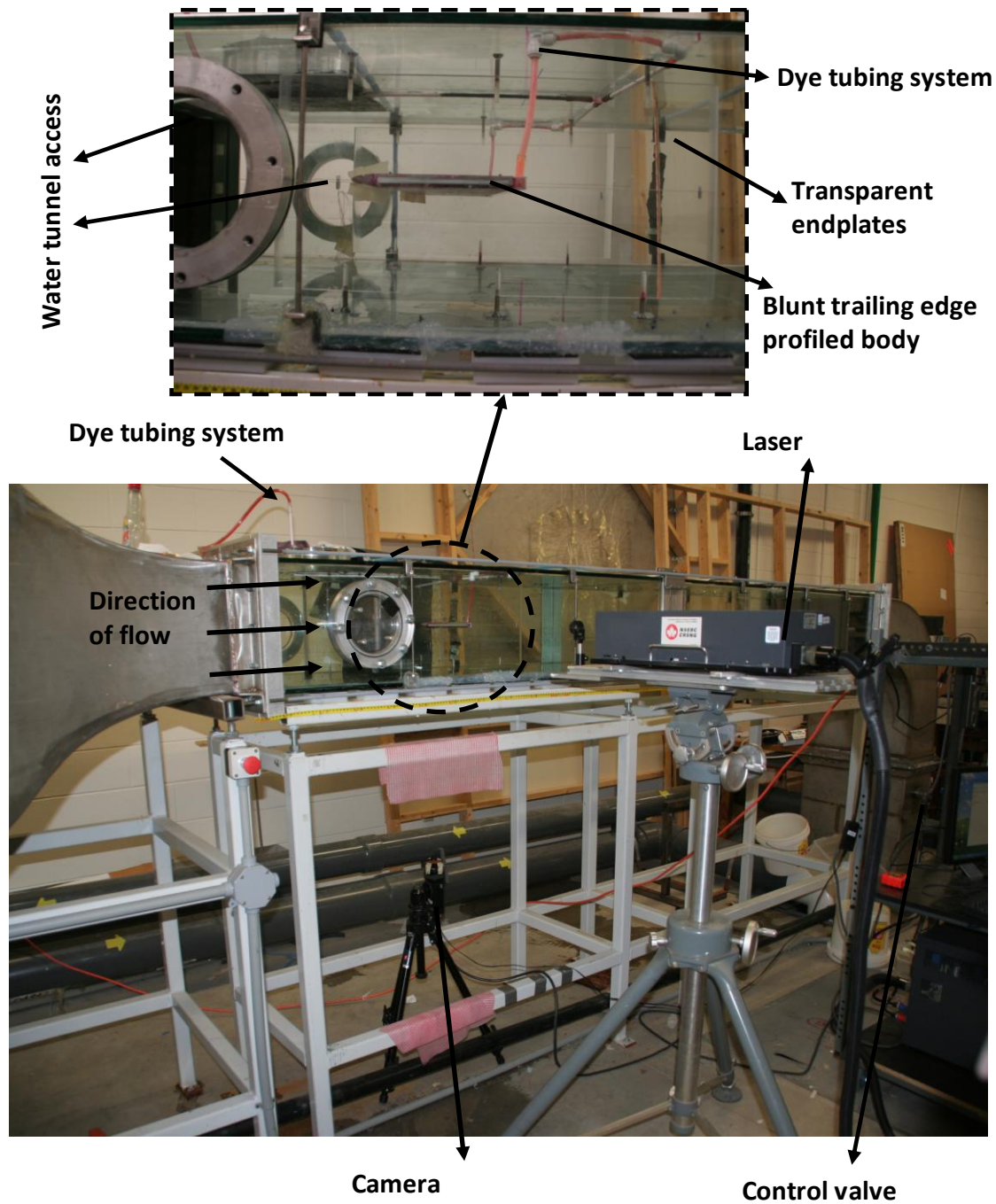


Figure 2-1 Water tunnel experimental setup

velocity in the water tunnel is controlled by a control valve situated at the end of test section where the water flows back to the reservoir.

Figure 2-2 shows the mean streamwise velocity variation at the centre line of the water tunnel at different downstream locations (reproduced with permission from Sarathi 2009). It is observed that the mean streamwise velocity profile is uniform and the maximum variation in the mean velocity varies within 1%. The increase in the mean streamwise velocity with downstream location, an effect of the boundary layer development in downstream, represents only 0.5% variation in the mean streamwise velocity over the extent of the measurement region downstream ($2.1 < X/h < 2.4$). Figure 2-3 shows the variation of (a) mean streamwise velocity and (b) turbulence intensity variation at different spanwise locations at $X/h = 0.33$. The variation in the mean streamwise velocity and the turbulence intensity is uniform across the span up to $Z/h = 0.65$. However, at $Z/h = 0.88$, the effect of the boundary layer growing on the side walls is visible in these profiles. For the current experiments, the measurements were performed in the water tunnel at $2.1 < X/h < 2.4$, $-0.04 < Y/h < 0.04$ and $-0.09 < Z/h < 0.09$. It is observed that the maximum variation in the mean velocity varies within 0.5% and that the

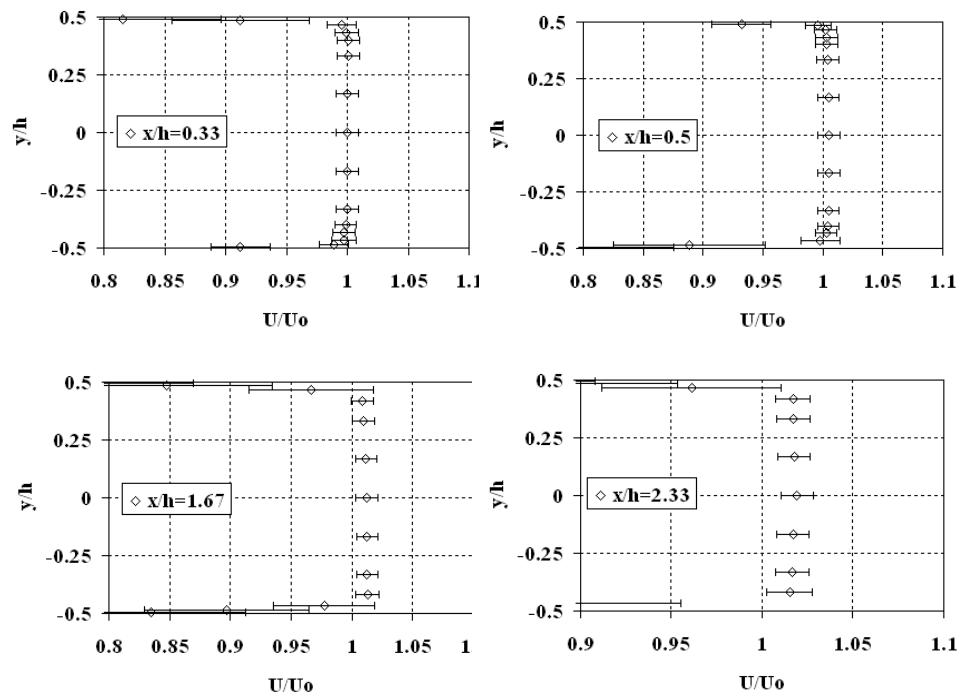


Figure 2-2 Mean streamwise velocity at the centre line of the water tunnel at different downstream locations (Sarathi 2009)

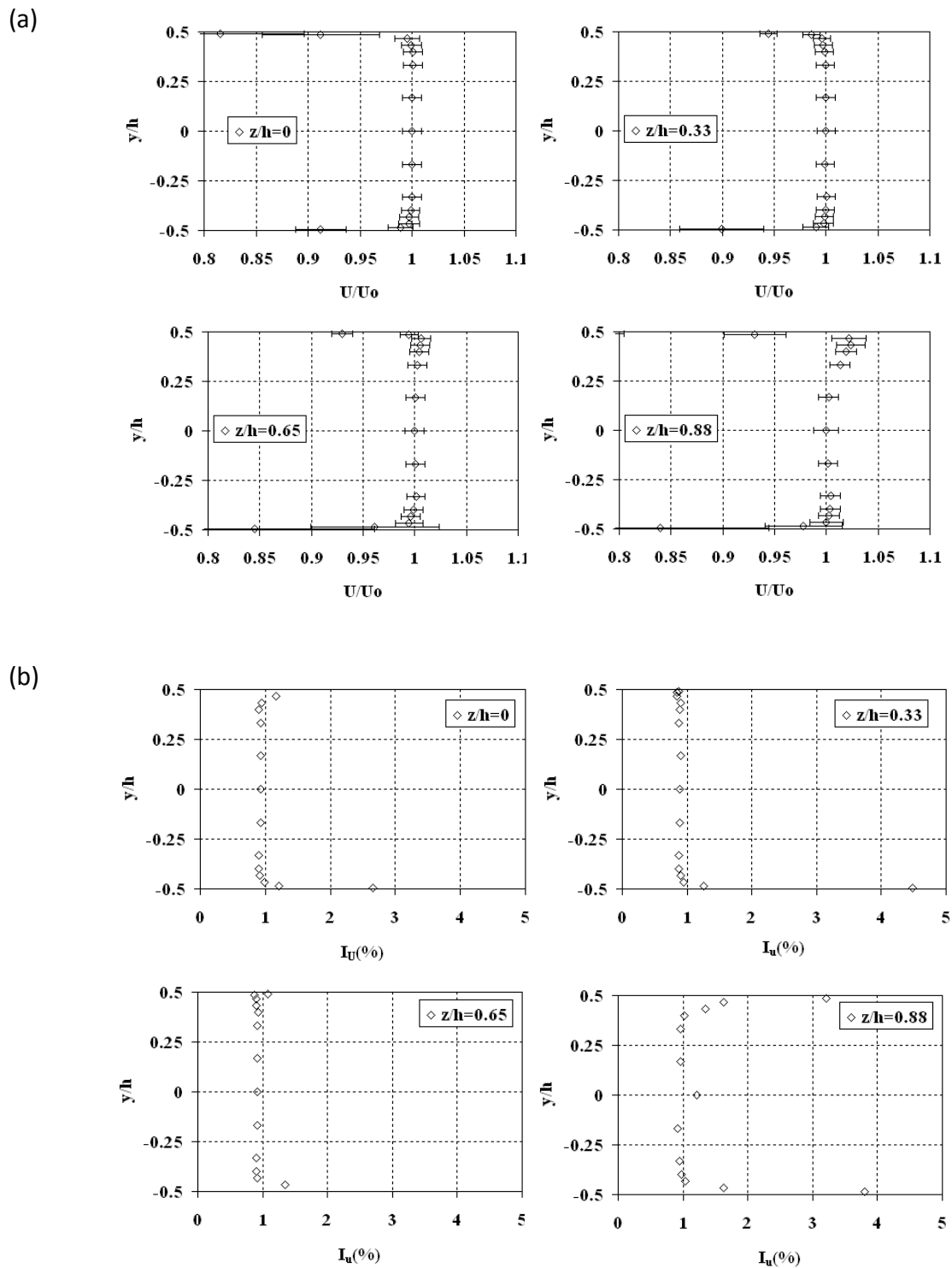


Figure 2-3 Variation of (a) mean streamwise velocity and (b) turbulence intensity at different spanwise locations at $X/h = 0.33$ (Sarathi 2009)

turbulence intensity is approximately 0.9% across the span where the measurements are performed.

2.1.2 Wind Tunnel Facility

All the wind tunnel experiments for this investigation were conducted in the subsonic wind tunnel facility (Figure 2-4) at the University of Wyoming Aeronautics Laboratories (UWAL) using a 0.61m x 0.61m x 1.21m test section. This is an open loop wind tunnel with a Variable Frequency Driven (VFD) motor capable of producing free-stream velocities between 10 and 50 m/s. The inlet section of the wind tunnel has a

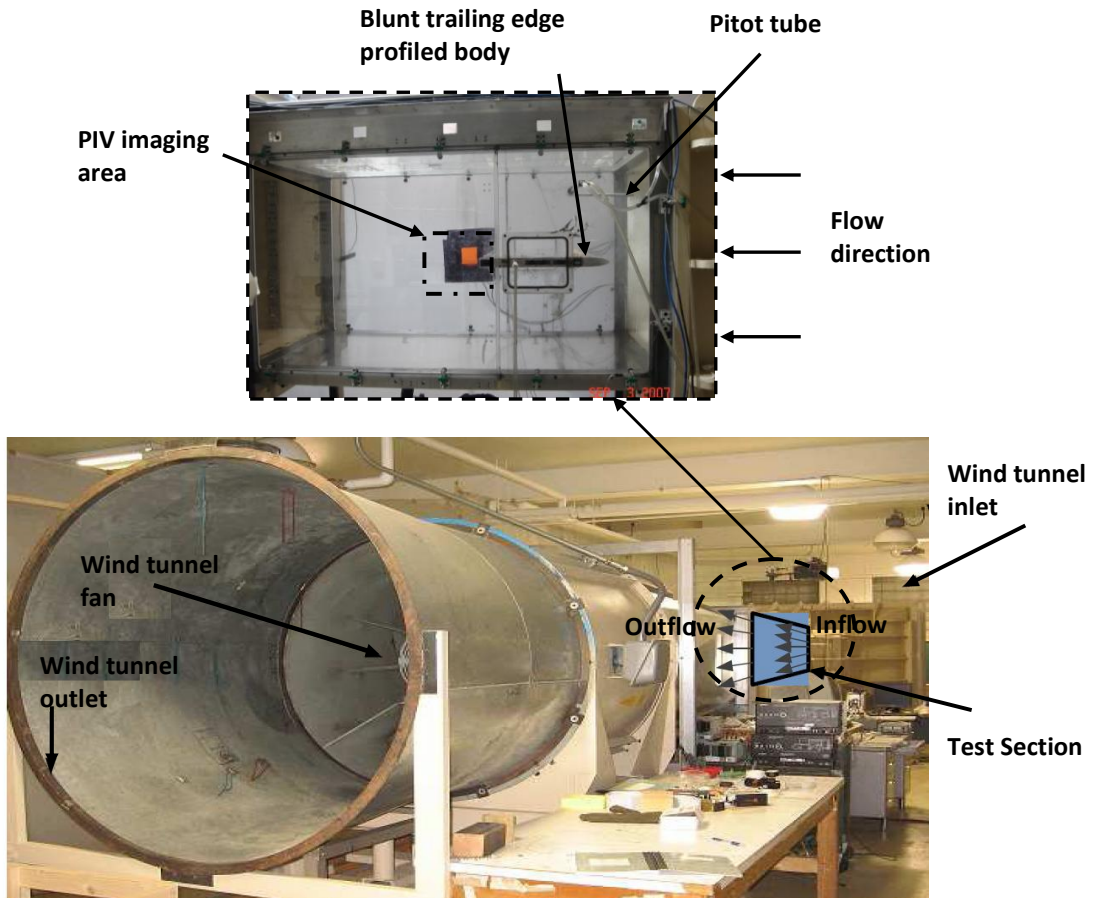


Figure 2-4 Wind tunnel experimental setup

honeycomb insert and three sets of screens to break down large-scale non-uniformities. For easy access and to provide support to the models, the side walls of the test section have been designed in two pieces. The two pieces of the side wall are made of plexiglass, as shown in Figure 2-4. The plexiglass section provides access to perform various optical measurements in the near wake of the models. Furthermore, there is a small window section on the plexiglass through which wires and tubes may be routed out of the test section for instrumentation and pressure measurements, respectively. The desired free-stream velocities are achieved using a Proportional Integral and Differential (PID) feedback control system. The input signal for the close-loop feedback system comes from a pitot tube installed in the upstream test section of the wind tunnel. A LabView program processes the input signal using the PID feedback control scheme and sends the final output control signal (0-10V) to the VFD, which controls the motor driving the fan.

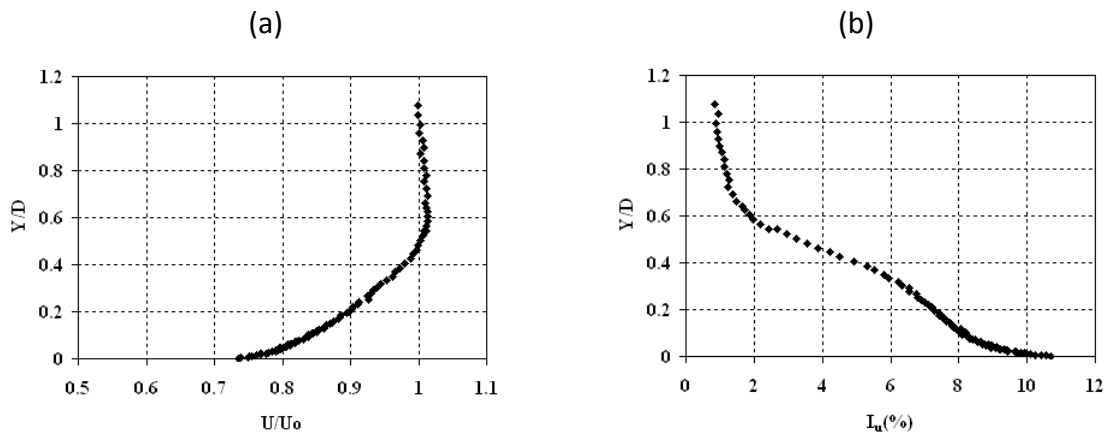


Figure 2-5 Variation of (a) mean streamwise velocity and (b) turbulence intensity profile in the boundary layer at $X/D = 0.4$ before separation

Figure 2-5 shows the streamwise velocity and the turbulence intensity profile developing in the boundary layer of the flat plate, just before separation at $X/D = 0.4$. The profiles indicate that the development of the mean streamwise velocity is uniform, the free-stream turbulence intensity being approximately 0.9%. Higher turbulence intensity very close to the wall of the flat plate is due to the sand strip used at the leading edge to trip the boundary layer.

2.2 Models

This investigation uses a flat plate model with an elliptic leading edge and blunt trailing edge to study

- the near wake dominant coherent structures, and
- the receptivity of spanwise sinusoidal perturbation with different spanwise wavelengths.

To cover an extensive range of Reynolds numbers and to check the influence of different inflow conditions, measurements were performed in both the water and the wind tunnel. The details of the models used in the current investigation are discussed in the following sections.

2.2.1 Water Tunnel Model

The fore-body length (L_x), spanwise length (L_z), and the base height (D) of this model are 0.1587m, 0.6m and 0.0127m respectively. The actual measurements were performed over a span of 0.43 m, which is bounded by two transparent endplates made of plexiglass (Figure 2-6). The endplates isolate the body from the effects of the boundary layers on the sidewalls of the tunnel, as well as from the dye supply tubing system. The effective aspect ratio L_x/D of the model is 12.5, and L_z/D is 34, with a blockage ratio of 4.2%. The important model dimensions along with the coordinate axis used are shown in Figure 2-6. The X-axis is the streamwise direction, the Y-axis is the transverse direction, and the Z-axis is the spanwise direction. The model covers the entire spanwise length of the wind tunnel, thereby achieving quasi two-dimensional flow over the model. The fluorescent dye was introduced into the flow through a thin spanwise slot ($\approx 0.5\text{mm}$) on the lower surface of the body, located $1D$ upstream of the trailing edge. The measurements are performed in XY, XZ and YZ planes.

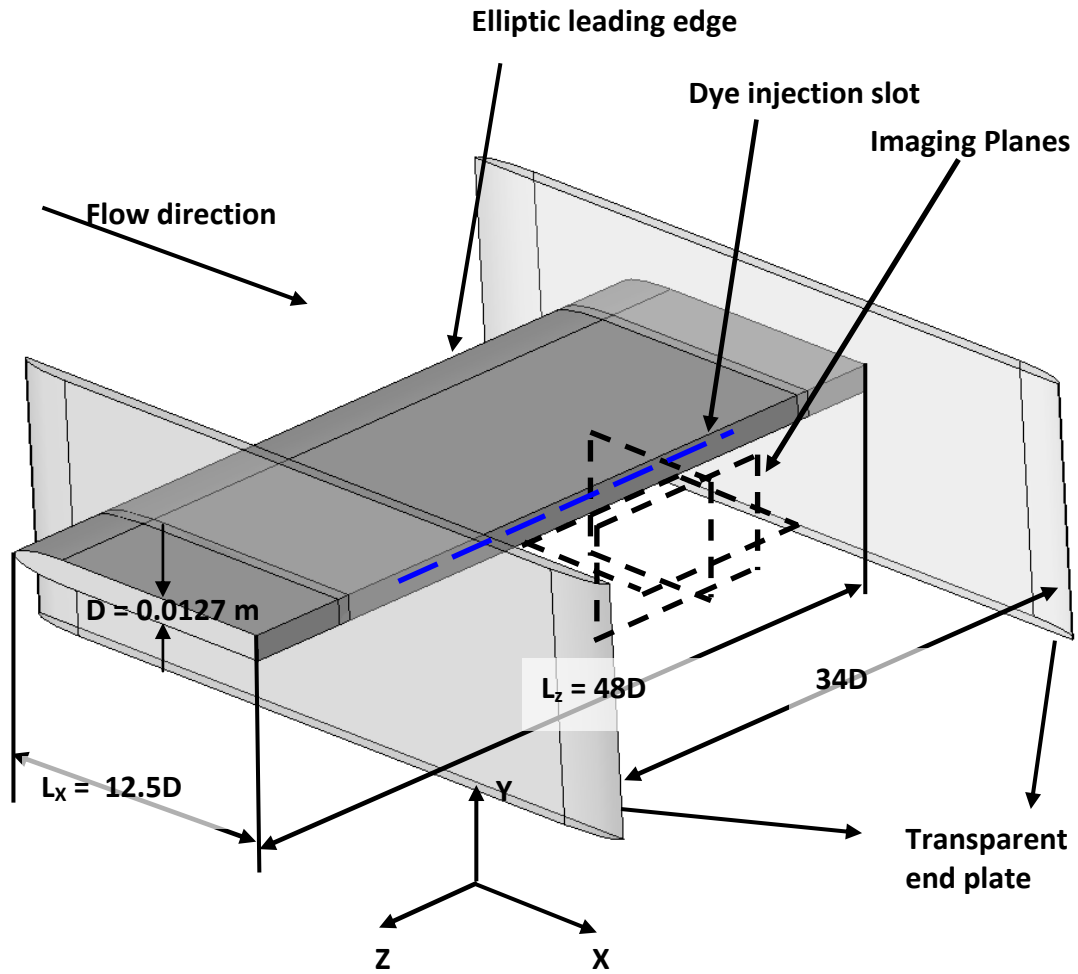


Figure 2-6 A schematic showing the flat plate model used in the water tunnel, along with the field of view for imaging planes and the coordinate axis

2.2.2 Wind Tunnel Model

The fore-body length (L_x), spanwise length (L_z) and the base height of this model are 0.3175m, 0.61m and 0.0254m respectively. The aspect ratio L_x/D of the model is 12.5 and L_z/D is 24, with a geometric blockage ratio of 4.2%. A 0.012m wide sand strip is applied along the leading edge to ensure that the boundary layer is fully turbulent on the model. This was not used in the water tunnel as transition effects were of interest. Important model dimensions along with the coordinate axis used are shown in Figure 2-7. The model covers the entire spanwise length of the wind tunnel, thereby achieving quasi two-dimensional flow over the model. The model has pressure ports on the fore-body as well as in the base region. The difference between mean pressure measurements from the top and bottom surfaces of the fore-body is minimized to align the model with the free-stream flow (that is, zero angle of attack). The pressure ports in the base of the model (Figure 2-8) serve two purposes: first, they are used to measure the base drag on the model, and second, they are used to calibrate the high-speed transducers. The calibration of high speed transducers is discussed later in this chapter (Section 2.3.3). PIV measurements were also performed on the flat plate model at different vertical (XY) and horizontal (XZ) planes, as shown in Figure 2-7.

Three different trailing edges were used for this investigation. Two wavy trailing edges with a spanwise wavelength (defined as the wavelength divided by base height) $\lambda_z/D = 2.4$ and 5.6, with corresponding wave steepness (defined as the ratio of peak-to-peak wave height divided by the wavelength) of $W/\lambda_z = 0.197$ and 0.09, were tested, and are referred to as *SSP 2.4* and *SSP 5.6* for the respective wavelengths. Details on selection of the wavelengths of SSP are discussed in chapter 4. The third model has no spanwise sinusoidal perturbation and will be referred to as the base case. The fore-body length (L_x) for the wavy trailing edges is measured up to the half amplitude of the SSP as shown in Figure 2-9, indicated with a blue dotted line, ensuring that the effective surface area of both the straight trailing edge and the wavy trailing edge are the same.

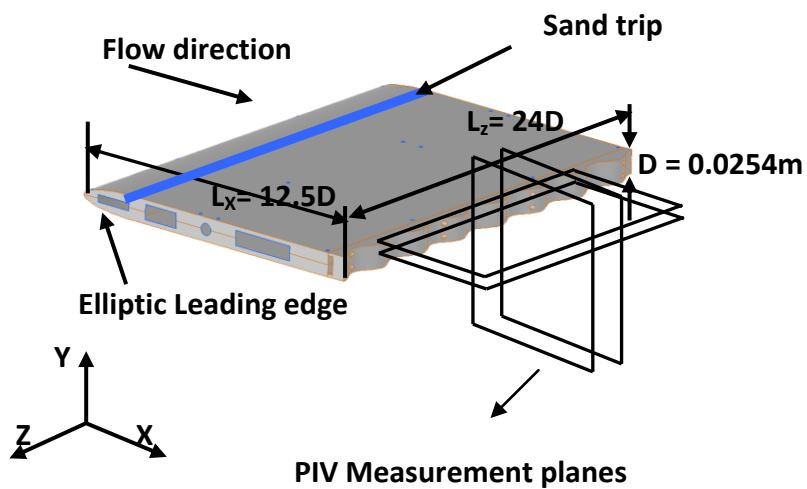


Figure 2-7 A schematic showing the flat plate model used in the wind tunnel, and the major dimensions along with the field of view for PIV images and the coordinate axis

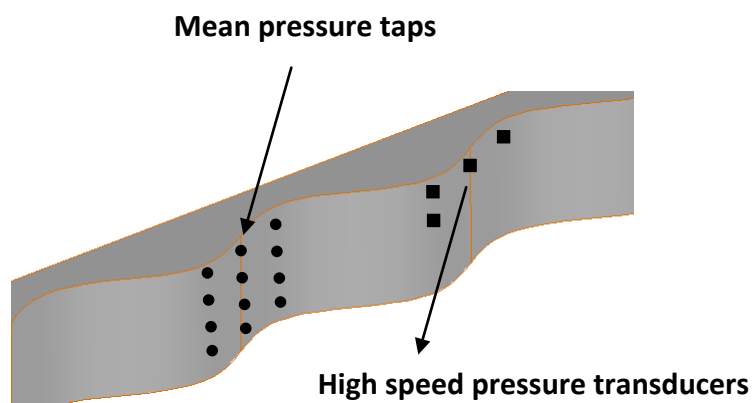


Figure 2-8 Location of the pressure transducers

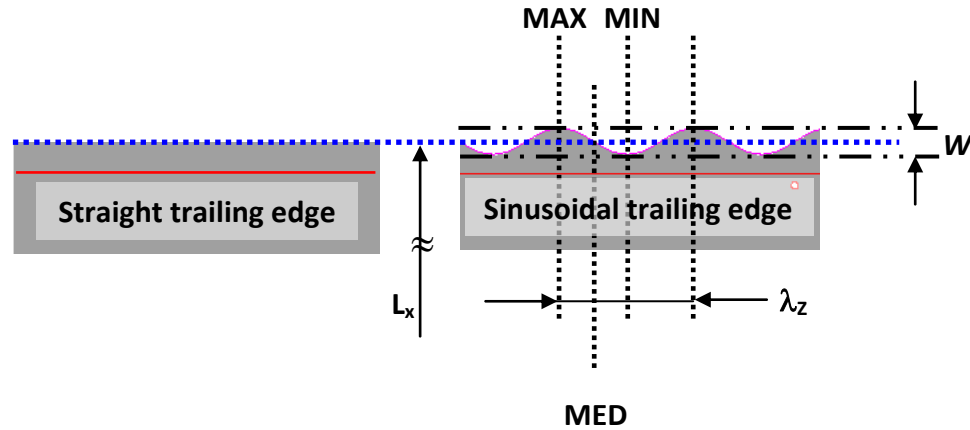


Figure 2-9 Details of the different trailing edges used in the wind tunnel measurements

Table 2.1 compares the dimensions of both the models and the tunnel dimensions used in the current study.

	Tunnel Dimensions (m)			Model dimensions (m)					Blockage ratio (%)
	Height	Width	length	L_x	L_z	D	AR		
							L_x/D	L_z/D	
Water Tunnel	0.305	0.61	3	0.1587	0.61	0.0127	12.5	48	4.2
Wind Tunnel	0.61	0.61	1.21	0.3175	0.61	0.0254	12.5	24	4.2

Table 2.1 Comparison of different dimensions of the tunnels and the models used in the study

2.3 Instrumentation

In order to achieve the objectives of this study, several experimental techniques were used to characterize the near wake flow structure; these are discussed in the following section.

2.3.1 Planar Laser Induced Fluorescence (PLIF)

Planar Laser Induced Fluorescence (PLIF) measurements are used in the water tunnel experiments to visualize the wake flow dynamics. PLIF uses a fluorescent material within the liquid phase, a monochromatic laser light, and a camera for observing the resulting fluorescence. The fluorescent dye, Rhodamine 6G, was introduced into the liquid to produce the visible fluorescence. This dye tints the water pink or red depending on the concentration, absorbs light maximally at 545 nm, and emits light maximally at 565 nm (Arcoumanis et al. 1990). The minimum amount of dye chosen to produce good images was selected, based on the volume and concentration of dye injected. A dye concentration of 200 mg/L was used in this current study.

The test section where the visualizations were performed was covered with black paper to minimize background light, improving the contrast of the resulting image. A 1 mm thick laser light sheet was produced by a PIV Nd: YAG laser (532 nm). A CCD camera with a resolution of 1200 x 1600 pixels was then focused on the light sheet to minimize the out-of-plane features. A red color filter (550nm) was used on the camera to ensure that the laser light reflections were blocked and the CCD camera captured only the fluorescent light emitted by the dye. The images were recorded using a capture rate of 15 frames per second. PLIF measurements were performed in XY, XZ and YZ planes.

2.3.2 Particle Image Velocimetry (PIV)

Particle Image Velocimetry was employed both in the water and the wind tunnels to provide quantitative description of the near wakes. Figure 2-10 shows the different component for a typical PIV system. Two different PIV systems were used for the water and wind tunnel measurements. An in-house assembled PIV system was used for the water tunnel measurements and a LaVision PIV system was used for the wind tunnel measurements. The PIV system used in the water tunnel measurements was the same system used for PLIF measurements. The camera resolution used with the LaVision PIV system was 1392 x 1024 pixels, which was sufficient to capture the necessary details for

the targeted wake velocity field. The cameras can capture two separate PIV images with an inter-frame time spacing of the order of few μsec . It was not necessary to add seeding particles to the flow as the water had enough contaminants to capture well-correlated PIV images. However, in the wind tunnel measurements, an oil based seeder was used, as shown in Figure 2-10(c). The oil was atomized using pressurized air, and the resulting particles were released near the inlet section of the wind tunnel to ensure even seeding density in the test section. Since the wind tunnel is an open return, the room became evenly seeded after some time, providing steady levels of seeding.

To perform PIV measurements, the laser system and camera must operate in synchronous mode. This was achieved using a Programmable Timing Unit (PTU), which is a PCI card used for the generating complex patterns of pulses on multiple outputs. The PTU pulses are programmed automatically according to the applications and the connected hardware. For this investigation, the difference between the two PIV images was in the range of 0.002-0.012 μsec and 10-50 μsec in the water tunnel measurements and wind tunnel experiments respectively, depending on the free-stream velocity of the experiment.

In this investigation, the camera was arranged perpendicular to the laser sheet, so that the optical distortion by the window and the camera lens was negligible. A simple calibration process was used before every PIV measurement. This calibration is a two-step process: The first step images two points at a known distance in the field of view, and the second step maps this known distance to the camera pixel space using a mapping function. A typical calibration sheet used for this investigation is shown in Figure 2-11. The locations in the near wake where PIV measurements were performed are shown in Figure 2-6 and Figure 2-7. The wake velocity field is determined from the PIV image pairs using software provided by Insight for the water tunnel measurements and by LaVision for the wind tunnel measurements. The in-house PIV system captures the images pairs in TIFF format. In order to calculate the particle displacements, the images are processed using Insight software. The software uses the cross-correlation

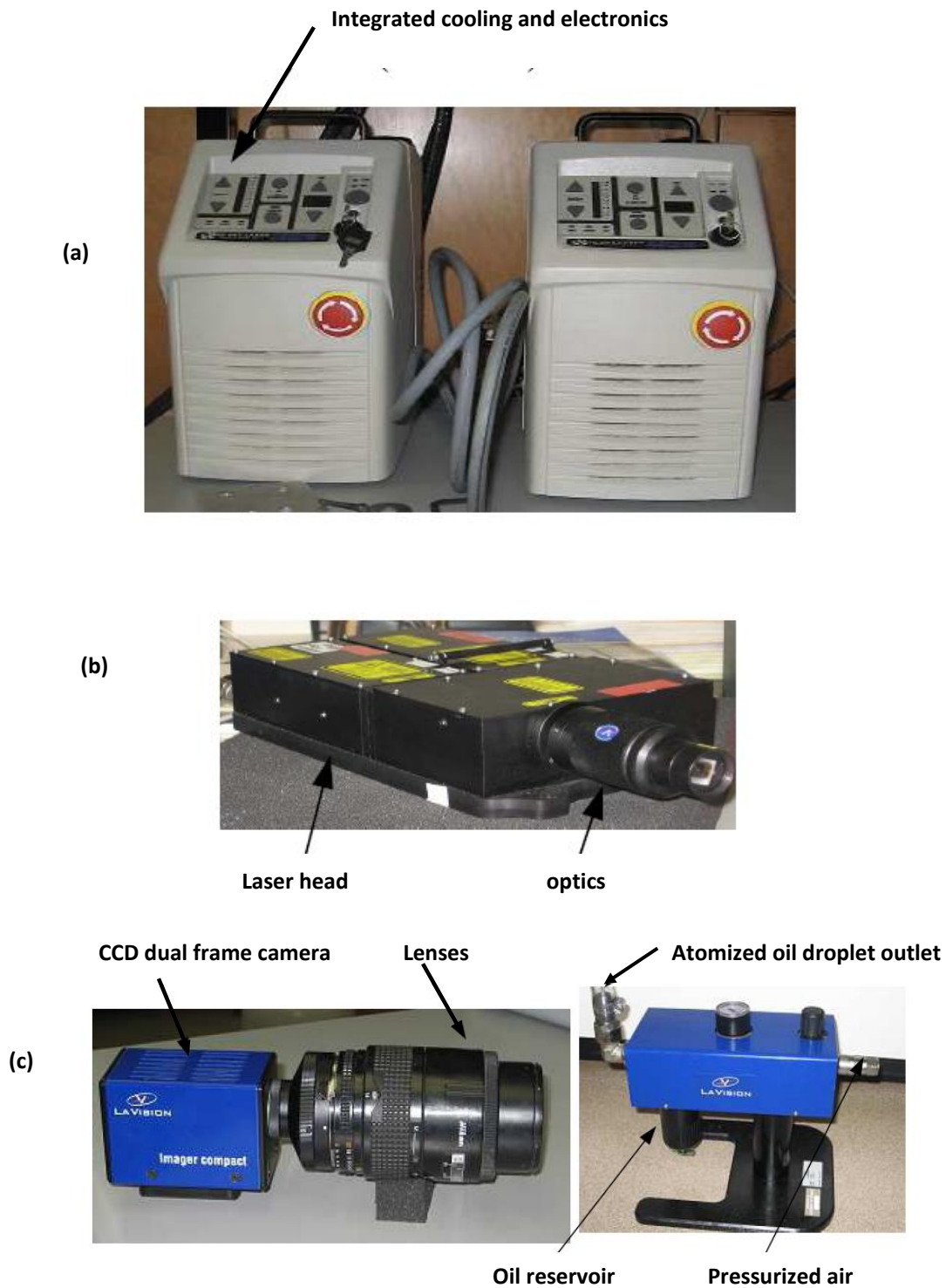
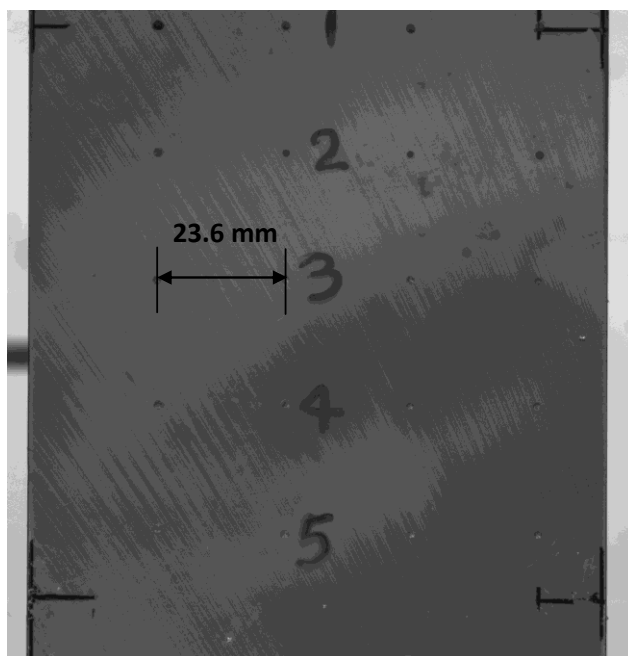
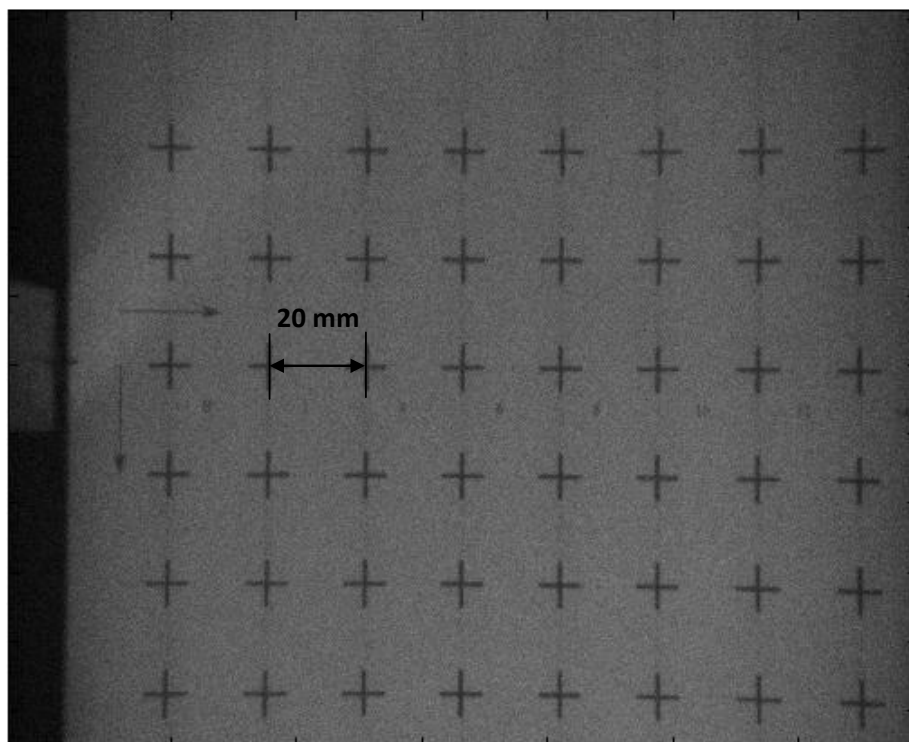


Figure 2-10 Typical PIV system with (a) Integrated Cooling and Electronics (ICE) unit, (b) laser head with sheet optics attached and (c) dual frame CCD camera and the particle seeder



(a)



(b)

Figure 2-11 The calibration sheet used for the PIV measurements in (a) water tunnel and (b) wind tunnel

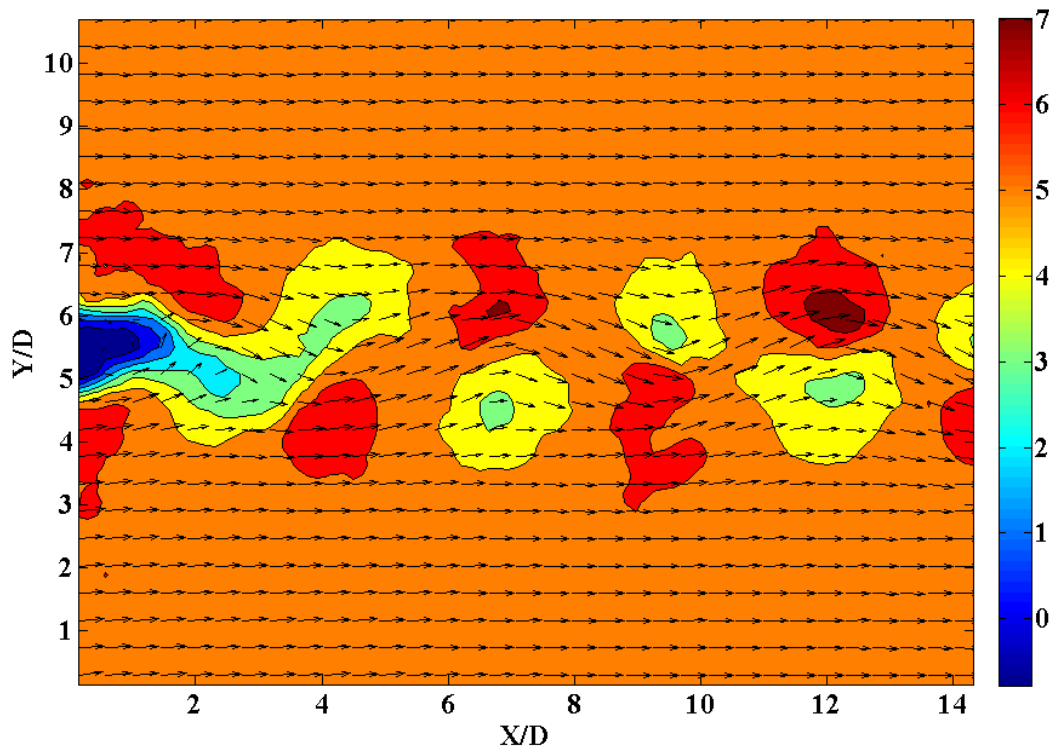


Figure 2-12 The velocity flow field data obtained after processing the PIV images

with multi-pass, decreasing window size technique to obtain the pixel displacements. The velocity vector field determined from these PIV images is shown in Figure 2-12. The error in velocity from the PIV measurements is estimated using the procedure described in Appendix A.1. The maximum error in the PIV measurements is found to be approximately 4% both in vertical (XY) and horizontal (XZ) planes at $Re_D = 550$.

2.3.3 Pressure Transducers

In order to reconstruct the near wake dynamics in the wind tunnel measurements, time-resolved base pressure signals are acquired simultaneously with PIV data by using four flush-mounted Kulite (XCS-093-2D) and Entran (EPE-541-2P) high-speed pressure transducers. A typical high-speed pressure transducer is shown in Figure 2-13. The transducers are solid state devices that use a piezo-resistive element, and pressure sensing is accomplished using a fully active four-arm Wheatstone bridge. Entran and

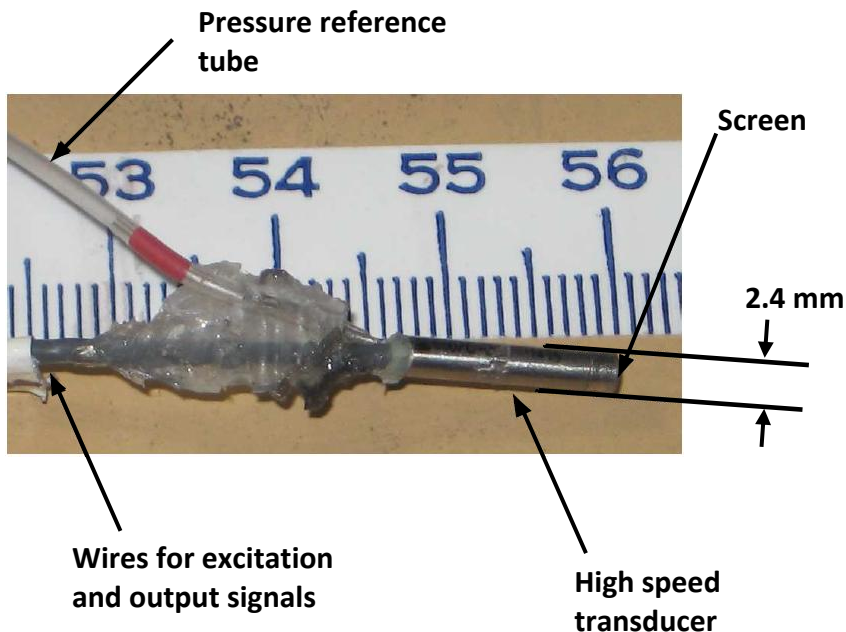


Figure 2-13 Flush mounted high speed transducers used in this investigation

Kulite transducers have sensitivities of 150 mV/FS and 250 mV/FS respectively, with a full scale pressure of 2 psi. The maximum possible data acquisition rate is 150 KHz for both transducers. For all of the measurements, the reference pressure ports are connected to free-stream total pressure. The pressure transducers need 10 volts excitation for their operation, which is provided using Validyne SG297A modules. These signal conditioner modules are housed in a Validyne MC170-L chassis. The output signals from these transducers are low-pass filtered before being acquired through data acquisition. For this purpose, Precision Filters 27000 programmable filters (TR8D) are used. The filters are linear in phase, which is important for this investigation as they are used in time-domain. A typical signal connection for these transducers is shown in Figure 2-14. To simultaneously acquire time-resolved pressure data from the transducers, a NI-PXI-1042 high speed simultaneous-sampling data acquisition system is used. The voltage signals from these transducers are acquired at a sampling frequency of 6250 Hz and low-pass filtered at 3000 Hz.

In this study, four high-speed transducers were used, located as shown in Figure 2-8.

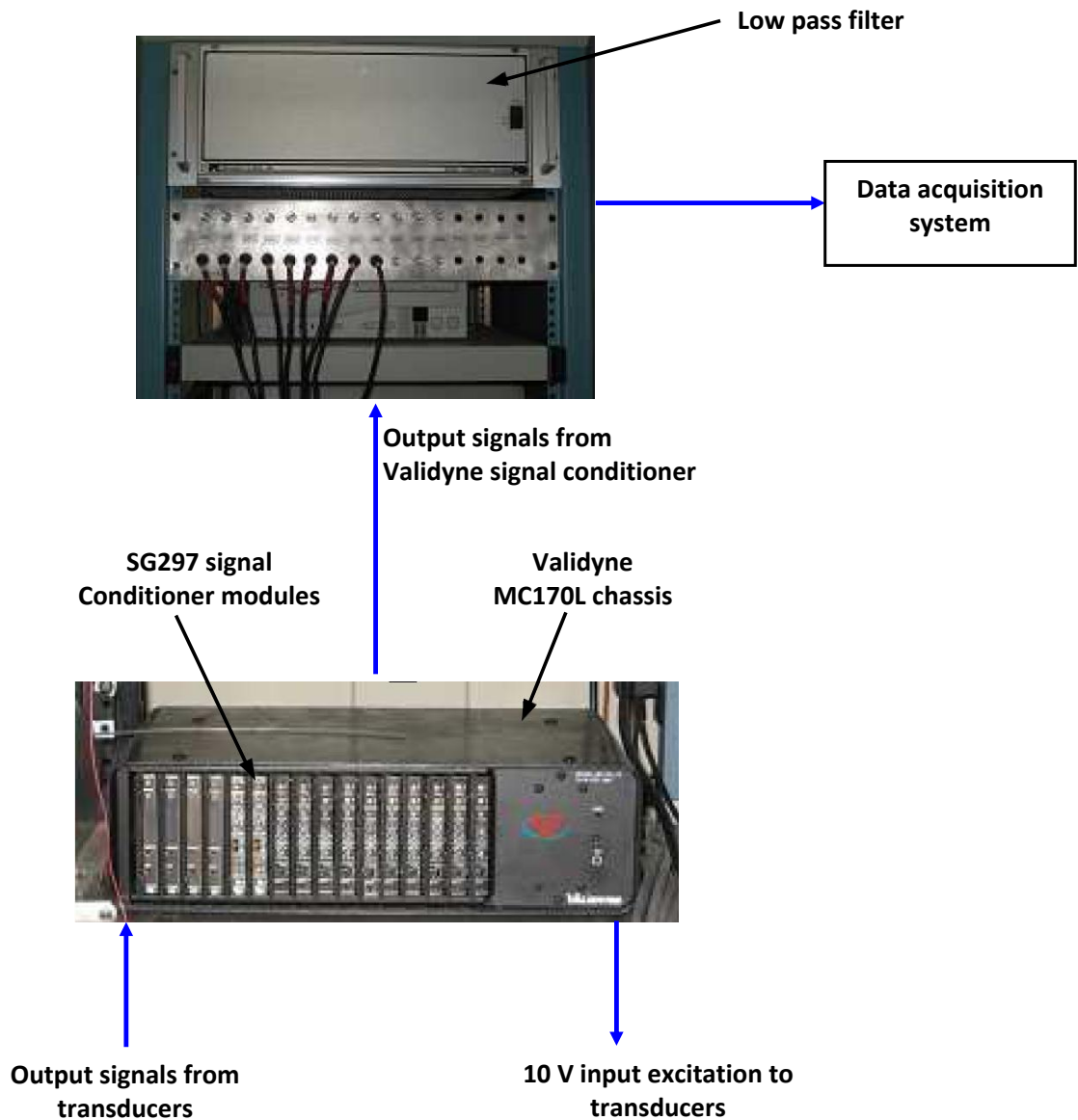


Figure 2-14 Typical high speed pressure data acquisition setup

These transducers require calibration before each test to acquire calibrated time-resolved pressure signals. The calibration was performed in situ using mean pressure measurements from previously calibrated DP-15 Validyne transducers. In order to calibrate the high speed transducers, a series of pressure ports are designed at the same location near the high speed transducers, as shown in Figure 2-8. These pressure ports are connected to DP-15 Validyne transducers, and DP-15 transducers are calibrated using

an Omega pressure calibrator as a pressure standard. The pressure calibrator is capable of producing a very accurate gauge pressure which is required for the calibration process. A typical calibration for a DP-15 Validyne transducer is shown in Figure 2-15 (a). To calibrate the high-speed transducers, the wind tunnel free-stream velocity is varied, and the mean pressure readings from a DP-15 along with mean voltages from high speed transducers are acquired. The mean pressure readings from the DP-15 transducers and the voltage signals from transducers are used for calibration. A typical calibration for a high-speed transducer is shown in Figure 2-15 (b).

2.3.4 Data Acquisition

In order to reconstruct the near wake dynamics, a synchronous data acquisition setup is required. A typical sampling procedure used in wind tunnel measurements is shown in Figure 2-16. For this investigation, data acquisition is achieved in such a way that when a PIV image is taken, a trigger from the PTU of the LaVision PIV system is sent to the NI-PXI simultaneous high-speed data acquisition system which acquires 3000 pre-trigger and 3250 post-trigger pressure samples. The sampling interval of one second covers approximately 100 vortex shedding cycles for the cases studied. Moreover, to ensure independent data, each pressure record and PIV image is separated from the next by approximately 1000 vortex shedding cycles. For this investigation, 1000 uncorrelated (random) PIV image pairs are acquired along with simultaneously sampled time-resolved pressure signals using the above-mentioned acquisition timing setup. However, in the case of water tunnel measurements, a reference signal was not acquired and a total of 3000 PIV image pairs were acquired at a sampling frequency of 15 Hz. Finally, the data is stored in SI units for later processing.

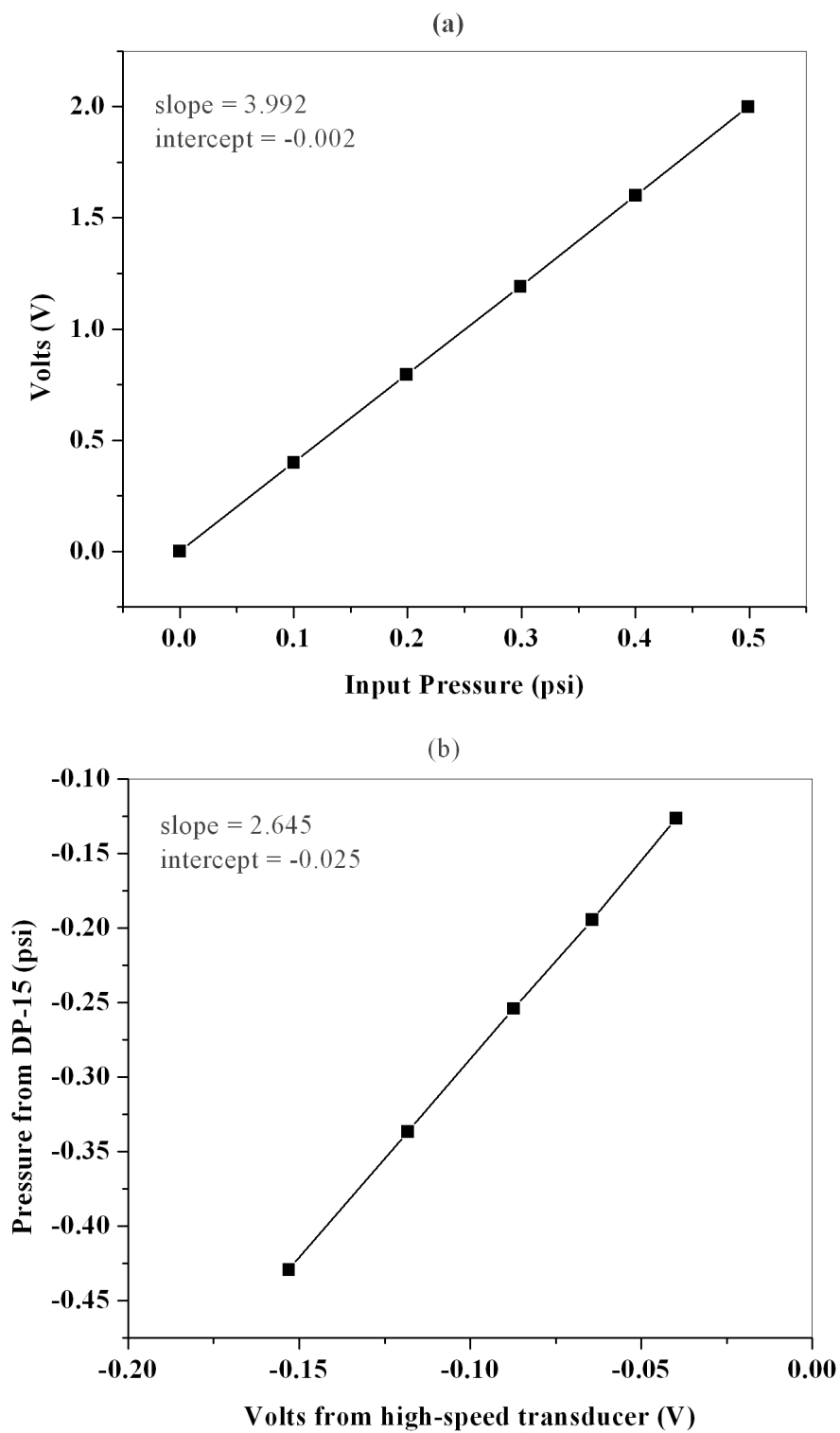


Figure 2-15 Calibration for (a) DP-15 transducer and (b) High speed pressure transducer

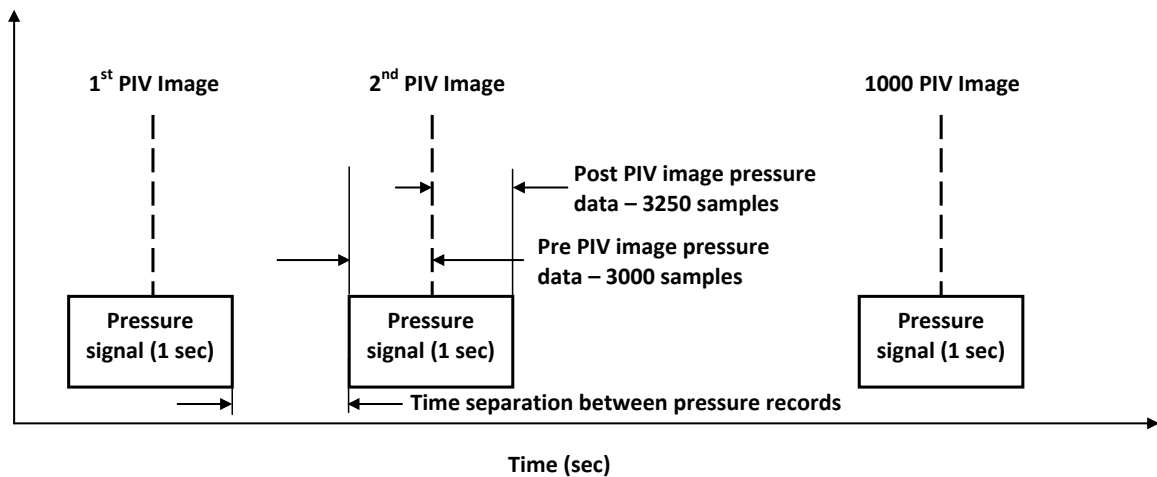


Figure 2-16 Acquisition timing for PIV and pressure records in wind tunnel measurements

2.4 Analysis Approach

2.4.1 Proper Orthogonal Decomposition (POD)

The POD analysis technique was first introduced in the field of turbulence by Lumley (1967) to characterize coherent structures of turbulent flows. It is a decomposition technique in which the orthogonal modes or basis functions $\phi(\bar{x})$ are not predefined, but are derived from an available data set (Holmes et al. 1996). A combination of these modes describes the coherent structures in a flow field. Since these modes are not predefined, they can be optimized for any desired quantity of flow. For the purposes of this investigation, the modes are optimized for turbulent kinetic energy (TKE) and enstrophy.

Due to recent advancements in computational abilities, it has now become possible to apply the POD analysis technique to a large set of turbulent data for identification of coherent structures in turbulent flows. Sirovich (1987) provided a detailed mathematical description of the implementation of POD to turbulent flow field data. He suggested two

different approaches for implementation: 1) a direct method, and 2) a snapshot method. Both these methods yield the same results. However, the latter method is computationally less intensive, and hence, has been used for large PIV data sets. In recent investigations, POD has been applied successfully to identify coherent structures in an axisymmetric jet (Citriniti 1996), in a backward facing step (Kostas et al. 2005), in the turbulent wake of a disk (Johansson et al. 2002), and in vortex shedding of a square cylinder (van Oudhensden 2005). Apart from identifying coherent structure, POD analysis has also been used in such applications as flow control (Gillies 2000; Cohen et al. 2004; Cruz et al. 2005) and low-order modeling (Rowley et al. 2004).

2.4.1.1 Mathematical Description

Here, POD is implemented using the snapshot method on the obtained planar PIV velocity vector data for both the vertical (XY) and the horizontal (XZ) plane. POD expands the velocity $\bar{u}(\bar{x}, t)$ into a finite sum of temporal component and spatial component as follows (Holmes et al. 1996):

$$\bar{u}(\bar{x}, t) = \sum_{n=1}^N a^n(t) \phi^n(\bar{x}) \quad (2.1)$$

The spatial component $\phi^n(\bar{x})$, also known as the basis function, is optimal in the sense that the error in the actual signal and the reconstructed velocity field square (i.e. turbulent kinetic energy) is minimal (Cizmas et al. 2003), resulting in

$$M = \left\langle \left\| \bar{u}(\bar{x}, t) - \sum_{i=1}^n a^i(t) \phi^i(\bar{x}) \right\|^2 \right\rangle \quad (2.2)$$

It can be shown (Holmes et al. 1996) that Equation (2.2) can be reduced to an eigenvalue problem:

$$\int \langle \bar{u}(\bar{x}, t) \bar{u}^*(\bar{x}', t) \rangle \cdot \phi^n(\bar{x}') d\bar{x}' = \lambda^n \phi(\bar{x}) \quad (2.3)$$

where $\langle \bar{u}(\bar{x}, t) \bar{u}(\bar{x}', t) \rangle$ is the spatial autocorrelation tensor at zero time lag obtained using temporal average over N various fields at different time t_n . * denotes the complex

conjugate. The eigenvalue λ^n represents the energy of the velocity associated with mode n .

The POD modes are orthogonal and, therefore verify (Holmes et al. 1996; Maurel et al. 2001; Cizmas et al. 2003; Smith et al. 2005)

$$\int \phi^n(\bar{x})\phi^m(\bar{x})d\bar{x} = \delta_{mn} \quad (2.4)$$

Once the POD modes are known, the temporal coefficients ($a^n(t)$) are obtained by projecting the velocity field onto the POD modes as follows (Holmes et al. 1996; Maurel et al. 2001; Cizmas et al. 2003; Smith et al. 2005):

$$a^n(t) = \int \bar{u}(\bar{x}, t) \cdot \phi^n(\bar{x}) d\bar{x} \quad (2.5)$$

The temporal coefficients have zero mean, and satisfy $\langle a_n \cdot a_m \rangle = \lambda^{(n)} \delta_{mn}$ (Holmes et al. 1996; Maurel et al. 2001; Cizmas et al. 2003; Smith et al. 2005).

The advantage of applying the snapshot method (Sirovich 1987) is that the spatial auto correlation tensor in equation 2.3 with a dimension of $n_c \times N$ (n_c being the number of vectors and N being the number of snapshots) can be replaced with a temporal two point correlation tensor with a dimension of N (Cizmas et al. 2003; Smith et al. 2005; Pininer et al. 2007). In the snapshot method, equation 2.3 is equivalent to the eigenvalue problem as follows (Smith et al. 2005; Pininer et al. 2007) (see Appendix A.2 for detailed POD formulation):

$$\int_N C(t, t') a_n(t') dt' = \lambda^n a_n(t) \quad (2.6)$$

where $C(t, t')$ is the temporal two-point correlation tensor defined as (Smith et al. 2005; Pininer et al. 2007)

$$C(t, t') = \frac{1}{N} \int_{\Omega} u_i(\bar{x}, t) u_i^*(\bar{x}, t') d\bar{x} \quad (2.7)$$

The spatial POD modes are defined as

$$\phi^n(x) = \frac{1}{N\lambda^n} \int a_n(t)u(\bar{x},t) \quad (2.8)$$

and verify equation 2.4 (Smith et al. 2005; Pininer et al. 2007).

However, the method of snapshots can be used only when $n_c > N$. For the current measurements, n_c is 7326 and 5568 vectors, and $N = 3000$ and 1000 snapshots in the case of water tunnel and wind tunnel measurements respectively. The POD technique is implemented using MATLAB. The typical run time to calculate the POD modes on a CPU with 2GB is approximately 40 to 60 minutes depending on the size of the correlation matrix. A Sample POD code is provided in Appendix A.3 for reference. Figure 2-17 shows the cumulative convergence of energy using snapshot POD in XY plane data for straight trailing edge at $Re_D = 24000$. Figure 2-17 shows that a significant percentage of the kinetic energy ($\approx 60\%$) in the flow is captured in the first two POD modes, indicating that the large-scale phenomena in the flow can be reconstructed using the first few POD modes.

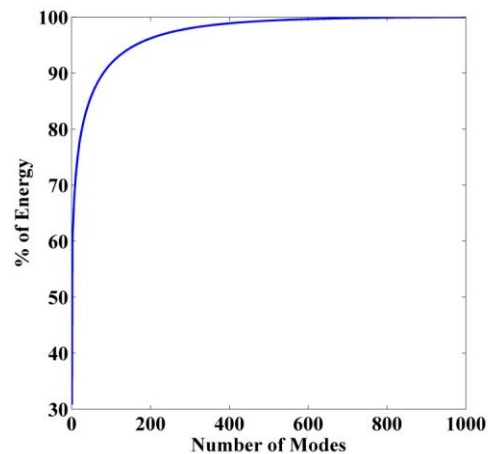


Figure 2-17 Cumulative convergence of energy using snapshot POD in vertical plane for straight trailing edge at $Re_D = 24000$.

2.4.1.2 POD Convergence

- **Number of PIV Images**

In order to determine the number of temporally uncorrelated PIV required for POD analysis, the convergence of the energy captured by the first two modes is analyzed. The convergence in the energy captured by the first two modes will suggest the number of PIV images required to obtain an accurate estimate of POD modes. For this purpose POD analysis is performed using 10, 50 100, 200, 400, 500 700, 800, 900 and 1000 PIV images, and energy captured by first two modes are plotted until a no significant variation in the energy is observed, as shown in Figure 2-18 for both vertical (XY) plane and horizontal (XZ) planes at $Y/D = 0$ and $y/D = -0.5$ for $Re_D = 24000$. As observed from these figures that after using 700 PIV images there is no significant variation in energy captured by the first two POD modes.

- **Number of POD modes**

The fluctuation velocity field can be obtained from the PIV data by calculating the standard deviation of the velocity field as

$$u_{rms} = \sqrt{\frac{1}{N} \sum_{i=1}^N (x_i - \bar{x})^2} \quad (2.9)$$

The fluctuation velocity field can also be reconstructed by projecting the instantaneous field on a finite number of POD modes as follows (Perrin et al., 2007):

$$\overline{u_i u_j(\bar{x})} = \sum_n \lambda_n \phi_i^{(n)}(\bar{x}) \phi_j^{*(n)}(\bar{x}) \quad (2.10)$$

Perrin et al. (2007) demonstrated that the coherent motion of flow and its corresponding turbulent statistics behind a circular cylinder can be predicted to a considerable accuracy by using the first 10 POD modes. To verify the accuracy of the method proposed by Perrin et al. (2007), the streamwise Reynolds stress component has been calculated from the PIV data by computing the standard deviation (equation 2.9), and also reconstructed by using equation 2.10, by combing different numbers of POD modes as shown in Figure 2-19. This comparison is made at different Reynolds numbers of $Re_D = 550, 1050, 1550, 2300, 24000$ and 46000 . Figure 2-19 indicates that 10 POD modes effectively capture the trend in the turbulence intensity profile. However, a

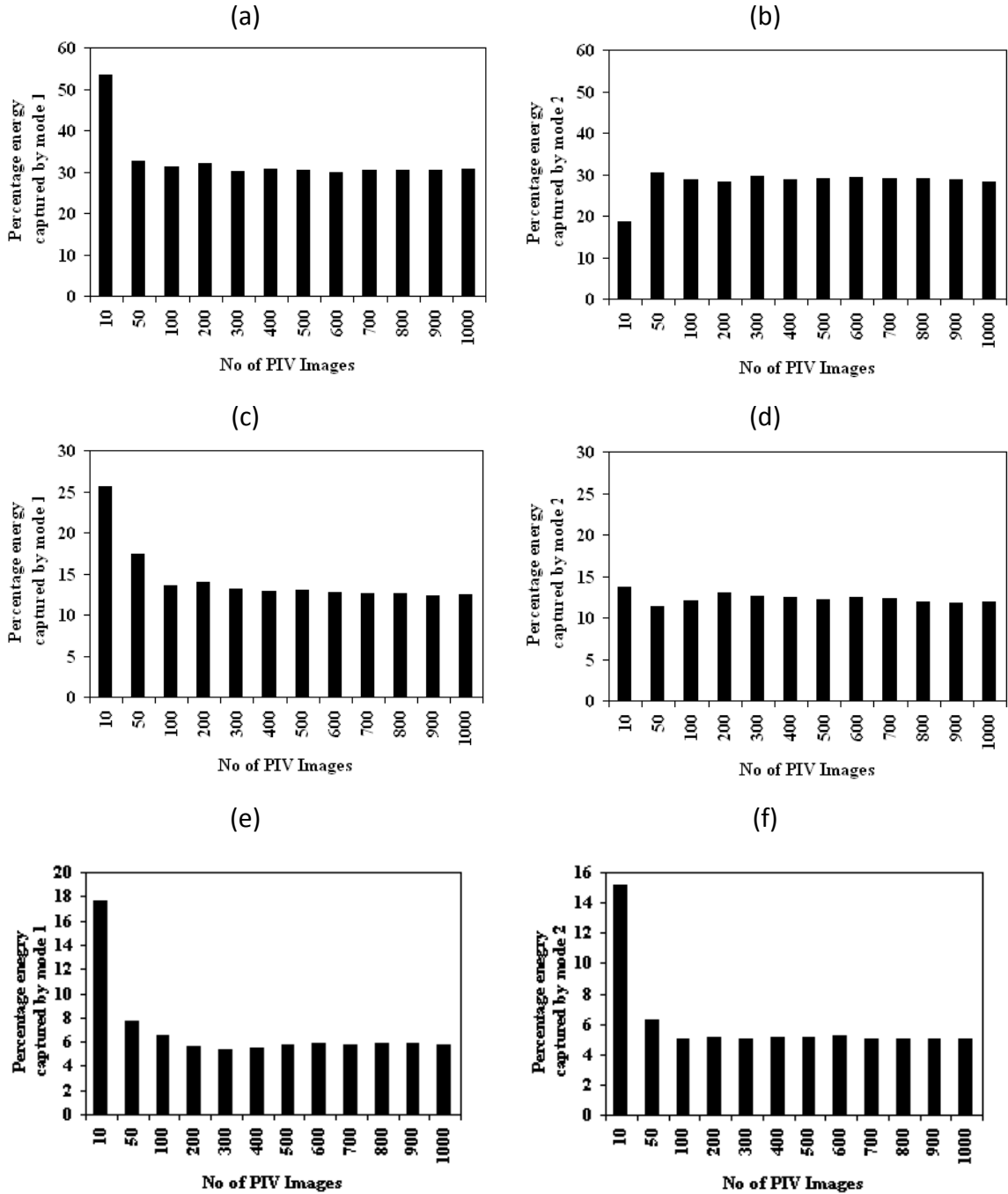


Figure 2-18 Convergence of energy captured by (a) mode 1 and (b) mode 2 in XY plane, (c) mode 1 and (d) mode 2 in XZ plane ($Y/D = -0.5$), and (e) mode 1 and (f) mode 2 in XZ plane ($Y/D = -0.8$) at $Re_D = 24000$. Energy is calculated using 10, 50, 100, 200, 300, 400, 500, 600, 700, 800, 900 and 1000 PIV images.

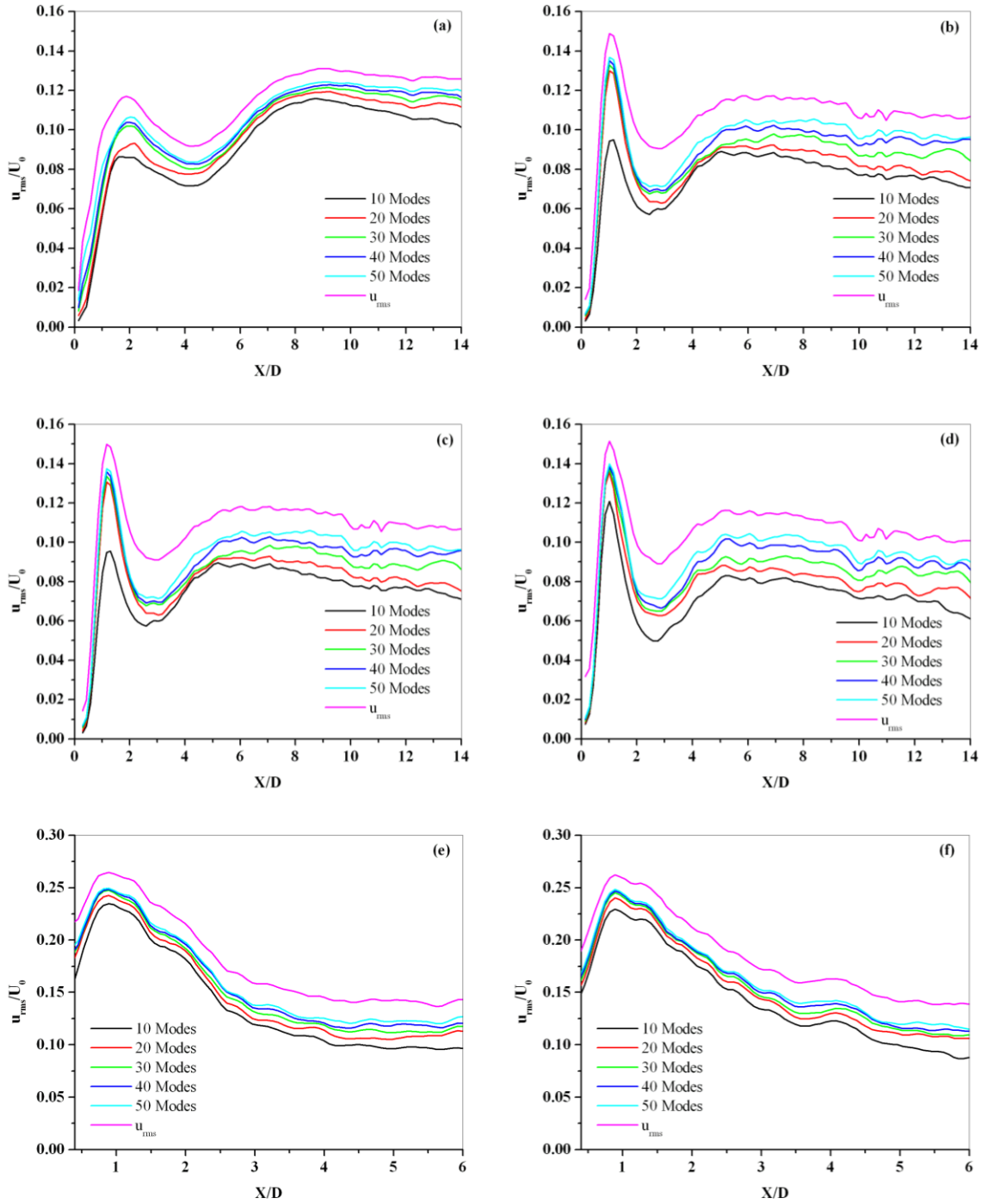


Figure 2-19. Comparison of streamwise turbulence intensity along the centre line calculated using standard deviation of the PIV data and reconstructed using different number of POD modes at (a) $Re_D = 550$, (b) $Re_D = 1050$, (c) $Re_D = 1550$, (d) $Re_D = 2300$, (e) $Re_D = 24000$ and (f) $Re_D = 46000$

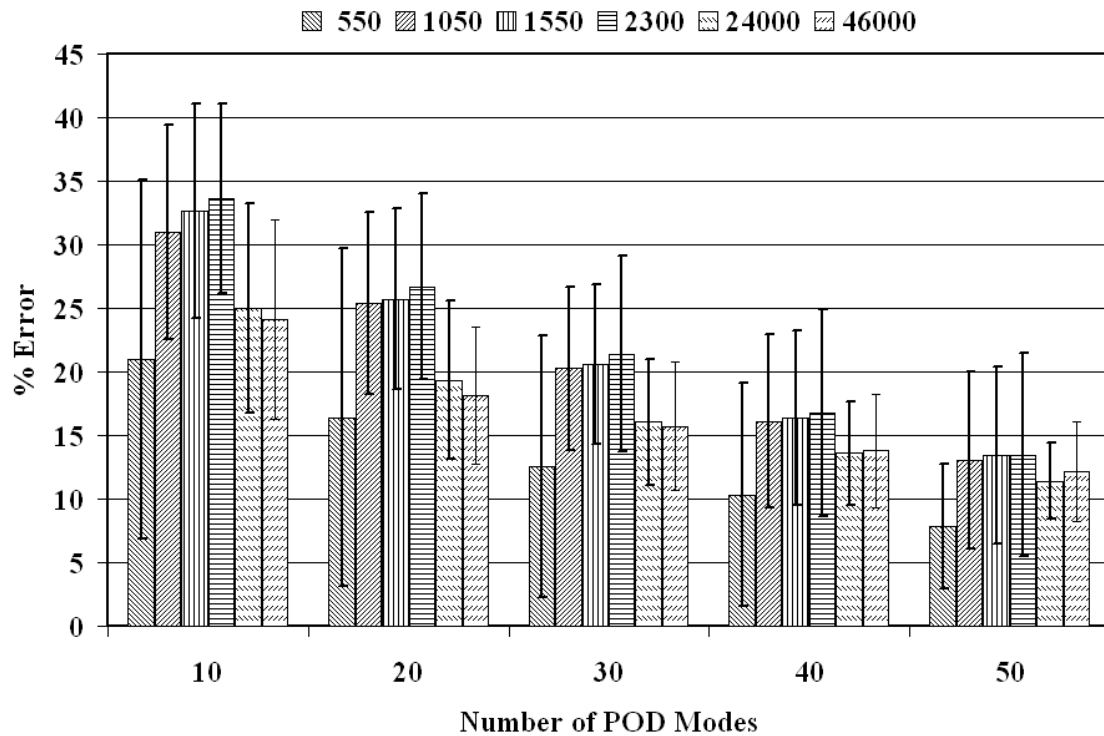


Figure 2-20. % error in predicting centre line streamwise turbulence intensity by combining different number of POD modes for $Re_D = 550, 1050, 1500, 2300, 24000$ and 46000

higher number of POD modes reduce the error in predicting the turbulence intensity, which is compared in Figure 2-20 for various Reynolds numbers. Figure 2-20 indicates that error reduces with increasing number of POD modes.

2.4.2 Phase Averaging

According to Reynolds and Hussain (1972), a flow field can be decomposed into a mean component, a periodic fluctuation and a chaotic one as

$$U_i = \bar{U}_i + \tilde{U}_i + u'_i \quad (2.11)$$

where \bar{U}_i is the time-independent mean flow, \tilde{U}_i is the quasi periodic fluctuating component, u'_i is the random fluctuating component, and $\langle U_i \rangle = \bar{U}_i + \tilde{U}_i$ is the phase averaged component

Several choices are available for the reference signal to construct the phase averaged component. Wlezien and Way (1979) used the velocity signal measured by the hotwire technique just above the boundary layer on the cylinder, near the separation line, and used the Hilbert transform technique to measure the phase of the signal. Cantwell and Coles (1983) used the pressure signal on the cylinder, and used a phase locked loop (PLL) component to measure the phase of the signal.

In this study, the reference signal was chosen as the pressure signal measured at the base of the flat plate very near to the shear layer in wind tunnel measurements, so that the signal had a strong quasi-periodic component at the Strouhal number. For this signal, the phase is determined using the Hilbert transform technique as recommended by Wlezien and Way (1979). Determination of the phase calculation using Hilbert transform is given in Appendix A.4.

To obtain phase averaged quantities, 1000 samples of simultaneous PIV and pressure were acquired in the wind tunnel experiments. From the pressure signal, the phase of the flow was determined by calculating the Hilbert transform. The velocity fields were then classified according to phase intervals of $2\pi/12$. Approximately 70 images were collected per phase interval (bin) and averaged.

In the case of water tunnel experiments, it was not possible to obtain a reference, and therefore, extracting phase data from the available PIV data was explored. The POD coefficients of the first two modes can be used to extract the phase of the vortex shedding instead of using a reference signal. Perrin et al. (2007) demonstrated that temporal evolution of the POD coefficients is sinusoidal or quasi sinusoidal, allowing us to extract the phase information from PIV data as

$$\varphi_{a_1-a_2} = \arctan\left(\frac{\sqrt{2\lambda_1}a_2}{\sqrt{2\lambda_2}a_1}\right) \quad (2.12)$$

where λ_1 and λ_2 are the eigenvalues and a_1 and a_2 are temporal coefficients of the first two POD modes. $\varphi_{a_1-a_2}$ versus $\varphi_{pressure}$ is plotted in Figure 2-21. It is observed that the phase angle defined by the POD coefficients and the phase angle defined by the pressure signal are very well correlated.

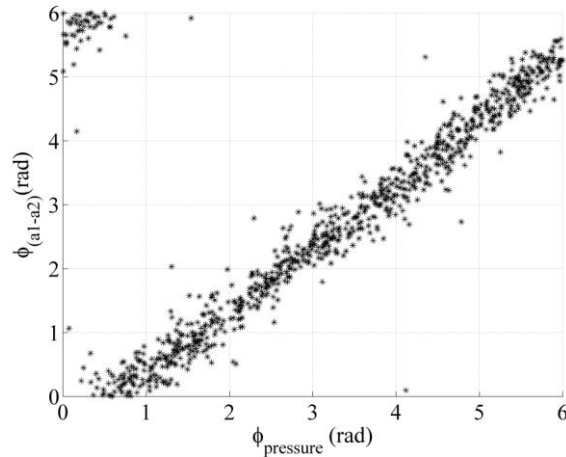


Figure 2-21 Correlation of phase angles determined from the POD coefficients and pressure signal in XY plane

Note that this method is valid only for the vertical (XY) plane results. When the same method is applied in the horizontal (XZ) plane, the phase defined by the POD coefficients and that obtained from pressures do not correlate, as shown in Figure 2-22. In the vertical plane, the POD coefficients capture the quasi sinusoidal evolution of the von Karman vortices. However, in the horizontal plane, since more than one dominant coherent structure is present, the POD coefficients are not correlated only to von Karman vortex street.

Hence, in order to identify the phase information from the PIV data in the horizontal (XZ) plane, where there is no reference signal and where the POD coefficients cannot be used, we explore the method proposed by Konstantinidis et al. (2005), which does not need a reference signal but which uses a conditional averaging approach. In this method, cross-correlation coefficients (R_{ij}) between the velocity vectors are computed and assumed to be in the same phase above a certain threshold value.

$$R_{ij} = \sum_n U_i^{(n)} \cdot U_j^{(n)}, \quad i, j = 1, \dots, N \quad (2.13)$$

Here, N is the number of snapshots obtained and n is the number of velocity vectors in the field of view. Figure 2-23 shows the phase averaged streakline plots in the XY plane obtained by calculating the phase using (a) pressure signal, (b) POD coefficients and (c) conditional averaging approach. All of the three methods yield very similar results. However, the phase averaged results in the XZ plane obtained by using the method proposed by Konstantinidis et al. (2005) did not properly characterize the topology of the secondary structure. The phase averaging washes out the features of the secondary structures, and hence phase averaging in the horizontal (XZ) plane is not performed for the water tunnel measurements.

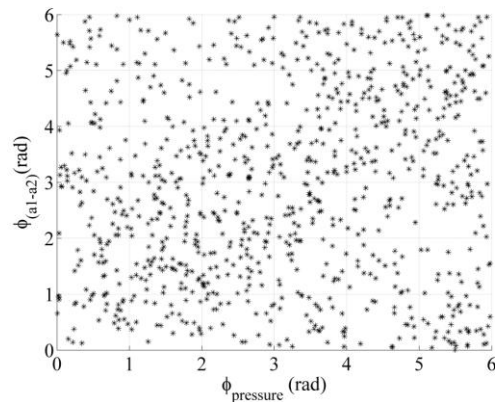


Figure 2-22 Correlation of phase angles determined from the POD coefficients and pressure signal in XZ plane

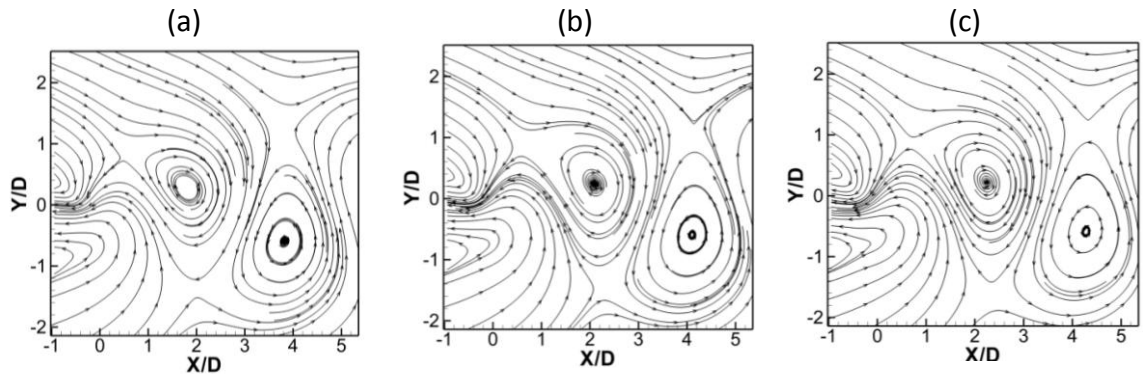


Figure 2-23 Phase averaged streakline plots obtained by calculating the phase from the (a) pressure signal, (b) POD coefficients and (c) conditional averaging approach.

3 NEAR WAKE COHERENT STRUCTURES OF A BLUNT TRAILING-EDGE-PROFILED BODY

As stated in Section 1.3, one of the main objectives of the current study is to experimentally verify the numerical findings of Ryan et al. (2005), who stated that the order of transition of the near wake instabilities in the wake of a blunt-trailing-edge profiled body is not same as for a circular cylinder. In order to achieve the above objective and to further understand the robustness of near wake instabilities with increasing Reynolds number, PLIF visualizations were conducted in the wake of the blunt trailing-edge-profiled body in vertical (XY), horizontal (XZ) and traverse (YZ) planes for low Reynolds number ranging from $Re_D = 250$ to 2300. In order to verify these observations, further PIV measurements were conducted in XY and XZ plane and POD analysis was performed to extract information associated with these dominant coherent structures in the same Reynolds number range. Finally to establish the robustness of these streamwise instabilities at very high Reynolds numbers, PIV measurements were performed in a wind tunnel at Reynolds number ranging from $Re_D = 24000$ to 46000. The results of these experiments are discussed in the following sections, with the following questions addressed:

- Do the secondary wake instability modes appear in the same sequence as in circular cylinder flows?
- Is the spacing of these observed secondary wake instabilities of the blunt trailing-edge-profiled body different from other bluff body flows?
- Are the modes the same in the near wake as in the intermediate wake?
- How can the streamwise spacing of spanwise vortices and spanwise spacing of the streamwise vortices be identified from the PIV measurements?

3.1 Integral Parameters

A summary of the flow field results are presented here in order to compare the results with those from previous studies. The results are presented here in terms of Strouhal number as a function of Reynolds number. Strouhal number (St) is the non-dimensional representation of the vortex shedding frequency (f_s), and is defined as

$$St = \frac{f_s D}{U_o} \quad (3.1)$$

where D is the thickness of the wake generator and U_o is the free stream velocity.

Figure 3-1 shows that the results from the current study compare very well with Petrusma and Gai (1996), who studied a blunt trailing-edge-profiled body with a thickness to chord ratio of $L_x/D = 10$. Figure 3-1 also shows the variation of St as a function of Re_D for a circular cylinder, indicating that a blunt trailing-edge-profiled body does not show asymptotic behavior as observed in the case of a circular cylinder up to $Re_D = 2500$.

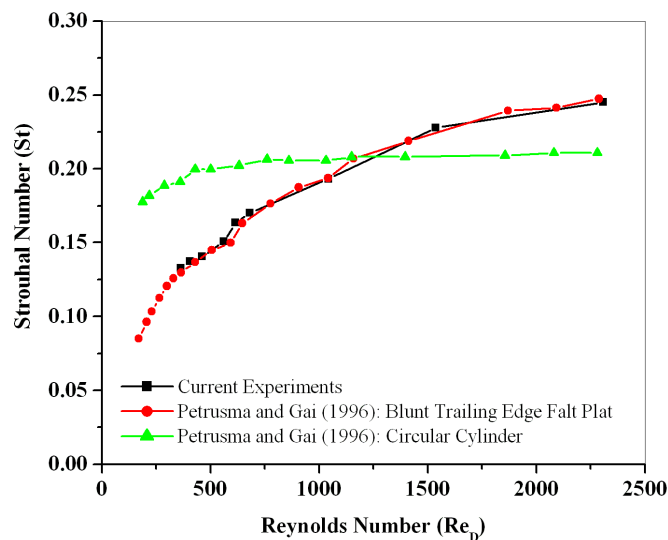


Figure 3-1. Comparison of Strouhal number as a function of Reynolds number with Petrusma and Gai (1996)

In Figure 3-2, results from the current study are compared with those of Eisenlohr and Eckelmann (1988) and Bull et al. (1995). Eisenlohr and Eckelmann (1988) conducted experiments for a blunt trailing-edge-profiled body with different thickness to chord ratios ($50 \leq L_x/D \leq 800$) and thickness to span ratios ($35 \leq L_z/D \leq 280$), allowing the boundary to transition naturally, up to a Reynolds number (Re_{d_1}) of 15000. Bull et al. (1995) extended the work of Eisenlohr and Eckelmann (1988) up to a Reynolds numbers (Re_{d_1}) of 30000 for the same geometry with different thickness to chord ratios ($20 \leq L_x/D \leq 50$), maintaining a constant thickness to span ratio of $L_z/D = 38$. However, Bull et al. (1995) conducted experiments allowing the boundary layer to transition naturally, as well as artificially triggering it with a trip wire. Eisenlohr and Eckelmann (1988) and Bull et al. (1995) presented the vortex shedding frequency as a product of Reynolds number and Strouhal number, also known as Roshko number. The Reynolds and Strouhal numbers use d_1 as the reference length instead of wake generator thickness (D), which is defined as

$$d_1 = D + 2\delta_1 \quad (3.2)$$

where δ_1 is the displacement thickness of the boundary layer. In the current study, the boundary layer displacement thickness for the low Reynolds number measurements is estimated using the formula (Schlichting and Gersten 2000)

$$\delta_1 = 1.7802 \frac{1}{\sqrt{Re_{L_x}}} \quad (3.3)$$

where L_x is the chord length of the blunt trailing edge body. However, for the high Reynolds number measurements, the displacement thickness of the boundary layer is estimated from the boundary layer profile measured at $0.4D$ before the separation, using the following formula (Schlichting and Gersten 2000).

$$\delta_1 = \int_0^{\infty} \left(1 - \frac{U}{U_o} \right) dy \quad (3.4)$$

Figure 3-2 indicates that the Strouhal number collapses onto a single curve, forming a linear relationship between the Reynolds and Roshko numbers. Bull et al. (1995) proposed the following relationship between the Roshko and Reynolds numbers based on the least square fit for naturally evolving boundary layer data:

$$Ro(d_1) = 0.286 Re_{d_1} \quad (3.5)$$

and based on the least square fit for the trip wire data:

$$Ro(d_1) = 0.229 Re_{d_1} \quad (3.6)$$

Upper and lower limits are shown in Figure 3-2. The data from the current study falls within the range proposed by Bull et al. (1995) when Reynolds number is expressed as a function of Roshko number (Figure 3-2).

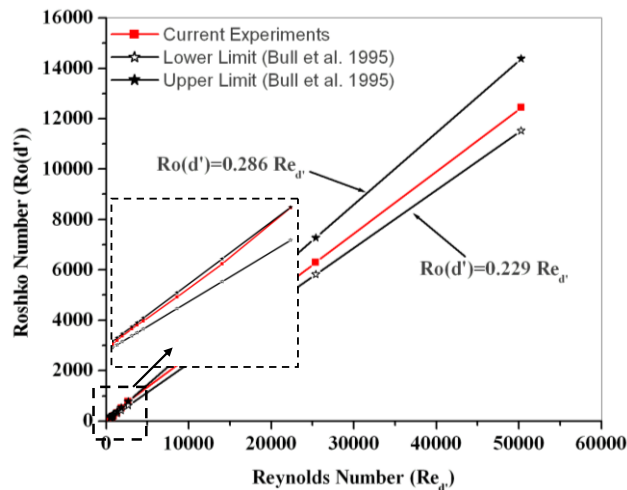


Figure 3-2. Comparison of Roshko number as a function of Reynolds number with Bull et al. (1995)

Ryan et al. (2005) conducted numerical simulation on a blunt trailing-edge-profiled body with different thickness to chord ratios ($2.5 \leq L_x/D \leq 17.5$) up to a Reynolds number of 700. They presented the vortex shedding frequency as a Roshko number

$$Ro(d_2) = St(d_2) \cdot Re_{d_2} \quad (3.7)$$

where d_2 is defined as

$$d_2 = 2\delta_2 + D \quad (3.8)$$

δ_2 being the momentum thickness of the boundary layer measured at the trailing edge of the body. In our study, the boundary layer momentum thickness for the low Reynolds number measurements is estimated using the formula (Schlichting and Gersten 2000)

$$\delta_2 = 0.664 \frac{1}{\sqrt{Re_{Lx}}} \quad (3.9)$$

Figure 3-3 indicates that the Strouhal number collapses onto a single curve and forms a linear relationship with the Reynolds number, comparing very well with the results of Ryan et al. (2005).

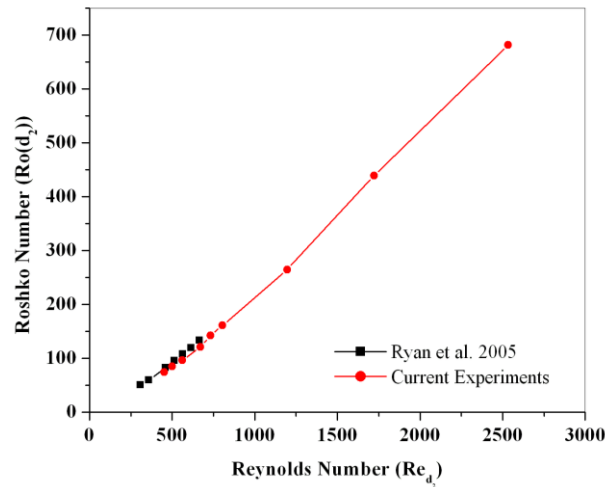


Figure 3-3. Comparison of Roshko number as a function of Reynolds number with Ryan et al. (2005)

3.2 Water Tunnel Measurements

3.2.1 XY Plane Results

Figure 3-4 shows the instantaneous (a) streamwise, (b) transverse velocities. Figure 3-4 (c) shows the vorticity field calculated from the velocity as follows:

$$\omega_z = \frac{\partial V}{\partial X} - \frac{\partial U}{\partial Y} \approx \frac{\Delta V}{\Delta X} - \frac{\Delta U}{\Delta Y} \quad (3.10)$$

Since the PIV measurement provides velocity data in a two-dimensional plane on an evenly spaced grid, a finite different scheme must be used to estimate the velocity gradient (that is, $\partial V/\partial X$ or $\partial U/\partial Y$). The least square difference (equation 3.11) scheme proposed by Raffel et al. (1998) is used to calculate the velocity gradients, is most suitable for PIV data as this method reduces that effect of random errors.

$$\left(\frac{df}{dx}\right)_i \approx \frac{2f_{i+2} + f_{i+1} - f_{i-1} - 2f_{i-2}}{10\Delta x} \quad (3.11)$$

The instantaneous velocity field shows in Figure 3-4 captures the features of the Karman vortices developing the flow at low Reynolds numbers. However as the Reynolds numbers increases the vortices appear to be smeared due to the turbulent chaotic motion in the flow. The same observation is also made from the instantaneous vorticity contours. In order to extract the feature of this dominant coherent structure, Proper Orthogonal Decomposition (POD) is performed on the velocity data which is discussed in the following section.

Figure 3-5 shows the first nine POD modes of (a) streamwise and (b) transverse velocity components in the vertical (XY) plane. This plane captures the signature of the spanwise von Karman Benard vortices or rolls. The POD modes act in pairs as previously pointed out by Deane et al. (1991), by Noack et al. (2003) for circular cylinder flows, by van Oudheusden (2005) for square cylinder, and by Durgesh and Naughton (2010) for a flat plate model. The first two modes appear as phase-shifted versions of each other, which, when combined, re-produce the Karman vortices. Modes 4 and 5 appear to be a distorted version of the first two modes. Similarly, modes 6 and 7, and 8 and 9 contribute to the higher harmonic structure of Karman vortices. Mode 3 appears to be a standing mode with no companion mode, likely related to the boundary layer developing in the flow. To further understand these modes, the relative energies and the relation between time varying coefficients are considered. Figure 3-6 shows the relative energy - defined as the ratio of the energy in each mode to the cumulative sum of the

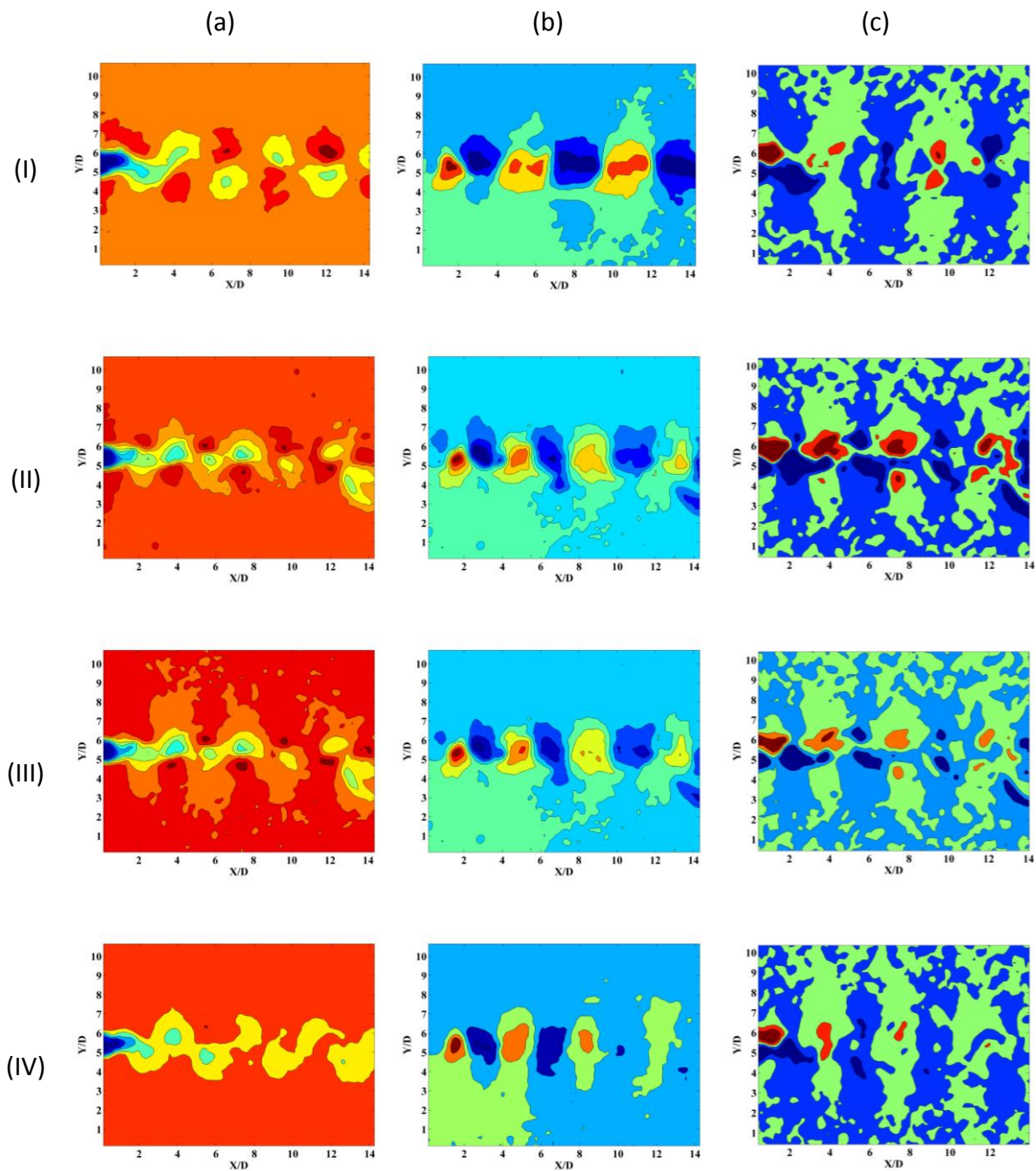


Figure 3-4. Instantaneous (a) streamwise velocity, (b) transverse velocity and (c) ω_z vorticity for Reynolds numbers of (I) $Re_D = 550$, (II) $Re_D = 1050$, (III) $Re_D = 1550$ and (IV) $Re_D = 2300$

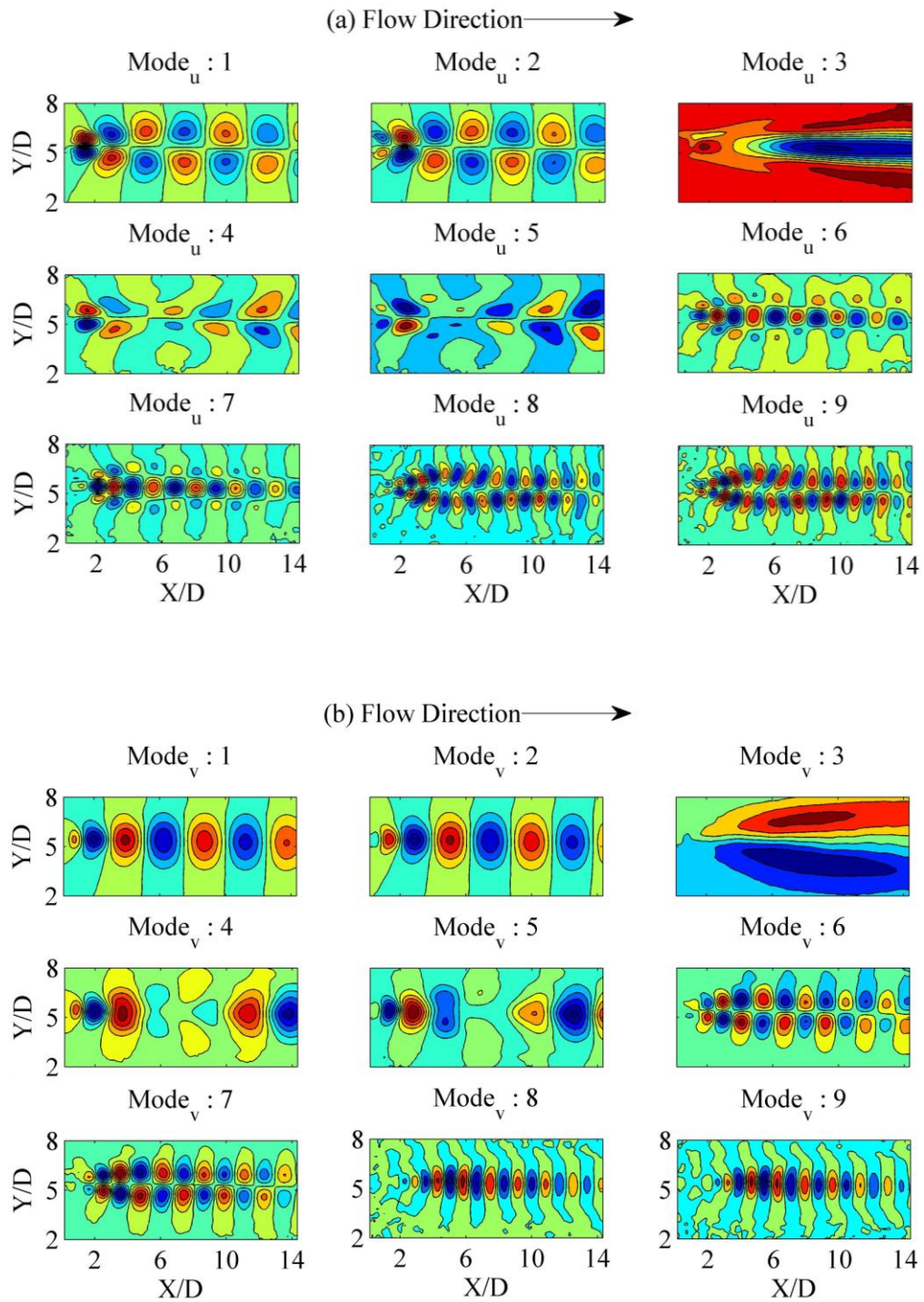


Figure 3-5. (a) Streamwise and (b) transverse velocity components for the first nine POD modes in XY plane at $Re_D = 550$

total energy captured in all modes - captured by the first ten POD modes in XY plane. It is evident that the flow structure is dominated by the first two modes representing the Karman vortices, which capture about 80% of the total relative kinetic energy in the flow. Figure 3-7 shows how the individual phase-averaged time-varying coefficients contribute to the instantaneous sum of the POD modes, and how the amplitude and phase variations develop. The first and second modes (Figure 3-7 a) are 90-degrees apart and the magnitude is of the same order, indicating that they represent the phase shifted Karman Benard vortices. Perrin et al. (2007) pointed out that the first two modes are related only to the fundamental frequency of vortex shedding. Similarly, modes 6 and 7, and 8 and 9 are 90-degrees phase shifted pairs. The wavelength of mode pair 6 and 7 (Figure 3-7 (c)) corresponds to the half wavelength of mode pair 1 and 2. Therefore, mode pair 6 and 7 corresponds to the first harmonic of mode pair 1 and 2 (which represents the Karman vortices). The wavelengths of mode pair 8 and 9 (Figure 3-7 d) correspond to one-third of the wavelength of mode pair 1 and 2, indicating that modes 8 and 9 are related to the second harmonic of the fundamental structure. Further insight can be gained from the phase portraits of the time varying coefficients (Figure 3-8). The axes of these plots are the time varying coefficients normalized with their respective eigenvalues, as defined by van Oudheusden et al. (2005). These curves represent the Lissajous curves, which show the complex harmonic motion of two sine curves orthogonal to one another:

$$\begin{aligned} x(t) &= a_x \sin(b_x t + c_x) \\ y(t) &= a_y \sin(b_y t + c_y) \end{aligned} \quad (3.12)$$

When the frequencies and phases of the two waves are the same ($b_x = b_y$ and $c_x = c_y$), the resulting Lissajous figure is a straight line passing through the origin of the X-Y axes. If the amplitudes are also the same, then the straight line lies at 45° to the X and Y axes. When the frequencies and amplitudes are the same ($b_x = b_y$ and $a_x = a_y$), the Lissajous figures are ellipses. In addition, if the phase difference is either 90-degrees or 270-degrees, the ellipses collapse to circles. When the amplitudes, frequencies, and phases of the two waves differ, the resulting figures are complicated intermeshing

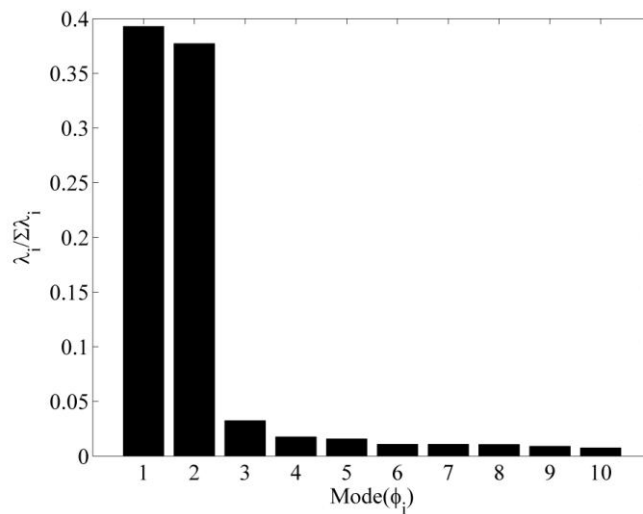


Figure 3-6. Relative energy captured by first ten POD modes in XY plan at $Re_D = 550$

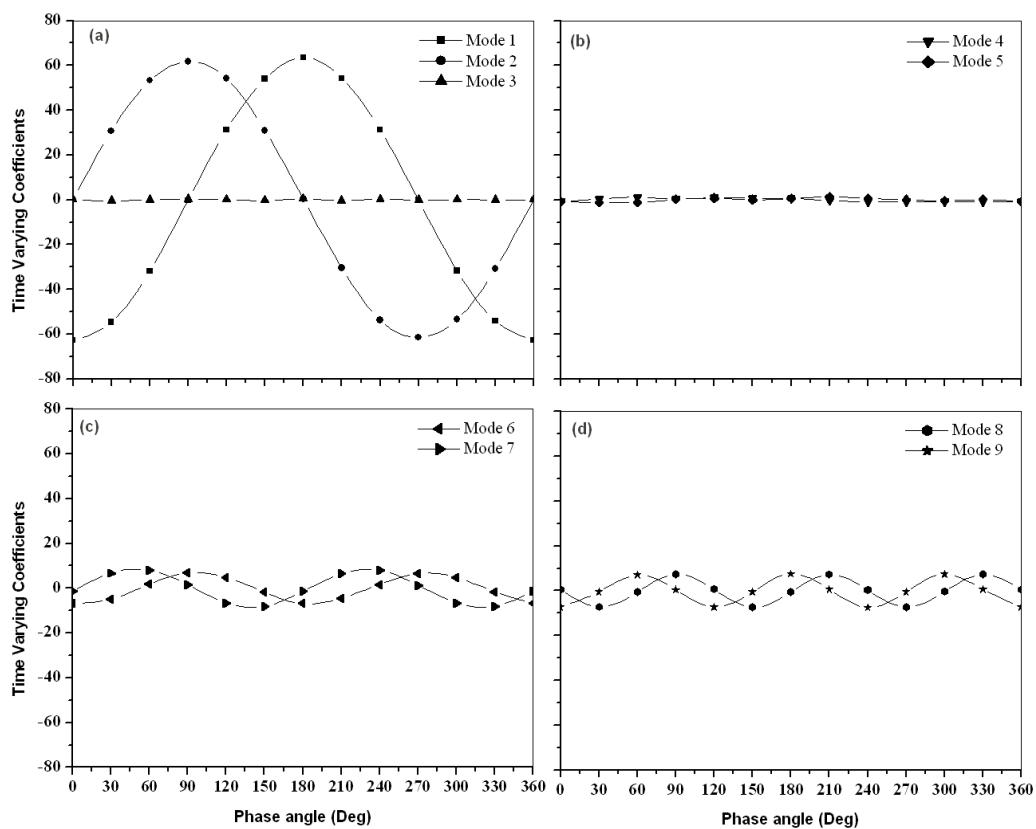


Figure 3-7. Phase averaged time varying coefficient in XY plane at $Re_D = 550$

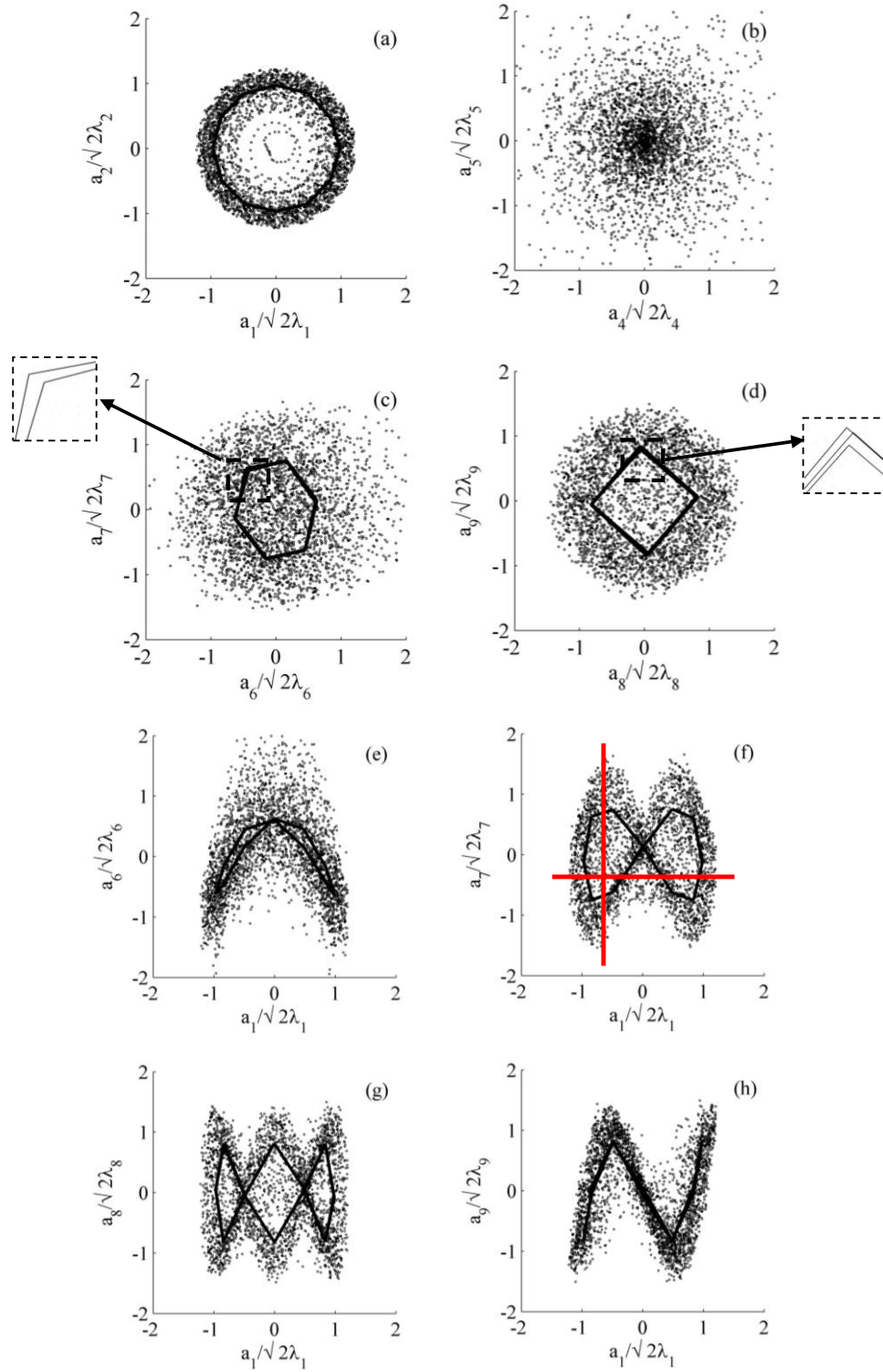


Figure 3-8. Phase portraits of time varying coefficient in XY plane at $Re_D = 550$. The solid line indicates the phase averaged relation between these POD modes.

curves. More information about Lissajous figures can be found in any standard book on Oscilloscopes.

It is evident from Figure 3-8 that mode pairs (a) 1 and 2, (b) 4 and 5, (c) 6 and 7, and (d) 8 and 9 are mode pairs as they represent the circle. The line plots in Figure 3-8 represent the phase averaged relation between the modes. Modes 1 and 2 are a 90 degree phase shifted pair, as the phase averaged relation between the two modes collapses to a circle. The phase averaged relation between modes 6 and 7 shows two concentric circles, indicating that the structure represented by these modes is a 90 degree phase shifted pair shedding at twice the frequency of the fundamental structure. Similarly, the phase averaged relation between modes 8 and 9 is represented by three concentric circles, indicating they are a 90 degrees phase shifted pair appearing at thrice the frequency of the fundamental structure. Even though modes 4 and 5 form a mode pair, they are weakly correlated, indicating that the combination of these modes contribute weakly to the dominant coherent structures, a fact also evident from the amplitude of the time varying coefficients (Figure 3-7 b). Modes 6 and 7 (Figure 3-8 e and f) represent the first harmonic structure of the Karman Benard vortices. This can be identified through the simple method of passing two lines perpendicular to each other as shown in Figure 3-8 (f). The vertical line passes through the phase curve twice and the horizontal line passes through the curve four times, indicating that the frequency of mode 7 is twice that of mode 1. Similarly, modes 8 and 9 correspond to the second harmonic of the fundamental structure.

Figure 3-9 (a) shows the Karman Benard vortices captured by the PLIF experiments, and Figure 3-9 (b) shows the phase averaged streakline plots in the vertical plane obtained from the PIV data, capturing the spanwise vortices as they would appear to an observer moving downstream at a convection velocity of $0.87U_\infty$ (Zhou and Antonia, 1992), at $Re_D = 550$. The velocities are reconstructed by combining the first two modes using equation 2.1. It is observed that the first two POD modes capture the dominant structure effectively. Both figures indicate that the streamwise distance (λ_x/D) of the spanwise vortices is 4.8D.

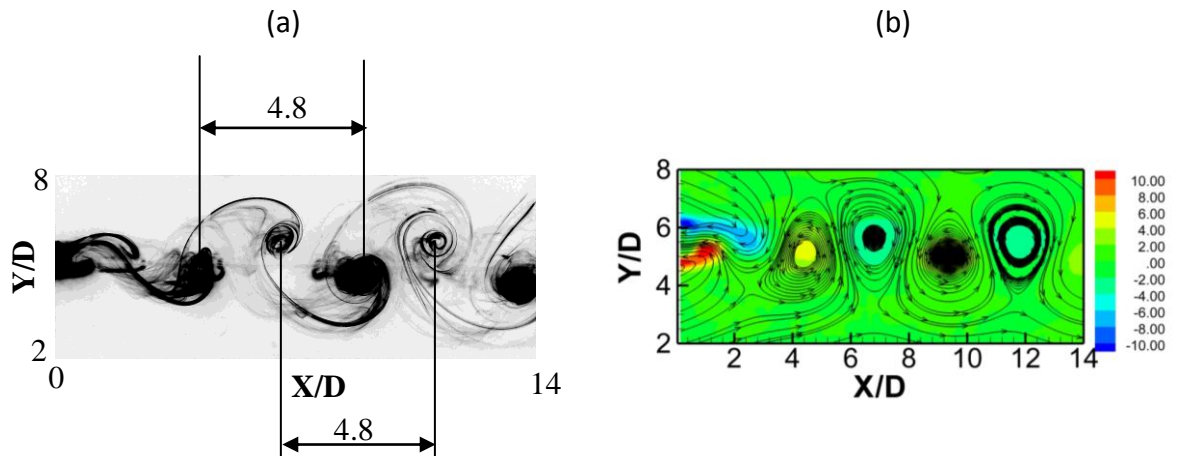


Figure 3-9. (a) PLIF Visualization (b) streakline plot along with vorticity contours of the first two POD modes in XY plane at $Re_D = 550$

Figure 3-10 shows the first five streamwise and transverse velocity POD modes at (a) $Re_D = 1050$, (b) $Re_D = 1550$ and (c) $Re_D = 2300$. The modes appear very similar to that observed at $Re_D = 550$ (Figure 3-5). The first two modes relate to the dominant von Karman vortex developing in the flow. Modes 3 appears to a standing mode with no companion mode, likely related to the boundary layer developing in the flow. Modes 4 and 5 appear to be a distorted version of the first two modes. This relation between these POD modes is also observed from the relative energies plot (Figure 3-11 a) and the relation between time varying coefficients (Figure 3-11 b, c and d) in XY plane for $Re_D = 1050$, 1550 and 2300, as previously interpreted for $Re_D = 550$ in Figure 3-6 and Figure 3-7.

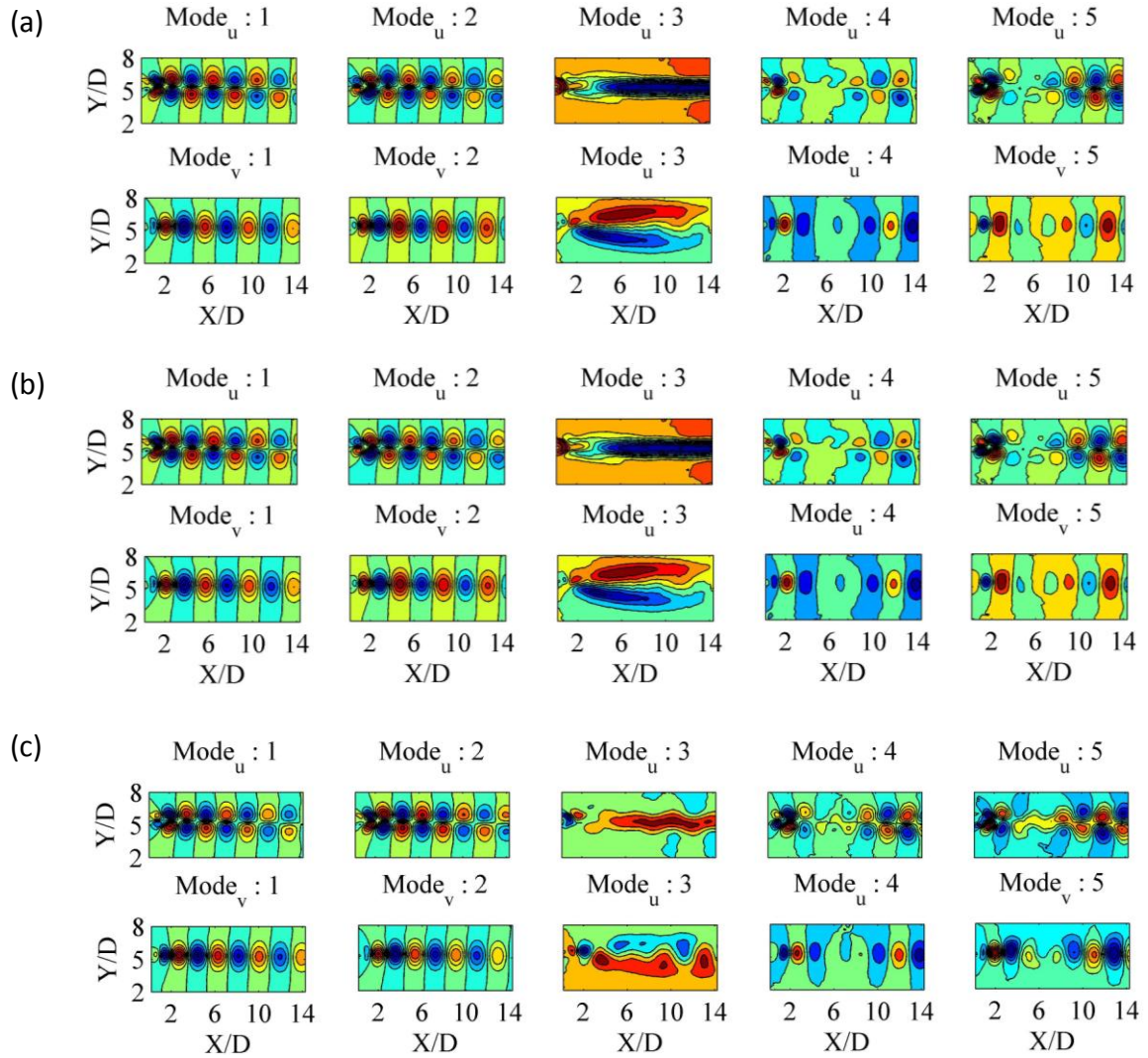


Figure 3-10. Streamwise and transverse velocity components for the first five POD modes in XY plane at (a) $Re_D = 1050$, (b) $Re_D = 1550$ and $Re_D = 2300$

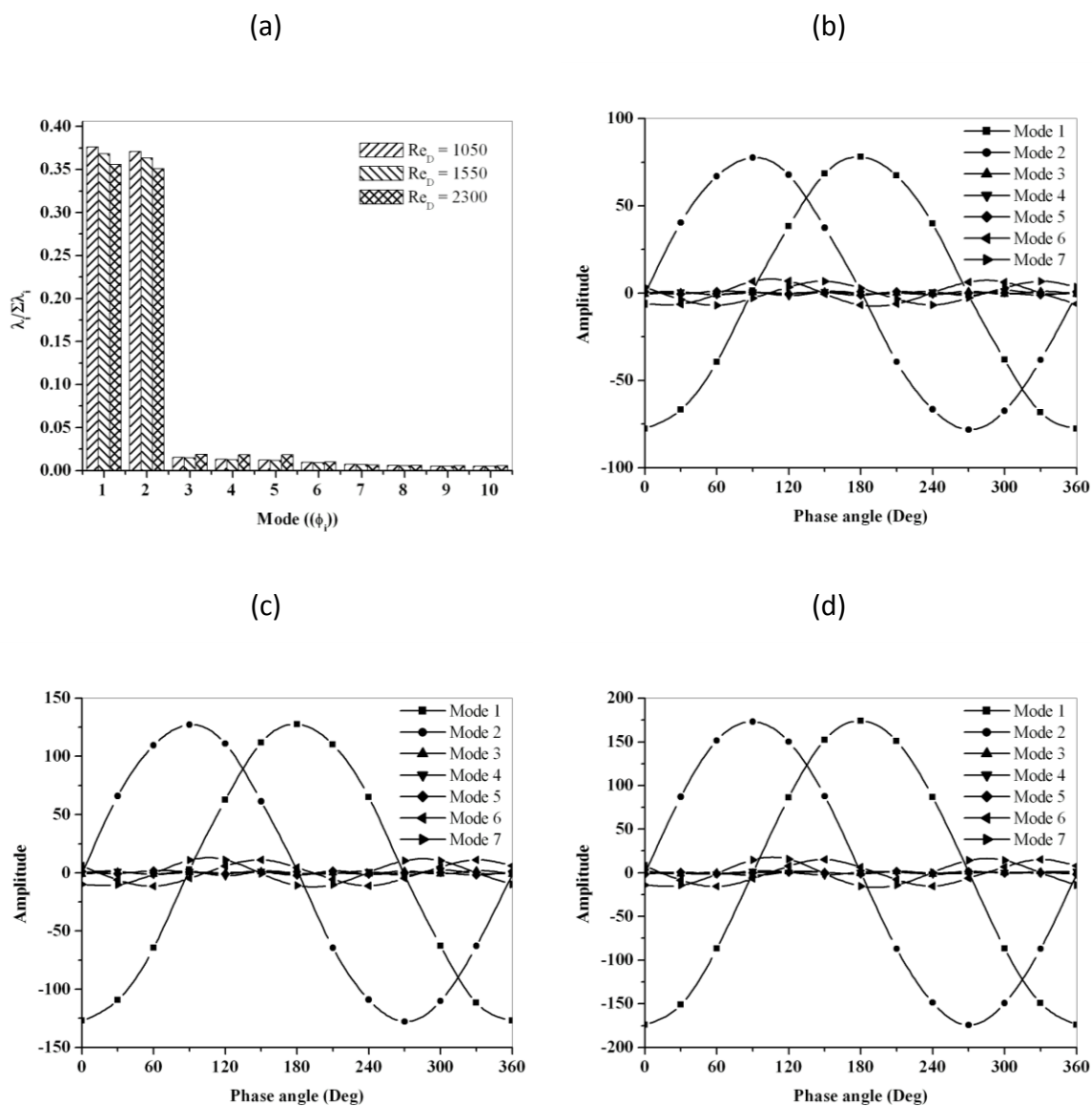


Figure 3-11. (a) Relative energy captured by first ten POD modes in XY plan at $Re_D = 1050$, 1550 and 2300. Phase averaged time varying coefficient in XY plane at (b) $Re_D = 1050$, (c) $Re_D = 1550$ and (a) $Re_D = 2300$

Figure 3-12 compares the flow field from both flow visualizations and from the PIV measurements for (a) $Re_D = 1050$, (b) $Re_D = 1550$ and (c) $Re_D = 2300$. The PLIF visualizations indicate that the von-Karman Benard vortices tend to distort because of the turbulent chaotic motion with increase in the Reynolds number. Further support to

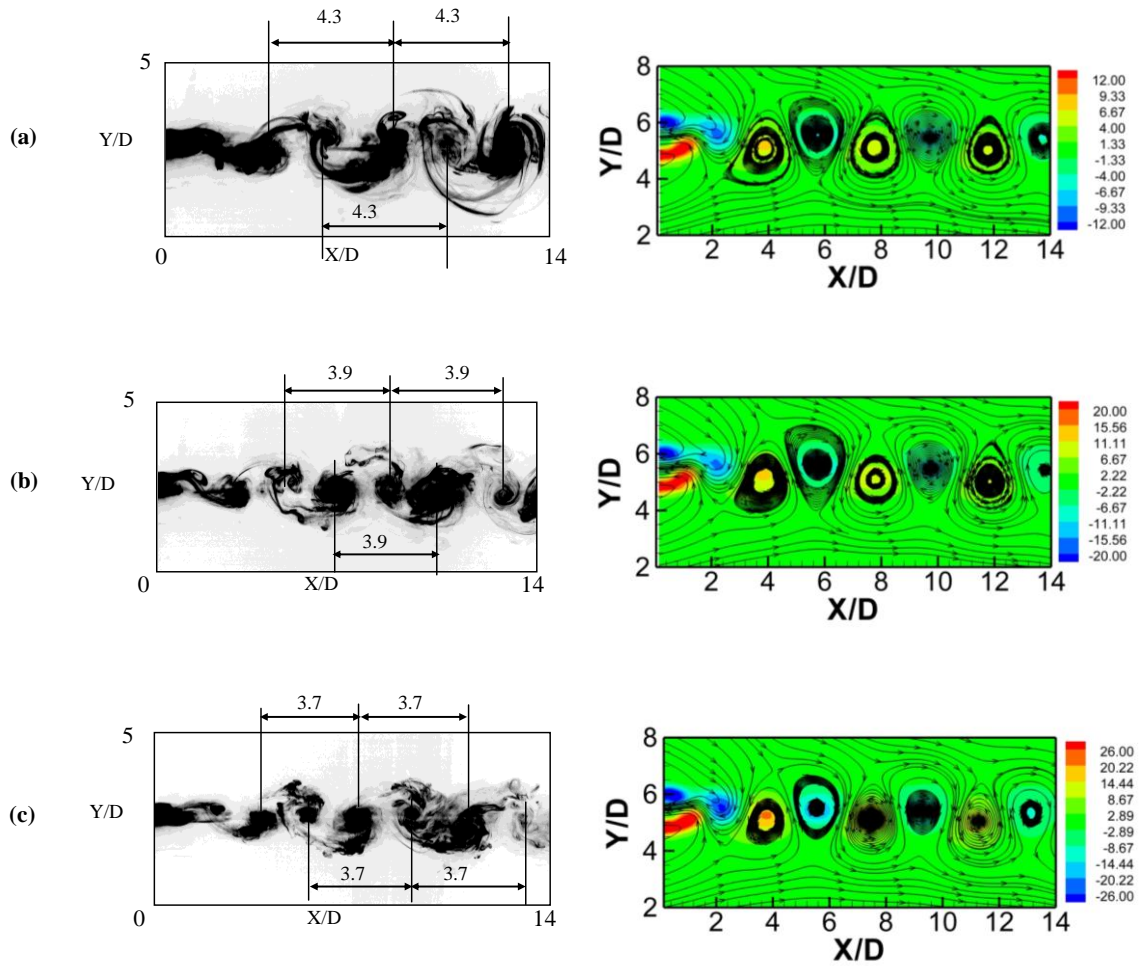


Figure 3-12. PLIF visualization and the streakline plots along with vorticity contours by combining first two POD modes of in XY plane for (a) $Re_D = 1050$, (b) $Re_D = 1550$ and (c) $Re_D = 2300$

this statement is obtained by comparing the relative energies in the first two POD modes at different Reynolds numbers, shown in Figure 3-11 (a). The relative energy in the first two POD modes decreases with increase in Reynolds number; this reduction is redistributed to higher POD modes, and hence additional POD modes are required to reconstruct the wake dynamics and the associated turbulent properties. Another observation from the PLIF visualizations is the decrease in the streamwise spacing of the spanwise vortices with increase in Reynolds number, show as a line plot in Figure 3-13. The streakline plots in Figure 3-12 are obtained by combining the first two POD modes

capture the features of the dominant von-Karman Benard vortices very well. These plots also indicate the reduction in streamwise spacing of spanwise vortices with increasing Reynolds number, confirming to the results from the PLIF visualizations.

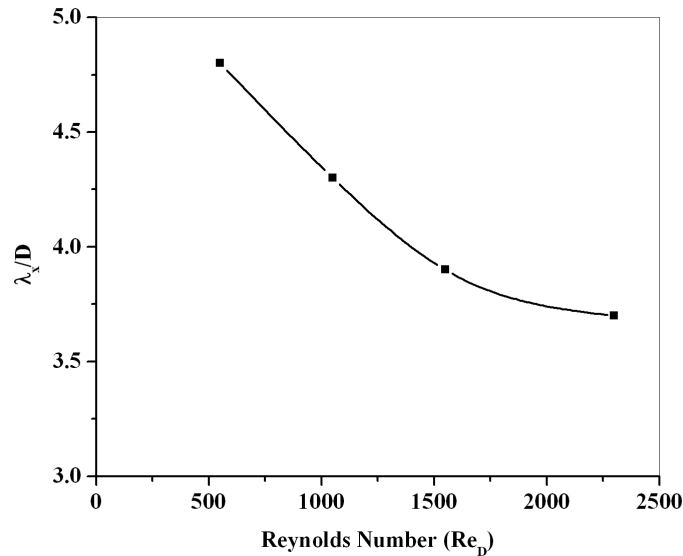


Figure 3-13. Streamwise spacing of spanwise vortices as a function of Reynolds number

3.2.2 XZ Plane Results

3.2.2.1 Different Near Wake Transition Modes

To capture the onset of two-dimensional dominant wake instability, that is the von Karman vortices and further transitions in the near wake due to three-dimensional instabilities, PLIF visualizations were performed at Reynolds numbers of $Re_D = 250, 300, 350, 400$ and 550 in XZ plane. To capture the wake field in the XZ plane, the dye was injected through a spanwise slot located at the lower part of the trailing edge (Figure 2-6). Hence, the structure formed by the bottom shear layer appears darker than those from the top shear layer (Figure 3-14).

Figure 3-14 shows the PLIF visualizations at a Reynolds number of $Re_D = 250$. Here, parallel shedding of the primary vortices is observed, with almost no three-dimensionality or vortex loops (Figure 3-14a). Nevertheless, local large-scale vortex dislocations are observed (Figure 3-14 b). Figure 3-14 (c) shows visualizations of a similar type of dislocation observed in the work of Williamson (1992) for a circular cylinder, with its schematic representation (Figure 3-14 d) taken from Williamson (1992). Similar

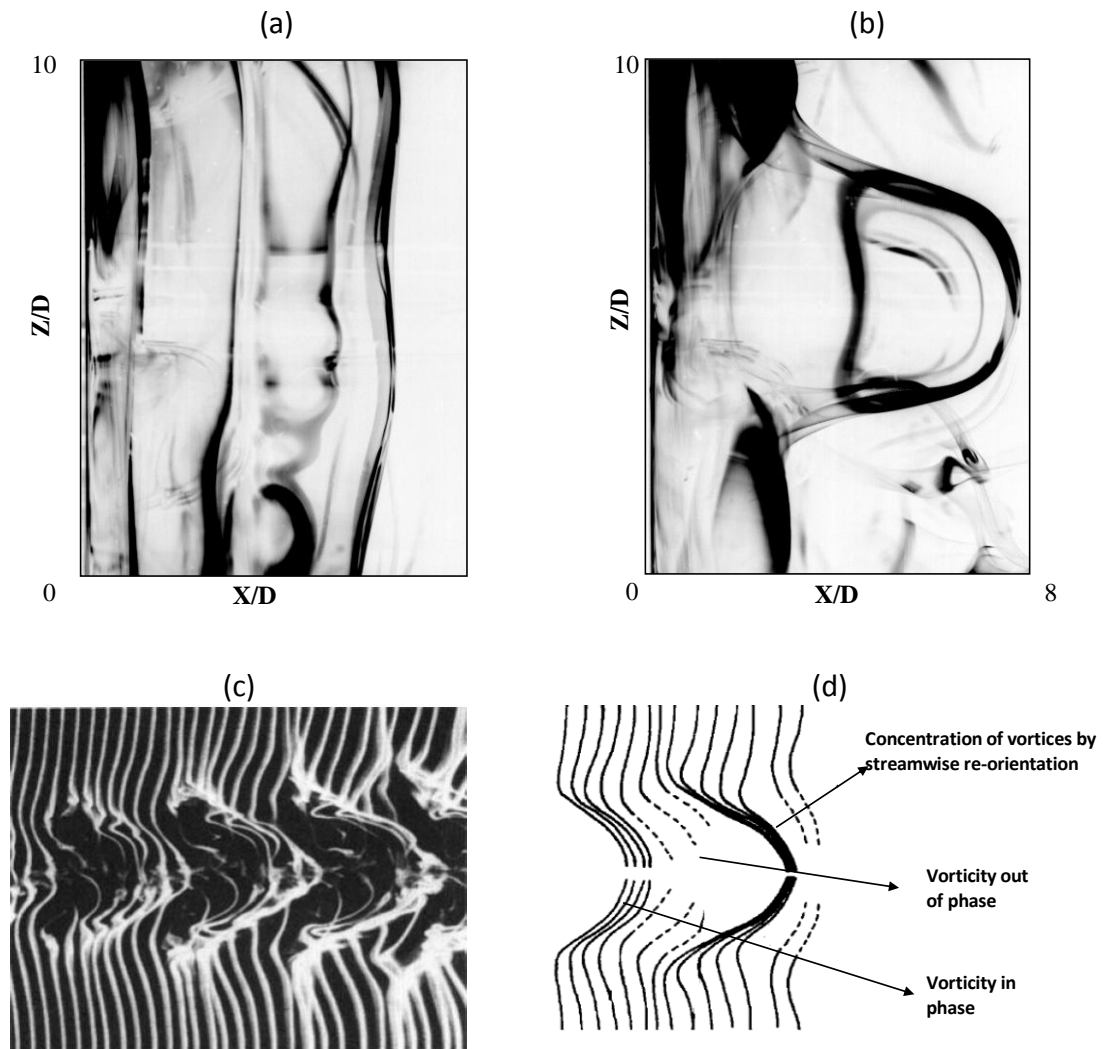


Figure 3-14. PLIF visualization at $Re_D = 250$ in XZ plane ($Y/D = -0.5$) (a) parallel vortex shedding (b) vortex dislocation, (c) visualization of the vortex dislocation (Williamson 1992), and (d) schematic representation of vortex dislocation (Williamson 1992).

observations were made by Zhang et al. (1995) for circular cylinder flows and Luo et al. (2003) for square cylinder flows. These dislocations persist over several shedding cycles before the flow is restored to parallel vortex shedding at this Reynolds number.

As the Reynolds number increases to $Re_D = 300$, the wake displays parallel vortex shedding (Figure 3-15 a), with intermittent large-scale vortex dislocations (Figure 3-15 b) and three-dimensional features (Figure 3-15 c) in the flow. These three-dimensional features are very weak and do not persist for multiple shedding cycles; they form intermittently and disappear quickly, indicating the advent of three-dimensionality in the flow at this Reynolds number.

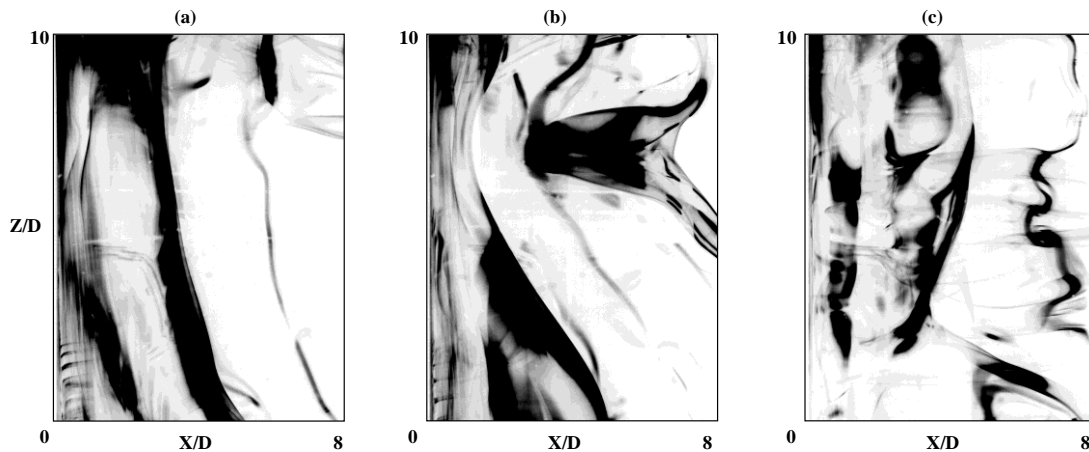


Figure 3-15. PLIF visualization at $Re_D = 300$ in XZ plane ($Y/D = -0.5$) (a) parallel vortex shedding (b) vortex dislocation and (c) three-dimensional features

The flow phenomena at $Re_D = 350$ (Figure 3-16) is very similar to that observed at $Re_D = 300$. However, one major difference is the appearance of the spanwise waviness in the von Karman vortices in the immediate vicinity of the blunt trailing (Figure 3-16 a). It is observed that this spanwise waviness does not manifest into streamwise vortices, as the Karman vortices appear without any distortion in the intermediate wake. The large-scale vortex dislocations (Figure 3-16 b) and the small-scale streamwise vortices in the form of mushroom structures (Figure 3-16 c) are also observed at this Reynolds numbers. These observations indicate the onset of three-dimensionality in the flow due

to two instability mechanisms, one which appears as the spanwise waviness in the primary vortex core and the other one as the mushroom structures.

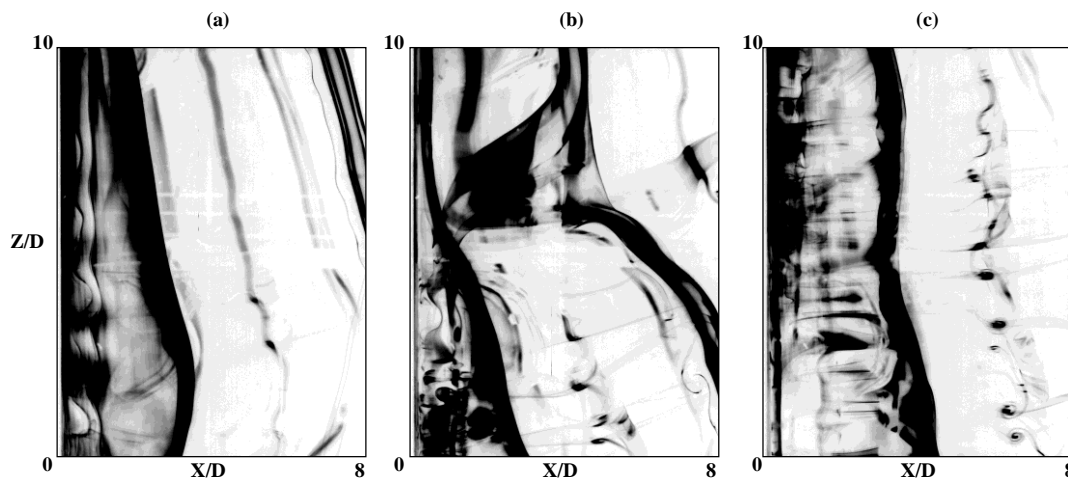


Figure 3-16. PLIF visualization at $Re_D = 350$ in XZ plane ($Y/D = -0.5$) (a) parallel vortex shedding (b) vortex dislocation and (c) mushroom structures

As the Reynolds number increase to $Re_D = 400$, the wake topology displays small-scale streamwise vortices (Figure 3-17) with an average spanwise spacing of $1.0D$. The secondary vortices appear to be simply connected over several shedding cycles and are not associated with the severe distortion of the Karman vortices. The above characteristic is indicative of mode-B instability (Williamson 1996 and Brede et al. 1996). This can also be confirmed from the symmetric pattern of the small-scale streamwise vortices observed in the flow visualizations (indicated by arrows in Figure 3-17 a). However, a closer look at the topology of this wake instability indicates the asymmetric pattern in some instances (indicated by arrows in Figure 3-17 b), which is indicative of mode-C wake instability as described in the schematic Figure 1-3 with a period of $2T$, T being the vortex shedding period. The literature refers to this as periodic doubling bifurcation (Robichaux et al. 1999). Similar types of observations were made by Karniadakis and Triantafyllou (1992) at $Re_D = 300$, and by Mittal and Balachndar (1995) at $Re_D = 525$, in their numerical work for circular cylinder flows. Williams et al. (1996)

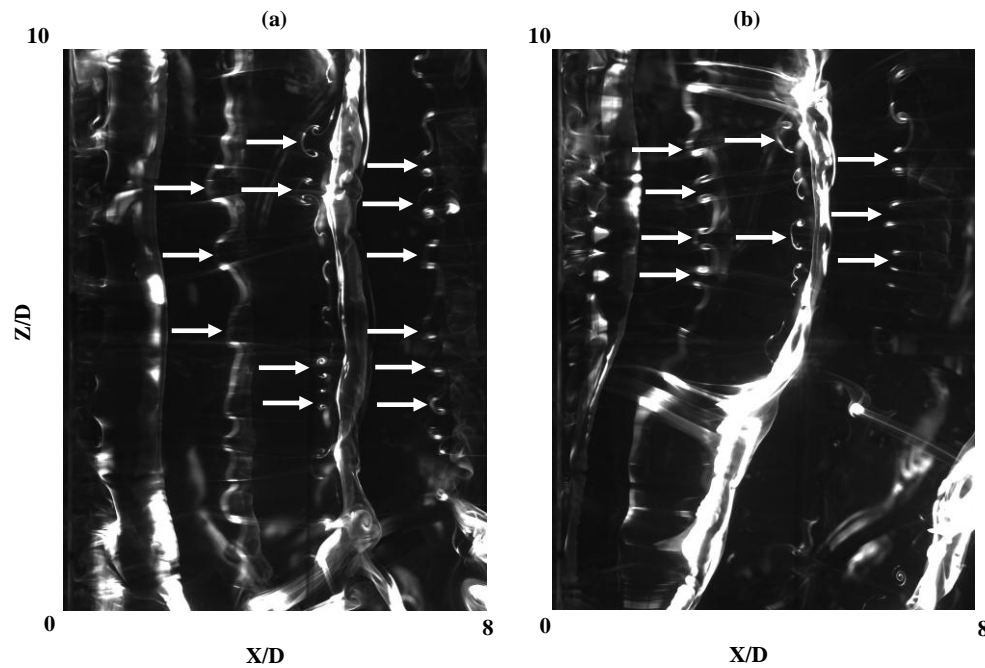


Figure 3-17. PLIF Visualization in XZ plane ($Y/D = -0.5$) at $Re_D = 400$

provided experimental evidence of periodic doubling bifurcation in the near wake of a circular cylinder in the transition regime at $Re_D = 300$. From previous studies, it can be inferred that such periodic doubling bifurcations can occur for mode-B instability in the wake development of a two-dimensional body.

For further clarity on the structure of the streamwise instability, transverse (YZ) plane visualization measurements were performed at $X/D = 3$, as shown in Figure 3-18. Figure 3-18 depicts the laser dye visualization of the similar small scale mushroom structure observed in the horizontal (XZ) plane visualizations (Figure 3-18). It is observed that these small scale vortices do not produce considerable distortion in the spanwise vortices and appear to be just connected, which are the features of mode-B instability (Williamson 1996, Brede et al. 1996). We can therefore conclude that a small-scale structure is representative of mode-B wake instability, and appears with an average spanwise spacing of $1D$; it is the first three-dimensional dominant wake instability observed for the blunt trailing-edge-profiled body.

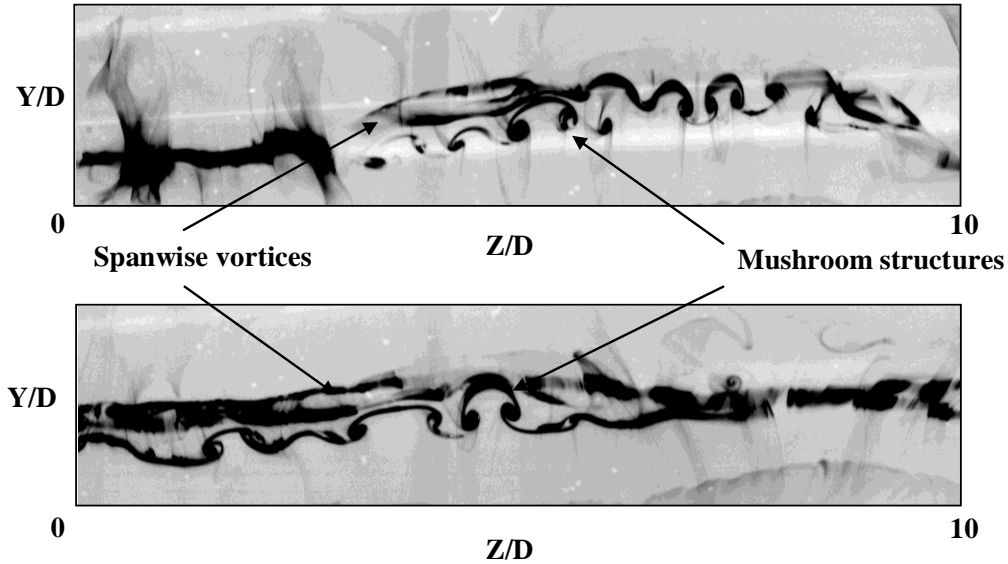


Figure 3-18. PLIF Visualization in YZ plane ($X/D = 3$) at $Re_D = 400$

As the Reynolds number increases to $Re_D = 550$, the wake topology (Figure 3-19) displays large-scale streamwise vortices compared with the structure observed at a Reynolds number of $Re_D = 400$. Figure 3-19 (a) and (b) show distinctively spanwise waviness in the near wake of the primary vortices. It is observed that the spanwise waviness grows with the downstream direction, evolving into a pair of counter rotating streamwise vortices due to the stretching in the shear layer connecting the spanwise vortices at the saddle point. The resulting streamwise vortices connect to the succeeding spanwise vortices, which generate vortex loops and eventually evolve into streamwise vortices. This preserves the production of streamwise vortices at the same spanwise location.

Figure 3-19 (a) and (b) reveals that an asymmetric pattern of the wavy structure is observed in the near wake (marked by arrows), indicative of mode-C instability. The spanwise spacing of the streamwise vortices varies between $2.0D$ to $2.8D$ in the near wake. In the intermediate wake, the flow visualizations show the appearance of mode-A at this Reynolds number. Another important observation is that the spanwise spacing between streamwise vortices continues to increase with downstream distance, and is

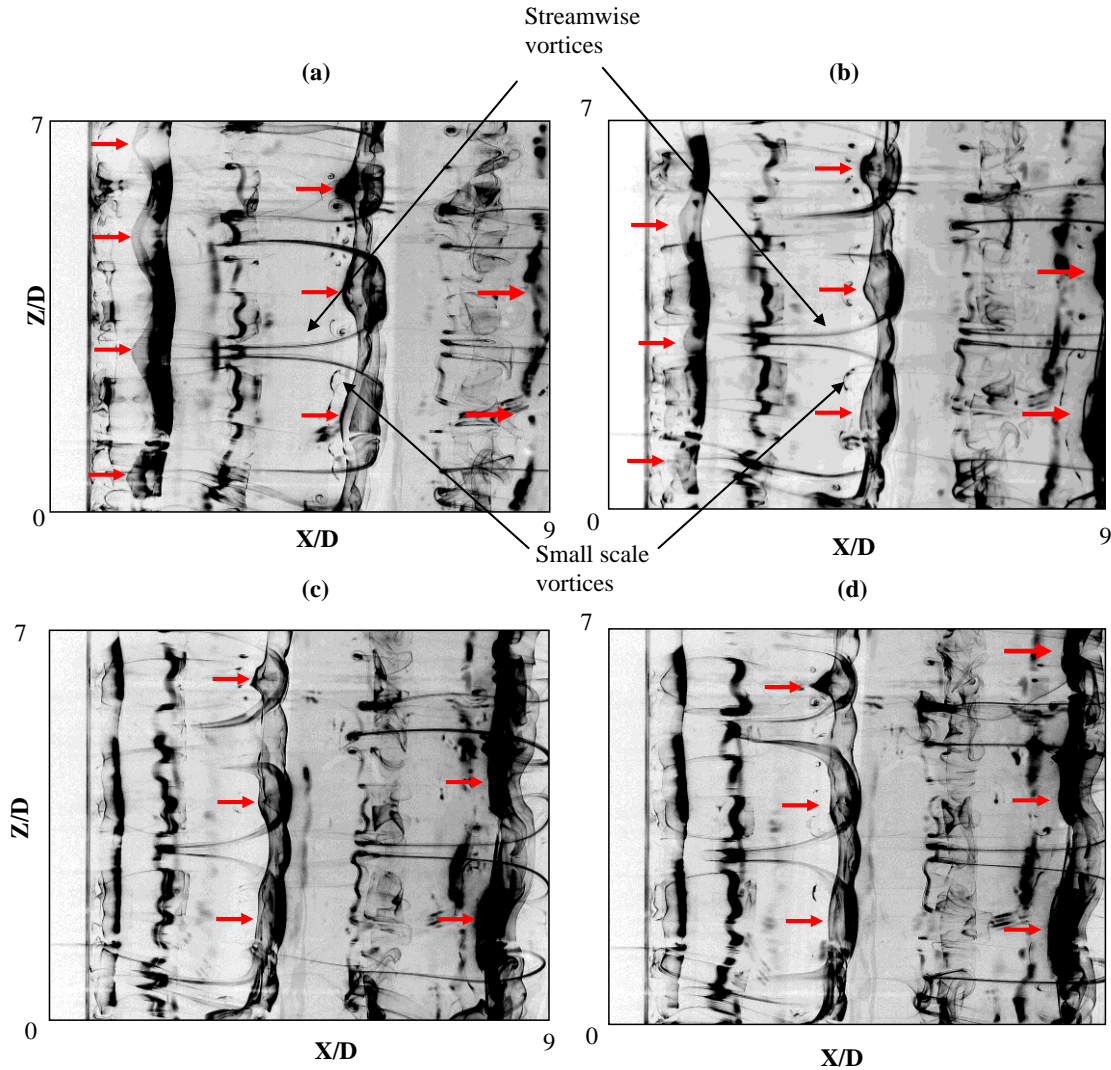


Figure 3-19. PLIF Visualization in XZ plane ($Y/D = -0.5$) at $Re_D = 550$

found to vary between $2.8D$ to $3.8D$ beyond $X/D > 3$. Hence, the dislocations caused by the streamwise vortices appear to be slightly out of phase, but the topology does not represent the mode-C asymmetric instability in the intermediate wake. A similar type of observation was made by Sheard et al. (2005) in the wake of a bluff ring: mode-C instability dominated the near wake and mode-A instability dominated the intermediate wake development at a $Re_D = 190$. To capture the evolution of mode-C independently in the near wake development, Sheard et al. (2005) conducted numerical simulations by restricting the domain size. Hence, it is experimentally difficult to identify mode-C wake

instability independently without the interfering presence of either mode-A or mode-B. At this Reynolds number, a small-scale structure is also present in the background, highlighted by arrows in Figure 3-19 (a) and (b). It is difficult to explain the topology of this small-scale structure; however, the spanwise spacing appears to be approximately $1.0D$. It can be concluded that asymmetric mode-C structure dominates the near wake formation region, whereas mode-A structure dominates the intermediate wake development at this Reynolds number.

To gain more insight into the structure at this Reynolds number, transverse (YZ) plane PLIF visualizations are performed at $X/D = 3$, as shown in Figure 3-20. Figure 3-20 indicates that deformation in the primary von Karman vortices due to streamwise vortices occurs to a noticeable extent, and also displays larger and smaller wavelengths of the streamwise vortices. Brede et al. (1996) indicated that the wider and shorter spacing is the feature of mode-A topology. A possible explanation for the presence of larger and smaller spanwise spacing for streamwise vortices with mode-A topology is provided in Section 3.2.2.2. We conclude that the cross section of the instability modes

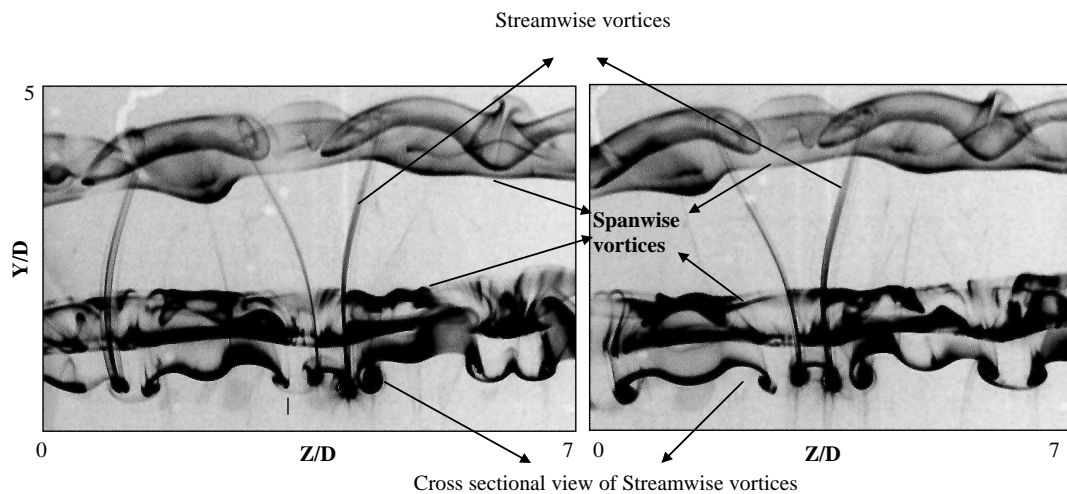


Figure 3-20. PLIF Visualization in YZ plane ($X/D = 3$) showing the dislocations caused due to streamwise vortices in spanwise vortices at $Re_D = 550$

observed in XZ plane (Figure 3-17 and Figure 3-19) and YZ plane (Figure 3-18 and Figure 3-20) PLIF visualizations show the same wake structure.

3.2.2.2 Schematics of mode-A and mode-B

On the basis of flow visualizations, three-dimensional representations of mode-A and mode-B are reconstructed, as shown in Figure 3-21. These representations also help in understanding the results from PIV measurements. As shown in the corresponding schematic of mode-A (Figure 3-21 a), vortex lines in the shape of ‘tongues’ are pulled out of each of the von-Karman vortex tubes and wrapped around the succeeding one. Each tongue is stretched in a streamwise direction and forms a pair of secondary vortices. The streamwise pattern displays a wider and shorter spacing of streamwise vortices. We can conclude from our mode-A vortex model that a wider spanwise spacing results from the vortex tongues being partly wrapped around a Karman vortex, while a shorter spanwise spacing results from the vortex tongues being wrapped further around the succeeding

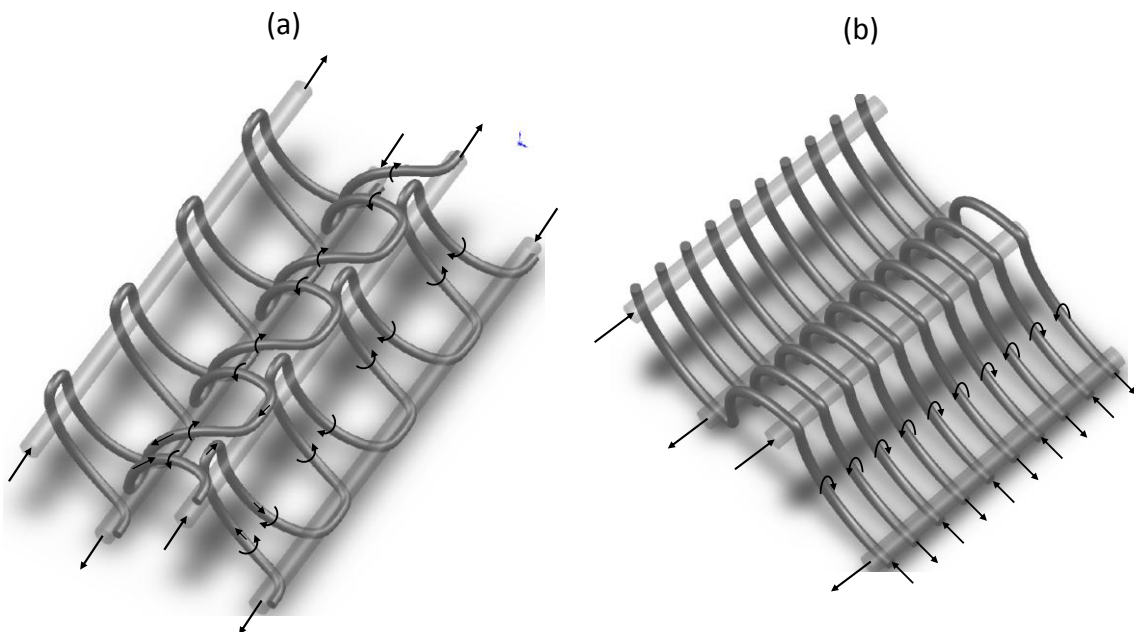


Figure 3-21. Schematics of the primary and secondary vortices of (a) mode-A (b) mode-B topologies. Vorticity sign is marked by arrows.

Karman vortex. The secondary vortices corresponding to mode-B (Figure 3-21 b) are simply connected over several shedding cycles and are not associated with the severe distortion or reorientation of segments of Karman vortices.

3.2.2.3 Origin of Asymmetric Mode C Instability

We have already established that wake structure at $Re_D = 550$ presents an asymmetric pattern in the near wake, which is termed mode-C, and a symmetric pattern in the intermediate wake, which is termed mode-A. In order to understand the evolution of the near wake development which predominantly presents these two structures, PLIF and PIV measurements were performed by artificially forcing the near wake using a Spanwise Sinusoidal Perturbation (SSP). The wavelength of the sinusoidal perturbation matches that of the average spanwise wavelengths of the near wake mode-C instability, which is $2.4D$. Figure 3-22 shows the PLIF images for (a) straight trailing edge, and (b) sinusoidal trailing edge. Figure 3-22 (b) shows the asymmetric wavy pattern in the spanwise vortices (marked by arrows) similar to the observation made with the straight trailing edge (Figure 3-22b). As with the straight trailing edge, small-scale structure is also observed in the background (indicated by arrows in Figure 3-22) at this Reynolds number for sinusoidal trailing edges. However it is difficult to predict the topology of this small scale structure from the PLIF visualizations. This small-scale structure appears with a spanwise wavelength of approximately $1D$. One major difference between the flow patterns evolving from the straight and sinusoidal trailing edges is that the dislocations tend to lock in phase and appear with a constant spanwise spacing of approximately $2.4D$ (that is, the wavelength of the SSP) in the near and intermediate wake with SSP. However, when the wake evolves naturally from the straight trailing edge, these dislocations are unsteady both in space and time, and the spacing between the dislocations caused by the streamwise vortices increases with increasing downstream distance. Further insight on the development of the wake structure with the SSP is obtained by plotting the mean streamwise velocity contours (Figure 3-23) obtained from the PIV measurements in the shear layer ($Y/D = -0.5$).

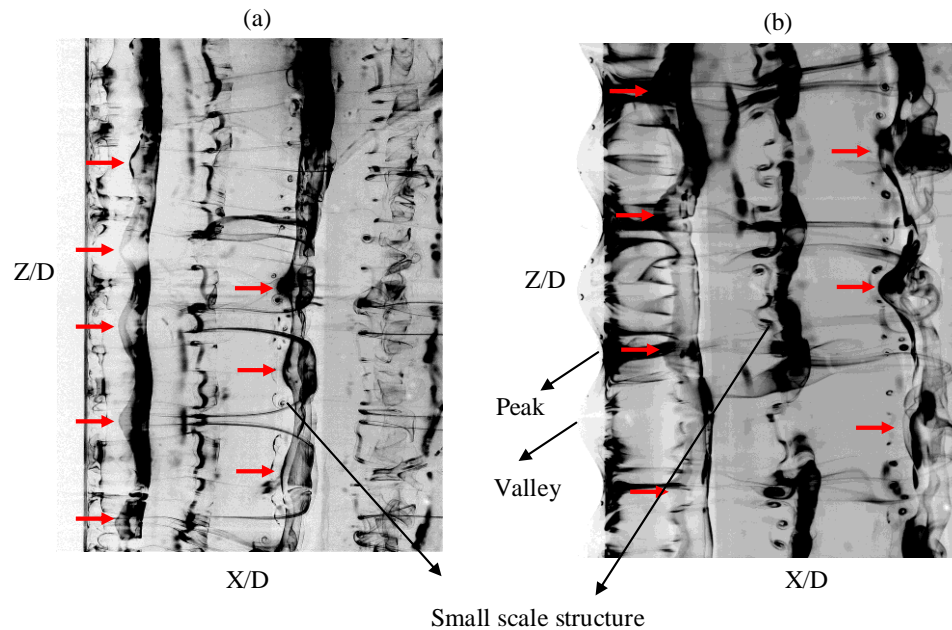


Figure 3-22. PLIF Visualization in XZ plane ($Y/D = -0.5$) at $Re_D = 550$ for (a) straight trailing edge and (b) sinusoidal trailing edge

To assess the development of the wake with and without SSP, the mean center line velocities are compared in Figure 3-24. The mean wake characteristics with and without the SSP appear to be similar. The streamwise velocity contour at $Y/D = -0.5$ for the straight trailing edge (Figure 3-23 a) does not show any signs of distortion due to the streamwise vortices, indicating that differentiating the streamwise vortices from the dominant spanwise vortices is difficult in a naturally evolving wake without perturbation. However, the streamwise velocity contours due to the SSP (Figure 3-23 b) shows considerable distortion. The asymmetric sinusoidal pattern observed in the near wake ($0 < X/D < 3$) shown in Figure 3-23 (b) is also observed in the PLIF images (Figure 3-22 b). Note that sinusoidal spanwise distortion patterns before $X/D < 2$ and after $X/D > 2$ are asymmetric, as observed in the mode-C structure. This asymmetric pattern in the near wake structure can be explained based on the basis of the streamwise velocity contour. Comparing velocities at point '1' and point '2' in Figure 3-23 (b), the velocity at point '1' is smaller than at point '2', and hence the velocity at point '1' shows slower recovery

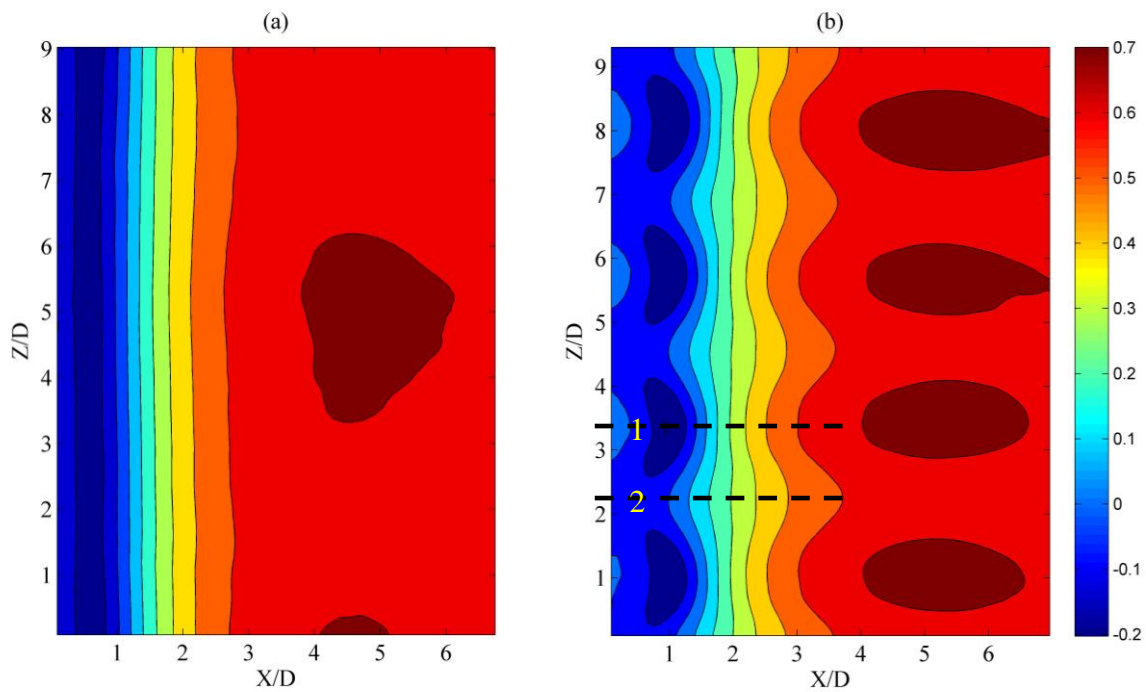


Figure 3-23. Mean streamwise velocity contours in XZ plane ($Y/D = -0.5$) at $Re_D = 550$ for (a) straight trailing edge and (b) sinusoidal trailing edge

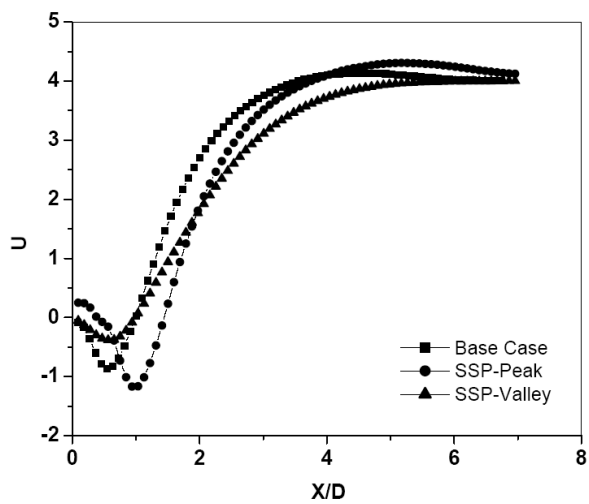


Figure 3-24. Comparison of mean centre line velocity for straight trailing edge and sinusoidal trailing edge

than at point '2'. When the velocity sign changes from negative to positive, point '2' represents a higher velocity than point '1'. This is what is observed in the streamwise velocity contour plot resulting in the asymmetric pattern, corresponding to mode-C structure, which is observed in the near wake of a blunt trailing-edge-profiled body.

3.2.2.4 Instantaneous Velocity and Vorticity Field

Figure 3-25 shows the instantaneous (a) streamwise, (b) transverse velocities at different Reynolds numbers of (I) $Re_D = 550$, (II) $Re_D = 1050$, (III) $Re_D = 1550$ and (IV) $Re_D = 2300$. Figure 3-25 (c) shows the vorticity field is calculated from the velocity using equation 3.10. The instantaneous velocity field shows in Figure 3-25 captures the features of the Karman vortices developing the flow at low Reynolds numbers. However, identifying the dislocation in the spanwise vortices caused due to streamwise vortices is difficult. Instantaneous spanwise velocity contours and the ω_y vorticity contours appear too noisy and difficult to visualize the flow features from these contours. Similar observations are made at other Reynolds numbers. For better insight into the near wake flow topology, and possible better assessment of the spanwise spacing between the streamwise vortex filaments, PIV measurements were conducted in horizontal planes corresponding to the shear layer ($Y/D = -0.5$) and the mid-plane ($Y/D = 0$). A Proper Orthogonal Decomposition (POD) analysis was then performed on the PIV data obtained in the XZ plane, the results of which are discussed in the following section.

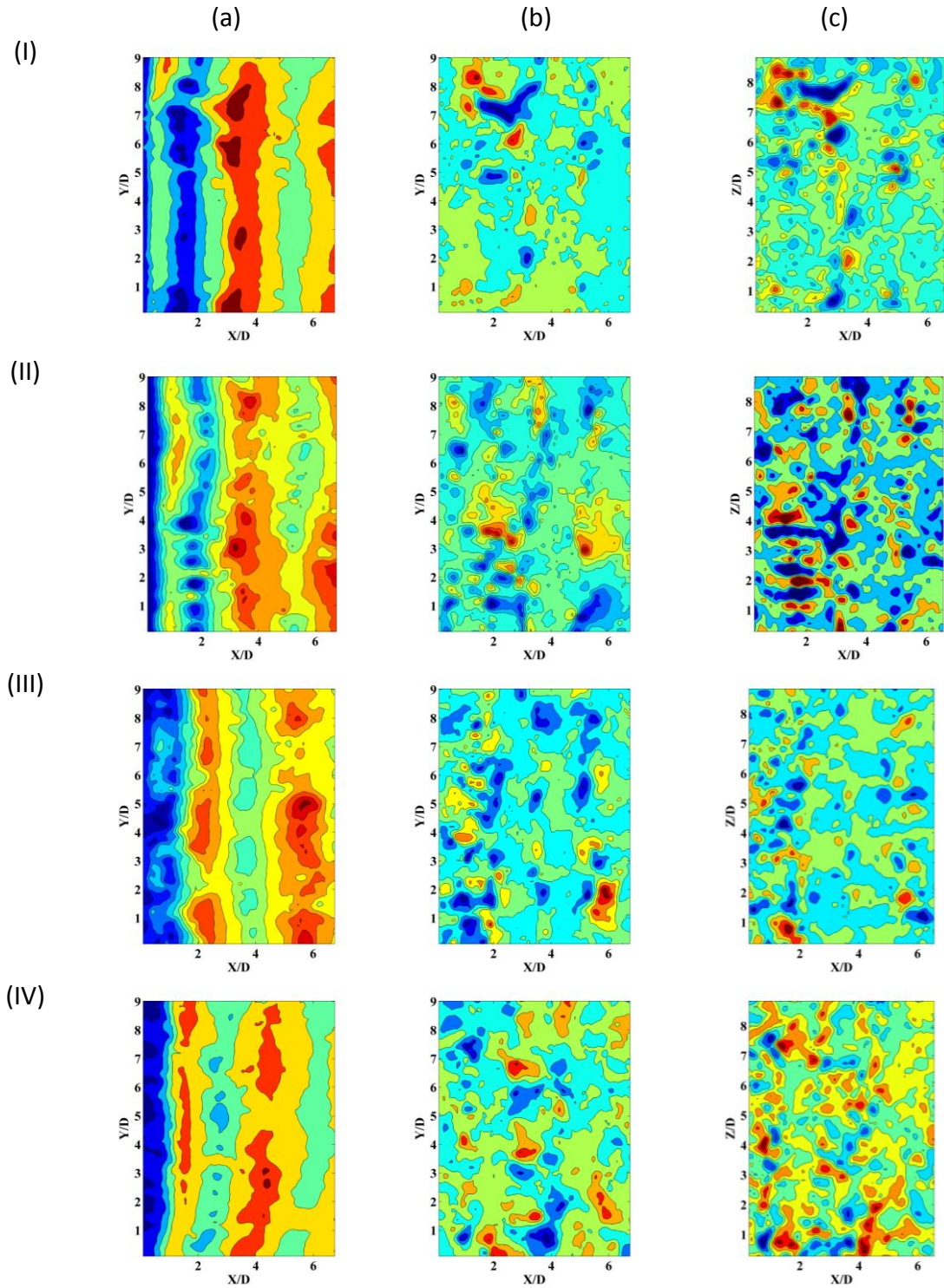


Figure 3-25. Instantaneous (a) streamwise velocity, (b) spanwise velocity and (c) ω_y vorticity for Reynolds numbers of (I) $Re_D = 550$, (II) $Re_D = 1050$, (III) $Re_D = 1550$ and (IV) $Re_D = 2300$

3.2.2.5 POD Analysis Results

Figure 3-26 shows the eigenvalues corresponding to the first 15 POD modes in shear layer ($Y/D = -0.5$) and in mid plane ($Y/D = 0$) for $Re_D = 400$ and $Re_D = 550$. The first 10 POD modes clearly capture significant relative energy in the horizontal plane corresponding to shear layer ($Y/D = -0.5$). However, a more even energy distribution in the POD modes (Figure 3-26 b) is observed in the mid-plane ($Y/D = 0$). This variation in the relative energy among the POD modes in the shear layer ($Y/D = -0.5$) and the mid-plane ($Y/D = 0$) is interpreted as follows: Usually the Karman Benard vortices are primarily associated with the spanwise vorticity (ω_z), a statement supported by the significant relative energy (approximately 80%) captured by the first two POD modes in the vertical (XY) plane (Figure 3-6), which maximizes the ω_z component of vorticity in the spanwise vortices.

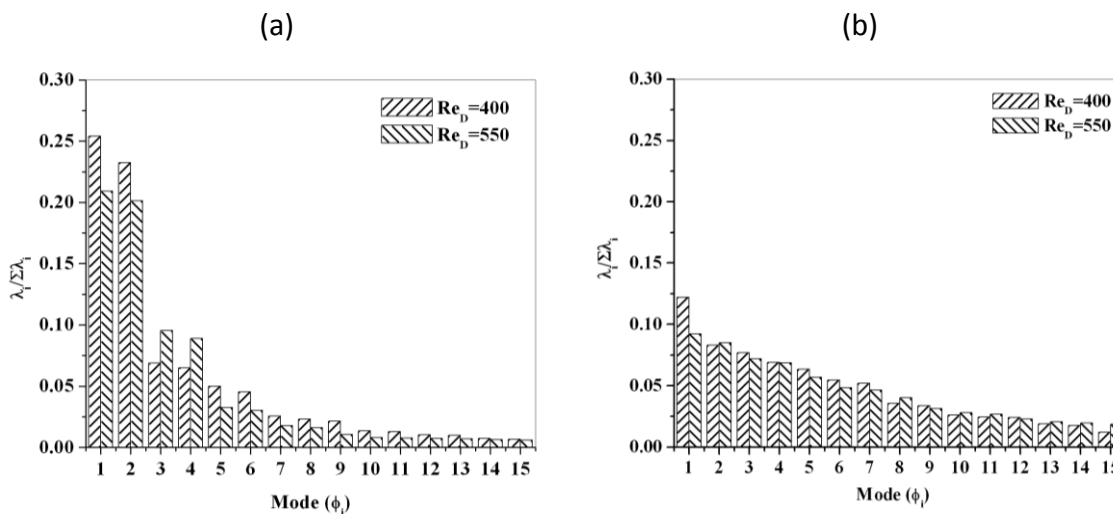


Figure 3-26. Relative energy captured by first fifteen POD modes in XZ plane at (a) $Y/D = -0.5$ and (b) $Y/D = 0$ for $Re_D = 400$ and 550

The other components of vorticity are weak if the spanwise vortices are two-dimensional, and are not associated without any stretching and rotation. However, this is not the case in bluff body flows, where the shear layers emerging from both sides of the body interact, resulting in stretching and reorientation of the spanwise vortices. This manifests into three-dimensional interactions and uneven displacements in the

spanwise direction of the Karman vortices (Meiburg and Lasheras 1998), contributing to other vorticity components (ω_x and ω_y). However, the effect may vary depending on the measurement location. In the shear layer ($Y/D = -0.5$), the contributions to transverse vorticity (ω_y) and streamwise vorticity (ω_x) are subjected to maximum amplification because of the stretching in the shear layer connecting the primary vortex cores at the saddle point; in the mid plane ($Y/D = 0$), however, the effect of stretching is minimal and, hence, the contribution of the transverse and streamwise vorticity components due to the von Karman Benard vortices is minimal in this plane, as observed in the relative energies captured in these planes (Figure 3-26).

To better illustrate the relation between the POD modes and the 3D vortex topology, wake combinations of POD modes are represented in terms of vorticity. Figure 3-27 shows the temporal and spatial evolution of the transverse (ω_y) vorticity contours expanded in time at $X/D = 1$. Here, only 10 s out of the total 200 s data is shown. Figure 3-27 (a) shows the ω_y vorticity contours by combining the first four POD modes at $Y/D = -0.5$ for $Re_D = 400$. This clearly indicates that these modes represent the primary coherent structure, that is, the Karman Benard vortices. Figure 3-27 (b) shows the vorticity contours by combining the POD modes 5 to 8. These modes also appear to represent the large-scale vortex dislocations of the Karman Benard vortices. Modes 9 and 10 represent the effect of streamwise vortices (i.e. mode-B structure) observed at this Reynolds number ($Re_D = 400$). Here, the modes display the effect of the streamwise vortices as undulations in the spanwise vortices as depicted in the schematic (Figure 3-28), which sketches the induced velocity field due to a pair of counter rotating streamwise vortices. The arrows represent the counter-rotating streamwise vortices and the solid line represents the undulations caused in the spanwise vortices due to the velocity induced by streamwise vortices. It is observed that the spanwise spacing of the streamwise vortices varies between 1.0 and 1.5D. To support the observation that the relative energy of the streamwise vortices in mode-B is relatively small and the vortices do not deform the spanwise vortices a lot, the streamwise velocity component is plotted by adding the first 32 POD modes, which correspond to 80% relative kinetic energy of the

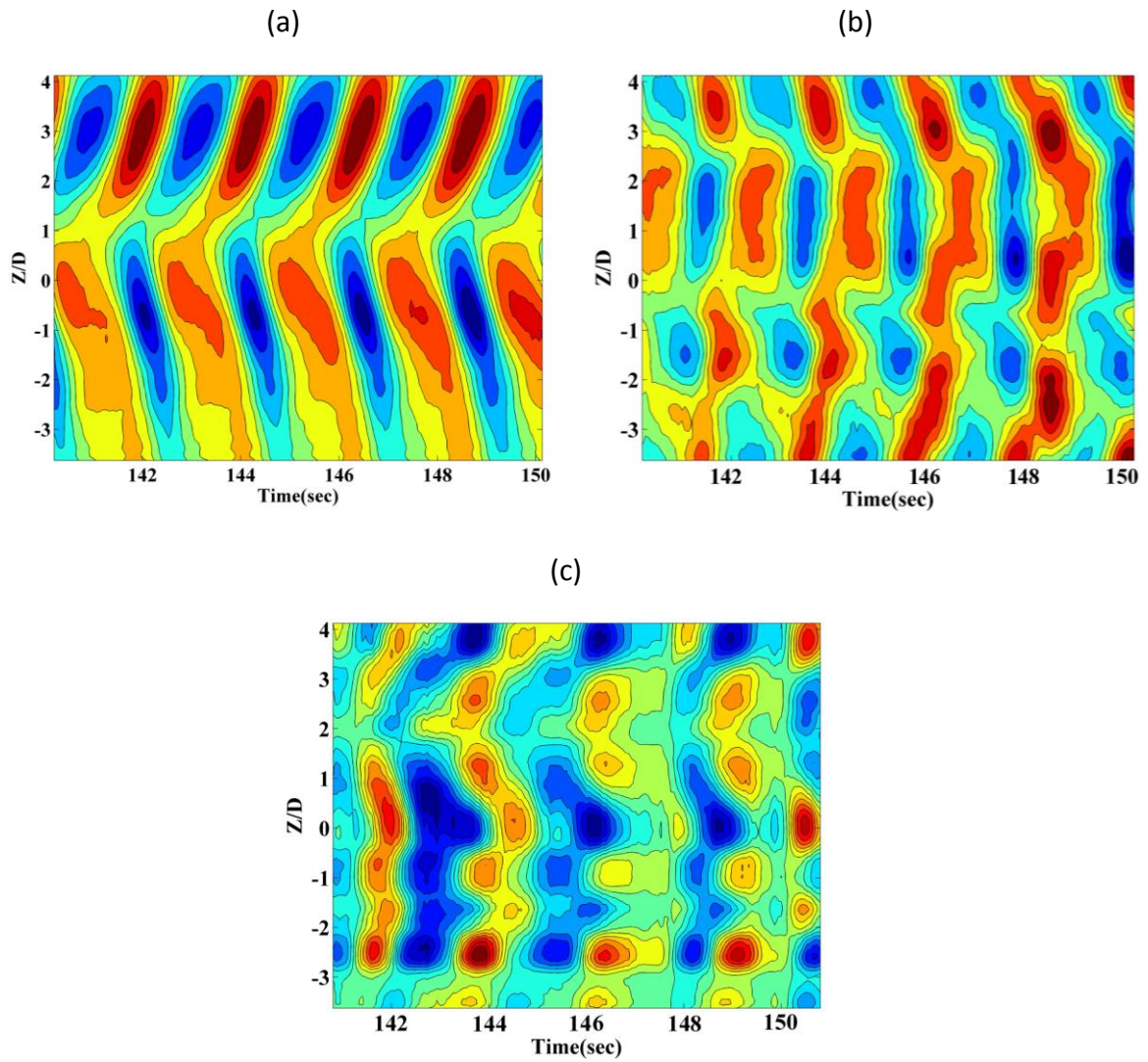


Figure 3-27. ω_y vorticity contours in XZ plane ($Y/D = -0.5$) at $Re_D = 400$ by combing POD modes (a) 1 to 4, (b) 5 to 8, and (c) 9 and 10.

Flow (Figure 3-29). If the streamwise vortices can distort the spanwise vortices, the streamwise velocity POD modes should display this effect as a sinusoidal oscillation, shown in the schematic in Figure 3-28. However, the streamwise velocity does not show a considerable deformation, ascertaining the results obtained from PLIF images at $Re_D = 400$.

Figure 3-30 (a) shows a section (XZ) plane (indicated by line) of the schematic (Figure 3-21 a) where PIV measurements are obtained. Figure 3-30 (b) shows the XZ

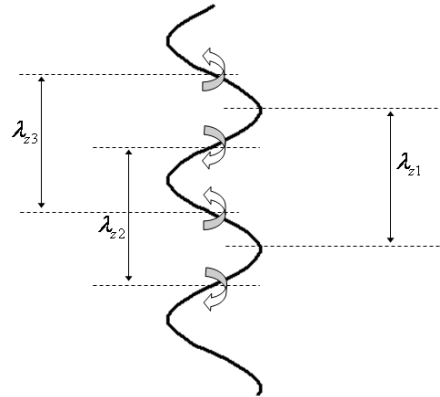


Figure 3-28. Schematic of the primary and secondary structures

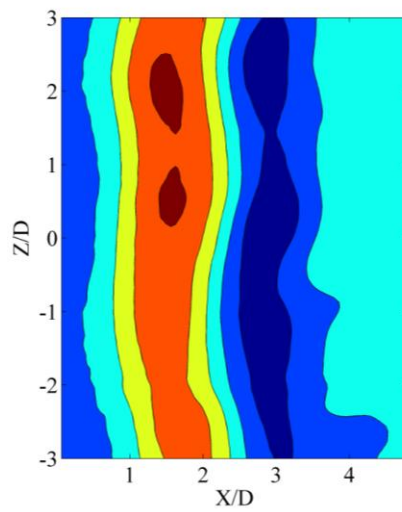


Figure 3-29. Streamwise velocity contour in XZ plane ($Y/D = -0.5$) at $Re_D = 400$ by combining POD modes 1 to 32

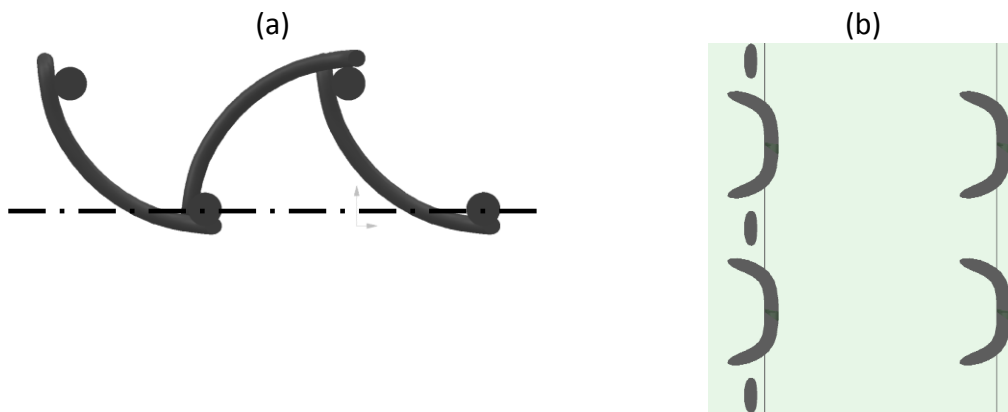


Figure 3-30. Schematic of mode-A in (a) XY plane and (b) XZ plane

plane view of the schematic, which indicates the effect of counter-rotating streamwise vortices as undulations of the Karman Benard vortices with smaller and larger wavelengths, as previously observed from the PLIF measurements (Figure 3-20).

Figure 3-31 shows the vorticity contours obtained by combining the different POD modes at $Y/D = -0.5$ for $Re_D = 550$. Specifically, Figure 3-31 (a) shows the contours obtained by combining the first four POD modes, which represent the primary coherent structure, that is, the Karman Benard vortices. Figure 3-31 (b) shows the contours obtained by combining modes 5 and 6. These latter modes represent a near wake ($X/D < 3$) structure corresponding to mode-C topology, observed as wavy pattern in the PLIF images (Figure 3-19). The spacing between the streamwise vortices is found to vary between $2.0D$ and $2.8D$, with an average wavelength of $2.4D$. Figure 3-31 (c) shows the vorticity contours obtained by combining modes 7 and 8. These represent the undulations caused by the streamwise vortices on the spanwise vortices in the intermediate wake ($X/D > 3$) of the mode-A topology. In these modes, the effect of the larger and smaller spanwise wavelengths is observed to be similar to the PLIF visualizations (Figure 3-20 c). The spacing between the undulations varies between $3.0D$ and $4.0D$, with an average wavelength of $3.5D$. Figure 3-31 (d) shows the vorticity contours obtained by combining modes 9 to 12, which display the background small-scale structures observed in the PLIF visualization (Figure 3-19). The topology of the structures indicates that the sign of vorticity remains the same for each shedding cycle, corresponding to mode-C topology, appearing with a spanwise spacing of approximately $1D$. Ryan et al. (2005) made similar observations at $Re_D = 600$. Since modes 9 to 12 display a structure with mode-C topology and appear with a wavelength similar to that of mode-B of a circular cylinder, this instability mode is called mode-C^l in the following discussion.

Figure 3-32 shows the eigenvalues corresponding to the first 15 POD modes at mid-plane ($Y/D = 0$) and shear layer ($Y/D = -0.5$) for $Re_D = 550$. As previously stated, significant relative energy is captured in the first 10 POD modes at $Y/D = -0.5$; however, in the mid-plane, several modes are involved, suggesting a more even energy distribution. In

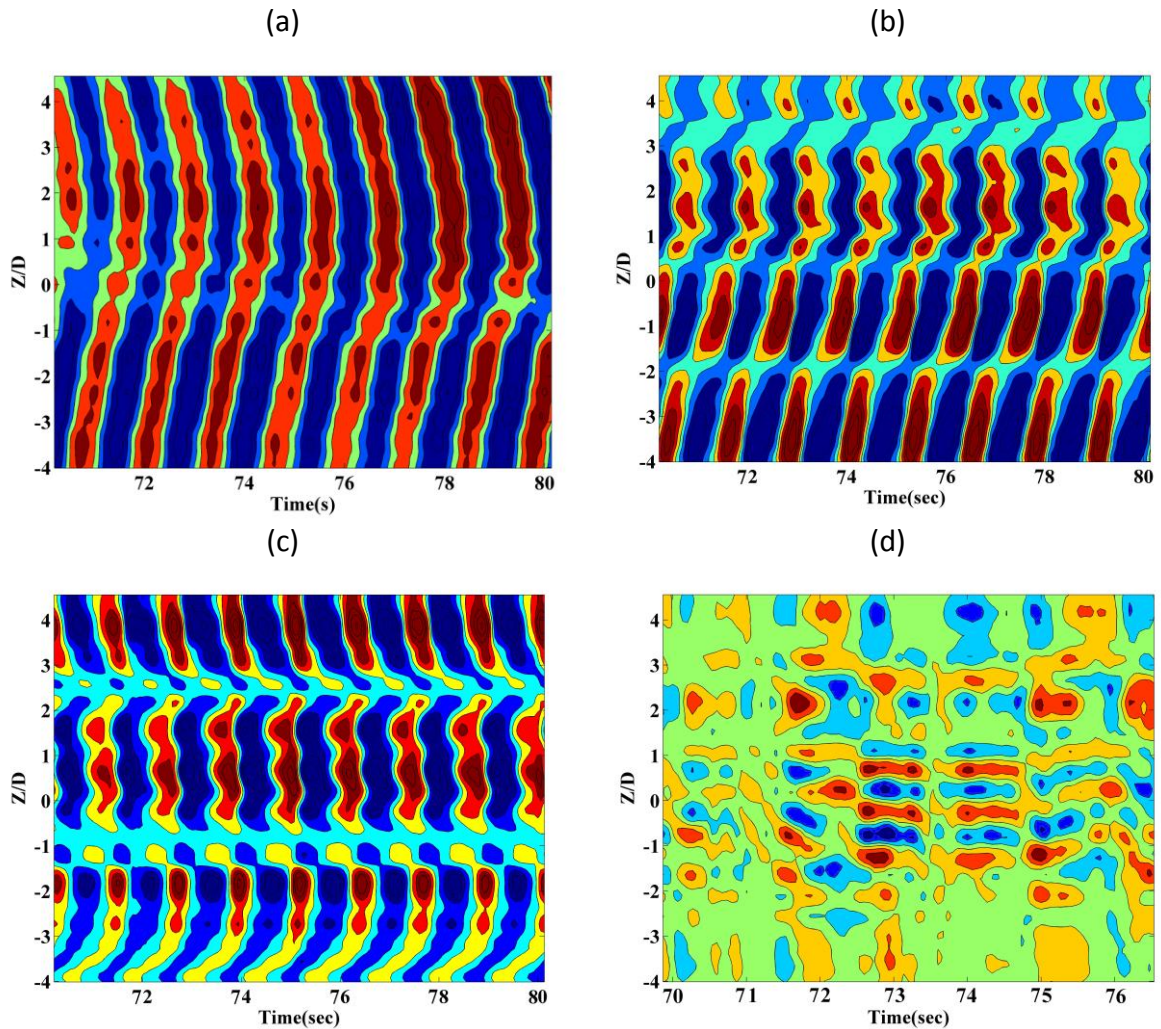


Figure 3-31. ω_y vorticity contours in XZ plane ($Y/D = -0.5$) at $Re_D = 550$ by combining POD modes (a) 1 to 4, (b) 5 and 6, (c) 7 and 8, and (d) 9 to 12

addition, the effect of the dominant coherent structure, the Karman vortex, is more pronounced in the shear layer where the first two modes show relatively high energy content compared with the mid-plane. In the mid-plane, von Karman vortices from both sides of the wake combine and counteract each other.

Figure 3-33 shows the vorticity contours obtained by combining modes 1 to 10 at $Y/D = 0$. This shows the lesser imprint of Karman Benard vortices in this plane. The spanwise spacing of the streamwise vortices is observed to vary between 2.0 and 3.0 D. Note that two ribs cut the horizontal mid-wake plane in one shedding period, indicating

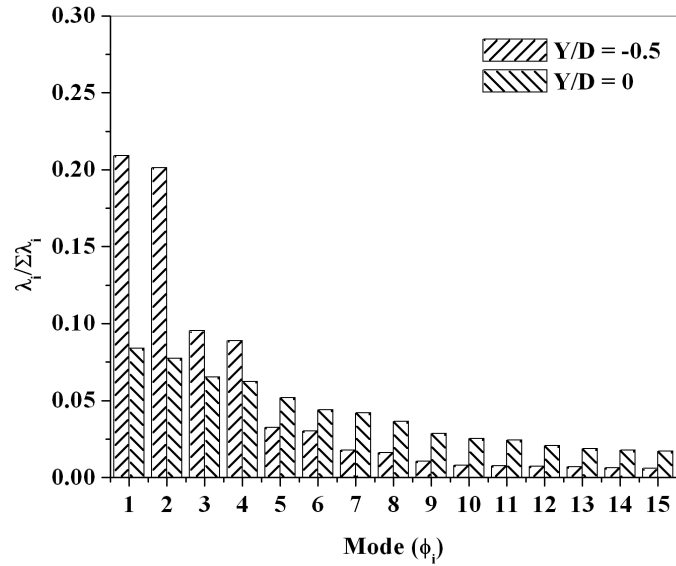


Figure 3-32 Relative energy captured by first 15 POD modes in XZ planes ($Y/D = -0.5$ and $Y/D = 0$) at $Re_D = 550$

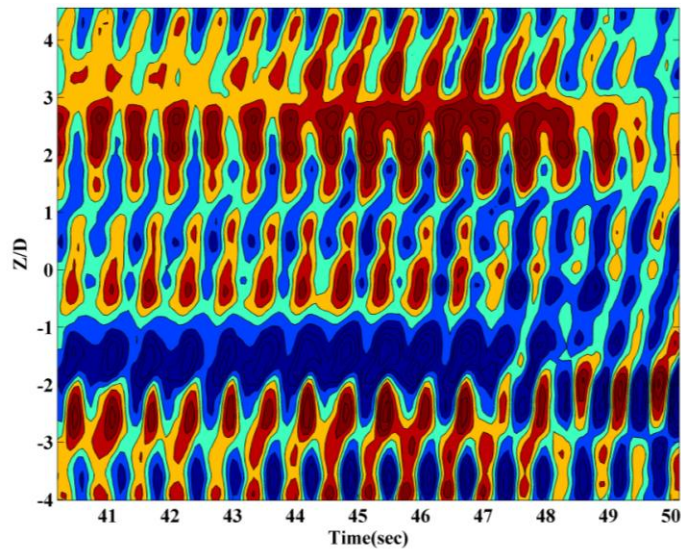


Figure 3-33 ω_y vorticity contours in XZ plane ($Y/D = 0$) at $Re_D = 550$ by combining POD modes 1 to 10

that the velocity signal acquired the alternate vortex shedding from both sides in this plane of measurements.

Figure 3-34 shows the vorticity contours using spatial coordinates by combining modes (a) 1 and 2, (b) 3 and 4, (c) 5 and 6, (d) 7 and 8 and (e) 9 to 12, respectively. The contours show that the same spanwise spacing is observed in the data when expanded in time. The topologies displayed by the vorticity contours in the spatial coordinates conceal details such as the inclined vortex shedding, and details such as the larger and smaller wavelength in mode 7 and 8 when expanded in time. These modes, however, distinctly illustrate the details of the dominant streamwise vortices. Figure 3-34 (f) shows the streamwise velocity component derived by adding the first 32 POD modes, which correspond to 80% relative kinetic energy of the flow. Here, the POD modes display the effect of the streamwise vortices as a sinusoidal oscillation (Figure 3-28), indicating considerable deformation in the streamwise vortices, confirming the results obtained from PLIF images at $Re_D = 550$. Similar observations are made in the mid-plane measurements (Figure 3-35).

Hence, we conclude that the wake is dominated by two wake instabilities, that is, mode-C in the near wake and mode-A in the intermediate wake respectively. In order to further understand the development of these secondary wake instabilities at higher Reynolds numbers, experiments were conducted at Reynolds number of $Re_D = 1050$, 1550 and 2300 which are discussed in the following section.

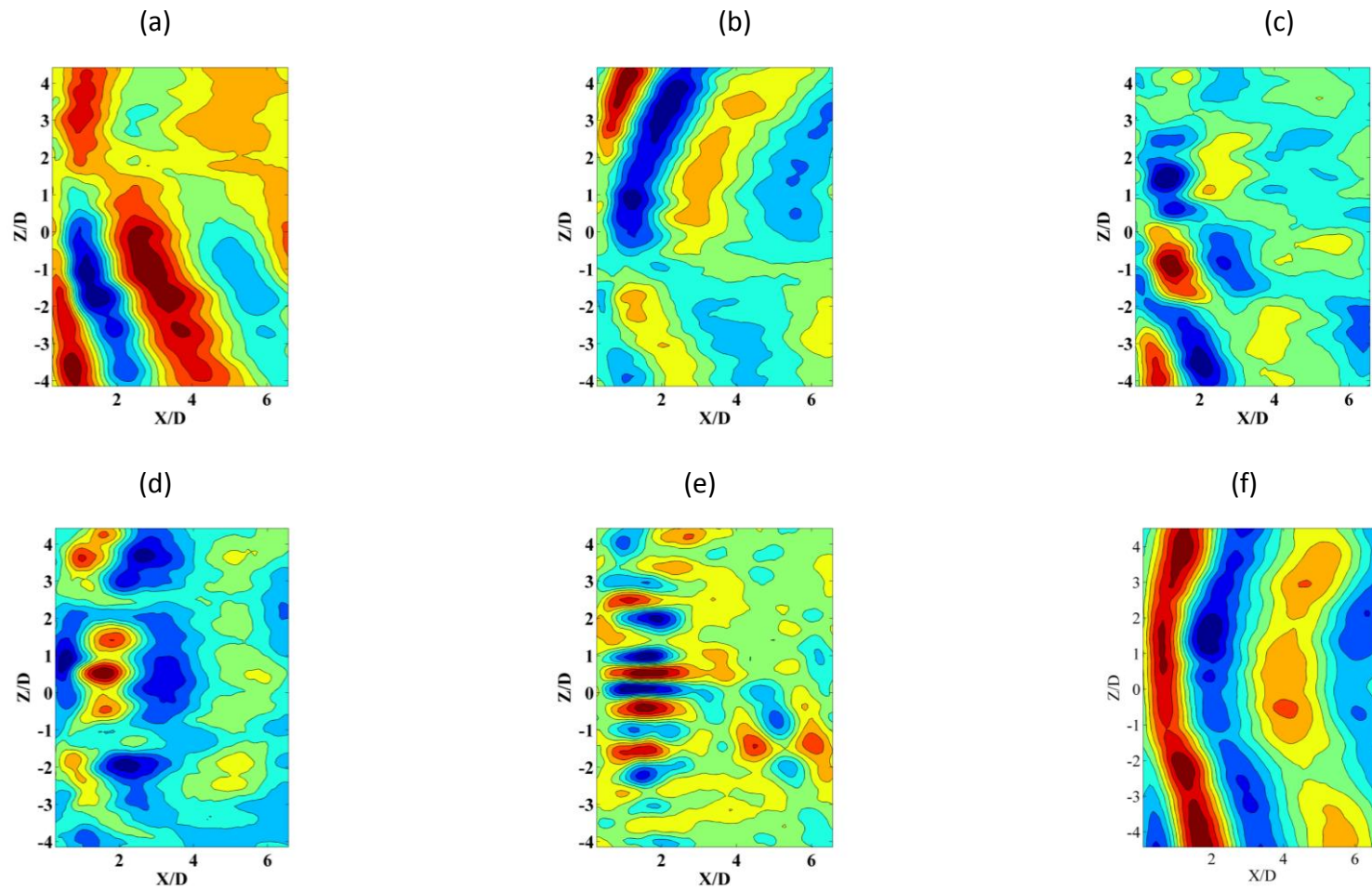


Figure 3-34. ω_y vorticity contour in XZ plane ($Y/D = -0.5$) at $Re_D = 550$ by combining POD modes (a) 1 and 2, (b) 3 and 4, (c) 5 and 6, (d) 7 and 9, (e) 9 to 12. (f) Streamwise velocity contour by combining POD modes 1 to 32

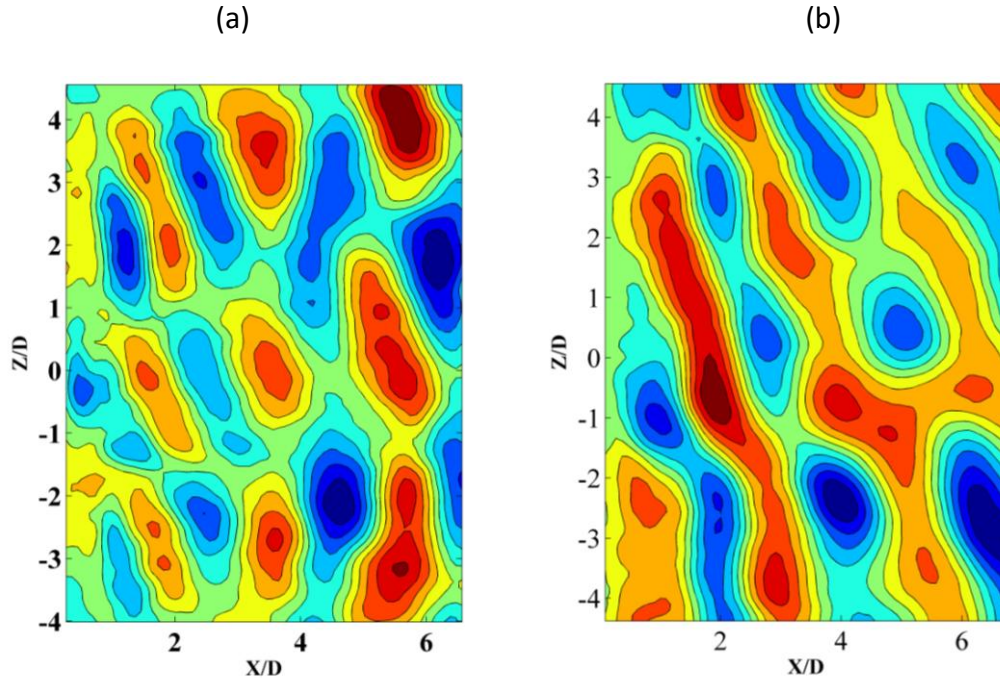


Figure 3-35. (a) ω_y vorticity contour in XZ plane ($Y/D = 0$) at $Re_D = 550$ by combining POD modes 1 to 10 and (b) streamwise velocity contour by combining POD modes 1 to 32

3.2.2.6 Effect of Higher Reynolds Numbers

Figure 3-36 shows the PLIF images in the horizontal (XZ) plane at Reynolds numbers of $Re_D = 1050$. The dye visualization indicates that the dislocations caused by streamwise vortices are smeared due to the turbulent motion in the wake. The PLIF visualization indicates that the wake displays the same features as observed at a Reynolds number of $Re_D = 550$. The near wake is dominated by an asymmetric mode-C structure (Figure 3-36 a) whereas the intermediate wake (Figure 3-36 b) is dominated by a symmetric mode-A structure, indicated by arrows in the Figure 3-36 (a) and (b) respectively. Similar observations are made at a Reynolds number of $Re_D = 1550$ (Figure 3-37). At a Reynolds number of $Re_D = 2300$, however, it is difficult to visualize (Figure 3-38) the topology of the wake instabilities that govern the wake development, because the dye diffuses quickly in the downstream wake. The dislocation caused by the streamwise vortices in

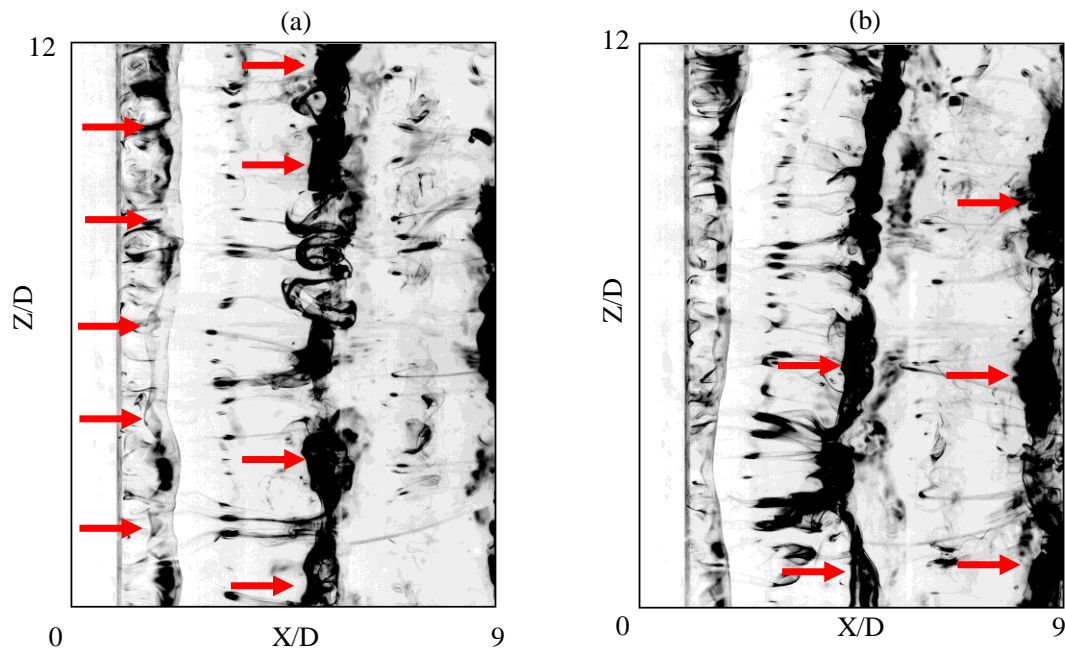


Figure 3-36. PLIF visualization in XZ plane ($Y/D = -0.5$) at $Re_D = 1050$

the near wake can be identified at this Reynolds number, marked by arrows in Figure 3-38. A general observation from the PLIF visualization at higher Reynolds numbers is that the spanwise spacing of the streamwise vortices decreases with increasing Reynolds number; in addition, the spacing between the streamwise vortices increases in the downstream direction of the wake. The spanwise spacing between the streamwise vortices is summarized in Table 3.1. To gain additional insight into the spanwise spacing of the streamwise vortices and further support the observation made from the PLIF visualizations, POD analysis is performed on the PIV data.

Figure 3-39 shows the relative energy captured by the first 15 POD modes in XZ plane at $Y/D = -0.5$ at $Re_D = 1050, 1550$ and 2300 . The plot indicates that the first two POD modes capture most of the kinetic energy in the flow, indicating that these modes relate to the dominant von-Karman Benard vortices developing in the flow. However in order to interpret these POD modes we look at the spatial topology of these POD modes, shown in Figure 3-40, Figure 3-41 and Figure 3-42 for Re_D of 1050, 1550 and

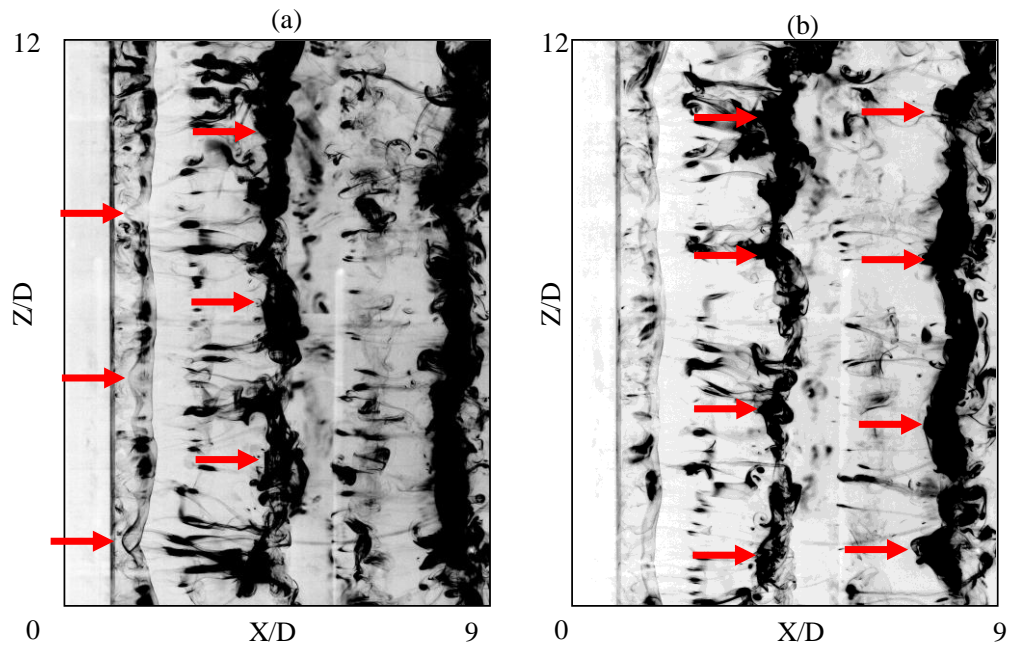


Figure 3-37. PLIF visualization in XZ plane ($Y/D = -0.5$) at $Re_D = 1550$

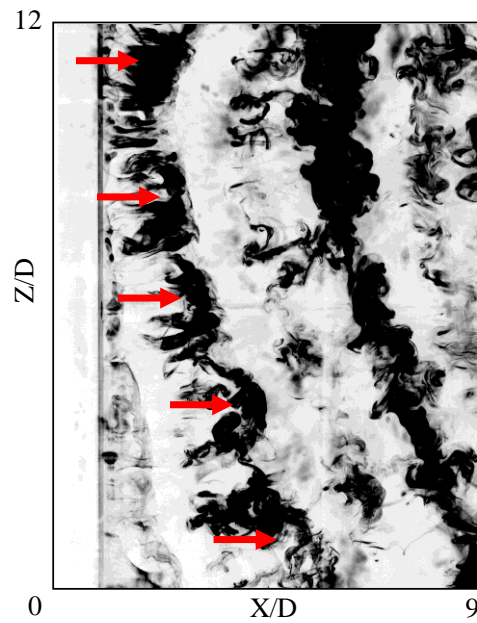


Figure 3-38. PLIF visualization in XZ plane ($Y/D = -0.5$) at $Re_D = 2300$

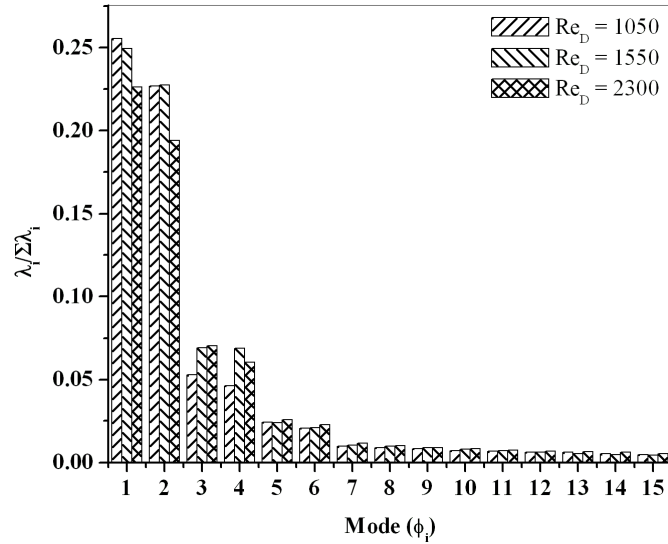


Figure 3-39 Relative energy captured by first 15 POD modes in XZ planes ($Y/D = -0.5$) at $Re_D = 1050, 1550$ and 2300

2300 respectively. The POD modes indicate that first four POD modes relate to the von-Karman Benard vortices and the large scale vortex dislocation associated with these vortices, similar to the observations made at $Re_D = 550$. One major difference between the vorticity POD modes at $Re_D = 550$ and $Re_D = 1050, 1550$ and 2300 is that at $Re_D = 550$, modes 5 and 6, and modes 7 and 8 relate to the dominant secondary wake instabilities that appear in the wake development, and modes 9 to 12 relate to the background small-scale structure in the flow. At the high Reynolds numbers of 1050, 1550 and 2300, however, only modes 5 and 6 relate to the dominant secondary wake instability in the flow, while modes 7 and 8 relate to the background small-scale structure with a spanwise spacing of $1D$. This shift in the POD modes indicates the reduction of coherence in the flow, also indicated by reduction in the relative energy in the POD modes (Figure 3-11 a) in the vertical (XY) plane.

As previously indicated, it is difficult to identify the topology of streamwise vortices from the spatial plots. However, the vorticity POD modes indicate that the spanwise spacing of the streamwise vortices decreases with increasing Reynolds numbers, supporting the PLIF visualization results. To provide further support for the finding, the

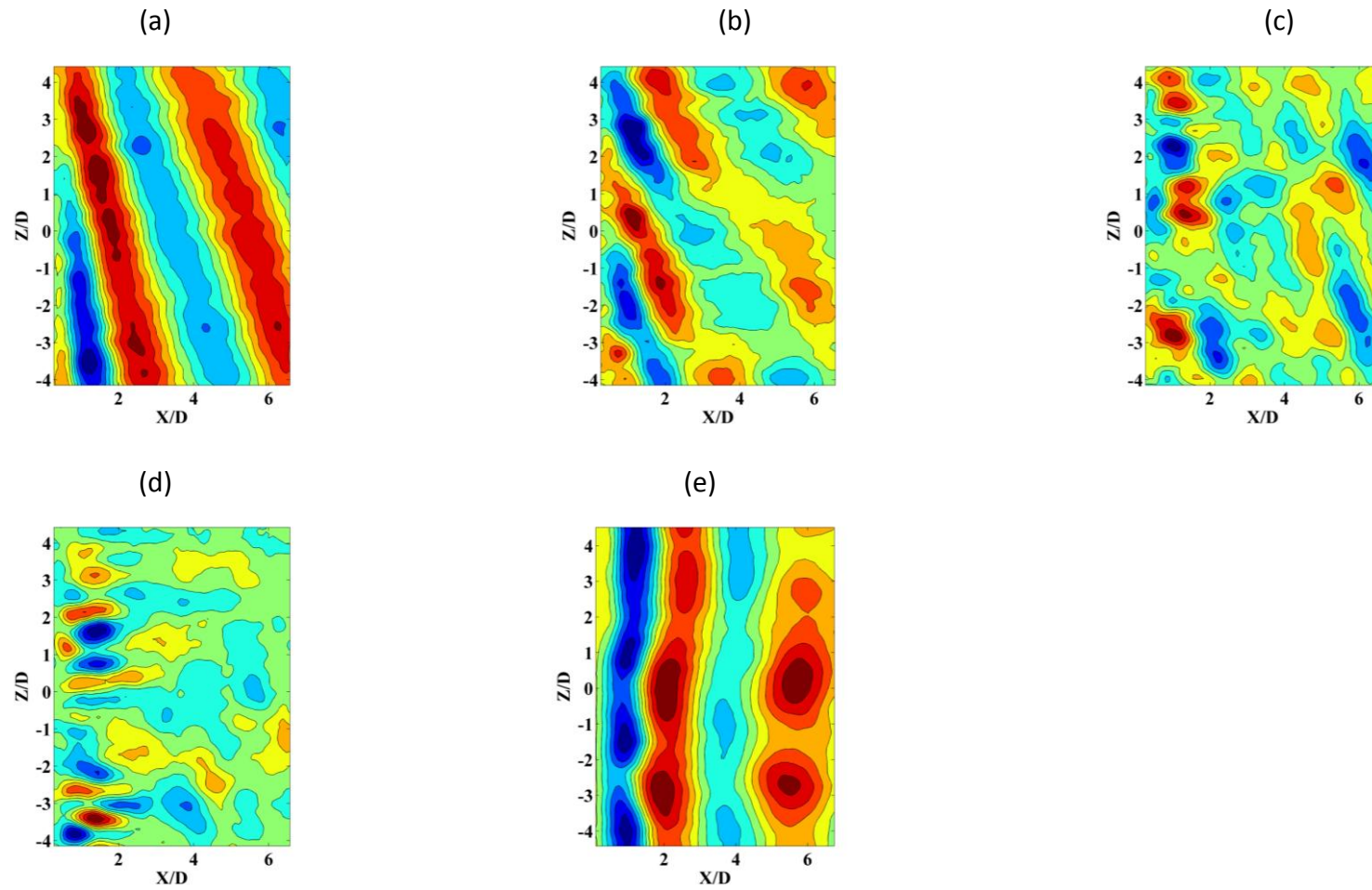


Figure 3-40. (a) ω_y vorticity contour in XZ plane ($Y/D = -0.5$) at $Re_D = 1050$ by combining POD modes (a) 1 and 2, (b) 3 and 4, (c) 5 and 6, (d) 7 and 8. (e) Streamwise velocity contour by combining POD modes 1 to 32

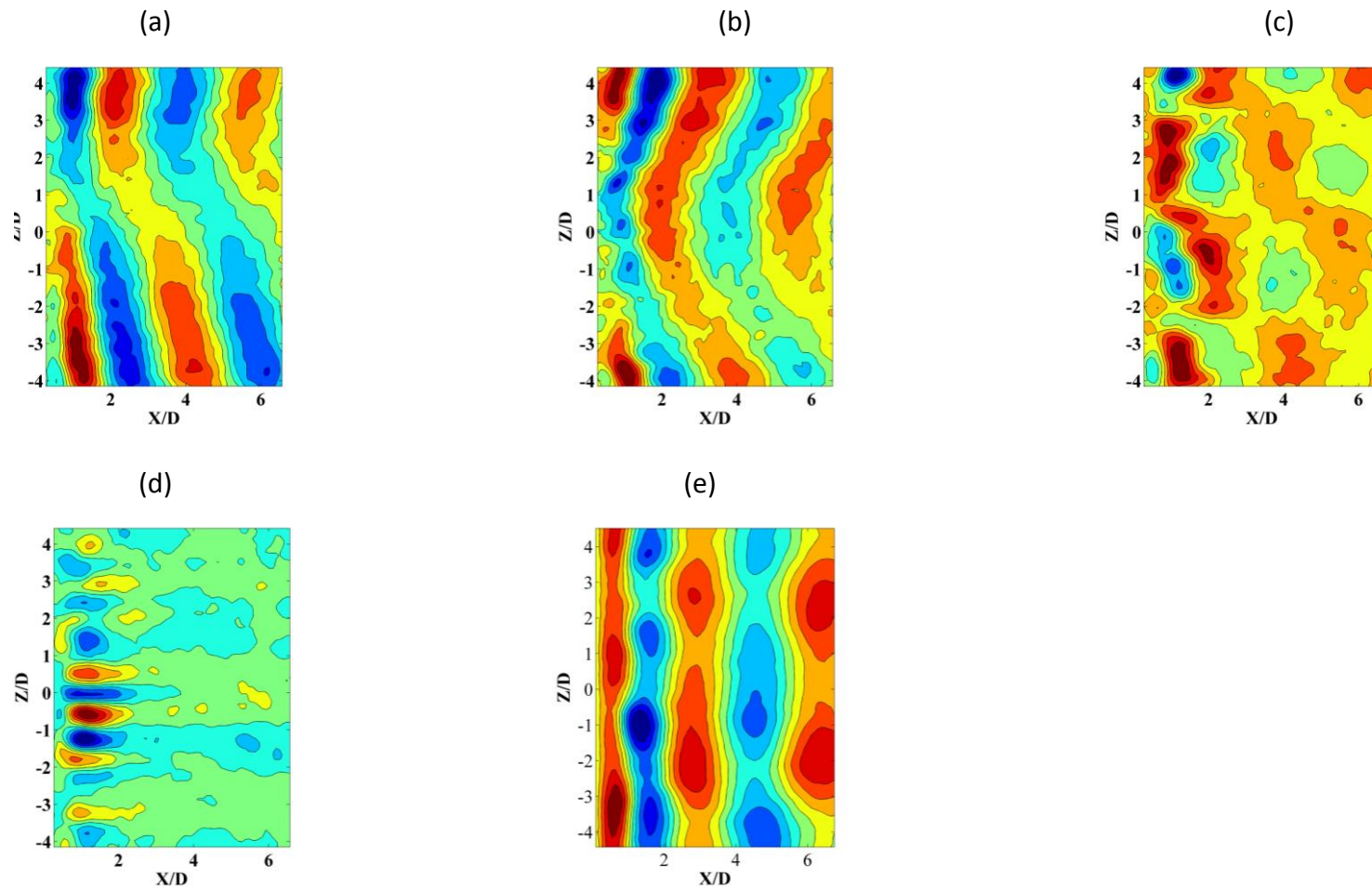


Figure 3-41. (a) ω_y vorticity contour in XZ plane ($Y/D = -0.5$) at $Re_D = 1550$ by combining POD modes (a) 1 and 2, (b) 3 and 4, (c) 5 and 6, (d) 7 and 8. (e) Streamwise velocity contour by combining POD modes 1 to 32

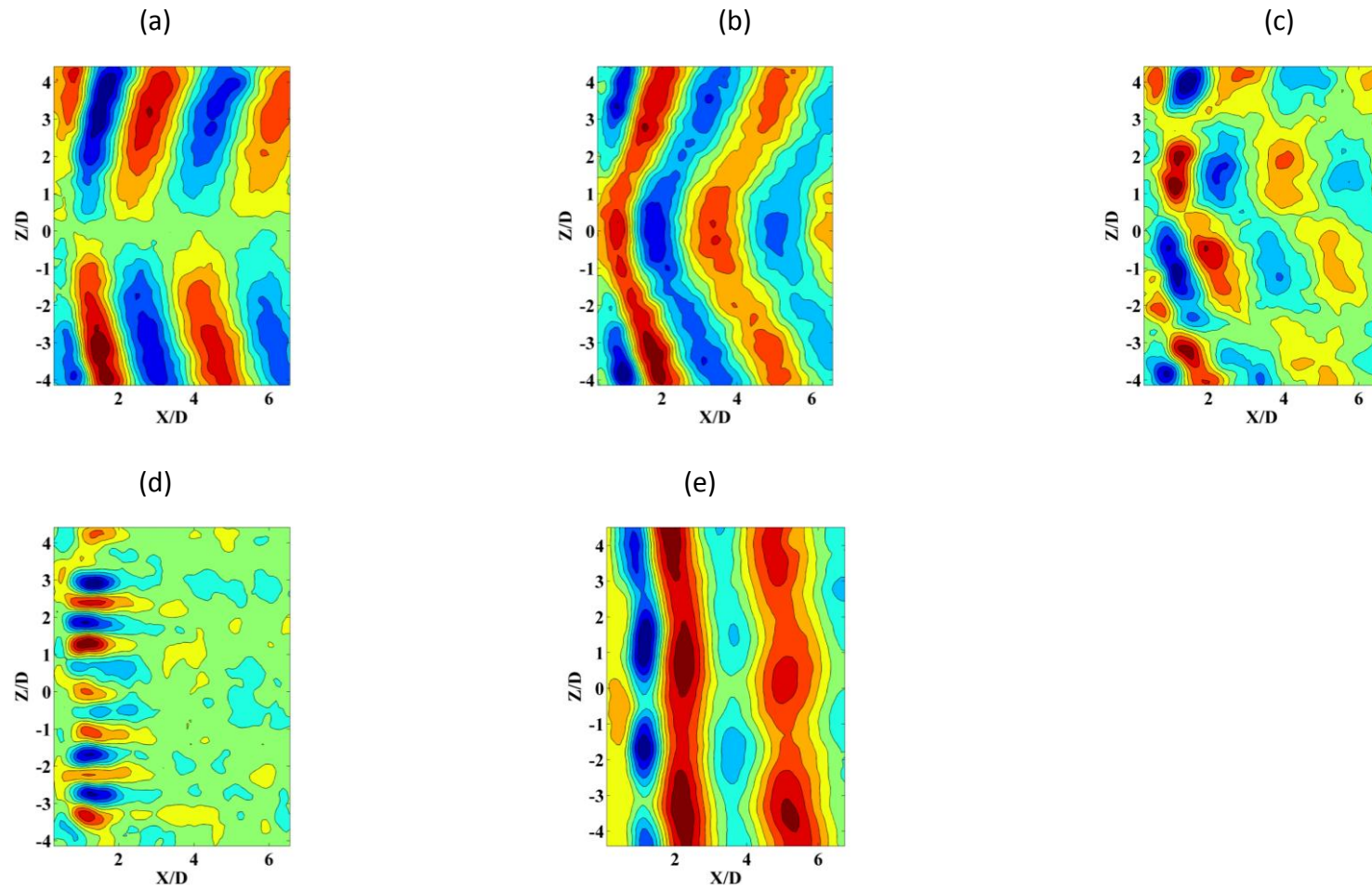


Figure 3-42. (a) ω_y vorticity contour in XZ plane ($Y/D = -0.5$) at $Re_D = 2300$ by combining POD modes (a) 1 and 2, (b) 3 and 4, (c) 5 and 6, (d) 7 and 8. (f) Streamwise velocity contour by combining POD modes 1 to 32

streamwise velocity POD modes are plotted by combining the first 32 POD modes (Figure 3-40 e, Figure 3-41 e and Figure 3-42 e), which correspond to 70-80% relative kinetic energy in the flow. The contours also confirm that the spanwise spacing of the streamwise vortices decreases with increasing Reynolds numbers. In addition, the spanwise spacing between the streamwise vortices increases with downstream distance.

As noted earlier, PLIF visualization at a Reynolds number of $Re_D = 2300$ (Figure 3-38) cannot provide adequate information regarding the wake instabilities that govern the wake development. From the POD modes, it can be established that the wake topology at $Re_D = 2300$ is very similar to those at $Re_D = 1050$ and 1550 . Hence, it can be concluded that the near wake is governed by asymmetric mode-C instability and the intermediate wake by symmetric mode-A instability.

3.3 Wind Tunnel Measurements

3.3.1 XY Plane Result

Figure 3-43 and Figure 3-44 shows the first five streamwise and transverse velocity POD modes at $Re_D = 24000$ and $Re_D = 46000$ respectively. The modes appear very similar to that observed at $Re_D = 550$ (Figure 3-5). The first two modes relate to the dominant von Karman vortex developing in the flow. Modes 3 appears to a standing mode with no companion mode, likely related to the boundary layer developing in the flow. Modes 4 and 5 relate to the first harmonic of the von-Karman Benard vortices. This relation between the POD modes is further supported by the relative energy plot (Figure 3-45 a) and phase averaged relation between the time varying coefficients of these POD modes, shown in Figure 3-45 (b) and (c), as interpreted in section 3.2.1.

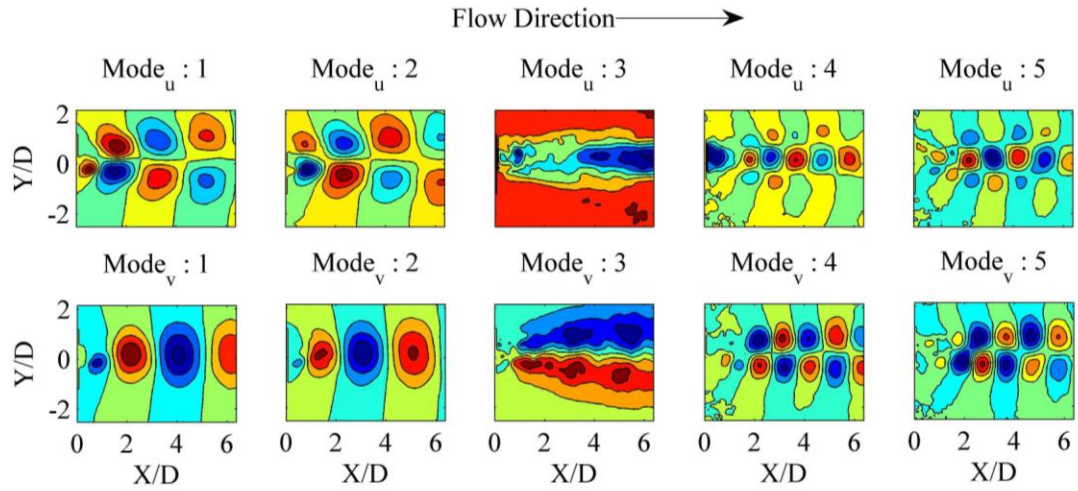


Figure 3-43. Streamwise and transverse velocity components for the first five POD modes in XY plane for the base case at $Re_D = 24000$

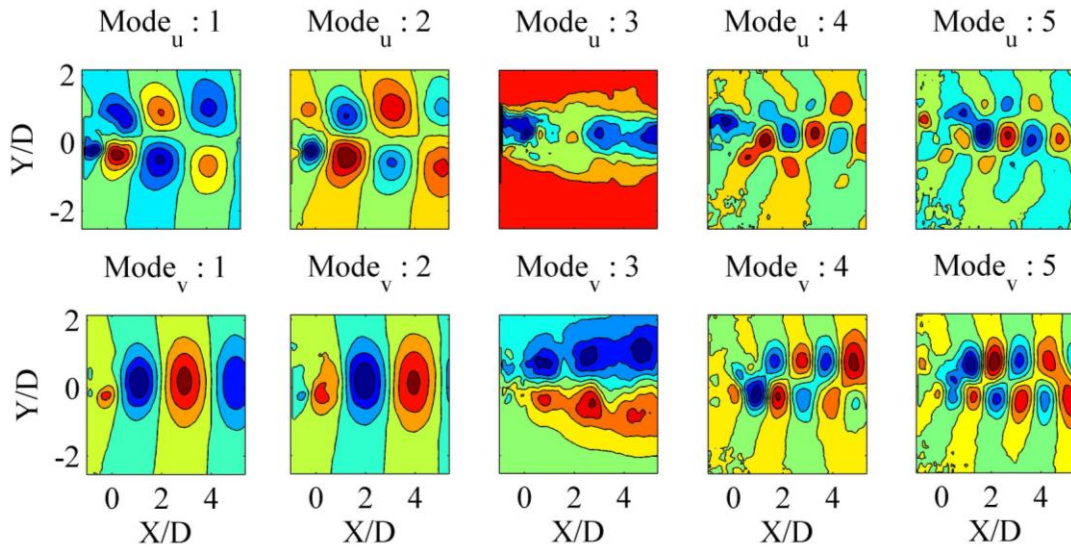


Figure 3-44. Streamwise and transverse velocity components for the first five POD modes in XY plane for the base case at $Re_D = 46000$

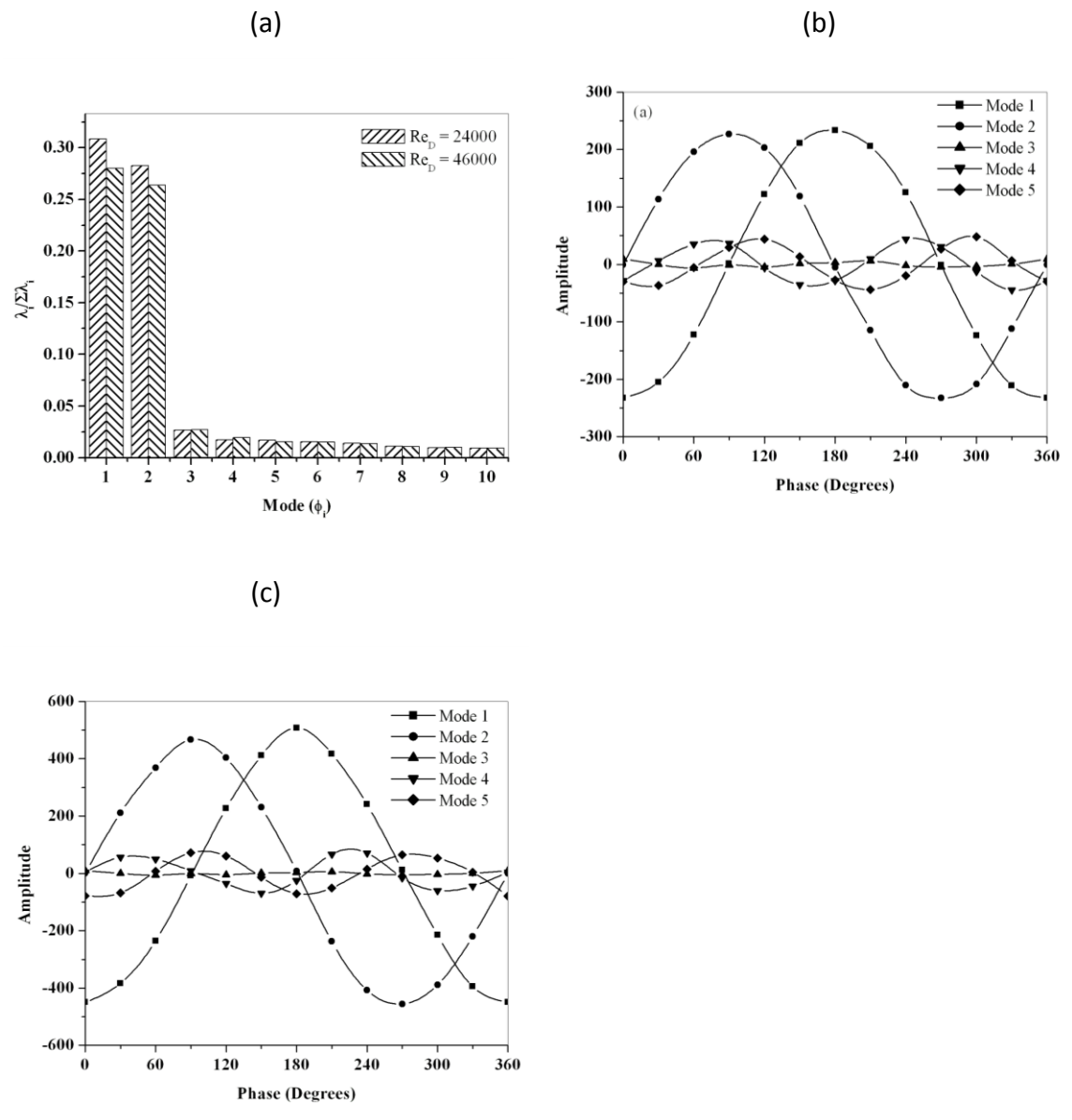


Figure 3-45. (a) Relative energy captured by first ten POD modes in XY plane at $Re_D = 24000$ and 46000 . Phase averaged time varying coefficient in XY plane at (b) $Re_D = 24000$ and (c) $Re_D = 46000$

Figure 3-46 (a) and (b) shows the streakline plots along with vorticity contours obtained by combining the first two POD modes. The plots clearly capture the effect of the dominant von-Karman Benard vortices. Streamwise spacing of the spanwise vortices

is observed to be approximately constant at $3.6D$ for both Reynolds numbers of $Re_D = 24000$ and $Re_D = 46000$, as opposed to decreasing values of λ_x (Figure 3-13) with increasing Reynolds number in water tunnel measurements ($550 \leq Re_D \leq 2300$), indicating that λ_x reaches an asymptotic value at very high Reynolds numbers.

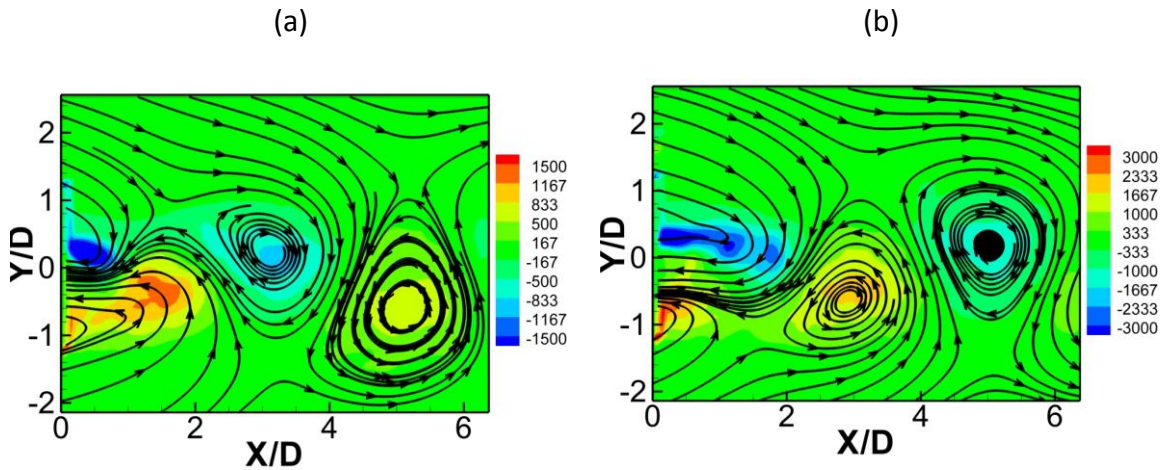


Figure 3-46. Streakline plots along with vorticity contours by combining first two POD modes of in XY plane for (a) $Re_D = 24000$ and (b) $Re_D = 46000$

3.3.2 XZ Plane Results

Figure 3-47 shows the eigenvalues corresponding to the first 15 POD modes in (a) shear layer ($Y/D = -0.5$) and (b) mid-plane ($Y/D = 0$) for Reynolds number of $Re_D = 24000$ and $Re_D = 46000$. As previously stated (Section 3.2.2.5), significant relative energy is captured in the first 10 POD modes at $Y/D = -0.5$; however, in the mid-plane, several modes are involved, suggesting a more even energy distribution. In addition, the effect of the dominant coherent structure, the Karman vortex, is more pronounced in the shear layer where the first two modes show relatively high energy content compared with the mid-plane. In the mid-plane, von Karman vortices from both sides of the wake combine and counteract each other.

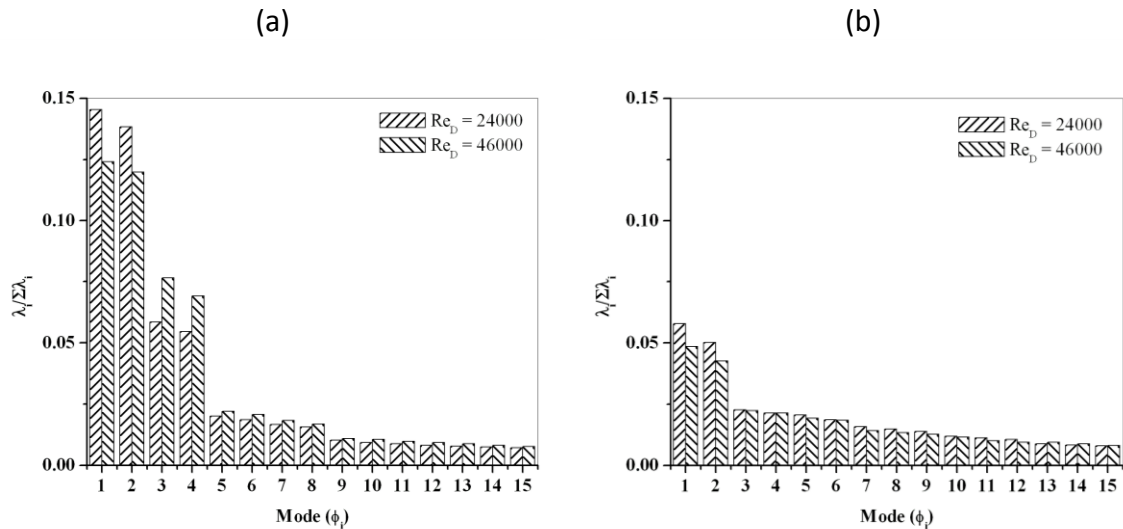


Figure 3-47. Relative energy captured by first 15 POD modes in XZ at (a) $Y/D = -0.5$ and (b) $Y/D = 0$ plane for $Re_D = 24000$ and $Re_D = 46000$

Figure 3-48 and Figure 3-49 shows the first ten POD modes of streamwise and transverse velocity components in the horizontal plane (XZ) at $Y/D = -0.5$ for Reynolds numbers of $Re_D = 24000$ and $Re_D = 46000$ respectively. This plane captures the signature of both the spanwise von Karman Benard vortices and streamwise vortices. The POD modes indicate that the first four POD modes relate to the dominant von-Karman vortices and the large scale dislocation that appear in these vortices. However modes 5 and 6, 7 and 8, and 9 and 10, which appear to represent the undulations caused by the streamwise vortices due to spanwise vortices, appear with different wavelengths in all these mode pairs. These dislocations appear with a spanwise wavelength of approximately $2.4 D$ in modes 5 to 8 and with an approximate spanwise wavelength of $1.2 D$ in modes 9 and 10. Hence, in order to understand the dynamic nature of the streamwise vortices, streamwise velocity POD modes are plotted by combining the first 32 POD modes which correspond to approximately 60-70% relative kinetic energy in the flow, shown in Figure 3-50 and Figure 3-51 for Reynolds number of $Re_D = 24000$ and $Re_D = 46000$ respectively. Figure 3-50 shows the streamwise velocity POD modes at different

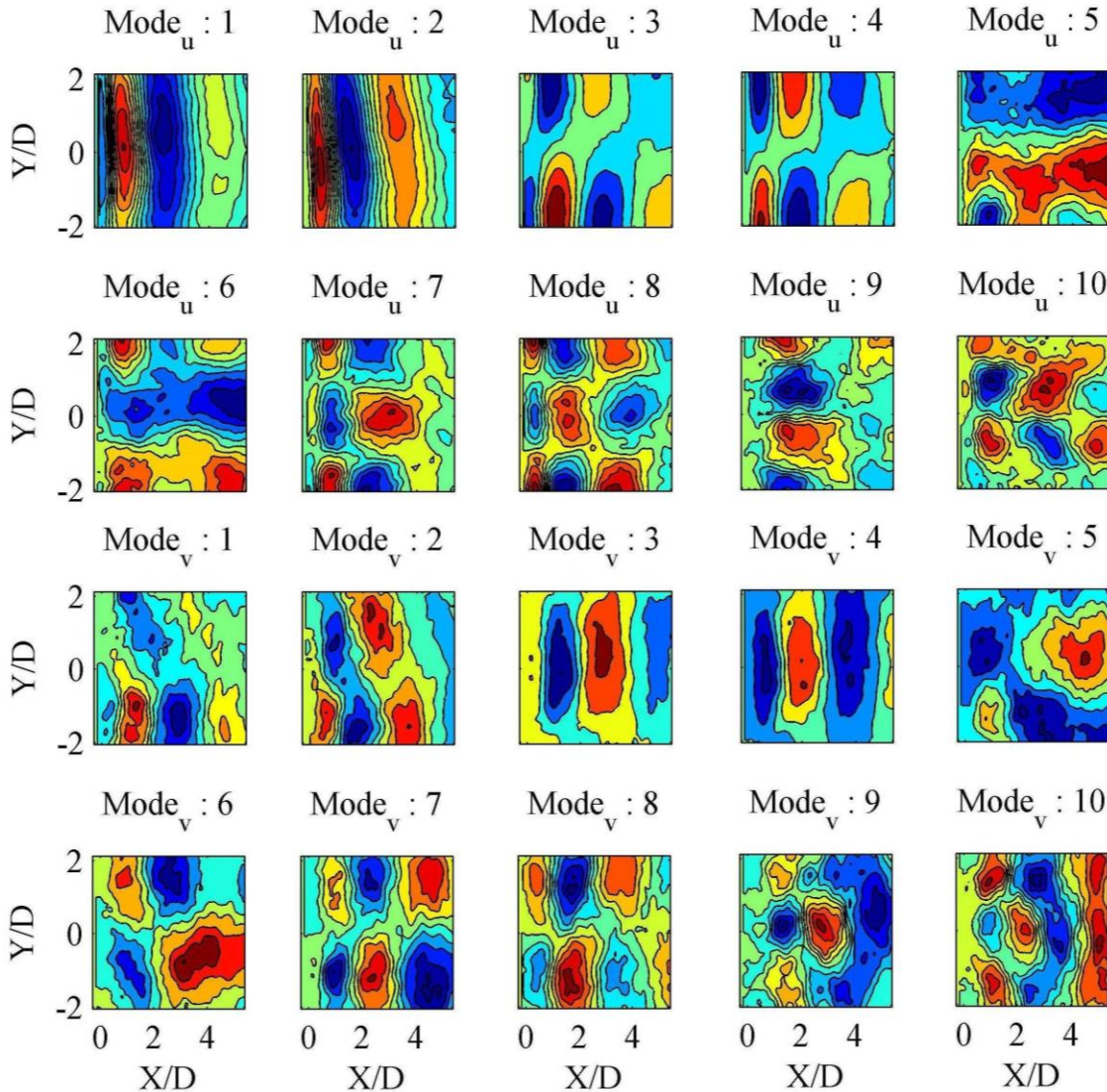


Figure 3-48. Streamwise and transverse velocity components for the first ten POD modes in XZ plane for the base case at $Re_D = 24000$

time instances in the flow. These POD modes which appear with various wavelengths at various instances in the flow demonstrate the unsteady nature of the streamwise vortices with wavelength varying in both space and time. Similar observations are made at Reynolds number of $Re_D = 46000$ (Figure 3-51). The streamwise vortices appear with a spanwise wavelength ranging from $1.2 D$ to $2.4D$. Table 3.1 summarizes the spanwise spacing of the streamwise vortices at various Reynolds numbers from the current study.

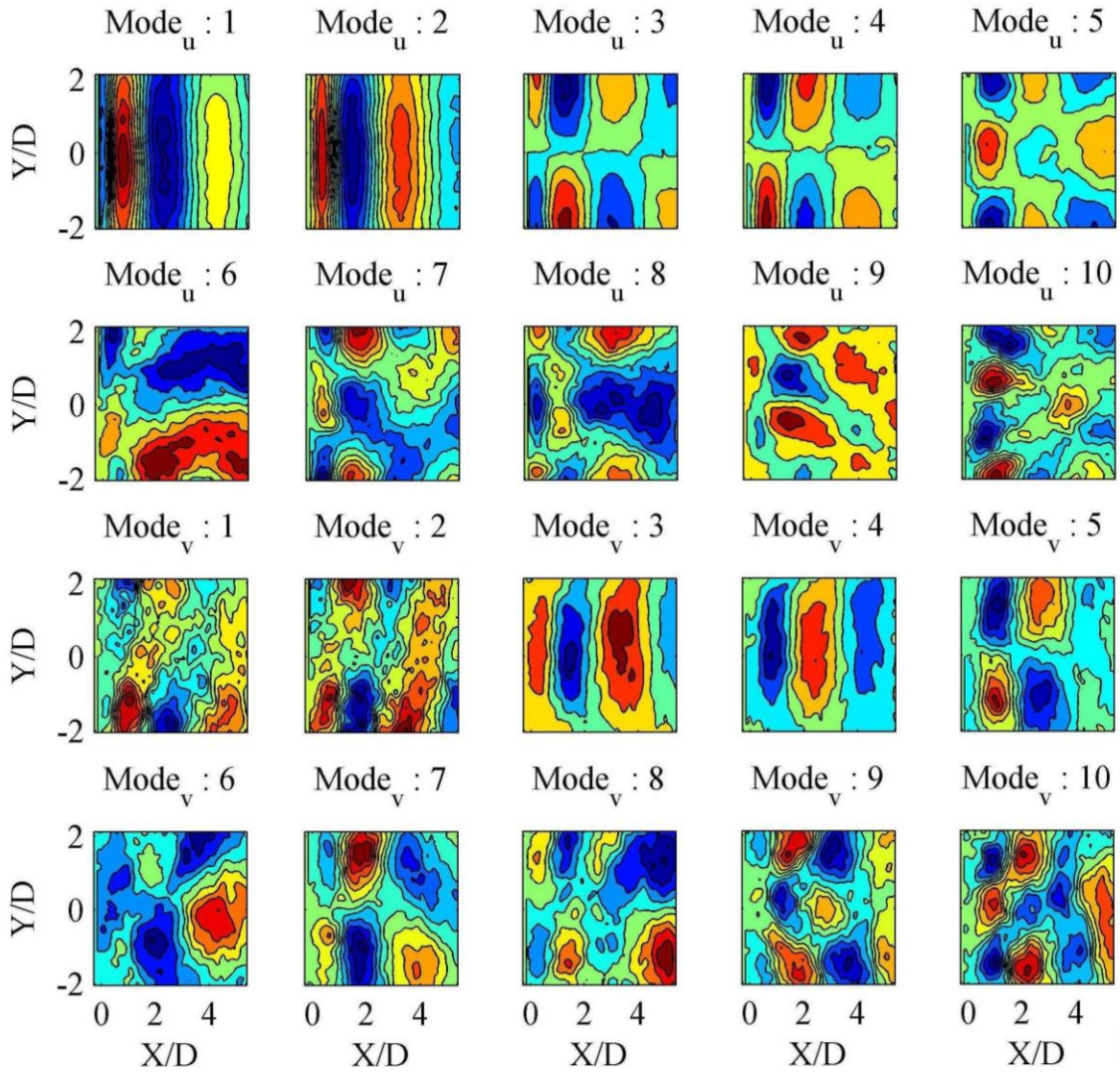


Figure 3-49. Streamwise and transverse velocity components for the first ten POD modes in XZ plane for the base case at $Re_D = 46000$

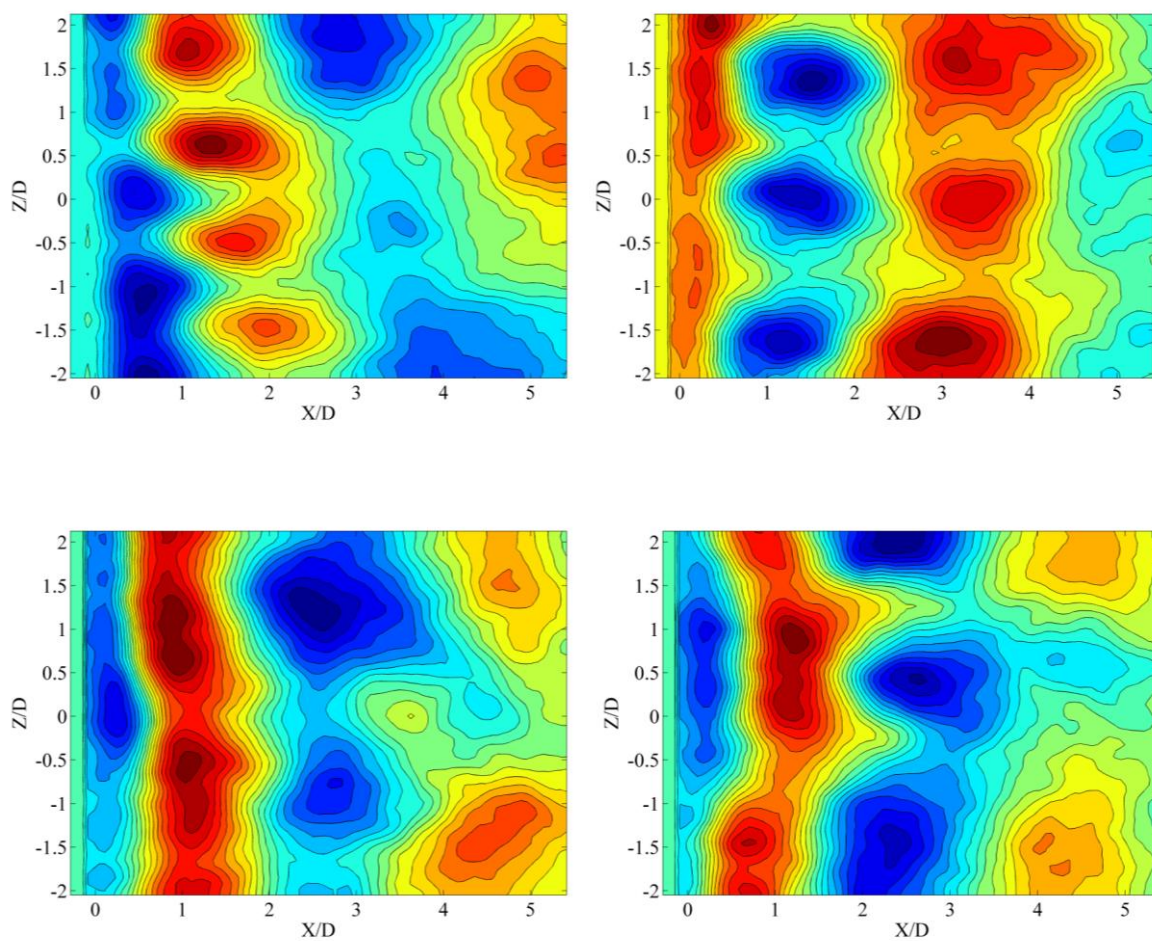


Figure 3-50 Streamwise velocity contours in XZ plane ($Y/D = -0.5$) at $Re_D = 24000$ by combining POD modes 1 to 32 at different instances in flow

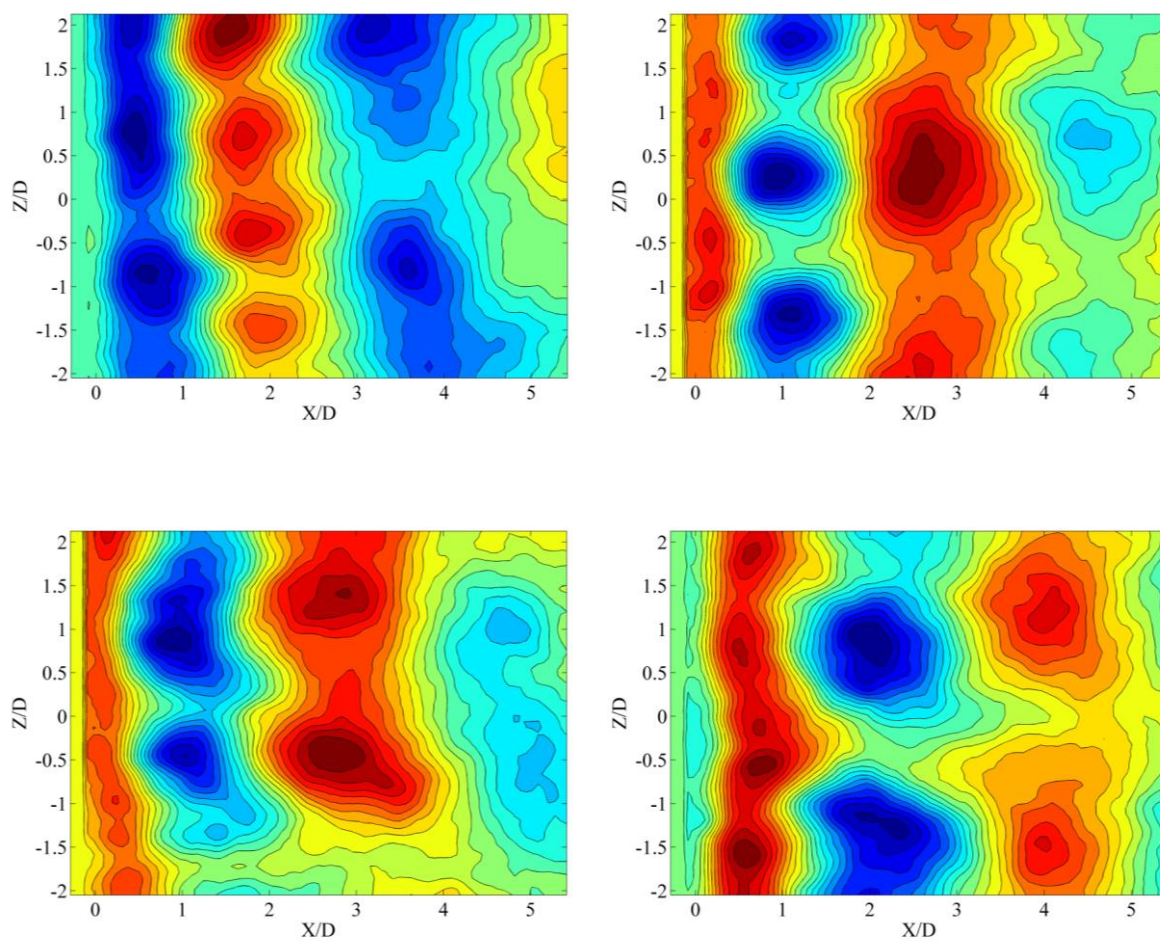


Figure 3-51 Streamwise velocity contours in XZ plane ($Y/D = -0.5$) at $Re_D = 46000$ by combining POD modes 1 to 32 at different instances in flow

Re _D	λ_x/D		λ_z/D						
	PLIF	PIV	PLIF			PIV			
			Mode-A	Mode-B	Mode-C	Mode-A	Mode-B	Mode-C	Mode-C ^l
400	--	--	--	1.0-1.5	--	--	1.0-1.5	--	--
550	4.8	4.8	2.8-3.8	--	2.0-2.8	3.0-4.0	--	2.2-2.8	1.0
1050	4.5	4.5	2.8-3.3	--	--	2.8-3.8	--	2.2-2.8	1.0
1550	4.0	4.0	2.8-3.0	--	--	2.7-3.5	--	2.2-2.8	1.0
2300	3.8	3.8	2.8-3.0	--	--	2.6-3.2	--	2.2-2.7	1.0
24000	--	3.6	--	--	--	2.0-2.8	--	1.2-1.8	--
46000	--	3.6	--	--	--	2.0-2.8	--	1.2-1.6	--

Table 3.1 Summary of the streamwise and spanwise wavelengths observed from PLIF and PIV measurements

3.4 Summary

Results from the current experiments on the blunt trailing-edge-profiled body indicate that the transition to turbulence follows a different path, that is, through mode-B, mode-C and mode-A, than the classical circular cylinder flow path, that is, through mode-A and mode-B, confirming the numerical findings of Ryan et al. (2005). The associated Reynolds numbers of these secondary wake instabilities are higher than that for the circular cylinder flows. In the current study, we have substantially extended Ryan et al.'s (2005) findings over a range of Reynolds numbers, from transition ($400 \leq Re_D \leq 2300$) to high Reynolds numbers ($24000 \leq Re_D \leq 46000$). The overall spanwise spacing (λ_z/D) of the streamwise vortices is somewhat robust through all of these regimes, with values ranging from 1.2 to 2.8. On the basis of these findings, a passive flow control is designed with the objective to mitigate vortex shedding and reduce base drag. The wake dynamic resulting from the proposed passive flow control is discussed in the next chapter.

4 WAKE DYNAMICS RESULTING FROM TRAILING EDGE SPANWISE SINUSOIDAL PERTURBATION (SSP)

In this chapter, the wake dynamics resulting from a passive flow control based on trailing edge Spanwise Sinusoidal Perturbation (SSP) (Figure 2-7) is discussed. Two wavelengths of the SSP are tested based on previous studies and the observations made in the current study. The effectiveness of the control is estimated by analyzing the mean flow parameters such as base drag, base pressure coefficient, formation length, as well as higher statistics such as power spectral density. Finally, Proper Orthogonal Decomposition (POD) is performed on the Particle Image Velocimetry (PIV) data in two planes to understand the wake energy redistribution due to SSP.

4.1 Wavelength selection for SSP

The elliptic leading edge and blunt trailing edge flat plate (Figure 2-6) studied herein is similar to the flat plate model investigated by Tombazis and Bearman (1997) and Ryan et al. (2005). Our base case (no trailing edge waviness) and two SSP control cases are investigated and compared. The two SSP trailing edges, with spanwise spacing of $\lambda_z/D = 2.4$ and 5.6 and corresponding wave steepness $W/\lambda_z = 0.197$ and 0.09 are tested and referred to as *SSP 2.4* and *SSP 5.6*, respectively. The spanwise spacing and wave steepness of the control are chosen based on the DNS work by Darekar and Sherwin (2001) on a square cylinder with wavy leading and trailing edges, and also from the observations made in the current study. Darekar and Sherwin (2001) investigated the receptivity of the near wake for a range of wavelengths ($0 < \lambda_z/D \leq 10$) and various wave steepnesses ($0 < W/\lambda_z \leq 0.25$), as shown in Figure 4-1. Darekar and Sherwin (2001) showed that maximum base drag reduction can be achieved for $\lambda_z/D = 5.6$ and amplitude of $W/\lambda_z = 0.03$. They also showed that for $\lambda_z/D = 2.8$, $W/\lambda_z = 0.2$ and

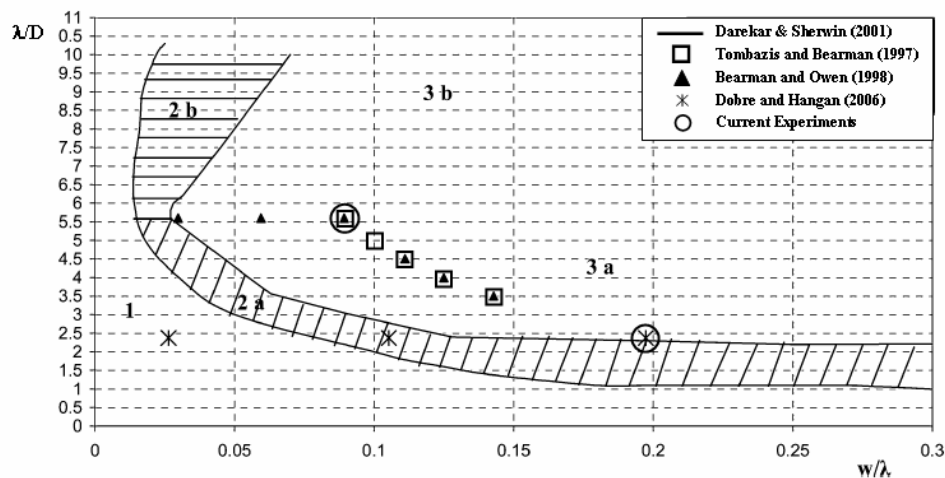


Figure 4-1. Wavy square cylinder flow regime (Darekar and Sherwin 2001)

$\lambda_z/D = 4.0$, $W/\lambda_z = 0.06$, the fluctuating lift was zero, indicating that the combination of wavelength and amplitude play an important role in reducing unsteadiness in the base region. Figure 4-1 presents other experimental data from Tombazis and Bearman (1997), Bearman and Owen (1998) and Dobre and Hangan (2006) of relative spanwise perturbation (λ_z/D) as a function of relative perturbation amplitude (W/λ_z). Three regions can be identified from this plot:

- Region 1 – SSP control is inefficient in reducing the unsteadiness caused by the von Karman Benard vortices, and hence, has a small effect on lift and drag forces.
- Region 2a – SSP control is somewhat efficient in reducing the unsteadiness caused by the von Karman Benard vortices, and hence, shows a reduction in lift and drag forces. This regime occurs only when $\lambda_z/D < 5.6$.
- Region 2b - This regime occurs only when $\lambda_z/D > 5.6$, where force histories appear with a low frequency modulation. However, this region also shows a reduction in unsteadiness caused by the von Karman Benard vortices.
- Region 3a – SSP control is most efficient in reducing the unsteadiness caused by the von Karman Benard vortices. The lift forces reach zero and the vortex shedding is completely mitigated.

- Region 3b – SSP control is also efficient in reducing the unsteadiness caused by the von Karman Benard vortices compared to other regions except region 3a. Here the lift force does not reach zero as in the case of region 3a and the vortex shedding is not completely mitigated.

The maximum base drag reduction occurred in Region 3a. On the basis of these previous studies and observations from the current study on the blunt trailing-edge-profiled body, two SSP control wavelengths $\lambda_z/D = 2.4$ and 5.6 were chosen, and are marked by circles in Figure 4-1. $\lambda_z/D = 2.4$ is the wavelength of the dominant instability for the studied geometry (Ryan et al. 2005), while $\lambda_z/D = 5.6$ is the wavelength for which maximum base drag reduction was observed for the square cylinder (Darekar and Sherwin 2001).

Since the SSP control produces three-dimensional instabilities, its effect on the wake is not uniform across the span, and hence, measurements in multiple sections are required to establish the effect of the SSP control. To accomplish this, PIV measurements were performed at two different vertical planes corresponding to the location of the peak in the SSP, termed as MAX, and the trough location of the SSP, termed MIN (Figure 2-9). PIV measurements were also performed in two different horizontal planes corresponding to mid-plane ($Y/D = 0$) and in the shear layer ($Y/D = -0.5$). The experiments were conducted at five different Reynolds numbers: $Re_D = 550, 1550, 2300, 24000$ and 46000 . For each Reynolds number, seven sets of data were recorded, as summarized in Table 4.1. For transitional low Reynolds numbers ($550 \leq Re_D \leq 2300$), measurements were conducted only with an SSP wavelength of $\lambda_z/D = 2.4$, and the boundary layer was allowed to transition naturally. In the case of high Reynolds number ($Re_D = 24000$ and 46000), experiments were conducted for two SSP wavelengths, corresponding to $\lambda_z/D = 2.4$ and 5.6 . In the high Reynolds number wind tunnel measurements, a 6.25-mm-wide sand strip was applied near the leading edge of these models to ensure that the boundary layer was fully turbulent. The main characteristics of the flat plate model and the coordinate system are shown in Figure 2-7.

Reynolds Number	Base Case			SSP Control Case			
	XY Plane	XZ Plane		XY Plane		XZ Plane	
		Y/D = 0	Y/D = -0.5	MAX	MIN	Y/D = 0	Y/D = -0.5
550	×	×	×	×	×	×	×
1550	×	×	×	×	×	×	×
2300	×	×	×	×	×	×	×
24000	×	×	×	×	×	×	×
46000	×	×	×	×	×	×	×

Table 4.1 Measurements performed for this study

4.2 Mean Flow Analysis

4.2.1 Mean Drag and Base Pressure Coefficient

To assess the effectiveness of the flow control, base pressure coefficients are compared here for the base case and the SSP control case for high Reynolds numbers, $Re_D = 24000$ and 46000 . However, in the case of low Reynolds number water tunnel measurements, where base pressure was not measured directly, and is estimated from the measured velocity field, is discussed in the later part of this section. The base pressure coefficient is defined as

$$C_{pb} = \frac{p - p_o}{\frac{1}{2} \rho U_o^2}, \quad (4.1)$$

where p_o is the free stream pressure, ρ is the density of the fluid, and U_o is the free

Reference	AR	Re_D	C_{pb}
Bearman (1967)	6.3	23000	-0.58
		41000	-0.58
Park et al. (2005)	6.3	40000	-0.57
Current Study	12.5	24000	-0.61
		46000	-0.61

Table 4.2 Comparison of base pressure coefficients with different experimental studies

stream velocity.

The mean value of the base pressure coefficient (C_{pb}) for the straight trailing edge is found to be -0.61 at both Re_D of 24000 and 46000. The base pressure values agree reasonably well with those reported by Bearman (1967) and Park et al. (2005) (Table 1.1) – even if their aspect ratio (L_x/D) is almost half that of the present one, as summarized in Table 4.2.

When the SSP is used, a significant reduction in the base drag is observed, as shown in Figure 4-2 (a), an observation similar to that made by Tombazis and Bearman (1997). The base drag reduction is attributed to the breaking of the separation line along the span as noted by Tanner (1972). Figure 4-2 (a) reveals that a maximum base drag reduction of 34% is achieved with $\lambda_z/D = 2.4$ and $W/\lambda_z = 0.197$. However, no significant base drag reduction (approximately 7%) was observed for $\lambda_z/D = 5.6$ and $W/\lambda_z = 0.09$. Tombazis and Bearman (1997) achieved a base drag reduction of approximately 10% and 36% by perturbing the flow with $\lambda_z/D = 5.6$ and 3.5, respectively, for the same geometry as that used in the current study with aspect ratio (L_x/D) of 6.3. Darekar and Sherwin (2001) achieved a maximum base drag reduction of approximately 16% with $\lambda_z/D = 5.6$ for a square cylinder. It appears that wavelength selection of the SSP to achieve

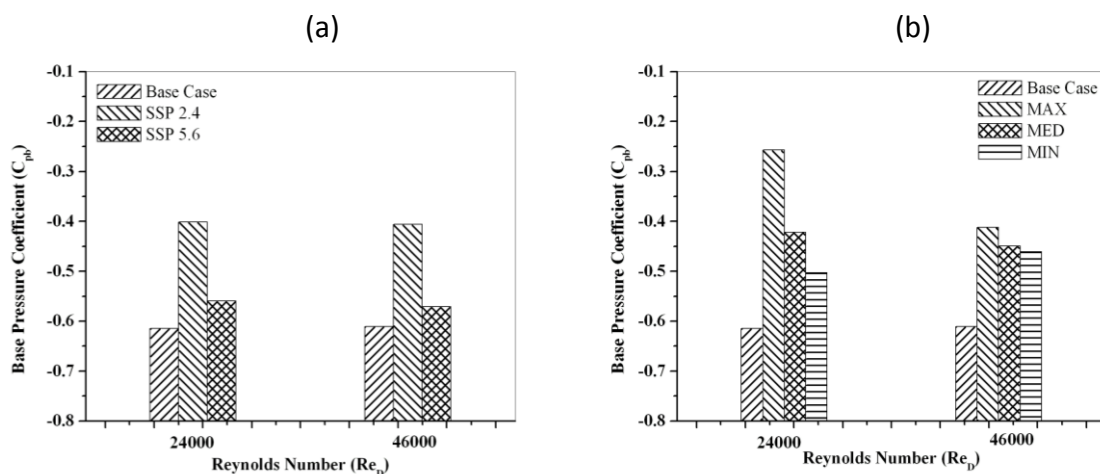


Figure 4-2. Comparison of base pressure coefficient for (a) straight and SSP ($\lambda_z/D = 2.4$ and 5.6) trailing edges, and (b) straight and SSP ($\lambda_z/D = 2.4$) trailing edges

maximum base drag reduction is dependent on the geometric shape and aspect ratio of the wake generator. To gain an understanding of the wake dynamic resulting from the trailing edge SSP, the analysis was further pursued only for $\lambda_z/D = 2.4$.

Figure 4-2 (b) shows the variation of base pressure coefficient at different spanwise locations corresponding to MAX, MED and MIN locations on the SSP ($\lambda_z/D = 2.4$). The maximum base pressure recovery is obtained at the MAX location, and less pressure is recovered at the MIN location. A similar trend is observed at Re_D of 46000. A possible reason for this variation in the base drag at different location of the SSP is provided in Section 4.2.2.

To estimate the base drag on the blunt trailing-edge body in the low Reynolds number water tunnel measurements, where base pressure was not directly measured, the method developed by van Oudhuesden et al. (2007) is used. The aerodynamics forces are estimated based on the velocity field data obtained from the PIV measurements:

$$\bar{F}_i = -\rho \iint_s \bar{u}_i \bar{u}_j n_j ds - \rho \iint_s \overline{u'_i u'_j} n_j ds - \iint_s \bar{p} n_i ds + \mu \iint_s \left(\frac{\partial \bar{u}_i}{\partial x_j} + \frac{\partial \bar{u}_j}{\partial x_i} \right) n_j ds \quad (4.2)$$

The first two terms in equation 4.2 represent the mean and fluctuating momentum transfers through the control volume surrounding the body, and can be calculated directly using the profiles of mean and fluctuating velocities. The third term represents the effect of pressure field at the boundaries of the control volume, and the last term represents the mean viscous term. van Oudhuesden et al. (2007) showed that the last term has negligible effect on the aerodynamic forces of the bluff body, unless the boundaries of the control volume are very close to the body.

When the boundaries of the control volume over which equation 4.2 is integrated are chosen far enough from the body, the effect of the pressure term also diminishes because the pressure recovers to the free stream level far downstream of the body. In the current study, the effect of the pressure term can be neglected, as the velocity profile converges to a constant profile at different downstream locations. To verify this convergence, profiles of mean streamwise velocity at different downstream locations are

compared in Figure 4-3 for $Re_D = 550$, which has the largest formation region among the three different Reynolds numbers investigated in water tunnel measurements. Figure 4-3 indicates very little difference between the streamwise velocity profile at $X/D = 12.5$ and $X/D = 13.5$, indicating that velocity profiles converge with downstream location. These results provide further agreement with hotwire measurements in the wake of the blunt

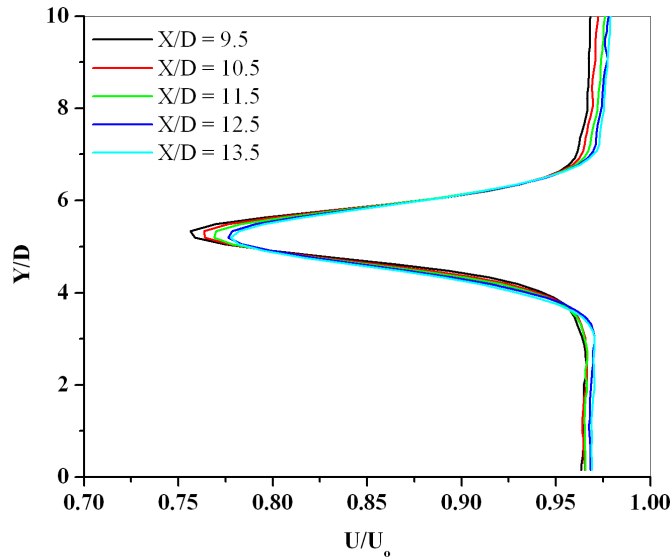


Figure 4-3. Comparison of the mean streamwise velocity profiles at various downstream locations for $Re_D = 550$

trailing-edge flat plate by Eisenlohr and Eckelmann (1988), who showed a constant velocity profile from $X/D = 6$ to $X/D = 20$ at $Re_D = 1400$.

Based on the above assumptions, equation 4.2 can be rewritten as

$$C_D \approx \frac{2}{A_w} \int \frac{\bar{u}}{U_o} \left(1 - \frac{\bar{u}}{U_o} \right) dy + \frac{2}{A_w} \int \left(\frac{u_{r.m.s}}{U_o} \right)^2 dy \quad (4.3)$$

The first term in equation 4.3 represents the mean component of the drag coefficient and the second component represents the fluctuating component of the drag coefficient.

Figure 4-4 shows the variation in the drag coefficients for the base case and the SSP control case at different Reynolds numbers of $Re_D = 550$, 1550 and 2300, indicating that the variation in the base drag reduction is similar to the trend observed for high

Reynolds number base pressure measurements. The reductions in the base drag for the SSP control case compared with the base case are 41%, 34% and 36% for $Re_D = 550$, 1550 and 2300, respectively. To better understand this variation in the base drag at various spanwise locations, we look at the mean velocity field in the shear layer and the variation in the mean centre line velocity.

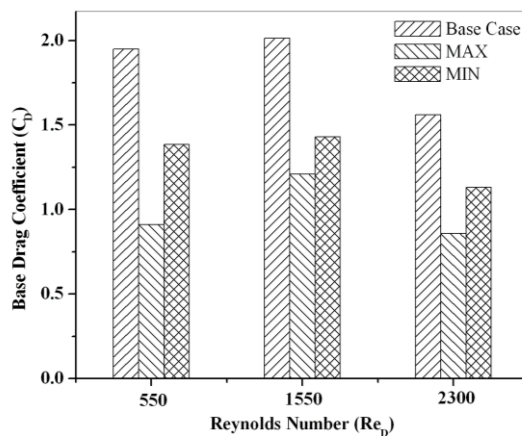


Figure 4-4. Comparison of base drag coefficient for straight and SSP ($\lambda_z/D = 2.4$) trailing edges at $Re_D = 550$, 1550 and 2300.

4.2.2 Mean Velocity

A possible reason for this variation in the base drag is due to the wavy pattern of the SSP, the amount of time that the fluid is in contact with the surface changes across span. The flow has a local maximum velocity at the MIN location, while exhibiting local minimum velocity at the MAX location. These results derive from the fact that the fluid at the MAX location is in contact with the flat plate for a longer time than at the MIN location, and hence, the effect of the boundary layer is visible in the immediate vicinity of the body. This effect can be also observed in the mean streamwise velocity contours (Figure 4-5) in the shear layer ($Y/D = -0.5$). It is observed that the velocity in the shear layer near the MAX location is less than at the MIN location in the near wake ($X/D < 1$).

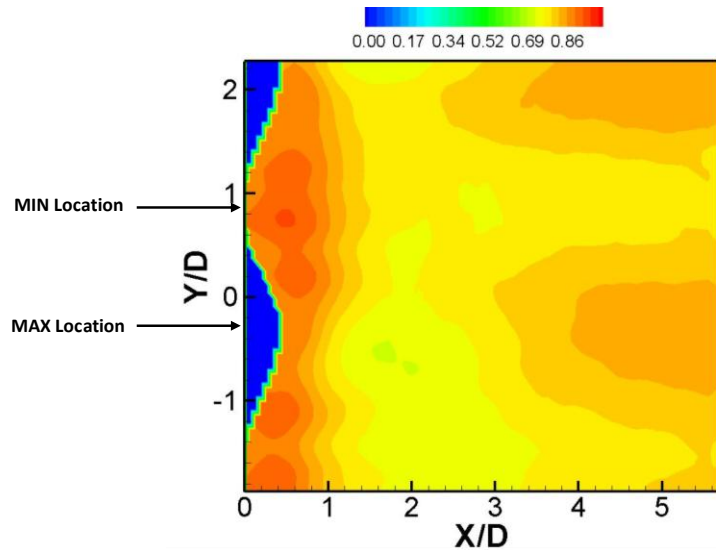


Figure 4-5. Streamwise mean velocity contour at $Y/D = -0.5$ for SSP ($\lambda_z/D = 2.4$) trailing edge at $Re_D = 24000$

However, the velocity at the downstream location shows a different trend; apparently, the velocity at the MAX location has recovered faster than that at the MIN location beyond $X/D > 3$. The possible reason for this change in trend is that the initial higher separation velocity at the MIN location pushes the higher velocity fluid in the spanwise direction in the immediate vicinity. On the other hand, the lower momentum fluid at MAX location has contracted, and the flow is accelerated at the downstream location. This effect is also observed in the recovery of the mean centerline velocity, as shown in Figure 4-6 for different Reynolds numbers. It is observed that the velocity recovers much faster at the MAX location than at the MIN location, supporting the primary argument. For $X/D < 2.0$ approximately, the velocity deficit is higher at the MAX location, but beyond $X/D > 2.0$, the velocity recovers faster at the MAX location than at the MIN location. This variation may be explained by the higher separation velocity at the MIN location than at the MAX location for the SSP. Similar observations were made by Lam et al. (2004) for a wavy circular cylinder. Note also that, as the Reynolds number increases, the difference in wake recovery at various spanwise locations becomes less pronounced. To gain a better understanding in the variation in the base drag, wake

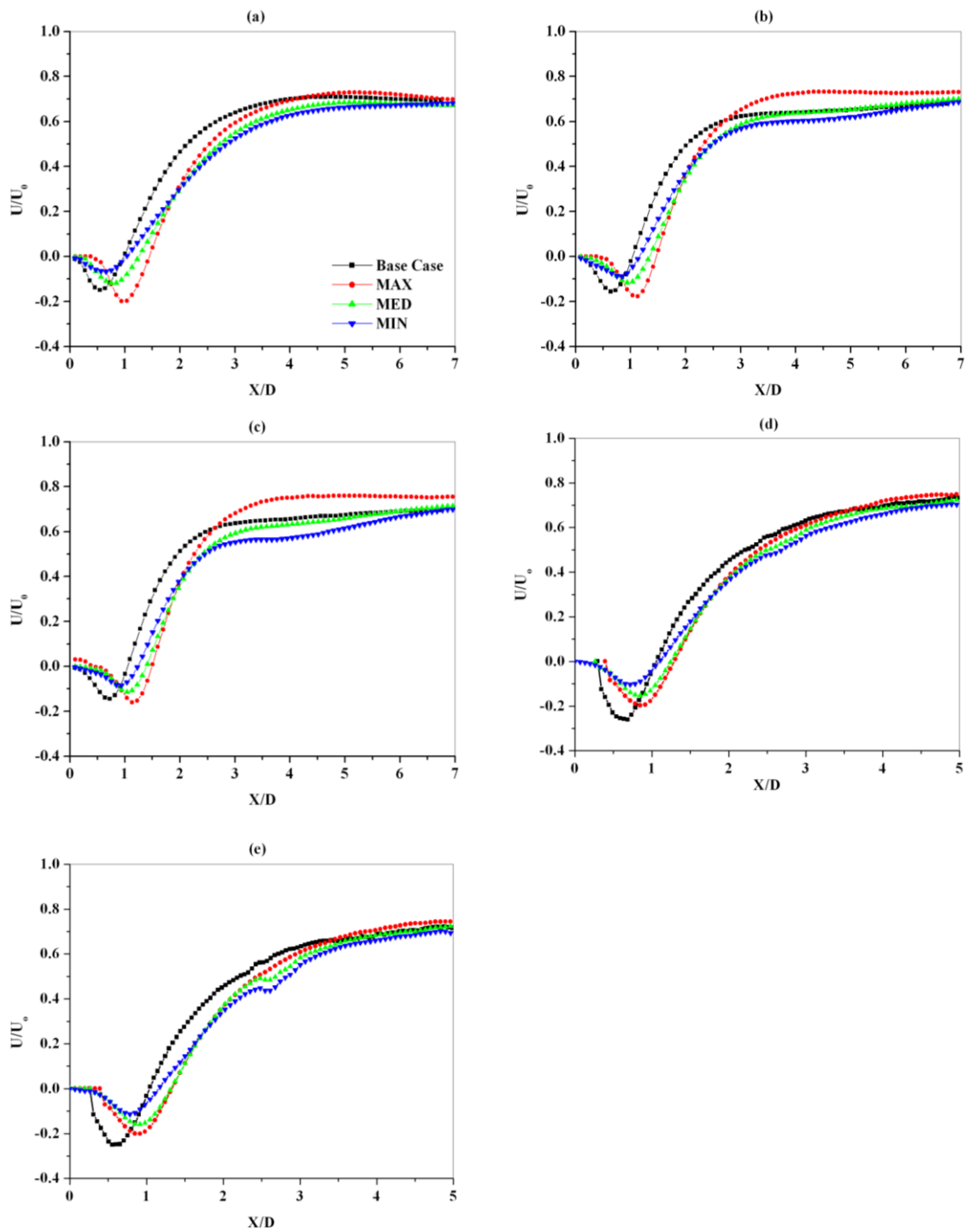


Figure 4-6. Comparison of mean streamwise centre line velocity for straight and SSP ($\lambda_z/D = 2.4$) trailing edges at (a) $Re_D = 550$, (b) $Re_D = 1550$, (c) $Re_D = 2300$, (d) $Re_D = 24000$ and (e) $Re_D = 46000$

formation length is calculated to understand the interaction of the SSP with the near wake.

4.2.3 Formation Length

The formation length can be defined as the location of the maximum wake velocity fluctuation at the wake centre line (Griffin 1995). The fluctuation velocity is estimated by using equation 2.9 for the low Reynolds number (water tunnel) measurements. However, in the case of high Reynolds number (wind tunnel) measurements, because of the lack of temporal resolution in the PIV measurements, equation 2.10 is used to estimate the fluctuation velocity by using the first 20 POD modes. Centre line turbulence intensity profiles for the base case is shown in Figure 2-19 and for SSP control case is shown in Figure 4-7 at different Reynolds numbers. Figure 4-7 (f) shows the formation lengths obtained by employing the procedure outlined above. Figure 4-8 shows the PIV measurement window which is used to obtain the velocity fields and the corresponding turbulent statistics. To measure the formation length at the MIN location, the amplitude of the SSP, W , is added to the length obtained for the peak in the fluctuation velocity at the MIN location.

Generally, an increase in the vortex formation length is linked to a reduction in base drag (Bearman 1965). This is attributed to the fact that an increase in vortex formation length (VFL) relates to an increase in the volume of fluid in the VFL and, therefore, entrainment of fluid into the forming vortices is unable to sustain low pressure. Further, if the base pressure increases, then the rate of shedding of the circulation from the body decreases, resulting in weaker vortices. This relation between base pressure and the formation length is observed in the present case (Figure 4-7 f). The formation length of the SSP control is elongated compared with the base case and, therefore, it weakens the vortex shedding process and, hence, yields lower the base drag. However, base pressure measurements and their corresponding formation lengths on the SSP contradict this trend. Similar observations were made by Tombazis and Bearman (1997), Lam et al. (2004) and Lee and Nguyen (2007). Tombazis and Bearman (1997) explained this relation

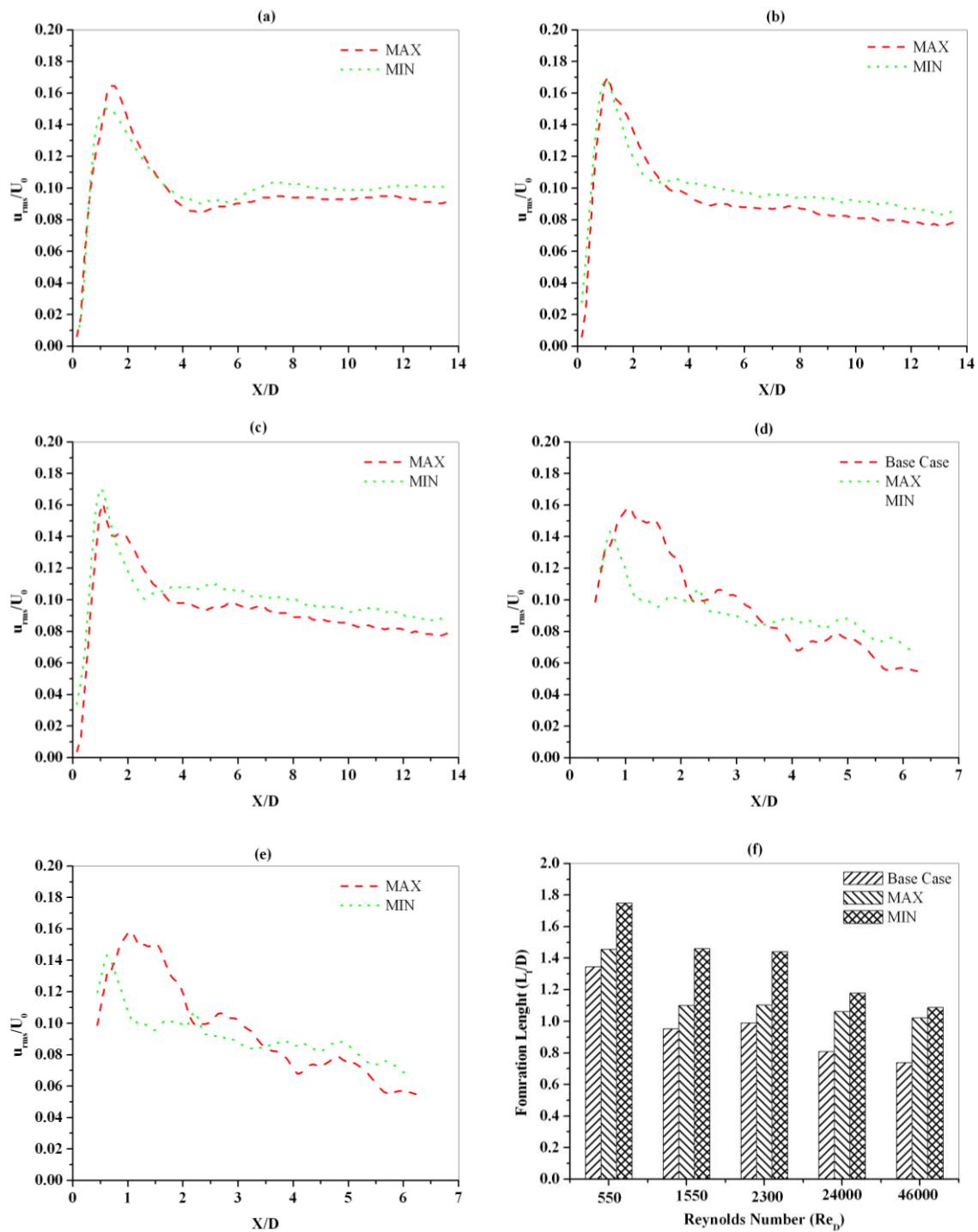


Figure 4-7. Comparing streamwise turbulence intensity profiles at mid-plane for base case and SSP ($\lambda_z/D = 2.4$) control case at (a) $Re_D = 550$, (b) $Re_D = 1550$, (c) $Re_D = 2300$, (d) $Re_D = 24000$ and (e) $Re_D = 46000$. (f) Comparing formation lengths for base case and SSP ($\lambda_z/D = 2.4$) control case at different Reynolds numbers

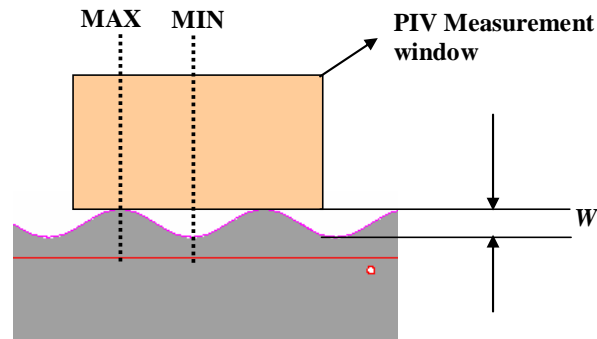


Figure 4-8. Schematic of the PIV measurement window in the horizontal (XZ) plane

between the formation length and the base drag as follows: In the case of SSP, which is three-dimensional along the span, assuming that the total circulation flux in the vortices does not vary along the span, the higher rate of circulation sheds at the trailing edge where higher separation velocity occurs, resulting in higher base drag. This finding is in line with observation higher separation velocity (Figure 4-5) at the MIN location compared with the MAX location of the SSP trailing edge. The peak vorticity for the base case and the control case is further calculated using equation 3.10. Figure 4-9 shows the streakline plots along with vorticity contours in the vertical plane at different phases of the vortex shedding for base case, MAX and MIN for SSP control locations at $Re_D = 24000$. The phase-averaged streakline plots represent the mean velocity field as it would appear to an observer moving downstream at a convective velocity of approximately $0.87U_\infty$ (Zhou and Antonia, 1992). For the base case, the vortices exhibit considerable transverse oscillations, whereas for the control case, the amplitude of these transverse oscillations diminishes. The vorticity contours indicate that the peak vorticity is reduced for the control case, implying a reduction in the strength of von-Karman vortices and, hence, less drag. Figure 4-10 shows that the maximum vorticity values for the SSP control are smaller than those for the base case, also indicative of lower base drag for the control case. Note that the vorticity at MAX location is higher than that at the MIN location. This supports the earlier statement that larger formation length at the MIN location results in weaker vortices.

An interesting analogy can be made between the current SSP configurations and that of the bluff body with splitter plate. In both cases, the base drag decreases because the wake formation length increases as the interaction length between the shear layer vortices increases compared with their respective base cases. The advantage of the SSP

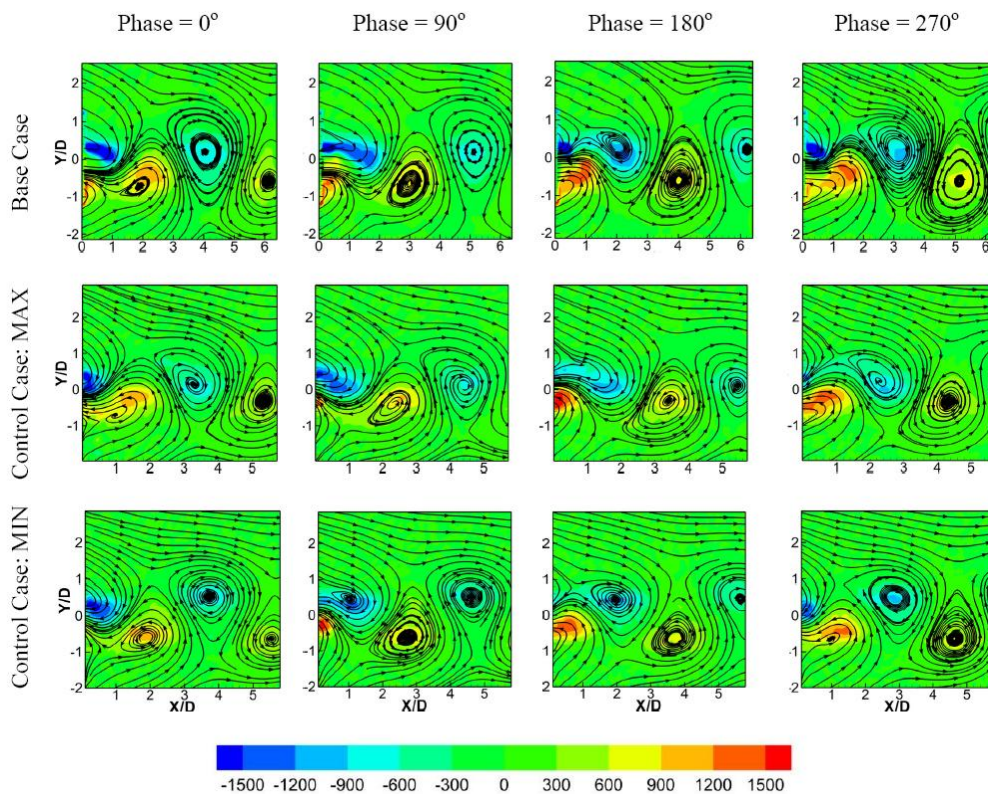


Figure 4-9. Streakline plots at different phases of vortex shedding in XY for base case and SSP ($\lambda_z/D = 2.4$) control case at $Re_D = 24000$

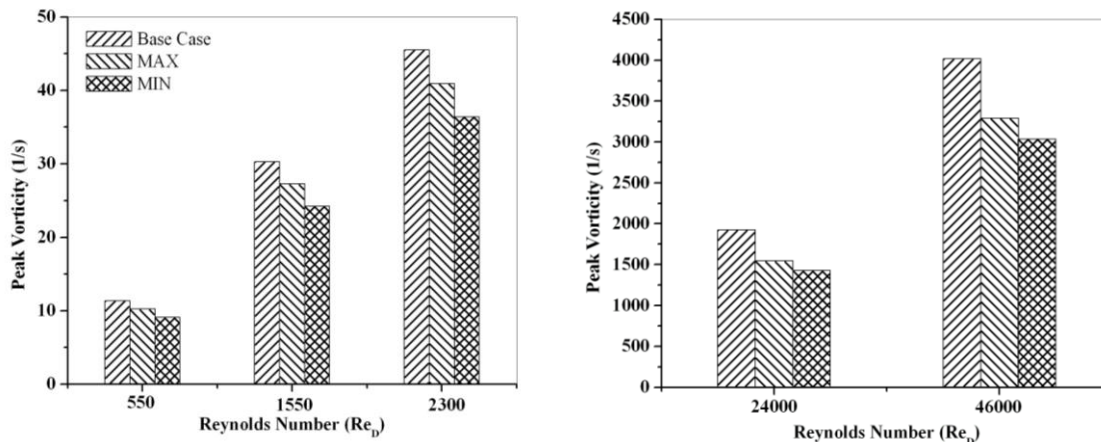


Figure 4-10. Comparison of peak vorticity variation for straight and SSP ($\lambda_z/D = 2.4$) trailing edges at different Reynolds numbers

is that, compared with the splitter plate, it does not add friction drag. In order to understand the changes in the dominant coherent structures of flow with and without SSP, further power spectrum is plotted and POD analysis is performed on the PIV data.

4.3 Turbulent Flow Analysis

4.3.1 Power Spectral Density

Figure 4-11 shows the frequency spectrum for (a) base case and (b, c, d) control cases at (I) $Re_D = 550$, (II) $Re_D = 1550$, (III) $Re_D = 2300$, (IV) $Re_D = 24000$ and (V) $Re_D = 46000$. For the low Reynolds number water tunnel measurements, the frequency spectrum is computed based on the velocity signal at $X/D = 2$ and $Y/D = 2$. For the high Reynolds number wind tunnel measurements, the PSD is computed based on the base pressure recorder using the high-speed pressure transducers. The results indicate that the primary shedding peak has decreased in strength for the control cases compared with the base case, indicating that the strength of the vortex shedding is reduced when the wavy trailing edge is used. The pronounced reduction in the strength is attributed to

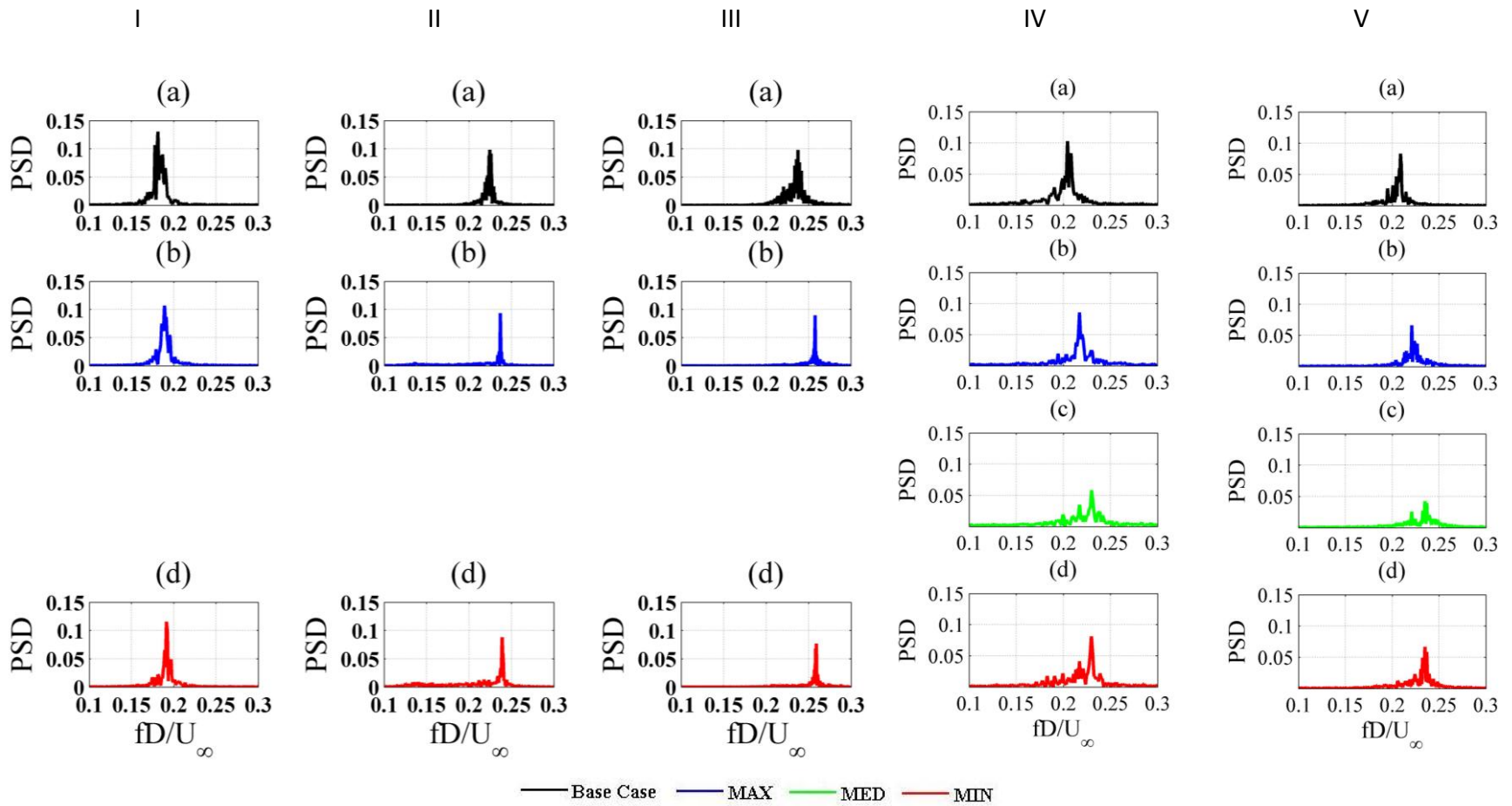


Figure 4-11. Comparison of power spectral density for straight and SSP ($\lambda_z/D = 2.4$) trailing edges for (a) base case (b) MAX (c) MED (d) MIN at (I) $Re_D = 550$, (II) $Re_D = 1550$, (III) $Re_D = 2300$, (IV) $Re_D = 24000$ and (V) $Re_D = 46000$

Re_D		550	1550	2300	24000	46000
Strouhal number	Base Case	0.181	0.224	0.242	0.204	0.208
	MAX	0.189	0.237	0.257	0.217	0.221
	MIN	0.191	0.239	0.258	0.229	0.235

Table 4.3 Comparison of Strouhal number for straight and SSP ($\lambda_z/D = 2.4$) trailing edges at $Re_D = 550, 1550, 2300, 24000$ and 46000 .

enhancement of the three-dimensional nature of the separated shear layer originating from the trailing edge, making them less susceptible to rolling up into organized two-dimensional vortices (Tombazis and Bearman 1997). Note the presence of two shedding frequencies corresponding to Strouhal numbers of $St = 0.217$ and $St = 0.229$ for the control case compared with only one ($St = 0.204$) for the base case at $Re_D = 24000$. Similar types of observations are made at other Reynolds numbers, as summarized in Table 4.3. Tombazis and Bearman (1997), termed the dual frequency in the near wake as ‘beat’ phenomenon, and attributed it to three-dimensionality due to SSP. At the MAX location, the lower of the two frequencies is stronger, but as we move towards the MIN location, the higher frequency component becomes increasingly strong and the lower frequency component becomes negligible. At the MED location, both the frequencies from the high Reynolds number measurements are prominent (Figure 4-11 IV and V).

4.3.2 POD Modes and Coefficients

Figure 4-12 shows the first five velocity POD modes, and Figure 4-13 (b, c) shows the phase averaged time-varying coefficients for the control case at locations MAX and MIN, respectively. For the POD modes of the straight trailing edge, refer to Section 3.3.1. As interpreted in Section 3.3.1, modes 1 and 2 represent the dominant von-Karman Benard rolls at both MAX and MIN locations. Mode 3 at MAX and MIN appears to be a standing mode, similar to the straight trailing edge (base case). If this mode relates to

the boundary layer development (as inferred already), little change in the development of the boundary layer with and without SSP is expected. Modes 4 and 5 appear to be severely distorted at the MAX location, and these modes are likely related to the ‘beat’ phenomenon occurring in the flow due to the SSP. In contrast, modes 4 and 5 at the MIN location appear to represent the higher harmonic structure of the von-Karman rolls (Figure 4-12 (b) and Figure 4-13 (b)). This finding indicates that ‘beat’ phenomena is more prominent at MAX location compared to the MIN location, in agreement with the observation made by Tombazis and Bearman (1997). Figure 4-13 (a) indicates that modes 6 and 7 at the MAX location represent the higher harmonic of the dominant coherent rolls.

Similar types of observation are made at low Reynolds numbers. Figure 4-14 and Figure 4-15 show the streamwise and transverse velocity components of the first nine POD modes at MAX and MIN locations for $Re_D = 550$. For the straight trailing edge (refer to Section 3.2.1), where modes 1 and 2 relate to the dominant coherent structure of the flow, modes 6 and 7 relate to the first harmonic, and modes 8 and 9 relate to the second harmonic of the dominant coherent structure. Looking at the POD modes at the MAX location of the SSP (Figure 4-14) at $Re_D = 550$, we observe that modes 6 and 7 relate to the ‘beat’ phenomenon in the flow, and modes 8 and 9 relate to the first harmonic structure of the dominant coherent structure in the flow, indicating a shift in the POD modes similar to that observed at high Reynolds numbers. POD modes at the MIN location of the SSP (Figure 4-15) indicate that modes 6 and 7 relate to the first harmonic of the dominant coherent structure, and modes 8 and 9 relate to the ‘beat’ phenomenon in the flow. This finding is in line with the observation at high Reynolds numbers – that ‘beat’ phenomena due to dual frequency of the dominant coherent structure is more prominent at MAX location compared to MIN location. Similar observations are made at other Reynolds numbers.

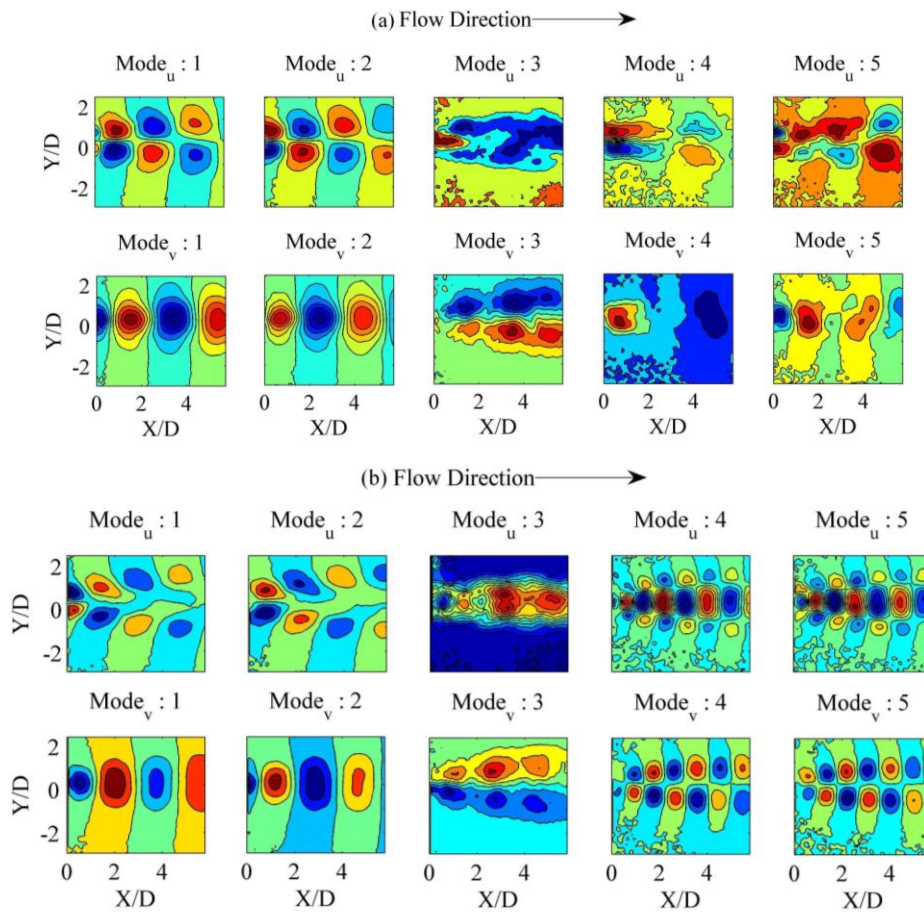


Figure 4-12. Streamwise and transverse velocity components for the first five POD modes in XY plane for SSP ($\lambda_z/D = 2.4$) control case at (a) MAX and (b) MIN locations for $Re_D = 24000$

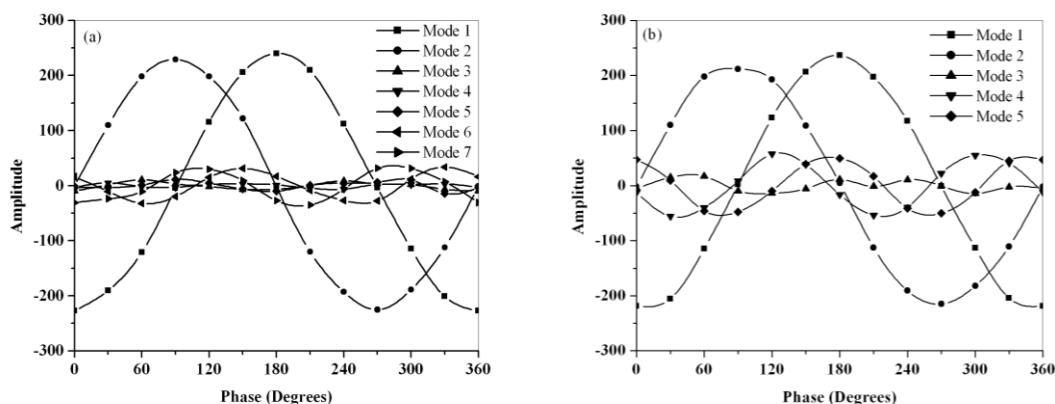


Figure 4-13. Phase averaged time varying coefficient in XY plane for (a) SSP 2.4: MAX and (b) SSP 2.4: MIN locations at $Re_D = 24000$

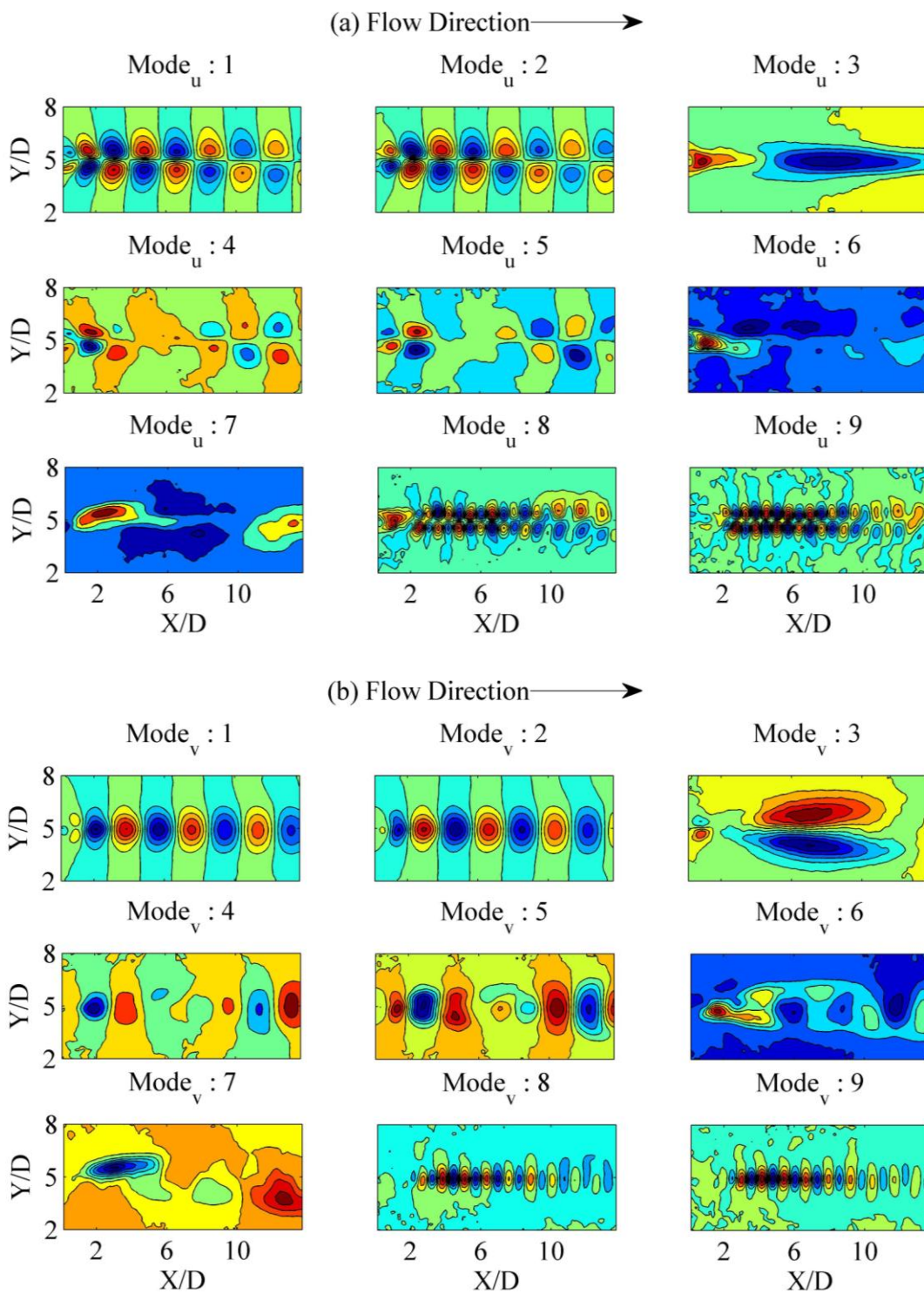


Figure 4-14. Streamwise and transverse velocity components for the first nine POD modes in XY plane for SSP ($\lambda_z/D = 2.4$) control case at MAX location for $Re_D = 550$

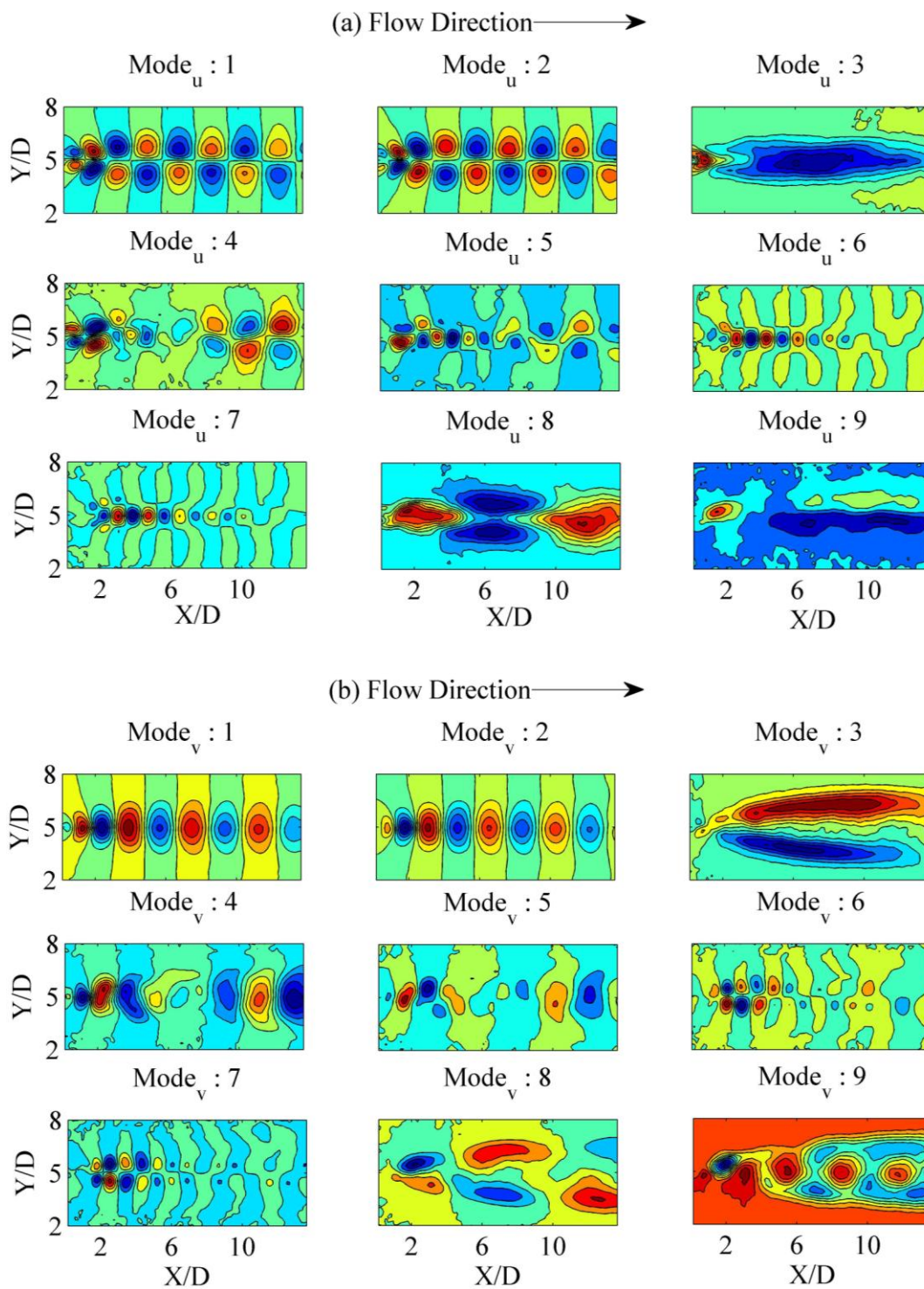


Figure 4-15. Streamwise and transverse velocity components for the first nine POD modes in XY plane for SSP ($\lambda_c/D = 2.4$) control case at MIN location for $Re_D = 550$

It can therefore be concluded that the control distorts the dominant coherent structure of the flow by reducing their relative energy. Further insight on the issue can be gained by examining the wake formation lengths and redistribution of relative energies among the different POD modes.

4.3.3 Wake Topology

Figure 4-16 shows the spanwise velocity contours in the horizontal mid-plane at $Y/D = 0$, captures the streamwise vortices piercing through the horizontal plane. As in Figure 4-9, the plots are shown at different phases of the vortex shedding for base case and SSP control case at $Re_D = 24000$. As stated earlier, the phase averaging in the horizontal (XZ) plane washes out the features of the secondary vortices. However, to understand the dynamic nature of the streamwise vortices, phase averaging is attempted here. Phase is estimated from the reference pressure signal sampled with high temporal resolution. For the base case, the spanwise velocity is reconstructed using equation 2.1 by combining the first 10 modes. It is difficult to identify coherent secondary structures in the base case because of low relative energy of the streamwise vortices and also masked due to phase averaging at some instances of phase. El Akoury et al. (2008) indicated that they had to use about 19 modes in order to capture the spanwise undulation due to streamwise vortices. On closer inspection, we observe that the streamwise structure is very unsteady and is varying both in time and in space. The spanwise spacing varies approximately in the range $1.2 \leq \lambda_z/D \leq 2.4$. When the SSP is applied, the streamwise vortices lock into fixed spanwise positions (Figure 4-16 b) corresponding to the SSP undulations.

Figure 4-17 shows the relative energy captured by the first 10 POD modes in the vertical plane for the base case compared with the control case at different Reynolds numbers. Approximately 60-80% of the total energy is carried by the first two modes, which represent the Karman vortices. However, several modes are involved in the horizontal plane (Figure 4-18), suggesting a more even energy distribution between the spanwise and streamwise structures. When the control is applied, the modes in the

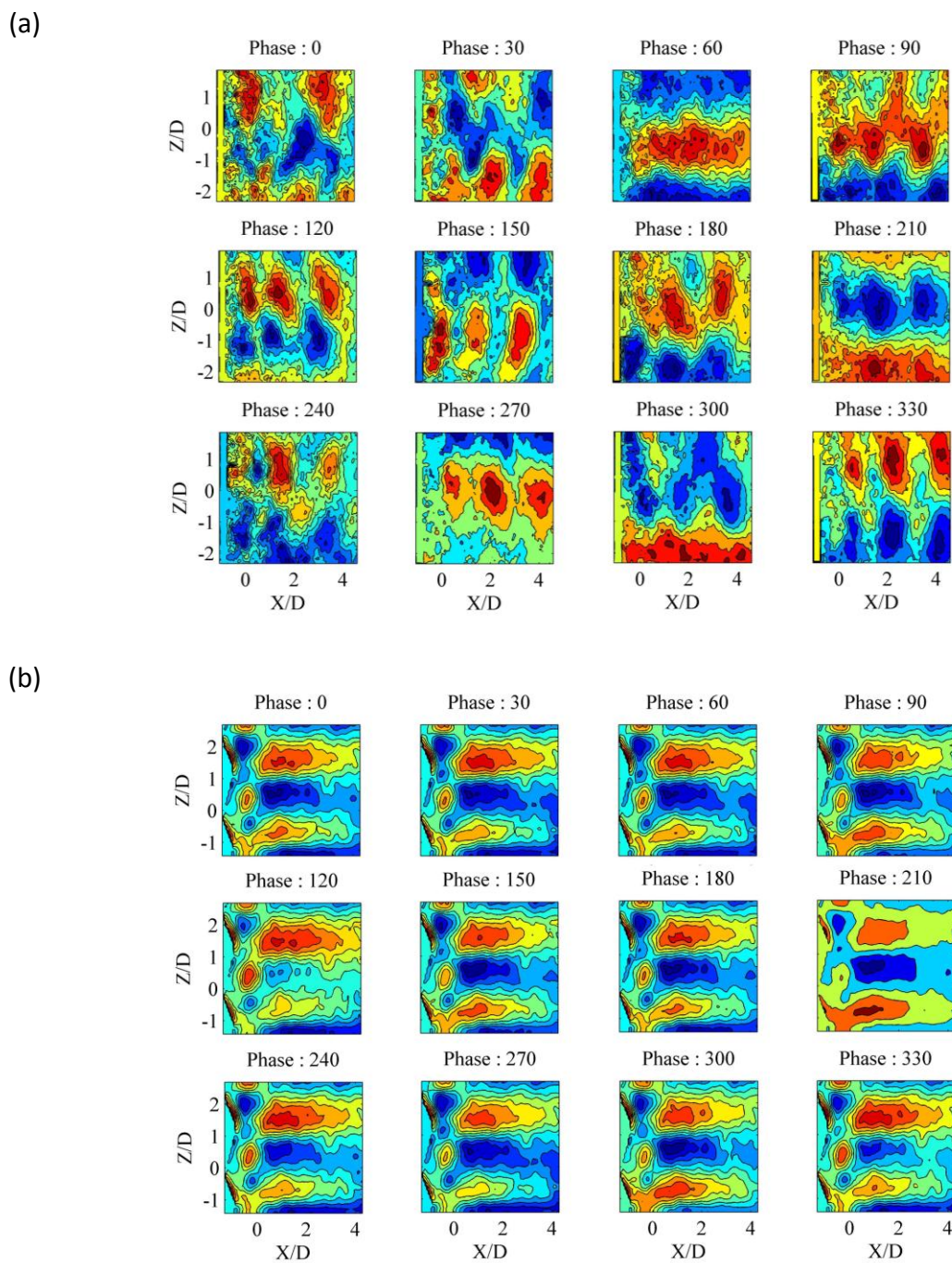


Figure 4-16. Phase averaged spanwise velocity component in XZ plane ($Y/D = 0$) for (a) Base case: Reconstructed using first 10 modes and (b) SSP ($\lambda_z/D = 2.4$): Reconstructed using first two modes

horizontal plane show an increase in relative energy compared with the base case, suggesting the formation of a more organized flow structure due to the control. At the same time, in the vertical plane, which captures the spanwise vorticity, a decrease of relative energy in the first two modes compared with the base case is observed. This finding suggests that the SSP control strengthens the streamwise vorticity and weakens the spanwise vorticity. Note also that less relative energy is concentrated in the first two modes at the MIN location than at the MAX location, supporting our previous observation of there being less vorticity at the MIN location than at the MAX location.

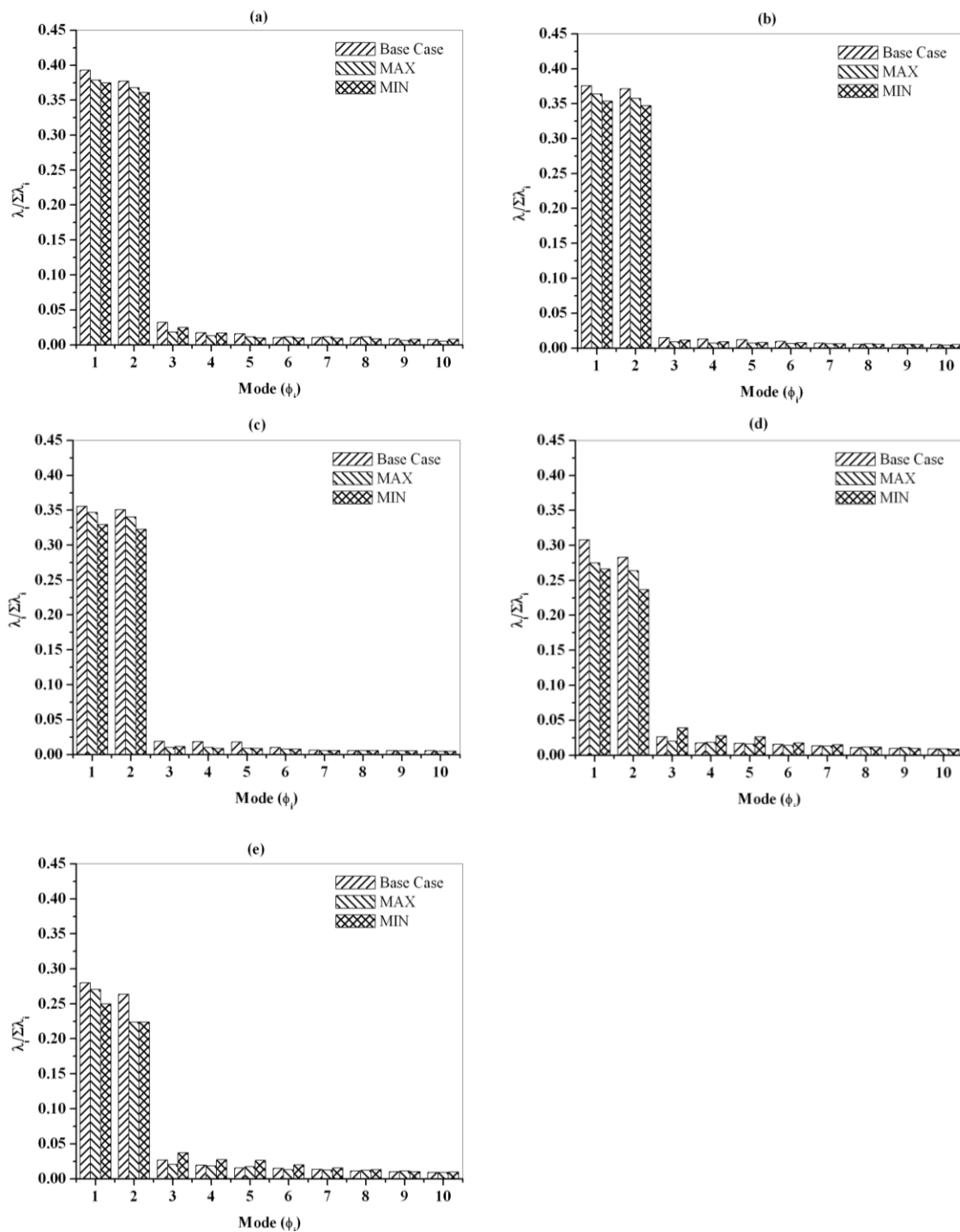


Figure 4-17. Comparison of relative energy for straight and SSP ($\lambda_z/D = 2.4$) trailing edges captured by first ten POD modes in XY plane at (a) $Re_D = 550$, (b) $Re_D = 1550$, (c) $Re_D = 2300$, (d) $Re_D = 24000$ and (e) $Re_D = 46000$.

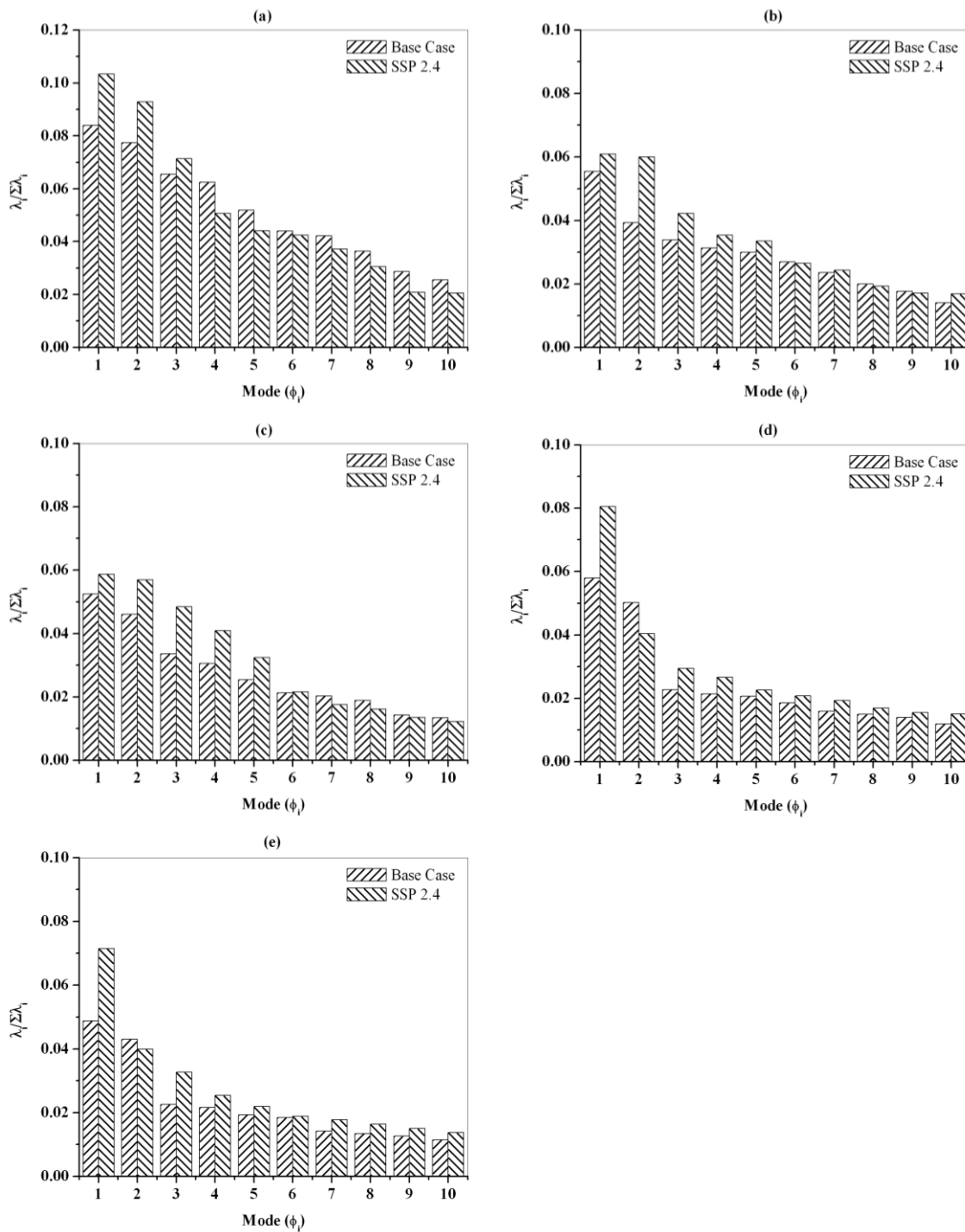


Figure 4-18. Comparison of relative energy for straight and SSP ($\lambda_2/D = 2.4$) trailing edges captured by first ten POD modes in XZ mid-plane ($Y/D = 0$) at (a) $Re_D = 550$, (b) $Re_D = 1550$, (c) $Re_D = 2300$, (d) $Re_D = 24000$ and (e) $Re_D = 46000$.

4.4 Summary

Results from the current experiments on the blunt trailing-edge-profiled body with trailing edge spanwise sinusoidal perturbation indicates that:

- The SSP control reduced base drag by decreasing the strength of vortex shedding.
- The SSP locks in the dislocations at a constant spanwise spacing, thereby reducing the unsteadiness in the flow.
- The SSP enhances the strength of streamwise vortices, which in turn reduces the strength of Karman vortices.

5 CONCLUSIONS AND RECOMMENDATIONS

Near wake dynamics of a blunt trailing-edge-profiled body was studied experimentally to determine the principal characteristics of the von Karman Benard vortices and the secondary streamwise vortices. Experiments were conducted in the low Reynolds number ($250 \leq Re_D \leq 2300$) wake transition regime, allowing the boundary layer to transition naturally, and in the high Reynolds number ($24000 \leq Re_D \leq 46000$) regime, tripping the boundary layer artificially using a sand strip to ensure that the boundary layer was turbulent. The resulting wake topology from these studies was used as a basis for implementing a passive three-dimensional flow control mechanism to mitigate the vortex shedding and collaterally reduce the drag force. The effectiveness of the proposed flow control mechanism was studied for Reynolds number ranging from $Re_D = 550$ to 46000.

The present study extends the range of Reynolds numbers at which the vortex street in the wake of the blunt trailing-edge-profiled body and its instabilities have been characterized. Moreover, the distinctive characteristics of the small-scale instabilities in the wake of the blunt trailing-edge-profiled body in the wake transition regime, which were predicted by Ryan et al. (2005), were demonstrated experimentally for the first time.

The process through which the flow control mechanism changes the aerodynamic forces and the flow structure in the wake was also described based on the extensive set of data acquired. The findings of the study in the area of flow control form a basis for the design and implementation of a control mechanism in real-life applications, such as blunt trailing edge airfoils used in wind turbine blades.

An overview of the research conducted and a summary of the specific findings will be presented in the following sections. Based on the findings reported in this thesis, recommendations regarding future research direction are made at the end of this chapter.

5.1 Near Wake Structure of a Blunt Trailing-Edge-Profiled Body

PLIF and PIV experiments were conducted for a range of Reynolds numbers ($Re_D = 250$ to 2300), and showed the transition of secondary wake instabilities in the near wake of a profiled leading edge and blunt trailing edge flat plate body. Further, the study was extended to high Reynolds numbers ($Re_D = 24000$ and 46000) to establish the dominant secondary wake instability. It is found that for this geometry, the sequence of transition modes is different from that observed in circular cylinder flows. Specifically, mode-B transitions occur first followed by mode-A transitions, supporting the results of Ryan et al. (2005). The spanwise wavelength for mode-A and mode-C are also in line with the observations made by Ryan et al. (2005); however, a different wavelength for mode-B is observed in the current study. The wavelengths of mode-B and mode-C observed in our study are typical wake three-dimensional arrangements observed in other studies (Williamson 1996; Robichaux et al. 1999; Sheard et al. 2005; Sheard et al. 2009); nevertheless, the transition Reynolds numbers are higher than those for circular cylinder flows, in agreement with Ryan et al.'s (2005) results.

POD analysis reveals a relation between POD modes and vortex structure, reconfirming the observation from PLIF experiments. Previous studies identified the spacing of the streamwise vortices at relatively low Reynolds numbers. Either mode A or mode B topology was observed to dominate depending on the flow Reynolds numbers, aspect ratios, and shapes of the wake generators, with a constant spanwise spacing. However, at the higher Reynolds numbers studied here, the spanwise spacing (λ_z/D) of the streamwise vortices vary both in space and time. The spacing ratio of the dominant wake instability is found to vary between $1.2 \leq \lambda_z/D \leq 2.8$. Mode-A appears to be the only mode responsible for von-Karman vortex dislocation. The three-dimensional wake through transition and turbulent regimes shows that the spanwise wavelength of the streamwise vortices is weakly dependent on Reynolds number, suggesting robustness of the flow structure with implications for control methodology. The data lead to the conclusion that the sequence of transition to three-dimensionality observed in the

circular cylinder flows is not universal. Other instability modes play a role in the near wake development, and the route to turbulence for vortex street depends on the geometric shape of the body.

5.2 Near Wake Dynamics Resulting From Trailing Edge Spanwise

Sinusoidal Perturbation (SSP)

A passive flow control mechanism has been implemented and evaluated based on the near wake topology findings. The design of the proposed passive flow control mechanism is based on Spanwise Sinusoidal Perturbation (SSP) with an average wavelength that matches the wavelength of the dominant secondary wake instability. The effect of the flow control mechanism on drag and wake flow structure of the blunt trailing-edge-profiled body was studied experimentally with a spanwise spacing and wave steepness of $\lambda_z/D = 2.4$, $W/\lambda_z = 0.197$, and $\lambda_z/D = 5.6$, $W/\lambda_z = 0.09$ for high Reynolds numbers of $Re_D = 24000$ and 46000 . Given the fact that maximum base pressure recovery was achieved for $\lambda_z/D = 2.4$, $W/\lambda_z = 0.197$, further analysis was pursued only for this wavelength so as to understand the resulting wake dynamics at various Reynolds numbers ($550 \leq Re_D \leq 2300$).

The process by which the flow control mechanism generates changes in drag was investigated by studying the effect of the flow control on the wake flow structures through the analysis of several parameters, including the wake formation length, frequency spectrum, peak vorticity, and POD mode energy content in multiple spanwise locations and Reynolds numbers.

Results indicate that the drag force is altered by the flow control mechanism due to interaction between the flow control and the secondary wake instabilities. The dislocations in the spanwise vortices are locked in at the SSP spanwise spacing, conforming to the idea of Tombazis and Bearman (1997). SSP enhanced the strength of streamwise vortices, which in turn reduced the strength of Karman vortices. The ratio λ_z/λ_x for the control ($\lambda_z/D = 2.4$) is in the range of 0.5 to 0.66 for the Reynolds number

investigated, which is close to the most amplified wavelength of the mixing layer of 0.67 (Bernal and Roshko 1986; Rogers and Moser 1993). This is one possible reason why the SSP control was successful. We conclude from this that perturbing the near wake flow with the spacing of streamwise vortices can result in maximum base drag reduction due to suppression of vortex shedding.

5.3 Recommendations for Future Work

Given the findings of this research, and given that the main goal of the work was to develop a robust wake control methodology based on the spacing of the natural instabilities of the near wake, the following recommendations are made for future work:

5.3.1 Near Wake Instabilities

To develop a robust SSP flow control mechanism, the spanwise spacing of these instabilities should be established in line with the normalization procedure proposed by Dobre et al. (2006) for different wake generators (Equation 1.1). This work can be achieved by the following methods.

- Sensitivity of the streamwise secondary wake instabilities should be tested for various inflow conditions. In the current study, we established that the effect of the type of boundary layer (naturally transitioning or artificially forced) on the development of the near wake instabilities is not of a major concern. Irrespective of the different inflow conditions of the two facilities used in the current study, the streamwise instabilities demonstrate considerable robustness in the spanwise spacing. However, a rigorous evaluation of the inflow conditions can be achieved by testing different turbulence grids at the inlet to artificially force the turbulence intensity at the inlet.
- Sensitivity to inclinations of the wake generator is important in determining the spanwise spacing of the streamwise vortices, and also in identifying the dominant secondary wake instability governing the near wake development. Sheard (2007)

and Sheard et al. (2009) provided some perspective on the sensitivity of the wake generator inclination and the corresponding secondary wake bifurcations for elliptic cylinder and square cylinder, respectively. They spotlighted the importance of the wake generator inclination by demonstrating that the wake flow topology of the secondary streamwise vortices is different at zero angle of incidence than at other inclinations. Since the blunt trailing-edge-profiled body studied here might undergo changes in the angle of incidence in practical applications, it is essential to investigate its wake flow structure in the range of angles of incidence which it is likely to experience. This investigation would characterize the secondary wake instability modes with different vorticity structures and spanwise wavelengths that may become prominent at non-zero angles. Thus, such an investigation would improve the versatility of the flow control mechanism.

- Sensitivity to aspect ratios of the wake generator is another important parameter for consideration. We have already demonstrated that the order of transition of the secondary wake instabilities changes depending on the aspect ratio of the body. To further improve on this finding, experiments should be conducted to verify the findings of the numerical work of Ryan et al. (2005) for other aspect ratios of the blunt trailing-edge-profiled body. However, the same analysis can be extended to other wake generators in order to develop an understanding of the near wake dynamics, information that will facilitate the development of a universal wake control mechanism.
- Even though it appears that the boundary layer developing in our flow configuration does not affect the near wake development, the nature of this boundary layer has not been studied rigorously.

5.3.2 SSP Control

- Julien et al. (2003) found that perturbing the flow with spanwise spacing $0.5 \leq \lambda_z/\lambda_x \leq 1.14$ triggered the flow instabilities in the wake of a thin flat plate. However, they found that $\lambda_z/\lambda_x = 0.76$ perturbation grew much faster than for any other case.

Hence, in order to optimize the control, the sensitivity of the SSP wavelength needs to be determined so as to improve the effectiveness of the flow control.

- To assess the effective range of the flow control, measurements should be performed for different inclinations of the wake generator with SSP.

5.3.3 Future Direction

In order to develop a universal flow control mechanism, as envisioned by the concept of triggering the secondary wake instabilities to achieve a reduction in the dynamics forces, future focus should be on developing an active flow control mechanism. This objective can be achieved by dynamically tracking the unsteady streamwise vortices and triggering them through an intelligent actuation mechanism.

The dynamical tracking can be achieved through linking the instantaneous location of the streamwise vortices by measuring flow variables and establishing the relationship between both through a possible low-dimensional model. Possible flow variables for achieving such a tracking are pressure and shear stresses on the surface of the body which can be measured with high temporal and spatial resolution. The actuation mechanism can be a series of injection ports controlled through an artificial neural network system, to trigger exactly these streamwise vortices.

Development of such a flow control mechanism would pave the way for introducing such technology in the practical development of wind turbines and flying machines, and eventually lead to more efficient machines.

APPENDIX

A.1 PIV Measurement Error Analysis

The method of Siddiqui (2002) is used here to estimate the error in the PIV measurements. This error is a cumulative sum of errors due to (a) velocity gradients, (b) particle density, (c) particle diameter, (d) out-of-plane motion, (e) peak locking, and (f) interpolation (Cowen and Monismith 1997). The error due to these parameters is calculated as described in the following paragraphs; all the values reported in the discussion are for XY plane measurements in wind tunnel measurements at a free stream velocity of 20m/s.

Velocity Gradient: The mean velocity gradients in the streamwise and transverse direction are computed for the PIV data. The maximum velocity gradients are found to be 0.12%, based on the maximum streamwise velocity gradient. The error due to velocity gradient was estimated from Figure 5(e) in Cowen and Monismith (1997). The figure estimates the error in velocity gradient based on a particle size of 2 pixels; the error was found to be 0.025 pixels.

Particle diameter: The particle diameter in our wind tunnel measurements was 0.00859 pixels. Figure 5(a) in Cowen and Monismith (1997) estimates error due to different particle diameters. However, the data from Cowen and Monismith (1997) can only estimate error for a smallest particle size of 1 pixel. To estimate the error due to particle sizes smaller than 1 pixel, data from Figure 13 of Prasad et al. (1992) were used; they present the variation in the bias (peak locking) and random (RMS) errors as a function of particle diameter. From the figure, the error with a particle size of 0.00859 pixels was estimated to be 40% larger than the error with particle diameter of 1 pixel. The error is estimated to be 0.084 pixels.

Out of plane motion: The mean particle displacement in the vertical plane was estimated to be 3.822 pixels, which is equivalent to 0.44 mm. The out of plane motion was assumed to be less than the vertical displacement. The thickness of the laser was

approximately 1 mm, which was less than the out of plane motion; hence, this error was neglected in the current analysis.

Peak locking: Peak locking refers to shifting of the correlation peak towards the nearest integer value. The error due to peak locking can be reduced by using an appropriate fitting scheme. Cowen and Monismith (1997) and Siddiqui (2002) showed that a three-point Gaussian estimator reduced peak locking, which was used for estimating the correlation peak in the current PIV software.

Interpolation: Interpolating random velocity vectors onto a uniform grid is required to calculate the turbulent statistics. The error due to interpolation was estimated from Figure 5(f) of Cowen and Monismith (1997) to be 0.08 pixels.

The total error in the streamwise velocity in the PIV measurement was estimated to be $0.084+0.08 = 0.164$ pixels, which is equivalent to 0.47 m/s. The error in the mean velocity measurements was 2.35%. Table A-1 and Table A-2 summarizes the error in PIV measurements at different velocities in water and wind tunnel measurements in both vertical (XY) and horizontal (XZ) planes.

	XY Plane				XZ plane			
Mean Velocity(m/s)	0.05	0.095	0.144	0.2	0.05	0.095	0.144	0.2
dt (s)	10e-3	9e-3	5.5e-3	3.7e-3	6e-3	4.8e-3	3.5e-3	2.3e-3
Mean streamwise velocity gradient	2.1e-4	2.3e-4	2.25e-4	2.2e-4	2.5e-5	4.3e-5	2e-5	1.1e-5
Mean transverse velocity gradient	2.1e-5	1.7e-5	1.65e-5	7e-6	1.9e-5	1.9e-5	1.9e-5	6e-6
Calibration coefficients (m/pixel)	1.1484e-4	1.1484e-4	1.1484e-4	1.1484e-4	7.2365e-5	7.2365e-5	7.2365e-5	7.2365e-5
Error (mean + rms) due to mean velocity gradient (pixels)	0.025	0.03	0.03	0.03	0.02	0.02	0.02	0.02
Particle diameter (pixels)	0.0175	0.0175	0.0175	0.0175	0.029	0.029	0.029	0.029
Error (mean + rms) due to particle diameter (pixels)	0.084	0.084	0.084	0.084	0.084	0.084	0.084	0.084
In plane vertical displacement (pixels)	0.601	0.6332	0.6332	0.6001	4.5147	5.4551	6.3537	6.4317
Error due to interpolation (pixels)	0.08	0.08	0.08	0.08	0.08	0.08	0.08	0.08
Total error (pixels)	0.164	0.164	0.164	0.164	0.164	0.164	0.164	0.164
% error in velocity measurement	3.8	2.2	2.3	2.5	3.9	2.6	2.3	2.6

Table A-1. PIV measurement error for low Reynolds numbers ($550 \leq Re_D \leq 2300$) in both vertical (XY) and horizontal (XZ) planes

	XY Plane		XZ Plane	
Mean Velocity(m/s)	20	40	20	40
dt (s)	40e-6	30e-6	30e-6	20e-6
Mean streamwise velocity gradient	0.0012	0.0013	0.0026	0.0035
Mean transverse velocity gradient	6.1e-4	5.9e-4	3.9e-5	8.1e-5
Calibration coefficients (m/pixel)	1.1629e-4	1.1629e-4	1.0404e-4	1.0404e-4
Error (mean + rms) due to mean velocity gradient (pixels)	0.025	0.025	0.03	0.03
Particle diameter (pixels)	0.00859	0.00859	0.0096	0.0096
Error (mean + rms) due to particle diameter (pixels)	0.084	0.084	0.084	0.084
In plane vertical displacement (pixels)	3.822	7.5896	2.6023	5.2284
Error due to interpolation	0.08	0.08	0.08	0.08
Total error (pixels)	0.164	0.164	0.164	0.164
% error in velocity measurement	2.4	1.6	2.8	2.1

Table A-2. PIV measurement error for high Reynolds numbers ($24000 \leq Re_D \leq 46000$) in both vertical (XY) and horizontal (XZ) planes

A.2 POD Formulation

The POD formulation is taken from Smith et al. (2005). The equation 2.3 can be rewritten by interchanging the sum and the integral as

$$\frac{1}{N} \sum_{k=1}^N u_k(\bar{x}, t) \int u_k^*(\bar{x}, t) \phi(\bar{x}) dx' = \lambda \phi(\bar{x}) \quad (\text{A.1})$$

For the method of snapshots, equation A.1 can be written as

$$\frac{1}{N} \sum_{j=1}^N a_j u_j(\bar{x}, t) = \lambda \phi(\bar{x}) \quad (\text{A.2})$$

where

$$a_i = \int u_i^*(\bar{x}', t) \phi(\bar{x}') dx' \quad (\text{A.3})$$

Multiplying equation A.2 on both sides by $u_i^*(\bar{x}, t)$ and integrating results into an eigenvalue problem in the following equation:

$$\frac{1}{N} \sum_{t=1}^N a_j \int u_i^*(\bar{x}, t) u_j(\bar{x}, t) dx = \lambda \int u_i^*(\bar{x}, t) \phi(\bar{x}) dx \quad (\text{A.4})$$

By defining c_{ij} as

$$c_{ij} = \frac{1}{N} \int_{\Omega} u_i^*(\bar{x}, t) u_j(\bar{x}, t) dx \quad (\text{A.5})$$

Then equation A.4 can be expressed in the matrix form as

$$\begin{bmatrix} c_{11} & \cdot & \cdot & c_{1N} \\ \cdot & \cdot & \cdot & \cdot \\ \cdot & \cdot & \cdot & \cdot \\ c_{N1} & \cdot & \cdot & c_{NN} \end{bmatrix} \begin{bmatrix} a_1 \\ \cdot \\ \cdot \\ a_N \end{bmatrix} = \lambda \begin{bmatrix} a_1 \\ \cdot \\ \cdot \\ a_N \end{bmatrix} \quad (\text{A.6})$$

From equation A.2, the POD modes can be defined as

$$\phi^n(x) = \frac{1}{\lambda^n N} \sum_{j=1}^N a_j^n u_j(\bar{x}, t)$$

(
A.7)

A.3 Sample POD Code

```

clc
clear all;
close all;
% *****
% READING PIV DATA
% *****
addpath 'E:\PIV-analysis\XY\turn8\Vector';

rootname = 'eight';           % Root filename
extname = '_TE00_V1_turn8';   % Run number and test number
save('extname.mat',extname');
extension_1 = '.vec';         % Extension of the PIV files
extension_2 = '.mat';         % Extension for saving files
save('extension_2.mat',extension_2');
m=99;                         % Enter from PIV file
n=74;                         % Enter from PIV file
save('shape.mat','m','n');
L=m*n;                         % Calculating length of matrix
save('L.mat','L');
N=3000;                       % No of PIV files to read
save('PIV.mat','N');
[I,x] = imread('E:\PIV-analysis\XY\calib_image\calibration.tif');
figure, imshow(I)
[p q] = ginput;
close;
pix_dis = max(p)-min(p);
% enter the pixel distance in centimeter
prompt = {'Distance in cm'}
answer = inputdlg(prompt,'Distance',1,{ '4'})
dis = str2double(sprintf('%s',answer{1}));
hs = dis/pix_dis; %spatial_resolution
% enter the pixel distance in centimeter
prompt = {'Enter dt in milli seconds'}
answer = inputdlg(prompt,'dt',1,{ '5.2'})
dt = str2num(sprintf('%s',answer{1}));
% conversion factor (Pixel to cm/s)
hcms=hs*1000/dt;
for i=1:N
    clear a;
    variable=num2str((i-1),'%05d');
    temp=strcat(rootname,variable);
    pivfilename=strcat(temp,extension_1);
    fid=fopen(pivfilename);
    a = textscan(fid,'%f %f %f %f',L, 'delimiter',' ', 'headerlines',1);
    U(:,i) = (a{1,3}{:,1});%*hcms;
    V(:,i) = (a{1,4}{:,1});%*hcms;
    fclose(fid);
end

```

```

end
x(:,1)=a{1,1}{:,1};%*hs;
y(:,1)=a{1,2}{:,1};%*hs;
clear a;
clear temp;
clear name;
clear filename;
name = 'given_vel';
temp = strcat(name,extname);
filename=strcat(temp,extension_2);
save (filename,'U','V');
clear temp;
clear name;
clear filename;
name = 'given_grid';
temp = strcat(name,extname);
filename=strcat(temp,extension_2);
save (filename,'x','y');
%*****
% CALCULATING FLUCTUATION VELOCITY
%*****
clc
clear all;
close all;
load extname;
load extension_2;
load PIV;
clear temp;
clear name;
clear filename;
name = 'given_vel';
temp = strcat(name,extname);
filename=strcat(temp,extension_2);
load (filename);
fluct_u = U - repmat(mean(U,2),1,size(U,2));
fluct_v = V - repmat(mean(V,2),1,size(V,2));
clear temp;
clear name;
clear filename;
name = 'fluct_vel';
temp = strcat(name,extname);
filename=strcat(temp,extension_2);
save (filename,'fluct_u','fluct_v');
%*****
% CALCULATING INNER PRODUCT MATRIX 'A' FOR EACH VELOCITY FIELD WITH ALL OTHER VELOCITY
%FIELDS. IT WILL BE A SYMMETRICAL MATRIX
%*****
clc
clear all;
close all;
load extname;
load extension_2;
load PIV;

```



```

clear temp;
clear name;
clear filename;
name = 'fluct_vel';
temp = strcat(name,extname);
filename=strcat(temp,extension_2);
load (filename);
c1 = fluct_u'*fluct_u;
c2 = fluct_v'*fluct_v;
c=(c1+c2)/size(fluct_u,2);
clear temp;
clear name;
clear filename;
name = 'C';
temp = strcat(name,extname);
filename=strcat(temp,extension_2);
save (filename,'c');
%*****
% THIS PART OF THE PROGRAM CALCULATES EIGNE VALUES AND EIGEN VECTORS OF THE C MATRIX
%*****
clc
clear all;
close all;
load extname;
load extension_2;
clear temp;
clear name;
clear filename;
name = 'C';
temp = strcat(name,extname);
filename=strcat(temp,extension_2);
load(filename);
[A B]= eigs(c,size(c,1));
eig_val=diag(B);
eig_vec=A;
for i = 1:length(eig_val)
    if eig_val(i) <= 0
        eig_val(i) = 0;
    end
end
clear temp;
clear name;
clear filename;
name = 'eig_val';
temp = strcat(name,extname);
filename=strcat(temp,extension_2);
save (filename,'eig_val');
clear temp;
clear name;
clear filename;
name = 'eig_vec';
temp = strcat(name,extname);
filename=strcat(temp,extension_2);

```

```

save (filename,'eig_vec');
tenergy = sum(eig_val);
eig_val_norm=eig_val/tenergy;
clear temp;
clear name;
clear filename;
name ='eig_val_norm';
temp = strcat(name,extname);
filename=strcat(temp,extension_2);
save (filename,'eig_val_norm');
%*****
% THIS PART OF THE PROGRAM CALCULATES NON-NORMALIZED MODES FROM THE EIGEN VECTORS
%OBTAINED
%*****
clc
clear all;
close all;
load extname;
load extension_2;
clear temp;
clear name;
clear filename;
name ='eig_vec';
temp = strcat(name,extname);
filename=strcat(temp,extension_2);
load(filename);
clear temp;
clear name;
clear filename;
name ='fluct_vel';
temp = strcat(name,extname);
filename=strcat(temp,extension_2);
load(filename);
phi_uu = fluct_u * eig_vec;
phi_vv = fluct_v * eig_vec;
clear temp;
clear name;
clear filename;
name ='modes';
temp = strcat(name,extname);
filename=strcat(temp,extension_2);
save (filename,'phi_uu','phi_vv');
%*****
% THIS PART OF THE PROGRAM CALCULATES THE INNER PRODUCT OF MODES
%*****
clc
clear all;
close all;
load extname;
load extension_2;
load PIV;
clear temp;
clear name;

```

```

clear filename;
name = 'modes';
temp = strcat(name,extname);
filename=strcat(temp,extension_2);
load(filename);
inner_phi_uu = (phi_uu'*phi_uu);
inner_phi_vv = (phi_vv'*phi_vv);
inner_product_phi=inner_phi_uu + inner_phi_vv;
clear temp;
clear name;
clear filename;
name = 'inner_phi';
temp = strcat(name,extname);
filename=strcat(temp,extension_2);
save (filename,'inner_product_phi');
%*****
% THIS PART OF THE PROGRAM CALCULATES THE NORMALIZED MODES
%*****
clc
clear all;
close all;
load extname;
load extension_2;
load PIV;
clear temp;
clear name;
clear filename;
name = 'modes';
temp = strcat(name,extname);
filename=strcat(temp,extension_2);
load(filename);
clear temp;
clear name;
clear filename;
name = 'inner_phi';
temp = strcat(name,extname);
filename=strcat(temp,extension_2);
load(filename);
value=diag(inner_product_phi);
clear phi_vv;
clear inner_product_phi;
value= value';
val = repmat(sqrt(value),size(phi_uu,1),1);
phi_u = phi_uu./val;
clear temp;
clear name;
clear filename;
name = 'phi_norm_u';
temp = strcat(name,extname);
filename=strcat(temp,extension_2);
save (filename,'phi_u');
clc
clear all;

```

```

close all;
load extname;
load extension_2;
load PIV;
clear temp;
clear name;
clear filename;
name = 'modes';
temp = strcat(name,extname);
filename=strcat(temp,extension_2);
load(filename);
clear temp;
clear name;
clear filename;
name = 'inner_phi';
temp = strcat(name,extname);
filename=strcat(temp,extension_2);
load(filename);
value=diag(inner_product_phi);
clear phi_uu;
clear inner_product_phi;
value= value';
val = repmat(sqrt(value),size(phi_vv,1),1);
phi_v = phi_vv./val;
clear temp;
clear name;
clear filename;
name = 'phi_norm_v';
temp = strcat(name,extname);
filename=strcat(temp,extension_2);
save (filename,'phi_v');
% Checking
clc;
clear all;
close all;
load extname;
load extension_2;
load PIV;
clear temp;
clear name;
clear filename;
name = 'phi_norm_u';
temp = strcat(name,extname);
filename=strcat(temp,extension_2);
load(filename);
clear temp;
clear name;
clear filename;
name = 'phi_norm_v';
temp = strcat(name,extname);
filename=strcat(temp,extension_2);
load(filename);
z1 = phi_u'*phi_u;

```

```

z2 = phi_v'*phi_v;
z = z1+z2;
clear temp;
clear name;
clear filename;
name = 'test_phi';
temp = strcat(name,extname);
filename=strcat(temp,extension_2);
save (filename,'z');
%*****
%THIS PART OF THE PROGRAM CALCULATES TIME VARYING COEFFICIENTS
%*****
clc
clear all;
close all;
load extname;
load extension_2;
clear temp;
clear name;
clear filename;
name = 'fluct_vel';
temp = strcat(name,extname);
filename=strcat(temp,extension_2);
load(filename);
clear temp;
clear name;
clear filename;
name = 'phi_norm_u';
temp = strcat(name,extname);
filename=strcat(temp,extension_2);
load(filename);
clear fluct_v;
aot_u = phi_u'*fluct_u;
clear phi_u;
clear temp;
clear name;
clear filename;
name = 'phi_norm_v';
temp = strcat(name,extname);
filename=strcat(temp,extension_2);
load(filename);
clear temp;
clear name;
clear filename;
name = 'fluct_vel';
temp = strcat(name,extname);
filename=strcat(temp,extension_2);
load(filename);
clear fluct_u;
aot_v = phi_v'*fluct_v;
clear fluct_v;
aot = aot_u+aot_v;
z = (aot*aot')/size(aot,1);

```

```
clear temp;
clear name;
clear filename;
name = 'aot';
temp = strcat(name,extname);
filename=strcat(temp,extension_2);
save (filename,'aot');
clear temp;
clear name;
clear filename;
name = 'test_aoti';
temp = strcat(name,extname);
filename=strcat(temp,extension_2);
save (filename,'z');
```

A.4 Hilbert Transform

The Hilbert transform is a mathematical technique which is defined as

$$x_h(t) = \frac{1}{\pi} \int_{-\infty}^{\infty} \frac{x(\tau)}{t - \tau} d\tau \quad \text{A.8}$$

This transform converts a real signal ($x_r(t)$) in time domain to another real signal ($x_h(t)$) in time domain with a 90-degree phase shift (Lyons 2004). Once the Hilbert transform of a signal is calculated, the analytic signal is obtained as follows:

$$x_a(t) = x_r(t) + jx_h(t) \quad \text{A.9}$$

The analytic signal ($x_a(t)$) is a complex signal obtained by adding a signal with its Hilbert transform in the imaginary part. Once the analytic signal is constructed, the phase of the real signal is defined as

$$\phi = \tan^{-1} \left(\frac{x_h}{x_r} \right) \quad \text{A.1}$$

0

REFERENCES

- Arcoumanis, C., McQuirk, J.J. & Palma, J.M.L.M. 1990 On the use of fluorescent dyes for concentration measurements in water flows. *Exp. Fluids* 10(2-3), 177-180.
- Bays-Muchmore, B. & Ahmed, A. 1993 On streamwise vortices in turbulent wakes of cylinders. *Phys. Fluids A* 5(2), 387-392.
- Bearman, P.W. 1965 Investigation of the flow behind a two-dimensional model with a blunt trailing edge and fitted with splitter plates. *J. Fluid Mech.* 21, 241-255.
- Bearman, P.W. 1967 The effect of base bleed on the flow behind a two-dimensional model with a blunt trailing edge. *Aero. Quart.* 18, 207-224.
- Bearman, P.W. & Owen, J.C. 1998 Reduction of bluff body drag and suppression of vortex shedding by the introduction of wavy separation lines. *J. Fluids and Struct.* 12, 123-130.
- Bernal, L.P. & Roshko, A. 1986 Streamwise vortex structure in plane mixing layers. *J. Fluid Mech.* 170, 499-525.
- Barkley, D. & Henderson, R.D. 1996 Three-dimensional floquet stability analysis of the wake of a circular cylinder. *J. Fluid Mech.* 322, 215-241.
- Brede, M., Eckelmann, H. & Rockwell, D. 1996 On secondary vortices in the cylinder wake. *Phys. Fluids* 8(8), 2117-2124.
- Blackburn, H.M. & Lopez, J.M. 2003 On three-dimensional quasi-periodic floquet instabilities of two-dimensional bluff body wakes. *Phys. Fluids* 15 (8), L57-L60.
- Bonnet, J.P., Lewalle, J. & Glauser, M.N. 1996 Coherent structures, past, present, and future. *Advances in Turbulence, Proceedings of the European Turbulence Conference*, 6, 83-90.
- Bull, M.K., Li, Y. & Pickles, J.M. 1995 Effects of boundary layer transition on vortex shedding from thick plates with faired leading edge and square trailing edge. Proc. 12th Australasian Fluid Mechanics Conference, Sydney, Australia, 231-234.
- Carmo, B. S., Sherwin, S.J., Bearman, P.W. & Willden, R.H.J. 2008 Wake transition in the flow around two circular cylinders in staggered arrangements. *J. Fluid Mech.* 597, 1-29.
- Cantwell, B. & Coles, D. 1983 An experimental study of entrainment and transport in the turbulent near-wake of a circular cylinder. *J. Fluid Mech.* 136, 321-374.

Chyu, C. & Rockwell, D. 1996 Evolution of patterns of streamwise vorticity in the turbulent near wake of a circular cylinder. *J. Fluid Mech.* **320**, 117-137.

Citriniti, J.H. & George, W.K. 2000 Reconstruction of the global velocity field in the axisymmetric mixing layer utilizing the proper orthogonal decomposition. *J. Fluid Mech.* **418**, 137-166.

Cizmas, P.G., Palacios, A., Brien, T.O. & Syamlal, M. 2003 Proper-orthogonal decomposition of spatio-temporal patterns in fluidized beds. *J. Chem. Engg. Sci.* **58** (19), 4417-4427.

Cohen, K., Siegel, S., Wetlsen, D., Cameron, J. & Sick, A. 2004 Effective sensor placements for the estimation of proper orthogonal decomposition mode coefficients in von Karman vortex street. *J. Vibration and Control*, **10**, 1857-1880.

Cowen, E.A. & Monismith, S.G. 1997 A hybrid digital particle tracking velocimetry technique. *Exp. Fluids* **22**, 199-211.

Cruz, A.S., David, L., Pecheux, J. & Texier, A. 2005 Characterization by proper orthogonal decomposition of the passive controlled wake flow downstream of a half cylinder," *Exp. Fluids*, **39**, 730-742.

Darekar, R.M. & Sherwin, S.J. 2001 Flow past a square-section cylinder with wavy stagnation face. *J. Fluid Mech.* **426**, 263-295.

Deane, A.E., Kevrekidis, I.G., Karniadakis, G.E. & Orszaga, S.A. 1991 Low-dimensional models for complex geometry flows: application to grooved Channels and circular cylinders. *Phys. Fluids* **3** (10), 2337-2354.

Dobre, A. & Hangan, H. 2004 Investigation of the three-dimensional intermediate wake topology for a square cylinder at high Reynolds number. *Exp. Fluids* **37** 518-530.

Dobre, A., Hangan, H. & Vickery, B.J. 2006 Wake control based on spanwise sinusoidal perturbation. *AIAA J.* **44** (3), 485-492.

Durgesh, V. & Naughton, J.W. 2010 Multi-time-delay LSE-POD complimentary approach applied to unsteady high-Reynolds-number near wake flow. *Exp. Fluids* **49** 571-583.

Eisenlohr, E. & Eckelmann, H. 1988 Observations in the laminar wake of a thin flat plate with a blunt trailing edge. *Proc. Conference on Experimental Heat Transfer, Fluid Mechanics, and Thermodynamics*, Dubrovnik, Yugoslavia, 264-268.

El-Akoury, R., Braza, M., Perrin, R., Harran, G. & Hoarau, Y. 2008 Three-dimensional transition in the flow around rotating cylinder. *J. Fluid Mech.* **607**, 1-11.

- El-Gammal, M. 2007 3-D Flow Dynamics and control of nominally 2-D shedding bodies. *PhD Thesis*, University of Western Ontario, London, ON, Canada
- El-Gammal, M. & Hangan, H. 2008 Three-dimensional wake dynamics of a blunt and divergent trailing edge airfoil. *Exp. Fluids* **44**, 705-717.
- Gad-el-Hak, M. 1988 Visualization techniques for unsteady flows: An overview. *J. Fluids* **110**, 231-243.
- Gad-el-Hak, M., Pollard, A. & Bonnet, J.P. 1998 Flow Control: Fundamentals and Practices. New York: Springer-Verlag.
- Gillies, E.A. 2000 Multiple Sensor Control of Vortex Shedding. *AIAA J.* **39**, No. 4, 748-750.
- Griffin, O.M. 1995 A note on bluff body vortex formation. *J. Fluid Mech.* **284**, 217-224.
- Holmes, P., Lumley, J.L. & Berkooz, G. 1996 Turbulence, Coherent Structures, Dynamical System and Symmetry. Cambridge, 1st ed.
- Hussain, A.K.M.F. & Hayakawma, M. 1987 Eduction of large-scale organized structure in a turbulent plane wake. *J. Fluid Mech.* **180**, 193-229.
- Johansson, P.B.V., George, W.K. & Woodward, S.H. 2002 Proper orthogonal decomposition of an axisymmetric turbulent wake behind a disk. *Phys. Fluids* **14**, 2508.
- Julien, S., Lasheras, J. & Chomaz, J. 2003 Three-dimensional instability and vorticity patterns in the wake of a flat plate. *J. Fluid Mech.* **479**, 155-189.
- Karniadakis, G. E. & Triantafyllou, G. 1992 Three-dimensional dynamics and transition to turbulence in the wake of bluff objects *J. Fluid Mech.* **238**, 1-30.
- Kim, J. & Choi, H. 2005 Distributed forcing of flow over a circular cylinder. *Phys. Fluids* **17**, 033103, 1-16.
- Konstantinidis, E., Balabani, S. & Yianneskis, M. 2005 Conditional averaging of PIV plane wake data using a cross-correlation approach. *Exp. in Fluids* **39**, 38-47.
- Kostas, J., Soria, J. & Chong, M.S. 2005 A Comparison Between Snapshot POD Analysis of PIV Velocity and Vorticity Data. *Exp. Fluids*, **38**, 146-160.
- Lam, K., Wang, F.H. & Soa, R.M.C. 2004 Three-dimensional nature of vortices in the near wake of a wavy cylinder. *J. Fluids and Struct.* **19**, 815-833.

- Lam, K. & Lin, Y.F. 2009 Effect of wavelength and amplitude of a wavy cylinder in cross flow at low Reynolds numbers. *J. Fluid Mech.* **620**, 195-220.
- Lee, S.J. & Nguyen, A. 2007 Experimental investigation on wake behind a wavy cylinder having sinusoidal cross-sectional area variation. *Fluid Dynamics Research* **39**, 292-304.
- Lumley, J.L. 1967 The Structure of Inhomogeneous Turbulence. *Atmospheric Turbulence and Radio Wave Propagation*, edited by Yaglom, A.M. & Tatarski, V.I., Nauka, Moscow, 166-178.
- Luo, S.C., Chew, Y.T. & Ng, Y.T. 2003 Characteristics of square cylinder wake transition flows. *Phys. Fluids* **15**(9), 2549-2559.
- Luo, S.C., Tong, X.H. & Khoo, B.C. 2007 Transition phenomena in the wake of a square cylinder. *J. Fluids Struct.* **23**, 227-248.
- Lyons, R.G. 2004 Understanding Digital Signal Processing. Prentice Hall, 2nd ed.
- Mansy, H., Yang, P.M. & Williams, D. 1994 Quantitative measurements of three-dimensional structures in the wake of a circular cylinder. *J. Fluid Mech.* **270**, 227-296
- Maurel, S., Boree, J. & Lumley, J.L. 2001 Extended Proper Orthogonal Decomposition: Application to Jet/Vortex Interaction. *Flow Turb. Combust.* **67**, 125-136
- Meiburg, E. & Lasheras, J.C. 1988 Experimental and Numerical Investigation of the Three-Dimensional Transition in Plane Wakes. *J. Fluid Mech.* **190**, 1-37.
- Mittal, R. & Balachandar, S. 1995 Generation of streamwise vortical structures in bluff body wakes. *Phys. Rev. Lett.* **75**, 1300
- Noack, B.R., Afanasiev, K., Morzynski, M., Tadmor, G. & Thiele, F. 2003 A hierarchy of low-dimensional models for the transient and post-transient cylinder Wake. *J. Fluid Mech.* **497**, 335-363.
- Park, H., Lee, D., Jeon, W., Hahn, S., Kim, J., Kim, J., Choi, J. & Choi, H. 2006 Drag reduction in flow over a two-dimensional bluff body with a blunt trailing edge using a new passive device. *J. Fluid Mech.* **563**, 389-414.
- Perrin, R., Braza, M., Cid, E., Cazin, S., Barthet, A., Sevrain, A., Mockett, C. & Thiele, F. 2007 Obtaining phase averaged turbulence properties in the near wake of a circular cylinder at high Reynolds number using POD. *Exp. Fluids* **43**, 341-355.
- Petrusma, M.S. & Gai, S.L. 1996 Bluff body wakes with free, fixed and discontinuous separation at low Reynolds numbers and low aspect ratio. *Exp. Fluids* **20**, 189-198

- Pinier, J.T., Ausseur, J.M., Glauser, M.N. & Higuchi, H. 2007 Proportional Closed-Loop Feedback Control of Flow Separation. *AIAA J.* **45**(1), 181-217.
- Prasad, A. & Williamson, C.H.K. 1997 The instability of the shear layer separating from a bluff body. *J. Fluid Mech.* **333**, 375-402.
- Prasad, A.K., Adrain, R.J., Landreth, C.C. & Offutt, P.W. 1992 Effect of resolution on the speed and accuracy of particle image velocimetry interrogation. *Exp. Fluids* **13**, 105-116.
- Raffel, M., Willert, C. & Kompenhans, J. 1998 Particle image velocimetry: a practical guide. 2nd ed., *Berlin: Springer*.
- Reynolds, W.C. & Hussain, A.K.M.F. 1972 The mechanics of an organized wave in turbulent shear flow. Part 3. Theoretical models and comparisons with experiments. *J. Fluid Mech.* **54**, 263-288.
- Robichaux, J., Balachandar, S. & Vanka, S.P. 1999 Three-dimensional floquet instability of the wake of square cylinder. *Phys. Fluids* **11**(3), 560–578.
- Robinson, S.K. 1991 Coherent motion in the turbulent boundary layers. *Ann. Rev. Fluid Mech.* **23**, 601-639.
- Rogers, M.M. & Moser, R.D. 1993 Spanwise scale selection in plane mixing layer. *J. Fluid Mech.* **247**, 321–337.
- Rowley, C.W., Colonius, T. & Murray, R. M. 2004 Model reduction for compressible flows using POD and Galerkin Projection. *Physica D*, **189**, 115-129.
- Ryan, K., Thompson, M.C. & Hourigan, K. 2005 Three-dimensional transition in the wake of elongated bluff bodies. *J. Fluid Mech.* **538**, 1-29.
- Sarathi, P. 2009 Experimental study of the scalar concentration field in turbulent flows. *PhD Thesis*, University of Western Ontario, London, ON, Canada.
- Schlichting, H. & Gersten, K. 2000 Boundary-Layer Theory, 8th ed., Springer-Verlag, Germany, ISBN: 3-540-66270-7.
- Sheard, G.J., Thompson, M.C., Hourigan, K. & Leweke, T. 2005 The evolution of a subharmonic mode in a vortex street. *J. Fluid Mech.* **534**, 23-28.
- Sheard, G.J. 2007 Cylinders with Elliptic Cross-Section: Wake Stability with Variation in Angle of Incidence. *Proc. IUTAM Symposium on Unsteady Separated Flows and Their Control*, Corfu Island, Greece.

- Sheard, G.J., Fitzgerald, M.J. & Ryan, K. 2009 Cylinders with square cross-section: wake instabilities with incidence angle variation. *J. Fluid Mech.* **630**, 43-69.
- Siddiqui, K. 2002 Laboratory measurements of the flow beneath microscale breaking waves. *PhD Thesis*, University of Toronto, Toronto, ON, Canada
- Sirovich, L. 1987 Turbulence and the Dynamics of Coherent Structures. *Quart. App. Math* **45**, 561-590.
- Smith, T.R., Moehlis, J. & Holmes, P. 2005 Low-dimensional modeling of turbulence using the Proper Orthogonal Decomposition: A Tutorial. *Non-linear Dynamics* **41**, 275-307.
- Tanner, M. 1972 A method for reducing the base drag of wings with blunt trailing edge. *Aero. Qrt.* **23**,15-23.
- Tombazis, N. & Bearman, P.W. 1997 A Study of three-dimensional aspects of vortex shedding from a bluff body with a mild geometric disturbance. *J. Fluid Mech.* **330**, 85-112.
- Tong, X.H., Luo, S.C. & Khoo, B.C. 2008 Transition phenomena in the wake of an inclined square cylinder. *J. Fluids Struct.* **24**, 994-1005.
- Unal, M. & Rockwell, D. 1988 On vortex shedding from a cylinder. Part 1. The initial instability. *J. Fluid Mech.* **190**, 491-512.
- Van Oudheusden, B.W., Scarano, F., Van Hinsberg, N.P. & Watt, D.W. 2005 Phase-resolved characterization of vortex shedding in the near wake of a square-section cylinder at incidence. *Exp. Fluids* **39**, 86-98.
- van Oudheusden, B.W., Scarano, F., Roosenboom, E.W.M., Casimiri, E.W.F. & Souverein, L.J. 2007 Evaluation of Integral Forces and Pressure Fields from Planar Velocimetry Data for Incompressible and Compressible Flows. *Exp. Fluids* **43**, 153-162.
- Wei, T. & Smith., C.R. 1986 Secondary vortices in the wake of circular cylinders. *J. Fluid Mech.* **169**, 513-533.
- Williams, D.R., Mansy, H. & Abouel-Fotouh, A. 1995 Three-dimensional subharmonic waves during transition in the near-wake region of a cylinder. *Phys. Fluids A* **8**, 1476-1485.
- Williamson, C.H.K. 1992 The natural and forced formation of spot-like 'vortex dislocations' in the transition of a wake. *J. Fluid Mech.* **243**, 393-441.

Williamson, C.H.K. 1996 Vortex dynamics in cylinder Wake. *Annu. Rev. Fluid Mech.* **28**, 477-539.

Wlezien, R.W. & Way, J.L. 1979 Techniques for the experimental investigation of the near wake of a circular cylinder. *AIAA J* **17**, 563-570.

Wu, J., Sheridan, J., Welsh, M.C. & Hourigan, K. 1996 Three-dimensional vortex structures in a cylinder wake. *J. Fluid Mech.* **312**, 201-222.

Zdravkovich, M.M. 1981 Review and classification of various aerodynamics and hydrodynamic means of suppressing vortex shedding. *J. Wind Engg. Indust. Aero.* **7**, 145-189.

Zhang, H., Fey, U., Noack, B.R., Konig, M. & Eckelmann, H. 1995 On the transition of the cylinder wake. *Phys. Fluids* **7**(4), 779-794.

Zhou, Y. & Antonia, R.A. 1992 Convection velocity measurements in a cylinder wake, *Exp. Fluids* **13**, 63-70.

CURRICULUM VITAE

Name	Lakshmana Sampat Doddipatla
Place of birth	Tanuku, India
Post-secondary Education and Degrees	<p>Mechanical Engineering, Indian Institute of Technology Madras, Chennai, India. 2002 – 2004, M.S.</p> <p>Mechanical Engineering, Andhra University, Visakhapatnam, India. 1997 – 2001, B.E.</p>
Honors and Awards	<p>Western Graduate Research Scholarship (WGRS), The University of Western Ontario, ON, Canada. (2006-2010)</p> <p>Ministry of Human Resource Development (MHRD) scholarship, Indian Institute of Technology Madras, Chennai, India. (2002-2004)</p>
Work Experience	<p>Teaching Assistant, The University of Western Ontario, ON, Canada. (2006-2010)</p> <p>Research Assistant, The University of Western Ontario, ON, Canada. (2006-2010)</p> <p>Sr. Engineer, Engineering Research Centre (ERC), TATA Motors, Pune, India. (2004-2006)</p> <p>Research Assistant, Indian Institute of Technology Madras, Chennai, India. (2002-2004)</p>

Publications:*Journal Papers*

1. Govardhan, M. & Doddipatla, L.S. 2005 Computational Studies of Flow through Cross Flow Fans - Effect of Blade Geometry. *J. Thermal Sci.* **14(3)**, 220-229.
2. Doddipatla, L.S., Lahouthi, A.N. & Hangan, H. Near wake topology of a profiled blunt trailing edge body. *J. Fluid Mech.*, in preparation
3. Doddipatla, L.S., Hangan, H., Durgesh, V. & Naughton, J.W. Wake dynamics resulting from trailing edge spanwise sinusoidal perturbation. *Exp. Fluids*, in preparation

Conference Papers

1. Doddipatla, L. S., Lahouti, A.N., Hangan, H. & Siddiqui, K. 2010 Coherent structures in the near wake of a blunt trailing edge profiled body. *ASME Fluids Engineering Summer Meeting*, Aug 1-4, Montreal, Quebec.
2. Doddipatla, L. S., Lahouti, A.N., Siddiqui, K. & Hangan, H. 2010 The near-wake structure of a blunt trailing edge profiled body - Part 2: PLIF and PIV measurements. *40th AIAA Fluid Dynamics Conference and Exhibit*, June 28- July 1, Chicago, Illinois.
3. Doddipatla, L. S., Lahouti, A.N., Hangan, H. & Siddiqui, K. 2010 The near-wake topology of a blunt trailing edge profiled body. *6th IUTAM Symposium on Bluff Body Wakes and Vortex-Induced Vibrations*, 22-25 June, Capri Island, Italy.
4. Doddipatla, L.S., Lahouti, A.N. & Hangan, H. 2010 Near wake structure of a blunt trailing edge profiled flat plate. *1000 Island Fluids Mechanics Meeting*, April 23-25, Gananoque, Ontario.
5. Doddipatla, L.S., Lahouti, A.N., Hangan, H. & Siddiqui, K. 2009 Near wake flow topology of a blunt trailing edge profiled flat plate. *62nd Annual Meeting of the APS Division of Fluid Dynamics*, November 22-24, Minneapolis, Minnesota.
6. Doddipatla, L.S., Hangan, H., Durgesh, V. & Naughton, J.W. 2009 Passive flow control of a flat plate with trailing edge spanwise sinusoidal perturbation. *ASME Fluids Engineering Summer Meeting*, August 2-6, Vail, Colorado.
7. Doddipatla, L.S., Lahouti, A.N. & Hangan, H. 2009 Reynolds number dependency of the near wake structure of a blunt trailing edge profiled body. *11th American Conference on Wind Engineering*, June 22-26, Puerto Rico.
8. Doddipatla, L.S., Hangan, H., Durgesh, V. & Naughton, J.W. 2008 Wake energy redistribution due to trailing edge spanwise perturbation. *6th International Colloquium on Bluff Bodies Aerodynamics and Applications*, 20 - 24 July, Milano, Italy

9. Doddipatla, L.S., Hangan, H., Durgesh, V. & Naughton, J.W. 2008 Near-wake flow dynamics resulting from trailing edge spanwise perturbation. *4th AIAA Flow Control Conference*, 23 - 26 June, Seattle, Washington.
10. Doddipatla, L.S., Hangan, H., Durgesh, V. & Naughton, J.W. 2008 POD analysis of near wake structure with and without spanwise perturbation. *1000 Island Fluids Mechanics Meeting*, April 25-27, 2008, Gananoque, Ontario.

M.Sc. Thesis

Doddipatla, L. S. 2004 Computational Studies of Flow through Cross Flow Fan. Indian Institute of Technology Madras, Chennai, India.